DISSERTATION / DOCTORAL THESIS

Titel der Dissertation /Title of the Doctoral Thesis

„ Deformation Behavior and Seismic Anisotropy of Tibetan Lithosphere: constraints from mantle xenoliths "

verfasst von / submitted by

Yu Yang

angestrebter akademischer Grad / in partial fulfilment of the requirements for the degree of

Doktorin der Naturwissenschaften (Dr. rer. nat.)

Wien, 2020 / Vienna 2020

Studienkennzahl lt. Studienblatt / degree programme code as it appears on the student record sheet:	A 796 605 426
Dissertationsgebiet lt. Studienblatt / field of study as it appears on the student record sheet:	Erdwissenschaften / Earth sciences
Betreut von / Supervisor:	Univ. -Prof. Dr. Rainer Abart
Betreut von / Supervisor:	Ao. Univ. -Prof. i.R. Dr. Theodoros Ntaflos
Mitbetreut von / Co-Supervisor:	

Dedicated to my parents

without whom this thesis would never have been completed

谨以此书献给我的父母

感谢他们一直以来对我的支持和鼓励

To everyone who inspired me during this journey

感谢这一路上帮助过我的人

Mount Kailash

is a 6638m high peak in the Gangdese Batholith which forms part of the Himalaya in the Lhasa terrane.

Sample collection site

Upper: in the Qiangtang National Reserve

Bottom: in the Songpan-Ganze terrane

TABLE OF CONTENTS

List of Figures

List of Tables

Abstract

Volcanism brings up mantle xenoliths that provide insights into the composition, structure and tectonic evolution of the Earth's mantle. Peridotite and subordinate pyroxenite are the main rock types in the continental lithospheric mantle. In this study, peridotite xenoliths from the southwestern, central and northeastern Tibetan Plateau were investigated using microstructural, geochemical and simulation techniques to constrain their deformation history and relationships to geophysical seismic analysis in each region.

Peridotite xenoliths in southwestern Tibet that were brought to the surface from upper mantle by Miocene potassic volcanism show crystal preferred orientation of their olivine with a concentration of the [010] directions and a large circle girdle of the [100] and [001] directions (AG-type) with a seismic polarization anisotropy of 4.6 % on average for shear waves propagating in directions parallel to the girdle plane. Peridotite and pyroxenite xenoliths in the central Tibet were exhumed by Eocene volcanism in the Qiangtang terrane. The peridotite xenoliths can be divided into two fabric types. The xenoliths that represent the uppermost lithospheric mantle are refractory and exhibit AG-type olivine fabric. In contrast, the xenoliths from the lower part were re-fertilized and display a different fabric characterized by B-type with dominant activation of the [001](010) slip system. Peridotite xenoliths in northeastern Tibet erupted between 7.1 and 23 Ma by alkaline and ultra-mafic volcanisms. The olivine fabric mainly shows AG-type, with a few (010)[100] patterns (A-type). Unlike the xenoliths from southwestern and central Tibet, these peridotite xenoliths are characterized by an extraordinary strong anisotropy with 8 % on average.

The limited seismic anisotropy of peridotite xenoliths from southwestern Tibet could not explain the large delay times (1.5 - 2.0 s) observed in this area. Thus, we propose that the additional mechanism is due to the presence of partially molten

Abstract

domains with high aspect ratio that are aligned sub-vertically enhancing the effect of the anisotropy of the peridotites on SKS splitting. The abrupt change of the fast polarization direction from south to central Tibet may reflect the change of the fabric of olivine, which is fundamentally different in the northward subducting Indian lithospheric mantle and in the lithospheric mantle beneath central Tibet. In central Tibet, the velocity structure from lower crust to upper mantle was reconstructed based on the seismic properties of xenoliths, which reveal a vertical dichotomy of the mantle. The possible scenario of deformation leading to a heterogenous mantle is that at an early stage a pre-existing refractory lithospheric mantle experienced a small degree of partial melting. Subsequently, it was heated from the bottom and formed a fertile mantle in the lower part with B-type olivine fabric. The peridotite xenoliths from northeastern Tibet with strong anisotropy of 8 % can cause about 1.16s delay times. This finding may end the long-term discrepancy on mechanisms for delay times that are comparable to those in central Tibet, while the thickness of lithosphere in northeastern Tibet is thinner than in southern and central Tibet.

Zusammenfassung

Durch Vulkanismus werden Xenolithe an die Erdoberfläche gefördert, welche Einblicke in die Zusammensetzung, die Struktur und die tektonische Entwicklung des umgebenden Erdmantels liefern. In dieser Studie wurden Peridotit Xenolithe aus dem südwestlichen, dem zentralen und dem nordöstlichen Tibetischen Plateau mittels microstructureller und geochemischer Methoden und mittels Simulationstechniken untersucht um ihre Deformationsgeschichte mit geophysikalisch seismologischen Analysen in den verschiedenen Regionen in Beziehung zu setzen.

Die Peridotite, die im südwestlichen Tibet durch miozänen kalireichen Vulkanismus an die Oberfläche gebracht wurden, zeigen kristallographisch bevorzugte Orientierungen ihrer Olivine mit einer Konzentration der [010] Richtungen und einer Gürtelverteilung der [100] und [001] Richtungen entlang eines Großkreises (AG-Typ) mit einer durchschnittlichen Polarisationsanisotropie von 4.6% für Scherwellen, deren Ausbreitungsrichtungen in der Ebene des Großkreisgürtels liegen. In der Qiangtang Region in Zentraltibet wurden Peridotit und Pyroxenit Xenolithe durch eozänen Vulkanismus an die Oberfläche gebracht. Die Peridotit Xenlithe können in zwei Gefügegruppen unterteilt werden: Die Xenolithe, welche den obersten lithosphärischen Mantel repräsentieren, sind refraktär und zeigen ein Olivingefüge des AG Typs. Im Gegensatz dazu sind die Xenolithe aus dem tieferen Bereich re-vertilisiert und zeigen ein anderes Gefüge vom B Typ, das durch eine bevorzugte Aktivierung des [001](010) Gleitsystems gekenzeichnet ist. Die Peridotite aus dem nordöstlichen Tibet wurden vor 7.1 bis 23 Millionen Jahren im Zuge von alkalischem und ultranafischem Vulkanismus gefördert. Das Olivingefüge ist vornehmlich vom AG Typ mit wenigen (010)[100] Mustern (A-type). Im Gegensatz zu den Xenolithen aus dem südwestlichen und zentralen Tibet, zeigen diese Xenolithe extrem starke Anisotropie von durchschnittlich 8%.

Abstract

Die schwache seismische Anisotropie der Peridotit Xenolithe aus dem südwestlichen Tibet konnte die grossen im südlichen Tibet beobachteten Wellenverzögerungen von 1.5 -2.0 s bei aufgespaltenen Scherwellen nicht erklären. Wir schlagen als Erklärung für die grossen Wellenverzögerungen das Vorhandensein von vertikal gelagerten linsen- bzw. lagenförmigen teilgeschmolzenen Bereichen vor, welche den Effekt der Anisotropie der Peridotite auf die Aufspaltung von Scherwellen verstärken. Der abrupte Wechsel der schnellen Polarisationsrichtung von südlichen zum zentralen Tibet dürfte einen Wechsel im Gefüge des Olivins reflektieren, welches in der nach Norden subduzierenden Indischen Lithosphäre grundsätzlich anders als im lithosphärischen Mantel unterhalb von Zentraltibet ist. Für Zentraltibet wurde die Geschwindigkeitsstruktur von der unteren Kruste in den Mantel basierend auf den seismischen Eigenschaften von Xenolithen rekonstruiert und zeigt eine vertikale Zweiteilung des Mantels. Ein mögliches Szeanrio für die Deformationsgeschichte, die zu einem heterogenen Mantel führte, besteht darin, dass in einem frühen Stadium ein prä-existierender Mantel partiell aufgeschmolzen wurde. Danach wurde der Mantel von unten aufgeheizt und im unteren Bereich bildete sich eine vertile Zone mit einem B-Typ Olivingefüge. Die Peridotite aus dem nordöstlichen Tibet mit einer starken Anisotropie von 8% würden Wellenverzögerungszeiten von ca. 1.16 s verursachen. Dies löst eine lange während Diskusiosn über die ähnlichen Wellenverzögerungszeiten wie im zentralen Tibet, während die Lithsophäre im nordöstlichen Tibet dünner als im südlichen und zentralen Tibet ist.

Chapter 1

私たちの征途は星の海です
我们的征途是星辰大海
——《银河英雄传说》

Introduction

Starting 70 million years ago, by the closure of the Neo-Tethyan Ocean, the Indian-Eurasian continental collision has built the largest and highest plateau in the world (Yin and Harrison, 2000). The Tibetan plateau is bounded by an active thrust zone along the leading edge of the Himalayan-Tibetan orogen in the south, and restricted to further northward extrusion by the stable North China Craton in the northeast and the strong Tarim basin in the northwest (Yin et al., 2007; Yin and Harrison, 2000; Yuan et al., 2013) (Fig. 1-1). Continuing convergence coincided with a complex tectonic deformation history from surface to deep, including the formation of new faults in the north, north-trending rifts in the center, post-collisional magmatism and thousand kilometers of crustal shortening within the entire plateau (Kapp et al., 2003; Yin and Harrison, 2000; Yuan et al., 2013). Over the past 100 years, despite the understanding of the Indian-Eurasian collision and its impact have advanced rapidly, the deformation processes and dynamic evolution of the Tibetan lithosphere are still unclear and controversial due to lack of detailed geological information (Chung et al., 2005; Yin, 2006).

1.1 Geologic setting of Tibetan Plateau

The Himalayan-Tibetan orogenic belt is a tectonic collage of continental fragments, mainly comprised of Paleozoic to Mesozoic units (Chung et al., 2005; Zhang et al., 2012c). From south to north, the entire region consists of four main terranes, including Himalaya, Lhasa, Qiangtang and Songpan–Ganze, divided by the Indus-Yarlung (IYS), Bangong-Nujiang (BNS), and Jinsha-River (JRS) suture zones,

representative of the Neo-, Meso- and Paleo-Tethyan relicts, respectively (Yin and Harrison, 2000) (Fig. 1).
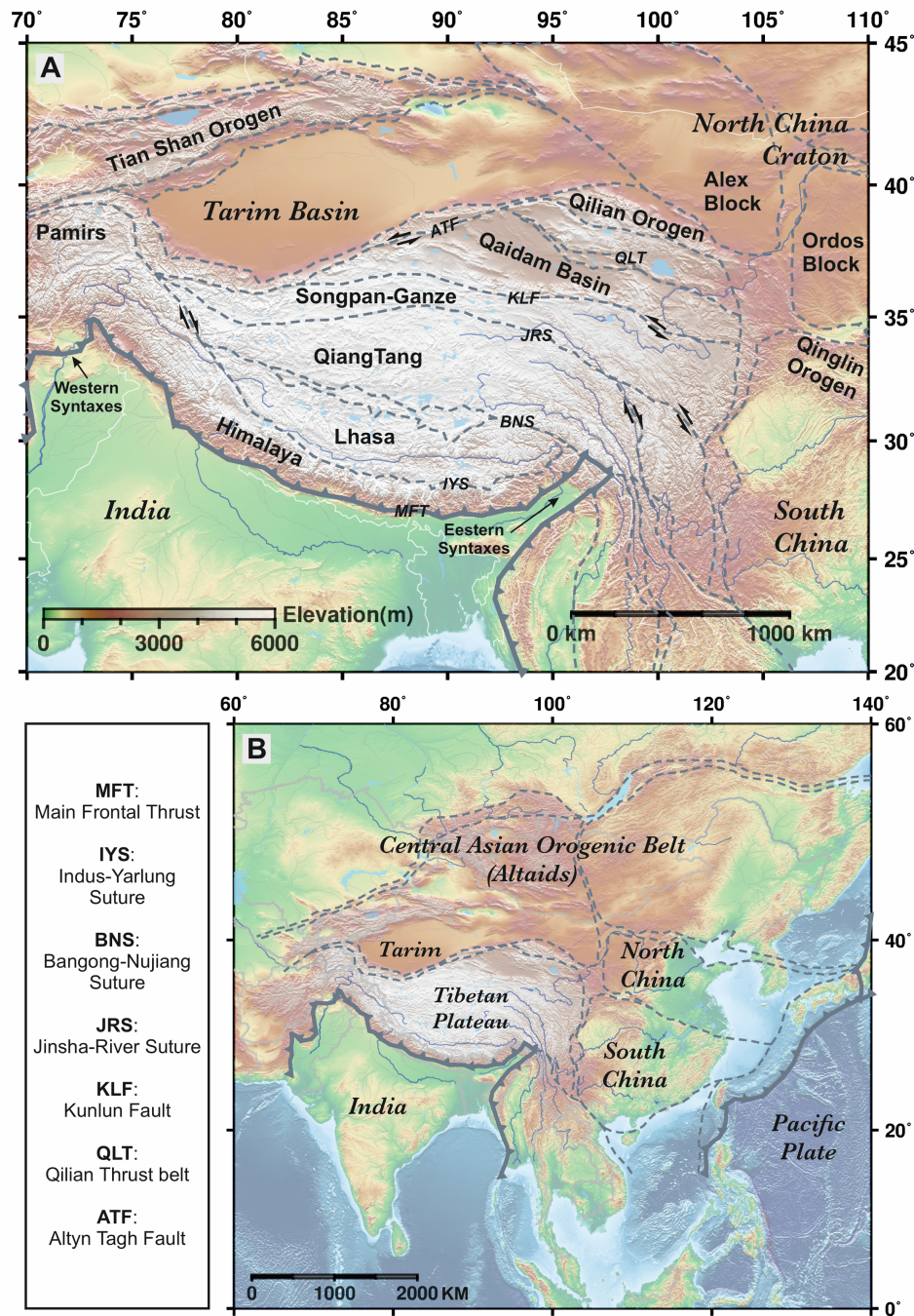
Fig.1-1 (A) Tectonic map of the Tibetan Plateau showing major faults and sutures. (B) Simplified topography of the Eurasia-Indian collision zone and neighboring regions.

1.1.1 Songpan-Ganze terrane

The Songpan-Ganze terrane lies between the left-slip Kunlun fault (KLF) to the north and the Jinsha-River suture to the south, which is floored from a Paleozoic oceanic crust and covered by a sequence of Triassic turbidite strata (Weislogel, 2008; Yin and Harrison, 2000). It experienced high degree of regional deformation and metamorphism, bonded with the North China Craton in northeast by the Qinling orogen, with the Tarim basin in the northwest by the Altyn Tagh fault system, and with the South China Craton in the southeast by the Longmenshan thrust belt (Roger et al., 2003; Weislogel, 2008) (Fig. 1-1). Post-collisional magmatism is distributed across the terrane from 25Ma to present. The magmatic units are comprised of mantle-derived K-rich alkaline rocks and interpreted as a result of both carbonatitic and silicate components in the mantle source (Guo and Wilson, 2019; Su et al., 2009) (Fig. 1-2). The simultaneous acceleration of the deformation rate is reflected by a sequence of fault deformations during Cenozoic time (Duvall et al.; Yuan et al., 2013). The fault systems are concentrated in the eastern Songpan-Ganze terrane with growing eastward expansion strike-slip faults before ~15Ma, and the switch toward northwestward trending thrust faults in the middle to late Miocene (Yuan et al., 2013). The transformation of crustal deformation patterns in northeastern Tibet is possibly a consequence of the northward movement of the entire Tibetan Plateau reaching a limit and migrating northeastward (Tapponnier et al., 1982; Yuan et al., 2013).

1.1.2 Qiangtang terrane

The Qiangtang terrane in the central Tibetan Plateau is divided into eastern and western blocks by an east-west belt of blueschist-bearing metamorphic complexes, which is interpreted to pertain to the Triassic Shuanghu suture zone separating Cathaysian affinity in the west and Gondwanan affinity in the east (Zhang et al., 2012c; Zhu et al., 2013). Alternatively, the intracontinental metamorphic belt may have been exhumed in response to the underthrusting of oceanic lithosphere from

Y

the Jinsha-River suture during the Triassic (Kapp et al., 2003; 2000; Pullen et al., 2008). Subsequent arc magmatisms related to the subduction of Jinsha and Shuanghu Paleo-Tethys overprinted the metamorphic complexes in the Early Mesozoic (Ding, 2003; Wang et al., 2007; Yang et al., 2011). In the Cenozoic (60-45 Ma), Na-rich alkali basalts occur in the northwest part of Qiangtang (Ding, 2003; Ding et al., 2007). Continued northward subduction of the Neo-Tethys oceanic and Indian continental lithosphere caused intensive magmatism and N-S trending rifts across the Qiangtang. Ultrapotassic rocks and calc-alkaline rocks are observed in the eastern and western block during the middle Eocene (46-38 Ma), respectively (Ding et al., 2007; Zhang et al., 2012c) (Fig. 1-2).
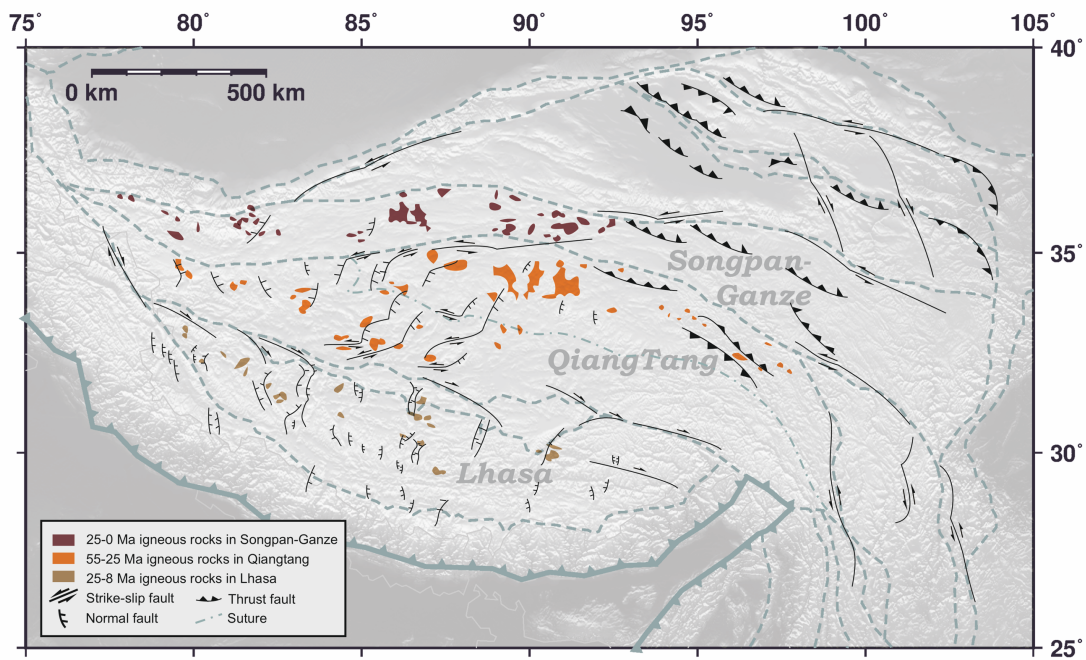
Fig. 1-2 The distribution of major late Cenozoic rifts and magmatism in Tibet

1.1.3 Lhasa terrane

The Lhasa terrane in southern Tibet is located to the south of the Qiangtang terrane and separated from it by the Bangong-Nujiang suture zone (BNS) (Yin and Harrison, 2000; Zhu et al., 2013). The Indus-Yarlung suture zone (IYS), as the

southern boundary, separates the Lhasa block from the Indian continent (Fig. 1-1). During its northward drift from eastern Gondwana, the Lhasa block underwent episodes of Tethyan seafloor subduction, which consequently gave rise to a reworked ancient crust in the west and juvenile additions to its northern and southern edges (Ji et al., 2009; Xu et al., 2017a; Zhu et al., 2013). As a consequence of the Tethyan seafloor subduction and the following continental collision between India and Asia, Mesozoic to early Cenozoic Gangdese batholith are widely distributed in the Lhasa block. Post-collisional magmatism comprising ultrapotassic rocks, potassic rocks and adakite-like rocks occur as lava flows outcropping throughout the Lhasa (Chung et al., 2005; Hou et al., 2015; Liu et al., 2014a; Xu et al., 2017a) (Fig. 1-2). Mantle-derived ultrapotassic rocks, with zircon U–Pb ages varying from 24 Ma to 10 Ma (Liu et al., 2014a; Xu et al., 2017a), are observed across the western Lhasa (Guo et al., 2015; Liu et al., 2011; Miller et al., 1999; Zhao et al., 2009). Concurrent potassic volcanic rocks of intermediate to felsic compositions erupted in the Miocene are mainly distributed in the central and southern Lhasa (Liu et al., 2014a; Miller et al., 1999). Postcollisional adakite-like rocks occur in a narrow, ~1500-km-long, E-W-trending belt, mainly sub-paralleled the IYS in southern Lhasa. The adakite-like magmatism in eastern Lhasa lasted from 38 to 10 Ma and from 19 to 16 Ma in the western part (Chung et al., 2003; Hou et al., 2004).

1.2 Geophysical background of Tibet

During the past several decades, large-scale seismic investigations have been developed in Tibet to delineate the lithospheric architecture at depth (Hirn et al., 1995; McNamara et al., 1994). Most passive-source broadband seismic projects, including the Yadong-Golmd Global Geosciences Transect (Wu et al., 1991), PASSCAL (Owens et al., 1993), INDEPTH (Haines et al., 2003; Kind et al., 1996; Tilmann et al., 2003; Zhao et al., 2011), Hi-CLIMB (Chen et al., 2010; Nábělek et

al., 2009; Nowack et al., 2010; Xu et al., 2011) and ANTILOPE (Xu et al., 2017b; Zhao et al., 2014a; Zhao et al., 2010), record high-quality seismic data and provide valuable findings on the seismic tomographic imaging, 3-D velocity model and seismic anisotropic features in Tibet (Fig. 1-3).
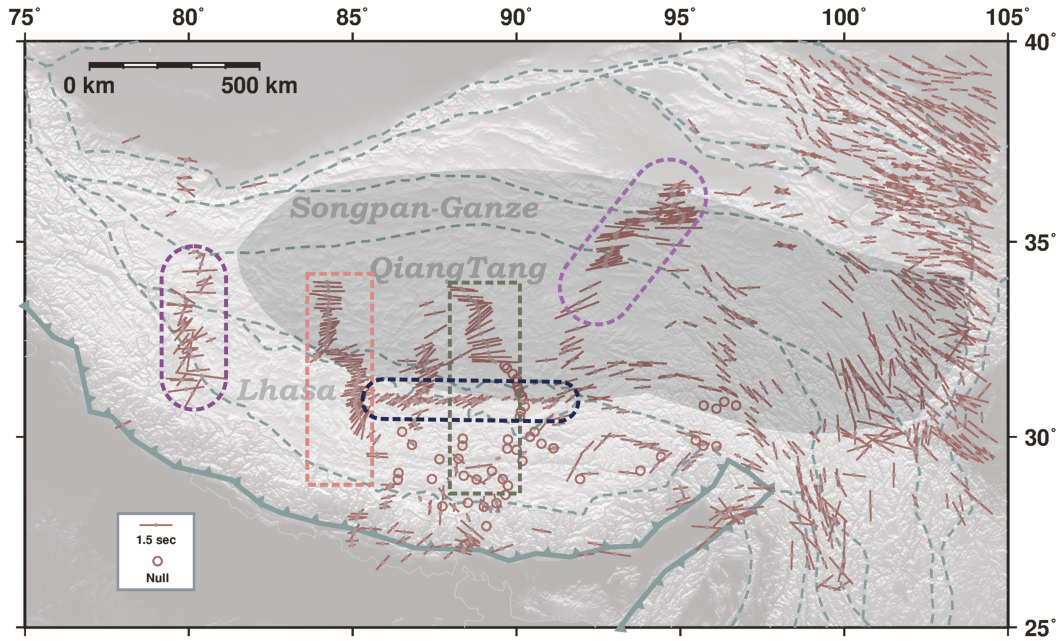
Fig.1-3 Average splitting parameters including fast polarization direction (FPD) and delay time of SKS wave splitting in Tibet from 1994 to 2018. The orientations and lengths of the red bars indicate the FPDs and splitting delay times, respectively. The red circles without lines are stations with only null measurements. The shadowed area is the zone of Sn-wave attenuation. The light purple square represents the PASSCAL and INDEPTH IV profile, the dark purple square represents the ANTILOPE profile. The light orange square represents the Hi-Climb profile. The dark green square represents the INDEPTH III and II profiles. The dark blue square represents Tibet-31N profile.

It is commonly agreed that seismic anisotropy is an important indicator of plate motion and deformation in the lithosphere and asthenosphere (Nicolas et al., 1987). Shear wave splitting from teleseismic phases (SKS, SKKS and PKS) is frequently used to estimate seismic anisotropy, which is a direct signal created by P-to-S wave

conversion at the core-mantle boundary (CMB) and record all transversely anisotropic media between the CMB and the earth surface (Silver, 1996).

1.2.1 Seismic anisotropy of Tibet

Results from SKS and SKKS splitting measurements in the Tibetan Plateau reveal obvious variations from the north to the south. Compared with uniform anisotropy in the Indian hinterland caused by absolute plate motion flow (NE-SW), in the southern margin of Tibet, the fast polarization direction (FPDs) is mainly parallel to the strike of the orogenic belt (E-W and ENE-WSW) with small delay times (~0.7-1 s) in the Himalaya terrane (Saikia et al., 2018; Singh et al., 2007) (Fig. 1-3). The stations located in the southern part of the Lhasa terrane record predominantly null or negligible splitting (red circles without lines in Fig. 1-3). In the central and northern part of the Lhasa terrane, the NNE-SSW and NE-SW FPDs are observed with the range of 0.45-1.3 s splitting time delays (Singh et al., 2016). The delay time increase to 0.9-2.54 s from the north of the BNS to the northern part of the Qiangtang and Songpan-Ganze terrane with a transition of FPDs from NE-SW to E-W (Fig. 1-3).

The anisotropic features observed by shear wave splitting measurements also show differences between the western part and eastern part of Tibet. We take Lhasa terrane as an example, the delay time overall raises from 0.2s in the west to 1s in the east, which is explained by an Indian lithospheric slab-tearing model. In the most western Tibet, the results from the ANTILOPE project near the western Himalayan Syntaxes suggest the existence of a double-layer anisotropy (Wu et al., 2015; Zhao et al., 2014b) (Fig. 1-1 & 1-3). The FPDs in the upper and lower layer are mostly E-W and N-S, respectively. The splitting time analyzed by the N-S profile across the Himalaya, Lhasa and Qiangtang terrane is 1.1s on average, with slight variation within three terranes (Wu et al., 2015) (Fig. 1-3).

In northern and northeastern Tibet, the average splitting times with NW-SE

FPDs are relatively small in the margin of the Qaidam basin (~0.6 s) and Songpan-Ganze terrane (~1 s) and increase up to ~1.6 s in the most western Qingling Orogen (Gao et al., 2019; Li et al., 2011) (Fig. 1-1&1-3). In general, the direction of fast polarization is parallel to the strike of the structures and presents a continuous trend of northeastern Tibet. In eastern Tibet, the junction area between Tibet and western South China (Sichuan Basin) is characterized by small delay times (~0.9 s) with NNW-SSE oriented FPDs (Fig. 1-3). In southeastern Tibet, near the eastern Himalayan Syntaxes (Fig. 1-1), multiple layers of anisotropy with large splitting time (~1.6 s) are observed (Kong et al., 2018; Shao et al., 2016) (Fig. 1-3).

1.2.2 Other results from seismic analysis in Tibet

Deep seismic reflection profiles are useful to provide images of important boundaries at depth, including the crust-mantle boundary (Moho), the lithosphere-asthenosphere boundary (LAB) and other seismic discontinuities. Previous seismic studies indicate that the Moho depth beneath the Lhasa terrane is located between 70 to 80 km, at twice the thickness of normal continental crust (Kind et al., 2002; Tian et al., 2015). The crustal thickness is $\sim 10 - 20$ km thinner in the Qiangtang and Songpan $-$ Ganze terranes (Tseng et al., 2009; Zhang et al., 2011; Zhao et al., 2001) and decreases to 40 km at the margin of northeast Tibet (Deng et al., 2018; Xu et al., 2019; Zheng et al., 2019). By using receiver function, Zhao (2010) identified a negative signal (seismic discontinuity) below the Moho as the LAB along three N-S trending profiles in the west, central and east (Fig.1-4), which indicate a difference of the northward Indian slab below the Tibet between sub-horizontal underthrusting in the west and steep subduction in the central-eastern Tibetan Plateau. The LAB of the Lhasa terrane along the western and central line varies from 120 km in the south to 200 km in the central line. Even larger depths are observed in the east line reaching up to over ~200 km beneath the central Lhasa terrane (Zhao et al., 2010) (Fig.1-4). A study that used similar methods conducted from Indian subcontinent to Himalayan revealed that the depth of the LAB gradually deepens from 70 km to 140 km with 30

and 56 km Moho depth, respectively (Kumar et al., 2013) (Fig.1-4). Further studies considering the thermal, compositional and seismological characteristics delineate two profiles crossing the entire central-eastern and western Tibetan Plateau, which show a thin lithosphere beneath central Tibet (Qiangtang and Songpan-Ganze terrane) with 140 km thickness in the east and 230 km thickness in the west (Chen et al., 2017; Tunini et al., 2016) (Fig.1-4).
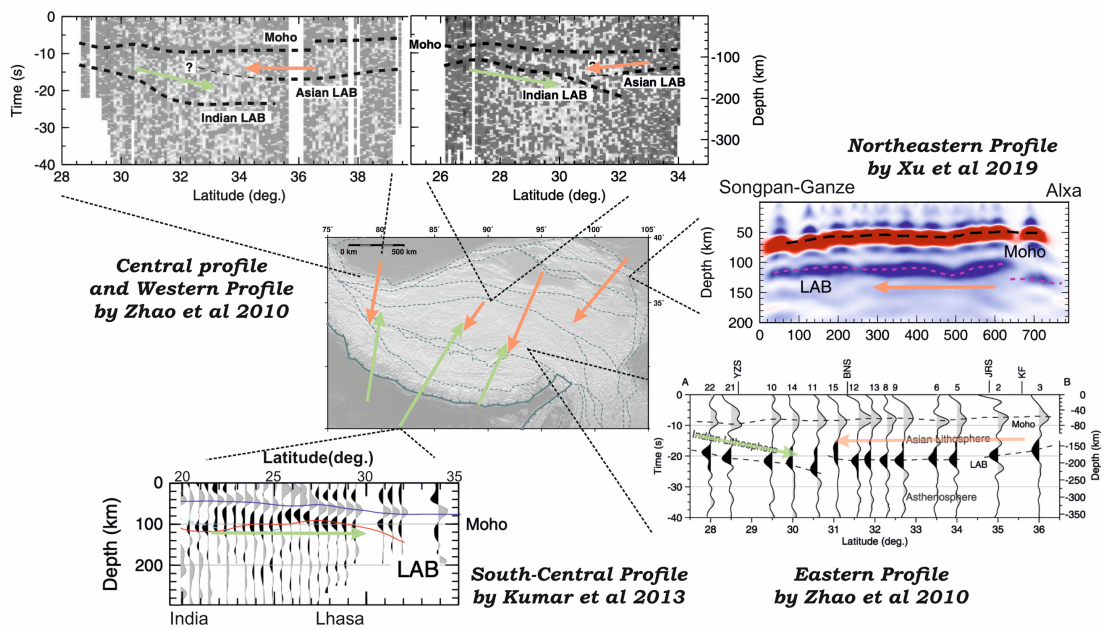
Fig.1-4 Map of the Tibetan plateau showing the seismic profiles and results of receiver functions. The Moho and LAB are marked by dashed lines. The orange and green arrows indicate the Asian and Indian plates, respectively. The eastern, western and central profile is from Zhao (2010). The northeastern profile is from Xu (2019). The south-central profile from India to Tibet is from Kumar (2013).

The analysis of P_n and S_n (S/P waves travelling in the uppermost mantle) data shows P_n and S_n wave attenuation in the Qiangtang and Songpan-Ganze terrane (Bakir and Nowack, 2012; Pei et al., 2007; Rapine et al., 1997) which combined with the observation of a low velocity zone and high Poisson's ratio (McNamara et al., 1995; Owens and Zandt, 1997) is interpreted as an indicator of partial melting in the

uppermost mantle and/or lower crust (Liu et al., 2014b) (Fig. 1-3). Liang (2006) determined the P_n tomography on the central-northern Tibet and they found that the low P_n velocity belt extends across the Qiangtang and Songpan-Ganze terranes from west to east and swings southward beneath eastern Tibet and further south to the Indian plate. The confinement of the low velocity zone coincides with the geological boundaries, suggesting vertically coupled deformation in the lithosphere (Liang and Song, 2006).

Previous surface wave studies provided the velocity structure of the Tibetan lithosphere at large scale, which generally explained the high-velocity anomalies in southern Tibet as the subducting cold Indian slab and the low-velocity anomalies in the center and north as the hot Tibetan lithosphere (Agius and Lebedev, 2017; Liang et al., 2012; Nunn et al., 2014). Thus, regarding the characteristics of the lateral velocity structure, it is a common feature that P (V_p) and S (V_s) wave velocities are low in the north but high in the south (Zhang et al., 2012b; Zhang et al., 2016). The detailed and specific regional velocity structures with depth in the different terranes also have been described and mark local velocity anomalies in the lithosphere caused by melt metasomatism (e.g. He et al., 2010; Jung, 2011; Zhang et al., 2014; Zhang et al., 2011).

1.3 Current hypotheses for the Tibetan lithosphere

1.3.1 Models for the evolution of the Tibetan lithosphere

To unravel the complex observations from petrology, tectonics, geochemistry and geophysics, different geo-dynamic models have been proposed for the evolution of the Tibetan Plateau.

Two fundamentally competing concepts are still disputed. A bidirectional subduction model with southwards subduction of the Eurasian plate and

simultaneous northwards subduction of the Indian plate has been proposed (Kumar et al., 2006; Zhao et al., 2011). In contrast, several lines of evidence indicate that the Eurasian plate does not subduct beneath Tibet (Chen et al., 2017; Liang et al., 2012).

Detailed collision models have been provided as interpretations for geodynamic process within the frame of plate tectonics. With regard to the northward underthrusting, the models can be divided into two types, where either the whole Indian lithosphere (Barazangi and Ni, 1982) or only the lower lithospheric portion is subducting (Owens and Zandt, 1997). Further analysis of plate geometry to explain lateral variations of the Indian lithospheric slab subducting beneath Tibet, put forward models such as a tearing slab model of the subducting Indian plate with different angles (Chen et al., 2015; Liang et al., 2016). Or a different extent of subduction model from west to east suggests that subhorizontal subduction beneath entire Tibet in the west, subduction no further than the Lhasa terrane in central Tibet and decreasing no further than Himalaya east of 90° E longitude (Li et al., 2008; Xu et al., 2011). Alternatively, a breakoff or roll-back slab model may induce the change in subduction geometry (Guo et al., 2015; Zhang et al., 2012c).

To explain the changes in the depth of the LAB between and even within terranes, the mechanism by which the lithosphere thins abruptly has been considered as lithospheric detachment in a piecewise (Duan et al., 2017), and/or convective removal of the lithospheric root by upwelling asthenosphere (Chung et al., 2005; Lu et al., 2018). With regard to the growth of the Tibetan Plateau and significant crustal shortening, Hodges (2001) proposed a time partitioning model of the collision process indicating two stages that are substantiated by significant plate uplift. Before 25 Ma the convergence was characterized by microcontinent-collisions. After 25 Ma, this was followed by the "hard" collision between the Indian and Eurasian plates, which is manifest, among others, from pronounced plateau growth (van Hinsbergen et al., 2012). The first phase of uplift is identified by crustal thickening by underthrusting

of the Indian lithosphere beneath Tibet, with obvious upper crustal shortening. As the cessation of crustal shortening deformation by 25 Ma, the second phases are developed by deep crustal thickening as a result of materials migration (Staisch et al., 2016). The crust mainly flows from south towards northeast and turns to southeast, which is around the rigid block surrounding Tibet (Clark and Royden, 2000). However, the flow idea is precluded based on viscosity and temperature structure beneath Tibet (Bendick and Flesch, 2007; Zhao et al., 2013). Combining the result of present- and paleo-elevation studies, the growth of the Tibetan plateau show a indeed spatial and temporal variations. Other models, like escape model or block extrusion model, have been invoked (Harrison et al., 1998). They supposed the existence of discrete intra continental subduction that accommodated with lateral extrusion along strike-slip faults, and formation of eastward escaping fragments in eastern Tibet (Tapponnier et al., 2001).

1.3.2 Models for Tibetan seismic anisotropy

Although controversial issues remain in the complex anisotropy and its mechanisms beneath Tibet and adjacent regions, numerous studies provide several lines of possibility or hypotheses to explain the deformation pattern in Tibet. Holt (2000) and Huang (2000) compared GPS observations and the distribution of FPDs analyzed by SKS in Tibet and inferred that deformation in the upper mantle has a vertical consistency with crustal deformation. On the contrary, Clark (2005) and Copley (2008) advocated decoupled deformation in the lithosphere based on a lower crustal flow model, supported by the results of seismic tomography and numerical simulation. Wang (2013) indicated an interpretation for anisotropy based on the results of regional small earthquake analysis that proposed that the mechanism for crust and mantle deformation are possibly different.

The low angle between the FPD and faults observed in northeastern Tibet and in the Tarim-Qaidam basin suggests that paleotectonic movement affects mantle

deformation (Wang et al., 2012; Zhang et al., 2012a). Hirn (1995) and Lave (1996) proposed that the anisotropy is caused by the asthenosphere as the result of whole block extrusion, since the FPDs in Tibet are sub-parallel to the present-day motion directions relative to the stable Eurasian continent. Conversely, McNamare (1994) and Silver (1996) suggested that the obvious anisotropy is preserved from the Tibetan mantle lithospheric deformation by Cenozoic north-south shortening. The anisotropy produced by mineral fabric probably reflects the finite strain accumulated over a long time (Davis et al., 1997).

Chen and Ozalzybey (1998) made further speculations on the obvious seismic anisotropy in central Tibet, which they interpreted as a sign for a boundary between deformed Asian lithosphere and rigid Indian cratonic lithosphere. The project Hi-CLIMB, Chen (2010) showed two distinct, rapid increases of anisotropy in the southern-central Tibetan hinterland: 75km north of the Indus-Yarlung suture (IYS) and 100km north of the Bangong-Nujiang suture (BNS). The interpretations are likely that the northern Indian lithospheric mantle has reached beyond the BNS and southward Eurasian lithospheric mantle terminated beneath the IYS. While, Ozacar and Zandt (2004) used a neighborhood algorithm and gained an anisotropy and isotropy interlayer structure model for the middle-crust beneath Tibet.

Obviously, the lack of an overview of the deformation history and strain distribution of the Tibetan lithospheric mantle, makes it difficult to explain significant anisotropy and its mechanism. The opposing hypotheses remains and renders non-unique solutions. Thus, more direct evidence and comprehensive methods are necessary to better understand the evolution of the Tibetan lithospheric mantle.

1.4 Theory of seismic anisotropy

Since the 1960s, Hess (1964) and Raitt (1969) presented azimuthal anisotropy

from the uppermost mantle in the ocean basins by P_n wave measurements. In 1975, (Forsyth) manifested the existence of azimuthal anisotropy by using long period surface waves, which marked the onset of numerous anisotropy measurements. With the advent of broadband seismic technology, the anisotropy in the mantle became detectable, especially in the range of 200 km from the surface (Dziewonski and Anderson, 1981; Mainprice, 2007; Montagner and Tanimoto, 1990; Savage, 1999). Compared with P_n wave and long period surface wave measurements, anisotropy analyzed by shear wave splitting of teleseismic waves effectively resolve the problem of non-uniqueness (Crampin, 1981). During the past decades, more and more seismic studies focus on the anisotropy in the mantle and worldwide seismic station networks allow us to see more clearly into the deep earth.

1.4.1 The genesis of seismic anisotropy

In 1978, (Crampin) proposed the EDA (Extensive Dilatancy Anisotropy) hypothesis for crustal anisotropy. Thereby cracks are created by the local stress lying along with the principle stress, which are practically perpendicular to the surface (Crampin, 1984). When a shear wave propagates into the crack-region, it will be split into two distinct waves with orthogonal polarizations and distinct velocities (Fig. 1-5). The waves with their polarization parallel to the crack arrive earlier in the receiver station than the waves with their polarization vertical to the crack. The time difference between the two waves is referred to as the delay time. This phenomenon is called shear wave splitting. Except aligned cracks near the surface, any anisotropic materials located from the core-mantle boundary (CMB) to the surface could be recorded by shear wave splitting. Upon propagation through an anisotropic region in the deep earth, a shear wave is split and accumulates a delay time between the fast and the slow splitting wave. Thus, the difference of arrival times between these two waves and their polarization direction is used to estimate the magnitude of anisotropy (Barruol and Mainprice, 1993; Long and Silver, 2009; Mainprice and Silver, 1993; Silver and Chan, 1988).

14
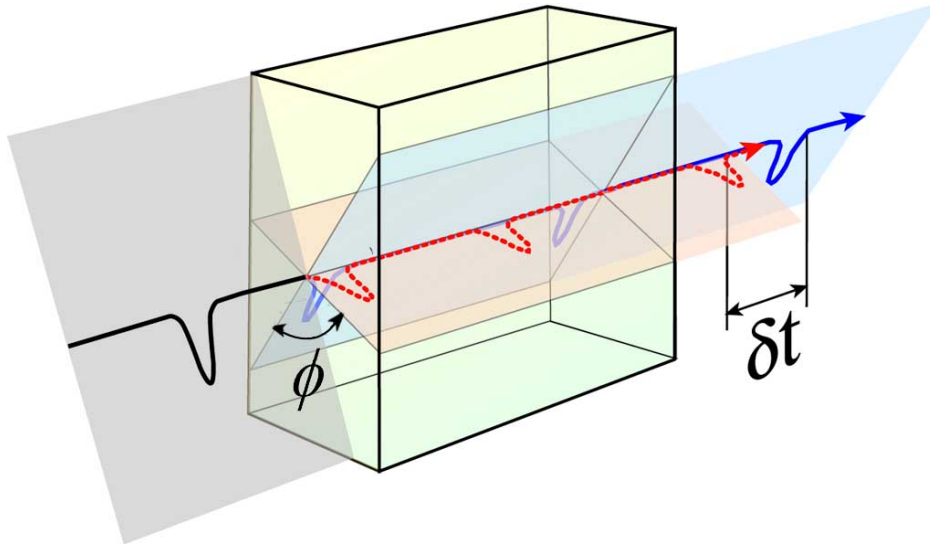
Fig.1-5 Schematic drawing of shear wave splitting in anisotropic media (by courtesy of Garnero)

Aligned cracks in sedimentary formations are the main factors for S wave splitting in the upper crust, which commonly appears up to 10~15 km below the surface and the polarization direction of the fast wave ordinarily is parallels to the cracks (Crampin, 1981). Due to ductile crack growth on the limited scale, the anisotropy from shallow area could be observed locally. The ubiquitous anisotropy beneath continents is mainly produced from the lower crust and upper mantle, where the mineral preferred orientation is probably the dominate source (Mainprice et al., 2000; McNamara et al., 1994; Silver, 1996; Silver and Chan, 1988). As the primary mantle is mainly comprised of olivine, the orientation of highly anisotropic olivine and its deformation behavior and resulting crystal preferred orientation (CPO) plays and important role in generating seismic anisotropy in the lithospheric mantle (Mainprice and Silver, 1993; Nicolas et al., 1987; Silver, 1996). Other mantle minerals, such as pyroxenes and garnets, make contributions to the anisotropy as well. In addition, part of the seismic anisotropy might be caused by the alignment of different elastic properties of materials (e.g. melt) with shape preferred orientation (SPO) (Long and Silver, 2009; Mainprice et al., 2000; Nicolas et al., 1987). Silver and Kaneshima

(1993) pointed out that the most of the lower mantle is homogenous, except for the bottom of the lower mantle (D" layer) (Kendall and Silver, 1998; Mainprice, 2007). Anisotropy in the D" layer is a result of alignment of partial melt and strong anisotropic minerals, including perovskite, post-perovskite, and periclase (Mainprice, 2007; Reiss et al., 2019; Tommasi et al., 2018).

1.4.2 Measurements of seismic anisotropy

Shear wave splitting exhibits sufficient sensitivities to anisotropic structures on different scales in different tectonic background. Anisotropy of the medium is quantified by comparing the time difference and polarization direction between two splitting waves. To evaluate the magnitude of anisotropy in different parts of the deep earth, there are several seismic phases usually used (Chen et al., 2015; Pei et al., 2007; Tommasi et al., 2018). SKS and other core phases (e.g. SKKS, PKS) are the most popular seismic phase for the property of unperturbed polarization (Fig. 1-6) (Long and Silver, 2009). The P-to-S conversion at the core-mantle boundary constrains all observed splitting events emerged on the receiver side from the CMB to the surface (Chen et al., 2015; Long and Silver, 2009; Silver, 1996). The sub-perpendicular propagation of seismic waves with negligible incidence angle effectively reduces the influences from nonlinear shear particle motion in the absence of anisotropy (Long and Silver, 2009; Savage, 1999).
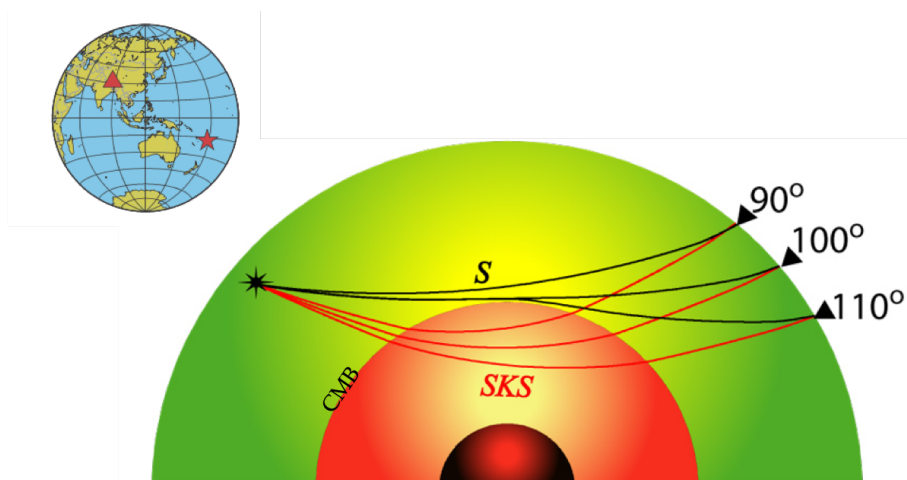
Fig. 1-6 Example for SKS-wave splitting analysis (by courtesy of Garnero and modified by Chen et al. (2015))

Theoretically, SKS wave splitting may be caused by anisotropic media anywhere along the propagation path. While, we generally interpret the main source of anisotropy is the upper mantle and ignored the potential contribution from D" layer (Long and Silver, 2009; Mainprice, 2007). Several studies that seek to analyze uncertainty about the SKS splitting measurements have been conducted by comparing pairs of phases (e.g. SKS and SKKS) with specific ray paths. In the majority of cases, there is no obvious discrepancies between the pair of phases that propagate along similar paths in the upper mantle and different paths in the rest of their travel, implying that the SKS split in the upper mantle (Meade et al., 1995; Niu, 2004; Restivo and Helffrich, 2006). Additionally, array measurements on SKS phases help to avoid the influence from the lower mantle, due to similar propagation in the lower mantle at all stations in the array (Long and Silver, 2009). Except for the regions that documented significant anisotropy from the crust, the contribution to SKS splitting from crustal anisotropy is commonly much smaller than that from the upper mantle (Savage, 1999; Silver, 1996). Therefore, it is generally accepted that the anisotropy measured by SKS splitting originates from the upper mantle.

In terms of splitting parameters, Silver (1988) proposed a formula to calculate the anisotropy from the delay time (δt) between two splitting waves:

$$\delta t = \frac{L \times \delta\beta}{\beta_0}$$

where δt is delay time, L is the thickness of anisotropy layer, β_0 is the average S wave velocity of a homogeneous layer and $\delta\beta$ is the magnitude of anisotropy.

From the equation, the relationship between the delay time obtained by SKS measurements and anisotropy is clear. The large delay times rely upon either the magnitude of anisotropy or the thickness of the anisotropic layer. For example, if the delay time is 1s observed at the seismic station and the 118 km thickness lithosphere

is detected with 4.7 km/s V_s. The average anisotropy of the lithosphere is calculated to be 4% (Chen and Molnar, 1981).

1.5 Crystal preferred orientation (CPO) of mantle minerals

Seismic anisotropy becomes more and more important for illustrating deformation and evolution of the Earth's mantle. The anisotropy of the mantle is controlled by the mineral's anisotropy and volume of main minerals in the mantle: olivine, clinopyroxene and orthopyroxene as well as their CPOs. For better understanding the seismic property of mantle rocks, the individual crystal behaviors are significant.

1.5.1 Olivine CPO and its anisotropy
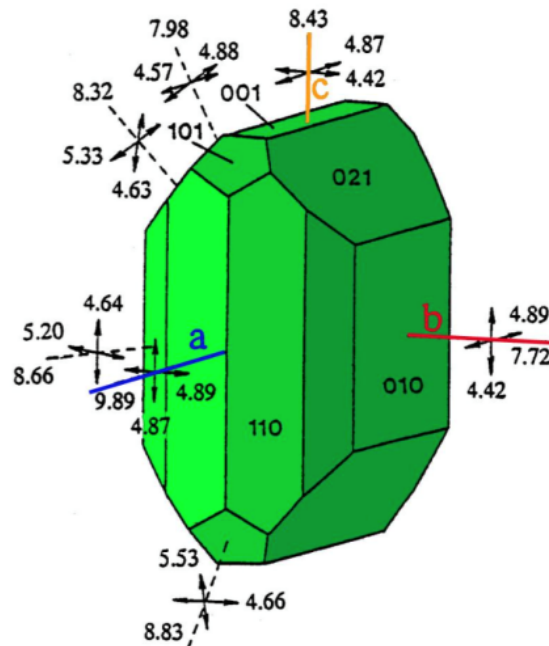
Fig.1-7. Seismic anisotropy of olivine. The P- and S-wave seismic velocities (km/s) along the a-, b- and c-crystal axis directions. (modified from Babuska and Cara (1991))

Olivine is the primary mineral in mantle peridotites. It has orthorhombic crystal structure. The P-wave anisotropy of an olivine single crystal is caused by different velocities for different propagation directions (Fig 1-7, V_p in a-axis (=9.89 km/s) > V_p in c-axis (=8.43 km/s) > V_p in b-axis (=7.72 km/s)). Fig.1-7, also shows the S-wave splitting velocity in the three mutually perpendicular direction of the crystal axes. For instance, the velocity of the fast polarization S-wave is 4.87 km/s and for the slow one it is 4.42km/s, when the S-wave propagate along the c-axis; while the velocities are 4.89 km/s and 4.87km/s, respectively, for waves propagating along the a-axis,. The anisotropy (A) is defined as A= [2*(V_{max} - V_{min})/(V_{max} + V_{min})]*100%. In the c-axis direction the S-wave anisotropy reaches 9.68%, whereas in the a-axis direction it is only 0.4%. Therefore, the path along which that seismic waves travel is one of the most critical factors for the anisotropy. In the mantle, the seismic analysis is expected to present significant seismic properties in response to the presence of abundant olivine with CPO.
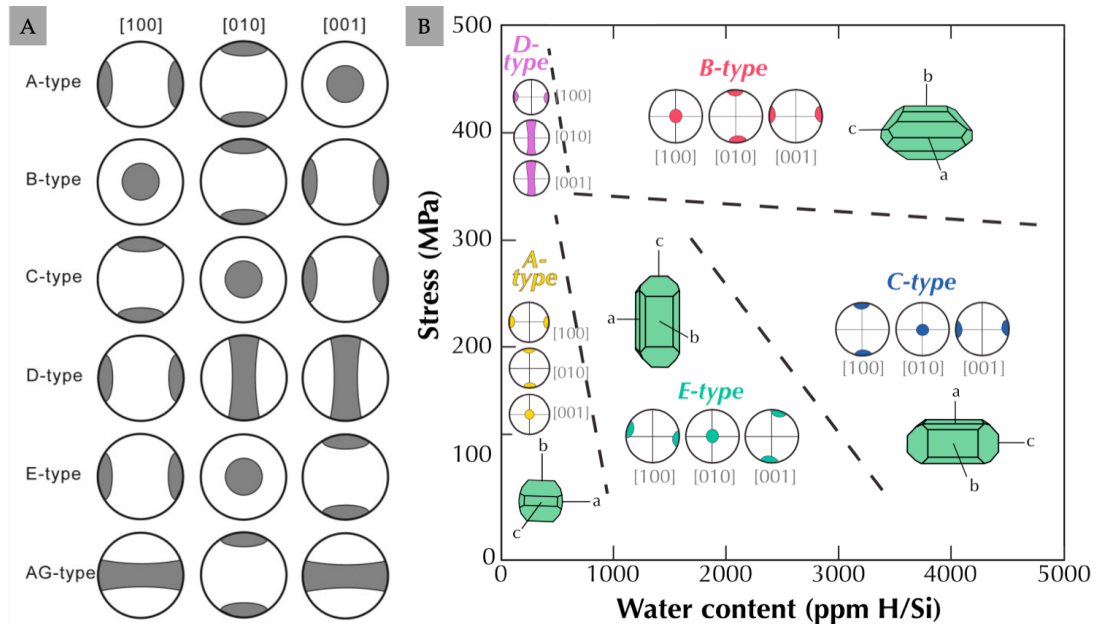
Fig.1-8 (A) schematic depiction of six types of olivine fabric (Cao et al., 2015). (B) Dominant fabric type as a function of stress and water content (Bernard et al., 2019).

So far, six types of olivine fabric have been found in experiments and in natural rocks, which are assumed to reflect activation of one or more specific slip systems (A-type: [100](010); B-type: [001](010); C-type: [001](100); D-type: [100] (010) and [100] (001); E-type: [100](010); AG-type: [100](010) and [001](010)) (Fig. 1-8) (Carter and Ave'Lallemant, 1970; Nicolas et al., 1987).

The nature of the CPO of olivine strongly effects many important physical properties of the Earth's upper mantle. To reveal the formation mechanism of olivine fabric, deformation experiments have been conducted. The relationship between CPO and physical conditions including temperature, pressure, water content, and differential stress have been performed (Fig. 1-8). Considering that the main mode of deformation in the upper mantle is simple shear, Zhang and Karato (1995) performed deformation experiments on dry olivine aggregates (~300 $H/10^6$ Si water content) under simple shear condition at 1500K temperature and 300 MPa confining pressure. When the strain is up to 150%, A-type orientation is clearly reproduced. It is confirmed by further studies that indicate A-type olivine fabric usually forms under low water and low stress condition (Zhang et al., 2000) (Fig. 1-8). The A-type fabric is generally regarded as the most common olivine fabric (Ismail and Mainprice, 1998), and it was extensively used for interpreting the SKS splitting observed from trench regions (Michibayashi et al., 2016).

B-type fabric is not sensitive to water content and preferentially forms under high pressure and low temperature, whereas formation of C-type fabric requires the highest water content out of the six fabric types (Fig. 1-8). The water content investigated by Jung and Karato (2001) is an effective factor related to fabric transitions in olivine. They firstly produced B-type and C-type orientation from experiments and attributed transformation from A- to B-type fabric to additional water, due to the enhanced mobility of grain boundaries at increased water content. Subsequent research by Katayama and Karato (2006) manifested that B-type olivine fabric formed at higher stress than C-type and the fabric transition from B- to C- type

occurs with temperature increase.

Bystricky (2000) emphasized that the mechanism of mantle flow is by non-coaxial deformation and the importance of steady-state deformation at high strains should not be ignored. Hence, he designed torsional shear experiment (P=300MPa, T=1200℃) under high bulk shear strains (up to γ =5), to achieve non-coaxial deformation conditions with a wider range of strain than former studies. Their results show the D-type olivine preferred orientation, which implied this girdled axis distribution develop in strongly deformed regions of the upper mantle and reach a steady-state microstructure. Thus, D-type fabric occurs in natural rocks commonly in lithospheric shear zones (Ismail and Mainprice, 1998; Michibayashi et al., 2016), which has been considered as an indicator of dislocation creep under high stress and low water content conditions (Jung et al., 2006). Alternatively, recent experiments revealed another mechanism for D-type formation in the course of low strain shear deformation (Hansen et al., 2012; Hansen et al., 2011). Dislocation-accommodated grain boundary sliding as the dominant generation mechanisms in the experiments has been demonstrated from numerical simulation and natural samples as well (Tommasi et al., 2000; Warren et al., 2008). While, in the higher strain torsion experiments, Hansen (2014) found that a steady-state fabric requires higher strains (~20) than previously anticipated and initial D-type change as A-type fabric at strains > 10.

E-type fabrics were first reported by Katayama (2004), which were produced by high-strain simple-shear deformation experiments with 0.5-2.2 GPa and 1470-1570 K. Under higher water contents (~200-1000 H/10^6 Si) the olivine fabric is likely to activate the [100](010) slip system (A-type) and finally the [100](001) slip system (E-type). Thus, it is speculated that the existence of E-type fabric substitutes the former A-type in the oceanic upper mantle and island arc, because of enough amount of water (Harigane et al., 2013; Katayama et al., 2004; Kumamoto et al., 2019; Mehl, 2003). Tielke (2019) further suggests that the (001)[100] slip system is most sensitive

to water fugacity and exhibits the largest degree of hydrolytic weakening. Olivine fabrics from natural samples show that the E-type is typically found in porphyroclastic and mylonitic samples in mantle shear zones (Bernard et al., 2019; Precigout et al., 2017; Skemer et al., 2013).

AG-type occurs during compression or in the presence of melt (Le Roux et al., 2008; Tommasi et al., 1999). Aligned fabrics weakened by melt have been demonstrated in the experiments. Holtzman (2003) carried out partial melting experiments at 300 MPa and 1523K with anhydrous conditions under simple shear deformation. The samples consisted of olivine aggregates and mid-ocean ridge basalt. During deformation, the distribution of the molten basalt changed from initially homogeneous into layers or bands. Owing to the presence of melt, olivine fabric is distinguished by a- and c-axis girdles distributions in the shear plane with point concentration of the b-axis (AG-type). When the volume fraction of basalt melt increased from 4% to 6%, the AG-type reoriented towards B-type. Holtzman (2003) explain the deformation mechanism is between dislocation and diffusion mechanisms based on anisotropic distribution of melt. The processes of CPO generated with melt was further studied by Qi (2018), who produced AG-type by sheared partially molten rocks of mantle composition. They concluded that the fabric developed by two simultaneous mechanisms: (1) the olivine grains rotate to align [001] paralleled to the flow direction which is induced by their shape preferred orientation; (2) the (010)[100] slip system is activated by dislocation-induced creep (Qi et al., 2018). Boneh (2014) supposed that the AG-type fabric should be expected under none pre-existing fabric condition, which is observed both in the simulation and experiments (Boneh et al., 2015).

1.5.2 Pyroxene CPO

Pyroxene including orthopyroxene and clinopyroxene is the second most abundant mineral in the upper mantle (Ringwood and Major, 1970). Raleigh (1971)

conducted plastic deformation experiment on enstatite at 1.5 GPa pressure and 1100-1300 ℃ temperature with a strain rate of 10^{-3}-10^{-6} s^{-1}, displaying the dominant slip system of (100)[001] in enstatite. Ross and Nielsen (1978) proposed that both temperature and strain rate are the main factors controlling orthopyroxene deformation. Their experiment of wet polycrystalline enstatite aggregates at a pressure of 1GPa and a temperature of 800-1300 ℃ showed that the (010)[001] slip system is activated once the uniaxial strains are above 40% (Ross and Nielsen, 1978). For the natural orthopyroxene in the mantle rock, the orthopyroxene fabric is mostly documented with slip system (100)[001] (Henry et al., 2017; Hidas et al., 2007; Skemer et al., 2010; Soustelle et al., 2009; Vauchez et al., 2005; Xu et al., 2006).
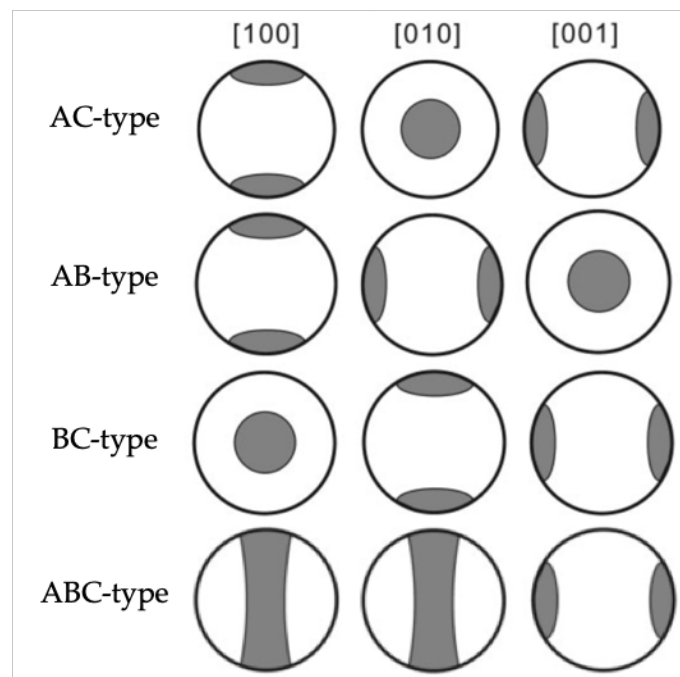
Fig.1-9 schematic depiction of four types of orthopyroxene fabric proposed by Jung (2010)

Jung (2010) grouped the orthopyroxene fabrics from 215 natural mantle xenoliths from different tectonic environments into 4 types (Fig. 1-9), of which AC-type with (100)[001] slip system represented 50% in all samples. Based on their observations, the orthopyroxene fabric is related to its modal composition, water

content and fabric of coexisting olivine. The strength of the orthopyroxene fabric decreased with increasing water content, and increased with increasing strength of the olivine fabric. For low content of enstatite (10% - 18%) the AC-type is found, the another three fabric types dominate at higher enstatite contents (17% - 33%) (Jung et al., 2010). Further research undertaken by Skemer (2010) also presented similar results that the dominant slip systems in orthopyroxene are (100)[001] and (010)[001], which indicates that both planes may be activated in nature (Chin et al., 2016; Frets et al., 2012; Raterron et al., 2016).

In both nature and laboratory experiments, the CPO of clinopyroxene generally represent as [001]-axis parallel to the lineation and [010]-axis normal to the foliation plane. The deformation mechanisms of clinopyroxene are mainly controlled by temperature and water content, which is accommodated by dislocation creep at higher temperature (<1050 ℃) and mechanical twining at lower temperature (AvéLallemant, 1978; Kirby and Kronenberg, 1984). According to the results of steady-state deformation experiments, the clinopyroxene (omphacite) fabrics is divided into three types (Helmstaedt et al., 1972; Zhang et al., 2006) (Fig. 1-10).
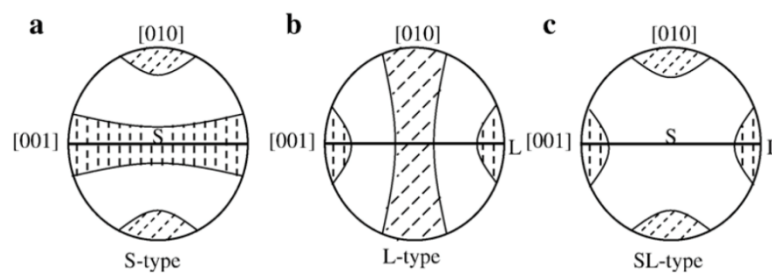
Fig.1-10 Classification of clinopyroxene fabrics (Zhang et al., 2006)

The S-type fabric displays a girdle distribution of the [001]-axes parallel to the lineation and of the [010]-axes normal to the foliation plane. The L-type fabric is characterized by the [001]-axes next to the lineation and the [010]-axes forming a girdle in the plane perpendicular to the foliation. And SL-type is defined as [001](010)

fabric (Fig. 1-10). On the report of deformation experiments, clinopyroxene fabric occur clear S-type fabric under compression (Mauler et al., 2000). Weak L-type clinopyroxene fabric developed under lower strain (γ =2.1) and the fabric strength increased with increasing strain up to γ =3.7. When the strain reached to γ =~5, the clinopyroxene CPO transformed into SL-type (Amiguet et al., 2009; Bascou et al., 2001; Zhang et al., 2006).

These three types of fabric with [010]-axes distributed in the plane normal to the foliation is considered as a result of slip along the {110} planes at high temperature (>1000 °C), where [001]{110}, and 1/2<110>{110} are activated (Amiguet et al., 2010; Bascou et al., 2002).The deformation experiments on diopside showed similar results at high temperature that 1/2<110>{110} is activated, while [001](100) is active at lower temperatures (900 – 1000 °C) (Raterron et al., 1994). The rare [001](100) slip system is also activated in the natural samples, which is reported at low-temperature in the eclogites (<660 °C), pyroxenites (=860 °C) and amphibolite (=700 °C) (Godard and van Roermund, 1995; Ji et al., 1993)

1.6 Seismic properties calculation from mineral fabric

Understanding the mineral fabric is important in the study of physical properties of mantle rock. There are several methods for the calculation of seismic properties by mineral CPOs as reviewed in Mainprice (2007). Here, to evaluate the effective elastic constants of whole rock, we choose the most frequently used averaging techniques, the Voigt (1928) and Reuss (1929) averages. In this calculation, we only used volume fraction of each phase, the orientation and the elastic constants of the single crystals or grains. In terms of statistical probability functions, these are first order bounds as only the first order correlation function is used, which is the volume fraction. Note no information about the shape or position of neighboring grains is

used. The Voigt average is found by simply assuming that the strain field is uniform everywhere. The strain at every position is set equal to the macroscopic strain of the sample. M^{voigt} is then estimated by a volume average of local stiffnesses $M(gi)$ with orientation gi and volume fraction V_i,

$$M^{voigt} = \Sigma V_i M(g_i)$$

Reuss average is found by assuming that the stress field is uniform everywhere. The stress at every position is set equal to the macroscopic stress of the sample. M^{Reuss} is estimated by the volume average of lock compliances $M(g_i)$.

$$1/M^{Reuss} = \Sigma V_i M(g_i)$$

These two estimates are not equal for anisotropic solids with the Voigt being an upper bound and the Reuss a lower bound. A physical estimate of the moduli should lie between the Voigt and Reuss average bound as the stress and strain distributions are expected to be somewhere between uniform strain (Voigt bound) and uniform stress (Reuss bound). Hill (1952) observed that arithmetic mean of the Voigt and Reuss bounds, sometimes called the Hill or Voigt-Reuss-Hill (VRH) average,

$$M^{VRH} = 1/2(M^{voigt} + M^{Reuss})$$

This average is often close to the experimental values, but it has no theoretical justification. As it is much easier to calculate the arithmetic mean of the Voight and Reuss elastic tensors all authors have tended to apply the Hill average as an arithmetic mean. In Earth sciences, the Voigt, Reuss and Hill averages have been widely used for averages for oriented polyphase rocks (i.e. Crosson and Lin, 1971). Although the Voigt and Reuss bounds are often far apart for anisotropic materials, they still provide the limits within which the experimental data should be found (i.e. Mainprice, 2007; Satsukawa, 2012).

1.7 Research targets and aims

The research presented in this thesis is concerned with the details of the deformation processes of the lithospheric mantle beneath the Tibetan Plateau, through studies on mantle peridotite xenoliths in southern, central and northeastern Tibet, using petrographic, petrochemical, microstructural and simulation techniques. The aims are:

(1) To figure out the dominant fabrics of the minerals in peridotite xenoliths from Tibet and the genesis of the fabrics

(2) To ascertain the contributions of mantle rocks to the anisotropy in Tibet and to illustrate the observations by SKS seismic analysis.

(3) To resolve the deformation mechanism and processes of the mantle xenoliths and to provide a comparable velocity structure model for the Tibetan lithosphere

(4) To reveal the geodynamic processes beneath the Tibetan lithosphere and to delineate the lithospheric mantle architecture by linking the microscale mechanisms to the macroscale response.

1.8 Thesis outline

This thesis is divided into 5 chapters. Chapter 1 presents the geological and geophysical background of Tibetan Plateau and the theory including the mineral fabrics and the relationships between mineral fabrics and seismic investigation. Chapter 2 reports the crystal preferred orientation of mantle xenoliths in Lhasa terrane, Tibet and discusses the different architecture of Tibetan lithosphere from east to west. Chapter 3 provides a new evidence for a heterogeneous lithospheric structure in central Tibet and tries to reconcile the discrepancies among the India-Asia collision hypotheses. Chapter 4 discusses the mechanism of seismic anisotropy beneath northeastern Tibet from peridotite xenoliths from mantle and provides constraints for the prevailing structure models. Chapter 5 summaries the conclusions reached in this study.

Chapter 1

References

1.   Agius, M.R. and Lebedev, S., 2017. Complex, multilayered azimuthal anisotropy beneath Tibet: evidence for co-existing channel flow and pure-shear crustal thickening. Geophysical Journal International, 210(3): 1823-1844.

2.   Amiguet, E., Cordier, P. and Raterron, P., 2010. Deformation of diopside single crystals at mantle pressure. TEM characterization of dislocation microstructures. European Journal of Mineralogy, 22(2): 181-187.

3.   Amiguet, E., Raterron, P., Cordier, P., Couvy, H. and Chen, J., 2009. Deformation of diopside single crystal at mantle pressure. 1: Mechanical data. Physics of the Earth and Planetary Interiors, 177(3-4): 122-129.

4.   AvéLallemant, H.G., 1978. Experimental deformation of diopside and websterite. Tectonophysics, 48(1-2): 1-27.

5.   Babuska, V. and Cara, M., 1991. Seismic anisotropy in the Earth, 10. Springer Science & Business Media.

6.   Bakir, A.C. and Nowack, R.L., 2012. Velocity and Attenuation Structure of the Tibetan Lithosphere Under the Hi-CLIMB Array From the Modeling of Pn Attributes. Pure and Applied Geophysics, 169(12): 2073-2089.

7.   Barazangi, M. and Ni, J., 1982. Velocities and propagation characteristics of Pn and Sn beneath the Himalayan arc and Tibetan plateau: Possible evidence for underthrusting of Indian continental lithosphere beneath Tibet. Geology, 10(4): 179-185.

8.   Barruol, G. and Mainprice, D., 1993. A quantitative evaluation of the contribution of crustal rocks to the shear-wave splitting of teleseismic SKS waves. Physics of the Earth and Planetary Interiors, 78(3-4): 281-300.

9.   Bascou, J., Barruol, G., Vauchez, A., Mainprice, D. and Egydio-Silva, M., 2001. EBSD-measured lattice-preferred orientations and seismic properties of eclogites. Tectonophysics, 342(1–2): 61-80.

10.   Bascou, J., Tommasi, A. and Mainprice, D., 2002. Plastic deformation and development of clinopyroxene lattice preferred orientations in eclogites. Journal of Structural Geology, 24(8): 1357-1368.

11.   Bendick, R. and Flesch, L., 2007. Reconciling lithospheric deformation and lower crustal flow beneath central Tibet. Geology, 35(10).

12.   Bernard, R.E., Behr, W.M., Becker, T.W. and Young, D.J., 2019. Relationships between olivine CPO and deformation parameters in naturally deformed rocks and implications for mantle seismic anisotropy. Geochemistry, Geophysics, Geosystems.

13.   Boneh, Y., Morales, L.F.G., Kaminski, E. and Skemer, P., 2015. Modeling olivine CPO evolution with complex deformation histories: Implications for the interpretation of seismic anisotropy in the mantle. Geochemistry, Geophysics, Geosystems, 16(10): 3436-3455.

14.   Boneh, Y. and Skemer, P., 2014. The effect of deformation history on the evolution of olivine CPO. Earth and Planetary Science Letters, 406: 213-222.

15.   Bystricky, M., Kunze, K., Burlini, L. and Burg, J., 2000. High shear strain of olivine aggregates: rheological and seismic consequences. Science, 290(5496): 1564-1567.

16.   Cao, Y., Jung, H., Song, S., Park, M., Jung, S. and Lee, J., 2015. Plastic Deformation and Seismic Properties in Fore-arc Mantles: A Petrofabric Analysis of the Yushigou Harzburgites, North Qilian Suture Zone, NW China. Journal of Petrology, 56(10): 1897-1944.

17.   Carter, N.L. and Ave'Lallemant, H.G., 1970. High Temperature Flow of Dunite and Peridotite. Geological Society of America Bulletin, 81(8).

18.   Chen, M., Niu, F., Tromp, J., Lenardic, A., Lee, C.A., Cao, W. and Ribeiro, J., 2017. Lithospheric foundering and underthrusting imaged beneath Tibet. Nat Commun, 8: 15659.

19.   Chen, W.-P., Martin, M., Tseng, T.-L., Nowack, R.L., Hung, S.-H. and Huang, B.-S., 2010. Shear-wave birefringence and current configuration of converging lithosphere under Tibet. Earth and Planetary Science Letters, 295(1-2): 297-304.

20.   Chen, W.-P. and Molnar, P., 1981. Constraints on the seismic wave velocity structure beneath the Tibetan Plateau and their tectonic implications. Journal of Geophysical Research: Solid Earth, 86(B7): 5937-5962.

21.   Chen, W.-P. and Özalaybey, S., 1998. Correlation between seismic anisotropy and Bouguer gravity anomalies in Tibet and its implications for lithospheric structures. Geophysical Journal International, 135(1): 93-101.

22.   Chen, Y., Li, W., Yuan, X., Badal, J. and Teng, J., 2015. Tearing of the Indian

lithospheric slab beneath southern Tibet revealed by SKS-wave splitting measurements. Earth and Planetary Science Letters, 413: 13-24.

23. Chin, E.J., Soustelle, V., Hirth, G., Saal, A.E., Kruckenberg, S.C. and Eiler, J.M., 2016. Microstructural and geochemical constraints on the evolution of deep arc lithosphere. Geochemistry, Geophysics, Geosystems, 17(7): 2497-2521.

24. Chung, S.-L., Chu, M.-F., Zhang, Y., Xie, Y., Lo, C.-H., Lee, T.-Y., Lan, C.-Y., Li, X., Zhang, Q. and Wang, Y., 2005. Tibetan tectonic evolution inferred from spatial and temporal variations in post-collisional magmatism. Earth-Science Reviews, 68(3-4): 173-196.

25. Chung, S.-L., Liu, D., Ji, J., Chu, M.-F., Lee, H.-Y., Wen, D.-J., Lo, C.-H., Lee, T.-Y., Qian, Q. and Zhang, Q., 2003. Adakites from continental collision zones: melting of thickened lower crust beneath southern Tibet. Geology, 31(11): 1021-1024.

26. Clark, M.K., Bush, J.W. and Royden, L.H., 2005. Dynamic topography produced by lower crustal flow against rheological strength heterogeneities bordering the Tibetan Plateau. Geophysical Journal International, 162(2): 575-590.

27. Clark, M.K. and Royden, L.H., 2000. Topographic ooze: Building the eastern margin of Tibet by lower crustal flow. Geology, 28(8): 703-706.

28. Copley, A., 2008. Kinematics and dynamics of the southeastern margin of the Tibetan Plateau. Geophysical Journal International, 174(3): 1081-1100.

29. Crampin, S., 1981. A review of wave motion in anisotropic and cracked elastic-media. Wave motion, 3(4): 343-391.

30. Crampin, S., 1984. Effective anisotropic elastic constants for wave propagation through cracked solids. Geophysical Journal International, 76(1): 135-145.

31. Crosson, R.S. and Lin, J.W., 1971. Voigt and Reuss prediction of anisotropic elasticity of dunite. Journal of Geophysical Research, 76(2): 570-578.

32. Davis, P., England, P. and Houseman, G., 1997. Comparison of shear wave splitting and finite strain from the India-Asia collision zone. Journal of Geophysical Research: Solid Earth, 102(B12): 27511-27522.

33. Deng, Y., Li, J., Song, X. and Zhu, L., 2018. Joint inversion for lithospheric structures: Implications for the growth and deformation in Northeastern

Tibetan Plateau. Geophysical Research Letters, 45(9): 3951-3958.

34. Ding, L., 2003. Cenozoic Volcanism in Tibet: Evidence for a Transition from Oceanic to Continental Subduction. Journal of Petrology, 44(10): 1833-1865.

35. Ding, L., Kapp, P., Yue, Y. and Lai, Q., 2007. Postcollisional calc-alkaline lavas and xenoliths from the southern Qiangtang terrane, central Tibet. Earth and Planetary Science Letters, 254(1): 28-38.

36. Duan, Y., Tian, X., Liang, X., Li, W., Wu, C., Zhou, B. and Iqbal, J., 2017. Subduction of the Indian slab into the mantle transition zone revealed by receiver functions. Tectonophysics, 702: 61-69.

37. Duvall, A.R., Clark, M.K., Kirby, E., Farley, K.A., Craddock, W.H., Li, C. and Yuan, D.-Y., 2013. Low-temperature thermochronometry along the Kunlun and Haiyuan Faults, NE Tibetan Plateau: Evidence for kinematic change during late-stage orogenesis. Tectonics, 32(5): 1190-1211.

38. Dziewonski, A.M. and Anderson, D.L., 1981. Preliminary reference Earth model ☆. Physics of the Earth & Planetary Interiors, 25(4): 297-356.

39. Forsyth, D.W., 1975. The early structural evolution and anisotropy of the oceanic upper mantle. Geophysical Journal International, 43(1): 103-162.

40. Frets, E., Tommasi, A., Garrido, C.J., Padrón-Navarta, J.A., Amri, I. and Targuisti, K., 2012. Deformation processes and rheology of pyroxenites under lithospheric mantle conditions. Journal of Structural Geology, 39: 138-157.

41. Gao, Y., Chen, L., Wang, X. and Ai, Y., 2019. Complex Lithospheric Deformation in Eastern and Northeastern Tibet from Shear-wave Splitting Observations and its Geodynamic Implications. Journal of Geophysical Research: Solid Earth.

42. Godard, G. and van Roermund, H.L., 1995. Deformation-induced clinopyroxene fabrics from eclogites. Journal of Structural Geology, 17(10): 1425-1443.

43. Guo, Z. and Wilson, M., 2019. Late Oligocene–early Miocene transformation of postcollisional magmatism in Tibet. Geology.

44. Guo, Z., Wilson, M., Zhang, M., Cheng, Z. and Zhang, L., 2015. Post-collisional Ultrapotassic Mafic Magmatism in South Tibet: Products of Partial Melting of Pyroxenite in the Mantle Wedge Induced by Roll-back and Delamination of the

Subducted Indian Continental Lithosphere Slab. Journal of Petrology, 56(7): 1365-1406.

45. Haines, S.S., Klemperer, S.L., Brown, L., Jingru, G., Mechie, J., Meissner, R., Ross, A. and Wenjin, Z., 2003. INDEPTH III seismic data: From surface observations to deep crustal processes in Tibet. Tectonics, 22(1): n/a-n/a.

46. Hansen, L.N., Zhao, Y.-H., Zimmerman, M.E. and Kohlstedt, D.L., 2014. Protracted fabric evolution in olivine: Implications for the relationship among strain, crystallographic fabric, and seismic anisotropy. Earth and Planetary Science Letters, 387: 157-168.

47. Hansen, L.N., Zimmerman, M.E., Dillman, A.M. and Kohlstedt, D.L., 2012. Strain localization in olivine aggregates at high temperature: A laboratory comparison of constant-strain-rate and constant-stress boundary conditions. Earth and Planetary Science Letters, 333-334: 134-145.

48. Hansen, L.N., Zimmerman, M.E. and Kohlstedt, D.L., 2011. Grain boundary sliding in San Carlos olivine: Flow law parameters and crystallographic-preferred orientation. Journal of Geophysical Research, 116(B8).

49. Harigane, Y., Michibayashi, K., Morishita, T., Tani, K., Dick, H.J.B. and Ishizuka, O., 2013. The earliest mantle fabrics formed during subduction zone infancy. Earth and Planetary Science Letters, 377-378: 106-113.

50. Harrison, T.M., Grove, M., Lovera, O.M. and Catlos, E., 1998. A model for the origin of Himalayan anatexis and inverted metamorphism. Journal of Geophysical Research: Solid Earth, 103(B11): 27017-27032.

51. He, R., Zhao, D., Gao, R. and Zheng, H., 2010. Tracing the Indian lithospheric mantle beneath central Tibetan Plateau using teleseismic tomography. Tectonophysics, 491(1-4): 230-243.

52. Helmstaedt, H., Anderson, O.L. and Gavasci, A.T., 1972. Petrofabric studies of eclogite, spinel-Websterite, and spinel-lherzolite Xenoliths from kimberlite-bearing breccia pipes in southeastern Utah and northeastern Arizona. Journal of Geophysical Research, 77(23): 4350-4365.

53. Henry, H., Tilhac, R., Griffin, W.L., O'Reilly, S.Y., Satsukawa, T., Kaczmarek, M.-A., Grégoire, M. and Ceuleneer, G., 2017. Deformation of mantle pyroxenites provides clues to geodynamic processes in subduction zones: Case

study of the Cabo Ortegal Complex, Spain. Earth and Planetary Science Letters, 472: 174-185.

54.   Hess, H., 1964. Seismic anisotropy of the uppermost mantle under oceans. Nature, 203(4945): 629-631.

55.   Hidas, K., Falus, G., Szabó, C., Szabó, P.J., Kovács, I. and Földes, T., 2007. Geodynamic implications of flattened tabular equigranular textured peridotites from the Bakony-Balaton Highland Volcanic Field (Western Hungary). Journal of Geodynamics, 43(4-5): 484-503.

56.   Hill, R., 1952. The elastic behaviour of a crystalline aggregate. Proceedings of the Physical Society. Section A, 65(5): 349.

57.   Hirn, A., Jiang, M., Sapin, M., Diaz, J., Nercessian, A., Lu, Q., Lepine, J., Shi, D., Sachpazi, M. and Pandey, M., 1995. Seismic anisotropy as an indicator of mantle flow beneath the Himalayas and Tibet. Nature, 375(6532): 571-574.

58.   Hodges, K., Hurtado, J. and Whipple, K., 2001. Southward extrusion of Tibetan crust and its effect on Himalayan tectonics. Tectonics, 20(6): 799-809.

59.   Holt, W., 2000. Correlated crust and mantle strain fields in Tibet. Geology, 28(1): 67-70.

60.   Holtzman, B.K. and Hustoft, J., 2003. Melt segregation and strain partitioning: implications for seismic anisotropy and mantle flow. Science, 301(5637): 1227-30.

61.   Hou, Z., Duan, L., Lu, Y., Zheng, Y., Zhu, D., Yang, Z., Yang, Z., Wang, B., Pei, Y. and Zhao, Z., 2015. Lithospheric architecture of the Lhasa terrane and its control on ore deposits in the Himalayan-Tibetan orogen. Economic Geology, 110(6): 1541-1575.

62.   Hou, Z.Q., Gao, Y.F., Qu, X.M., Rui, Z.Y. and Mo, X.X., 2004. Origin of adakitic intrusives generated during mid-Miocene east–west extension in southern Tibet. Earth and Planetary Science Letters, 220(1-2): 139-155.

63.   Huang, W.C., Ni, J.F., Tilmann, F., Nelson, D., Guo, J., Zhao, W., Mechie, J., Kind, R., Saul, J. and Rapine, R., 2000. Seismic polarization anisotropy beneath the central Tibetan Plateau. Journal of Geophysical Research: Solid Earth, 105(B12): 27979-27989.

64.   Ismail, W.B. and Mainprice, D., 1998. An olivine fabric database: an overview

of upper mantle fabrics and seismic anisotropy. Tectonophysics, 296(1): 145-157.

65.   Ji, S., Matthew, H.S. and Simon, H., 1993. Petrofabric, P-wave anisotropy and seismic reflectivity of high-grade tectonites. Tectonophysics, 222(2): 195-226.

66.   Ji, W.-Q., Wu, F.-Y., Chung, S.-L., Li, J.-X. and Liu, C.-Z., 2009. Zircon U–Pb geochronology and Hf isotopic constraints on petrogenesis of the Gangdese batholith, southern Tibet. Chemical Geology, 262(3-4): 229-245.

67.   Jung, H., 2011. Seismic anisotropy produced by serpentine in mantle wedge. Earth and Planetary Science Letters, 307(3-4): 535-543.

68.   Jung, H. and Karato, S., 2001. Water-induced fabric transitions in olivine. Science, 293(5534): 1460.

69.   Jung, H., Katayama, I., Jiang, Z., Hiraga, T. and Karato, S., 2006. Effect of water and stress on the lattice-preferred orientation of olivine. Tectonophysics, 421(1-2): 1-22.

70.   Jung, H., Park, M., Jung, S. and Lee, J., 2010. Lattice preferred orientation, water content, and seismic anisotropy of orthopyroxene. Journal of Earth Science, 21(5): 555-568.

71.   Kapp, P., Murphy, M.A., Yin, A., Harrison, T.M., Ding, L. and Guo, J., 2003. Mesozoic and Cenozoic tectonic evolution of the Shiquanhe area of western Tibet. Tectonics, 22(4): n/a-n/a.

72.   Kapp, P., Yin, A., Manning, C.E., Murphy, M., Harrison, T.M., Spurlin, M., Lin, D., Xi-Guang, D. and Cun-Ming, W., 2000. Blueschist-bearing metamorphic core complexes in the Qiangtang block reveal deep crustal structure of northern Tibet. Geology, 28(1): 19-22.

73.   Karato, S.I., Zhang, S. and Wenk, H.R., 1995. Superplasticity in Earth's Lower Mantle: Evidence from Seismic Anisotropy and Rock Physics. Science, 270(5235): 458-461.

74.   Katayama, I., Jung, H. and Karato, S.-i., 2004. New type of olivine fabric from deformation experiments at modest water content and low stress. Geology, 32(12).

75.   Katayama, I. and Karato, S.-i., 2006. Effect of temperature on the B- to C-type olivine fabric transition and implication for flow pattern in subduction zones. Physics of the Earth and Planetary Interiors, 157(1-2): 33-45.

76. Kendall, J.M. and Silver, P., 1998. Investigating causes of D″ anistropy. The core-mantle boundary region: 97-118.

77. Kind, R., Ni, J., Zhao, W., Wu, J., Yuan, X., Zhao, L., Sandvol, E., Reese, C., Nabelek, J. and Hearn, T., 1996. Evidence from earthquake data for a partially molten crustal layer in southern Tibet. Science, 274(5293): 1692-1694.

78. Kind, R., Yuan, X., Saul, J., Nelson, D., Sobolev, S.V., Mechie, J., Zhao, W., Kosarev, G., Ni, J., Achauer, U. and Jiang, M., 2002. Seismic Images of Crust and Upper Mantle Beneath Tibet: Evidence for Eurasian Plate Subduction. Science, 298(5596): 1219-1221.

79. Kirby, S.H. and Kronenberg, A.K., 1984. Deformation of clinopyroxenite: Evidence for a transition in flow mechanisms and semibrittle behavior. Journal of Geophysical Research: Solid Earth, 89(B5): 3177-3192.

80. Kong, F., Wu, J., Liu, L., Liu, K.H., Song, J., Li, J. and Gao, S.S., 2018. Azimuthal anisotropy and mantle flow underneath the southeastern Tibetan Plateau and northern Indochina Peninsula revealed by shear wave splitting analyses. Tectonophysics, 747-748: 68-78.

81. Kumamoto, K.M., Warren, J.M. and Hauri, E.H., 2019. Evolution of the Josephine Peridotite Shear Zones: 1. Compositional Variation and Shear Initiation. Geochemistry, Geophysics, Geosystems.

82. Kumar, P., Ravi Kumar, M., Srijayanthi, G., Arora, K., Srinagesh, D., Chadha, R.K. and Sen, M.K., 2013. Imaging the lithosphere-asthenosphere boundary of the Indian plate using converted wave techniques. Journal of Geophysical Research: Solid Earth, 118(10): 5307-5319.

83. Kumar, P., Yuan, X., Kind, R. and Ni, J., 2006. Imaging the colliding Indian and Asian lithospheric plates beneath Tibet. Journal of Geophysical Research: Solid Earth, 111(B6): n/a-n/a.

84. Lavé, J., Avouac, J., Lacassin, R., Tapponnier, P. and Montagner, J., 1996. Seismic anisotropy beneath Tibet: evidence for eastward extrusion of the Tibetan lithosphere? Earth and Planetary Science Letters, 140(1-4): 83-96.

85. Le Roux, V., Tommasi, A. and Vauchez, A., 2008. Feedback between melt percolation and deformation in an exhumed lithosphere–asthenosphere boundary. Earth and Planetary Science Letters, 274(3): 401-413.

86. Li, C., van der Hilst, R.D., Meltzer, A.S. and Engdahl, E.R., 2008. Subduction of the Indian lithosphere beneath the Tibetan Plateau and Burma. Earth and Planetary Science Letters, 274(1-2): 157-168.

87. Li, Y., Wu, Q., Zhang, F., Feng, Q. and Zhang, R., 2011. Seismic anisotropy of the Northeastern Tibetan Plateau from shear wave splitting analysis. Earth and Planetary Science Letters, 304(1-2): 147-157.

88. Liang, C. and Song, X., 2006. A low velocity belt beneath northern and eastern Tibetan Plateau from Pn tomography. Geophysical Research Letters, 33(22).

89. Liang, X., Chen, Y., Tian, X., Chen, Y.J., Ni, J., Gallegos, A., Klemperer, S.L., Wang, M., Xu, T., Sun, C., Si, S., Lan, H. and Teng, J., 2016. 3D imaging of subducting and fragmenting Indian continental lithosphere beneath southern and central Tibet using body-wave finite-frequency tomography. Earth and Planetary Science Letters, 443: 162-175.

90. Liang, X., Sandvol, E., Chen, Y.J., Hearn, T., Ni, J., Klemperer, S., Shen, Y. and Tilmann, F., 2012. A complex Tibetan upper mantle: A fragmented Indian slab and no south-verging subduction of Eurasian lithosphere. Earth and Planetary Science Letters, 333-334: 101-111.

91. Liu, C.-Z., Wu, F.-Y., Chung, S.-L. and Zhao, Z.-D., 2011. Fragments of hot and metasomatized mantle lithosphere in Middle Miocene ultrapotassic lavas, southern Tibet. Geology, 39(10): 923-926.

92. Liu, D., Zhao, Z., Zhu, D.-C., Niu, Y., DePaolo, D.J., Harrison, T.M., Mo, X., Dong, G., Zhou, S., Sun, C., Zhang, Z. and Liu, J., 2014a. Postcollisional potassic and ultrapotassic rocks in southern Tibet: Mantle and crustal origins in response to India–Asia collision and convergence. Geochimica et Cosmochimica Acta, 143: 207-231.

93. Liu, G.C., Shang, X.F., Ri-Zheng, H.E., Gao, R., Zou, C.Q. and Wen-Hui, L.I., 2014b. Topography of Moho beneath the central Qiangtang in North Tibet and its geodynamic implication. Chinese Journal of Geophysics, 57(7): 2043-2053.

94. Long, M.D. and Silver, P.G., 2009. Shear wave splitting and mantle anisotropy: measurements, interpretations, and new directions. Surveys in Geophysics, 30(4-5): 407-461.

95.   Lu, H., Tian, X., Yun, K. and Li, H., 2018. Convective removal of the Tibetan Plateau mantle lithosphere by ~26 Ma. Tectonophysics, 731-732: 17-34.

96.   Mainprice, D., 2007. Seismic anisotropy of the deep Earth from a mineral and rock physics perspective, Treatise Geophys., 2, 437–491, doi: 10.1016, B978-044452748-6.00045-6.

97.   Mainprice, D., Barruol, G. and Ismaïl, W.B., 2000. The Seismic Anisotropy of the Earth's Mantle: from Single Crystal to Polycrystal. American Geophysical Union, 237-264 pp.

98.   Mainprice, D. and Silver, P.G., 1993. Interpretation of SKS-waves using samples from the subcontinental lithosphere. Physics of the Earth & Planetary Interiors, 78(3-4): 257-280.

99.   Mauler, A., Bystricky, M., Kunze, K. and Mackwell, S., 2000. Microstructures and lattice preferred orientations in experimentally deformed clinopyroxene aggregates. Journal of Structural Geology, 22(11–12): 1633-1648.

100.   McNamara, D.E., Owens, T.J., Silver, P.G. and Wu, F.T., 1994. Shear wave anisotropy beneath the Tibetan Plateau. Journal of Geophysical Research: Solid Earth, 99(B7): 13655-13665.

101.   McNamara, D.E., Owens, T.J. and Walter, W.R., 1995. Observations of regional phase propagation across the Tibetan Plateau. Journal of Geophysical Research: Solid Earth, 100(B11): 22215-22229.

102.   Meade, C., Silver, P.G. and Kaneshima, S., 1995. Laboratory and seismological observations of lower mantle isotropy. Geophysical Research Letters, 22(10): 1293-1296.

103.   Mehl, L., 2003. Arc-parallel flow within the mantle wedge: Evidence from the accreted Talkeetna arc, south central Alaska. Journal of Geophysical Research, 108(B8).

104.   Michibayashi, K., Mainprice, D., Fujii, A., Uehara, S., Shinkai, Y., Kondo, Y., Ohara, Y., Ishii, T., Fryer, P., Bloomer, S.H., Ishiwatari, A., Hawkins, J.W. and Ji, S., 2016. Natural olivine crystal-fabrics in the western Pacific convergence region: A new method to identify fabric type. Earth and Planetary Science Letters, 443: 70-80.

105. Miller, C., Schuster, R., Klötzli, U., Frank, W. and Purtscheller, F, 1999. Post-collisional potassic and ultrapotassic magmatism in SW Tibet: geochemical and Sr–Nd–Pb–O isotopic constraints for mantle source characteristics and petrogenesis. Journal of Petrology, 40(9): 1399-1424.

106. Montagner, J.P. and Tanimoto, T., 1990. Global anisotropy in the upper mantle inferred from the regionalization of phase velocities. Journal of Geophysical Research: Solid Earth, 95(B4): 4797-4819.

107. Nábělek, J., Hetényi, G., Vergne, J., Sapkota, S., Kafle, B., Jiang, M., Su, H., Chen, J. and Huang, B.-S., 2009. Underplating in the Himalaya-Tibet collision zone revealed by the Hi-CLIMB experiment. Science, 325(5946): 1371-1374.

108. Nicolas, A., Christensen, N.I., Nicolas, A. and Christensen, N.I., 1987. Formation of Anisotropy in Upper Mantle Peridotites - A Review. Composition, Structure and Dynamics of the Lithosphere-Asthenosphere System: 111-123.

109. Niu, F., 2004. Seismic anisotropy in the lower mantle: A comparison of waveform splitting of SKS and SKKS. Geophysical Research Letters, 31(24).

110. Nowack, R.L., Chen, W.P. and Tseng, T.L., 2010. Application of Gaussian-Beam Migration to Multiscale Imaging of the Lithosphere beneath the Hi-CLIMB Array in Tibet. Bulletin of the Seismological Society of America, 100(4): 1743-1754.

111. Nunn, C., Roecker, S.W., Priestley, K.F., Liang, X. and Gilligan, A., 2014. Joint inversion of surface waves and teleseismic body waves across the Tibetan collision zone: the fate of subducted Indian lithosphere. Geophysical Journal International, 198(3): 1526-1542.

112. Owens, T.J., Randall, G.E., Wu, F.T. and Zeng, R., 1993. PASSCAL instrument performance during the Tibetan Plateau passive seismic experiment. Bulletin of the Seismological Society of America, 83(6): 1959-1970.

113. Owens, T.J. and Zandt, G., 1997. Implications of crustal property variations for models of Tibetan plateau evolution. nature, 387(6628): 37.

114. Ozacar, A.A. and Zandt, G., 2004. Crustal seismic anisotropy in central Tibet: Implications for deformational style and flow in the crust. Geophysical Research Letters, 31(23).

115. Pei, S., Zhao, J., Sun, Y., Xu, Z., Wang, S., Liu, H., Rowe, C.A., Toksöz, M.N.

and Gao, X., 2007. Upper mantle seismic velocities and anisotropy in China determined through Pn and Sn tomography. Journal of Geophysical Research, 112(B5).

116. Precigout, J., Prigent, C., Palasse, L. and Pochon, A., 2017. Water pumping in mantle shear zones. Nat Commun, 8: 15736.

117. Pullen, A., Kapp, P., Gehrels, G.E., Vervoort, J.D. and Ding, L., 2008. Triassic continental subduction in central Tibet and Mediterranean-style closure of the Paleo-Tethys Ocean. Geology, 36(5).

118. Qi, C., Hansen, L.N., Wallis, D., Holtzman, B.K. and Kohlstedt, D.L., 2018. Crystallographic Preferred Orientation of Olivine in Sheared Partially Molten Rocks: The Source of the "a-c Switch". Geochemistry, Geophysics, Geosystems, 19(2): 316-336.

119. Raitt, R., Shor, G., Francis, T. and Morris, G., 1969. Anisotropy of the Pacific upper mantle. Journal of Geophysical Research, 74(12): 3095-3109.

120. Raleigh, C.B., Kirby, S.H., Carter, N.L. and Lallemant, H.G.A., 1971. Slip and the clinoenstatite transformation as competing rate processes in enstatite. Journal of Geophysical Research, 76(17): 4011-4022.

121. Rapine, R.R., Ni, J.F. and Hearn, T.M., 1997. Regional wave propagation in China and its surrounding regions. Bulletin of the Seismological Society of America, 87(6): 1622-1636.

122. Raterron, P., Doukhan, N., Jaoul, O. and Doukhan, J., 1994. High temperature deformation of diopside IV: predominance of {110} glide above 1000 C. Physics of the Earth and Planetary Interiors, 82(3-4): 209-222.

123. Raterron, P., Fraysse, G., Girard, J. and Holyoke, C.W., 2016. Strength of orthoenstatite single crystals at mantle pressure and temperature and comparison with olivine. Earth and Planetary Science Letters, 450: 326-336.

124. Reiss, M.C., Long, M.D. and Creasy, N., 2019. Lowermost Mantle Anisotropy Beneath Africa From Differential SKS-SKKS Shear-Wave Splitting. Journal of Geophysical Research: Solid Earth.

125. Restivo, A. and Helffrich, G., 2006. Core-mantle boundary structure investigated usingSKSandSKKSpolarization anomalies. Geophysical Journal International, 165(1): 288-302.

126. Reuss, A. and Angnew, Z., 1929. A calculation of the bulk modulus of polycrystalline materials. Math Meth, 9: 55.

127. Ringwood, A.E. and Major, A., 1970. The system Mg 2 SiO 4   Fe 2 SiO 4 at high pressures and temperatures. Physics of the Earth and Planetary Interiors, 3: 89-108.

128. Roger, F., Arnaud, N., Gilder, S., Tapponnier, P., Jolivet, M., Brunel, M., Malavieille, J., Xu, Z. and Yang, J., 2003. Geochronological and geochemical constraints on Mesozoic suturing in east central Tibet. Tectonics, 22(4): n/a-n/a.

129. Ross, J.V. and Nielsen, K.C., 1978. High-temperature flow of wet polycrystalline enstatite. Tectonophysics, 44(1−4): 233-261.

130. Saikia, D., Kumar, M.R., Singh, A., Roy, S.K., Solomon Raju, P. and Lyngdoh, A.C., 2018. Mantle deformation in the Eastern Himalaya, Burmese arc and adjoining regions. Geochemistry, Geophysics, Geosystems.

131. Satsukawa, T., 2012. Microstructural/petrological characteristics of peridotite xenoliths in the back-arc spreading/rifting zones and implication for the evolution and seismic anisotropy in the uppermost mantle.

132. Savage, M.K., 1999. Seismic anisotropy and mantle deformation: What have we learned from shear wave splitting? Reviews of Geophysics, 37(1): 65-106.

133. Shao, T., Ji, S., Oya, S., Michibayashi, K. and Wang, Q., 2016. Mica-dominated seismic properties of mid-crust beneath west Yunnan (China) and geodynamic implications. Tectonophysics, 677-678: 324-338.

134. Silver, P.G., 1996. Seismic anistropy beneath the continents: probing the depths of geology. Annual Review of Earth & Planetary Sciences, 24(1): 385-432.

135. Silver, P.G. and Chan, W.W., 1988. Implications for continental structure and evolution from seismic anisotropy. Nature, 335(6185): 34-39.

136. Silver, P.G. and Kaneshima, S., 1993. Constraints on mantle anisotropy beneath Precambrian North America from a transportable teleseismic experiment. Geophysical Research Letters, 20(12): 1127-1130.

137. Singh, A., Eken, T., Mohanty, D.D., Saikia, D., Singh, C. and Ravi Kumar, M., 2016. Significant seismic anisotropy beneath southern Tibet inferred from splitting of direct S-waves. Physics of the Earth and Planetary Interiors, 250: 1-11.

138.   Singh, A., Kumar, M.R. and Raju, P.S., 2007. Mantle deformation in Sikkim and adjoining Himalaya: Evidences for a complex flow pattern. Physics of the Earth and Planetary Interiors, 164(3-4): 232-241.

139.   Skemer, P., Warren, J.M., Hansen, L.N., Hirth, G. and Kelemen, P.B., 2013. The influence of water and LPO on the initiation and evolution of mantle shear zones. Earth and Planetary Science Letters, 375: 222-233.

140.   Skemer, P., Warren, J.M., Kelemen, P.B. and Hirth, G., 2010. Microstructural and Rheological Evolution of a Mantle Shear Zone. Journal of Petrology, 51(1): 43-53.

141.   Soustelle, V., Tommasi, A., Bodinier, J.L., Garrido, C.J. and Vauchez, A., 2009. Deformation and Reactive Melt Transport in the Mantle Lithosphere above a Large-scale Partial Melting Domain: the Ronda Peridotite Massif, Southern Spain. Journal of Petrology, 50(7): 1235-1266.

142.   Staisch, L.M., Niemi, N.A., Clark, M.K. and Chang, H., 2016. Eocene to late Oligocene history of crustal shortening within the Hoh Xil Basin and implications for the uplift history of the northern Tibetan Plateau. Tectonics, 35(4): 862-895.

143.   Su, B., Zhang, H., Ying, J., Xiao, Y. and Zhao, X., 2009. Nature and processes of the lithospheric mantle beneath the western Qinling: Evidence from deformed peridotitic xenoliths in Cenozoic kamafugite from Haoti, Gansu Province, China. Journal of Asian Earth Sciences, 34(3): 258-274.

144.   Tapponnier, P., Peltzer, G., Le Dain, A., Armijo, R. and Cobbold, P., 1982. Propagating extrusion tectonics in Asia: New insights from simple experiments with plasticine. Geology, 10(12): 611-616.

145.   Tapponnier, P., Zhiqin, X., Roger, F., Meyer, B., Arnaud, N., Wittlinger, G. and Jingsui, Y., 2001. Oblique stepwise rise and growth of the Tibet Plateau. science, 294(5547): 1671-1677.

146.   Tian, X., Chen, Y., Tseng, T.-L., Klemperer, S.L., Thybo, H., Liu, Z., Xu, T., Liang, X., Bai, Z., Zhang, X., Si, S., Sun, C., Lan, H., Wang, E. and Teng, J., 2015. Weakly coupled lithospheric extension in southern Tibet. Earth and Planetary Science Letters, 430: 171-177.

147.   Tielke, J., Mecklenburgh, J., Mariani, E. and Wheeler, J., 2019. The influence

of water on the strength of olivine dislocation slip systems. Journal of Geophysical Research: Solid Earth.

148. Tilmann, F., Ni, J., Hearn, T., Ma, Y.S., Rapine, R., Kind, R., Mechie, J., Saul, J., Haines, S., Klemperer, S., Brown, L., Pananont, P., Ross, A., Nelson, K.D., Guo, J., Zhao, W. and Team, I.I.S., 2003. Seismic imaging of the downwelling Indian lithosphere beneath central Tibet. Science, 300(5624): 1424-1427.

149. Tommasi, A., Goryaeva, A., Carrez, P., Cordier, P. and Mainprice, D., 2018. Deformation, crystal preferred orientations, and seismic anisotropy in the Earth's D″ layer. Earth and Planetary Science Letters, 492: 35-46.

150. Tommasi, A., Mainprice, D., Canova, G. and Chastel, Y., 2000. Viscoplastic self-consistent and equilibrium-based modeling of olivine lattice preferred orientations: Implications for the upper mantle seismic anisotropy. Journal of Geophysical Research: Solid Earth, 105(B4): 7893-7908.

151. Tommasi, A., Tikoff, B. and Vauchez, A., 1999. Upper mantle tectonics: three-dimensional deformation, olivine crystallographic fabrics and seismic properties. Earth and Planetary Science Letters, 168(1): 173-186.

152. Tseng, T.-L., Chen, W.-P. and Nowack, R.L., 2009. Northward thinning of Tibetan crust revealed by virtual seismic profiles. Geophysical Research Letters, 36(24).

153. Tunini, L., Jiménez-Munt, I., Fernandez, M., Vergés, J., Villaseñor, A., Melchiorre, M. and Afonso, J.C., 2016. Geophysical-petrological model of the crust and upper mantle in the India-Eurasia collision zone. Tectonics, 35(7): 1642-1669.

154. van Hinsbergen, D.J., Lippert, P.C., Dupont-Nivet, G., McQuarrie, N., Doubrovine, P.V., Spakman, W. and Torsvik, T.H., 2012. Greater India Basin hypothesis and a two-stage Cenozoic collision between India and Asia. Proceedings of the National Academy of Sciences, 109(20): 7659-64.

155. Vauchez, A., Dineur, F. and Rudnick, R., 2005. Microstructure, texture and seismic anisotropy of the lithospheric mantle above a mantle plume: Insights from the Labait volcano xenoliths (Tanzania). Earth and Planetary Science Letters, 232(3-4): 295-314.

156. Voigt, W., 1928. Textbook of crystal physics. BB Teubner, Leipzig, 2.

157. Wang, C., Chang, L., Ding, Z., Liu, Q., Liao, W. and Flesch, L.M., 2013. Upper mantle anisotropy and crust-mantle deformation pattern beneath the Chinese mainland. Science China Earth Sciences, 57(1): 132-143.

158. Wang, Q., Wyman, D.A., Xu, J., Wan, Y., Li, C., Zi, F., Jiang, Z., Qiu, H., Chu, Z., Zhao, Z. and Dong, Y., 2007. Triassic Nb-enriched basalts, magnesian andesites, and adakites of the Qiangtang terrane (Central Tibet): evidence for metasomatism by slab-derived melts in the mantle wedge. Contributions to Mineralogy and Petrology, 155(4): 473-490.

159. Wang, Y., Tian, W., Wei, C., Chen, M. and Qian, J., 2012. Discovery of pyroxenite xenoliths in the Cenozoic basalt from Xikeer, Tarim, northwest China and its geological implications. Acta Petrologica Sinica, 28(4): 1139-1147.

160. Warren, J.M., Hirth, G. and Kelemen, P.B., 2008. Evolution of olivine lattice preferred orientation during simple shear in the mantle. Earth and Planetary Science Letters, 272(3-4): 501-512.

161. Weislogel, A.L., 2008. Tectonostratigraphic and geochronologic constraints on evolution of the northeast Paleotethys from the Songpan-Ganzi complex, central China. Tectonophysics, 451(1-4): 331-345.

162. Wu, G., Gao, R., Yu, Q., Cheng, Q., Meng, L. and Dong, X., 1991. Integrated investigations of the Qinghai-Tibet Plateau along the Yadong-Golmud geoscience transect. Chin J Geophys, 34: 552-562.

163. Wu, J., Zhang, Z., Kong, F., Yang, B.B., Yu, Y., Liu, K.H. and Gao, S.S., 2015. Complex seismic anisotropy beneath western Tibet and its geodynamic implications. Earth and Planetary Science Letters, 413: 167-175.

164. Xu, B., Griffin, W.L., Xiong, Q., Hou, Z.-Q., O'Reilly, S.Y., Guo, Z., Pearson, N.J., Gréau, Y., Yang, Z.-M. and Zheng, Y.-C., 2017a. Ultrapotassic rocks and xenoliths from South Tibet: Contrasting styles of interaction between lithospheric mantle and asthenosphere during continental collision. Geology, 45(1): 51-54.

165. Xu, Q., Pei, S., Yuan, X., Zhao, J., Liu, H., Tu, H. and Chen, S., 2019. Seismic evidence for lateral asthenospheric flow beneath the northeastern Tibetan Plateau derived from S receiver functions. Geochemistry, Geophysics, Geosystems.

166. Xu, Q., Zhao, J., Pei, S. and Liu, H., 2011. The lithosphere-asthenosphere boundary revealed by S-receiver functions from the Hi-CLIMB experiment. Geophysical Journal International, 187(1): 414-420.

167. Xu, Q., Zhao, J., Yuan, X., Liu, H. and Pei, S., 2017b. Detailed Configuration of the Underthrusting Indian Lithosphere Beneath Western Tibet Revealed by Receiver Function Images. Journal of Geophysical Research: Solid Earth, 122(10): 8257-8269.

168. Xu, Z., Wang, Q., Ji, S., Chen, J., Zeng, L., Yang, J., Chen, F., Liang, F. and Wenk, H.-R., 2006. Petrofabrics and seismic properties of garnet peridotite from the UHP Sulu terrane (China): Implications for olivine deformation mechanism in a cold and dry subducting continental slab. Tectonophysics, 421(1-2): 111-127.

169. Yang, T.N., Zhang, H.R., Liu, Y.X., Wang, Z.L., Song, Y.C., Yang, Z.S., Tian, S.H., Xie, H.Q. and Hou, K.J., 2011. Permo-Triassic arc magmatism in central Tibet: Evidence from zircon U–Pb geochronology, Hf isotopes, rare earth elements, and bulk geochemistry. Chemical Geology, 284(3-4): 270-282.

170. Yin, A., 2006. Cenozoic tectonic evolution of the Himalayan orogen as constrained by along-strike variation of structural geometry, exhumation history, and foreland sedimentation. Earth-Science Reviews, 76(1-2): 1-131.

171. Yin, A., Dang, Y., Zhang, M., McRivette, M.W., Burgess, W.P. and Chen, X., 2007. Cenozoic tectonic evolution of Qaidam basin and its surrounding regions (part 2): Wedge tectonics in southern Qaidam basin and the Eastern Kunlun Range, Geological Society of America Bulletin Special Paper 433, pp. 369-390.

172. Yin, A. and Harrison, T.M., 2000. Geologic Evolution of the Himalayan-Tibetan Orogen. Annual Review of Earth & Planetary Sciences, 28(28): 211-280.

173. Yuan, D.-Y., Ge, W.-P., Chen, Z.-W., Li, C.-Y., Wang, Z.-C., Zhang, H.-P., Zhang, P.-Z., Zheng, D.-W., Zheng, W.-J., Craddock, W.H., Dayem, K.E., Duvall, A.R., Hough, B.G., Lease, R.O., Champagnac, J.-D., Burbank, D.W., Clark, M.K., Farley, K.A., Garzione, C.N., Kirby, E., Molnar, P. and Roe, G.H., 2013. The growth of northeastern Tibet and its relevance to large-scale continental geodynamics: A review of recent studies. Tectonics, 32(5): 1358-

1370.

174.   Zhang, H., Teng, J., Tian, X., Zhang, Z., Gao, R. and Liu, J., 2012a. Lithospheric thickness and upper-mantle deformation beneath the NE Tibetan Plateau inferred from S receiver functions and SKS splitting measurements. Geophysical Journal International, 191(3): 1285-1294.

175.   Zhang, H., Zhao, J. and Xu, Q., 2012b. Crustal and upper mantle velocity structure beneath central Tibet by P-wave teleseismic tomography. Geophysical Journal International, 190(3): 1325-1334.

176.   Zhang, H., Zhao, J., Zhao, D., Yu, C., Liu, H. and Hu, Z., 2016. Complex deformation in western Tibet revealed by anisotropic tomography. Earth and Planetary Science Letters, 451: 97-107.

177.   Zhang, J., Greenii, H. and Bozhilov, K., 2006. Rheology of omphacite at high temperature and pressure and significance of its lattice preferred orientations. Earth and Planetary Science Letters, 246(3-4): 432-443.

178.   Zhang, K.-J., Zhang, Y.-X., Tang, X.-C. and Xia, B., 2012c. Late Mesozoic tectonic evolution and growth of the Tibetan plateau prior to the Indo-Asian collision. Earth-Science Reviews, 114(3-4): 236-249.

179.   Zhang, S., S.-I, K., Fitz, G.J., Faul, U.H. and Zhou, Y., 2000. Simple shear deformation of olivine aggregates. Tectonophysics, 316(1-2): 133-152.

180.   Zhang, X., Teng, J., Sun, R., Romanelli, F., Zhang, Z. and Panza, G.F., 2014. Structural model of the lithosphere–asthenosphere system beneath the Qinghai–Tibet Plateau and its adjacent areas. Tectonophysics, 634: 208-226.

181.   Zhang, Z., Deng, Y., Teng, J., Wang, C., Gao, R., Chen, Y. and Fan, W., 2011. An overview of the crustal structure of the Tibetan plateau after 35 years of deep seismic soundings. Journal of Asian Earth Sciences, 40(4): 977-989.

182.   Zhao, J., Murodov, D., Huang, Y., Sun, Y., Pei, S., Liu, H., Zhang, H., Fu, Y., Wang, W., Cheng, H. and Tang, W., 2014a. Upper mantle deformation beneath central-southern Tibet revealed by shear wave splitting measurements. Tectonophysics, 627: 135-140.

183.   Zhao, J., Yuan, X., Liu, H., Kumar, P., Pei, S., Kind, R., Zhang, Z., Teng, J., Ding, L., Gao, X., Xu, Q. and Wang, W., 2010. The boundary between the Indian and Asian tectonic plates below Tibet. Proceedings of the National

Academy of Sciences, 107(25): 11229-11233.

184. Zhao, J., Zhao, D., Zhang, H., Liu, H., Huang, Y., Cheng, H. and Wang, W., 2014b. P-wave tomography and dynamics of the crust and upper mantle beneath western Tibet. Gondwana Research, 25(4): 1690-1699.

185. Zhao, L.-F., Xie, X.-B., He, J.-K., Tian, X. and Yao, Z.-X., 2013. Crustal flow pattern beneath the Tibetan Plateau constrained by regional Lg-wave Q tomography. Earth and Planetary Science Letters, 383: 113-122.

186. Zhao, W., Kumar, P., Mechie, J., Kind, R., Meissner, R., Wu, Z., Shi, D., Su, H., Xue, G., Karplus, M. and Tilmann, F., 2011. Tibetan plate overriding the Asian plate in central and northern Tibet. Nature Geoscience, 4(12): 870-873.

187. Zhao, W., Mechie, J., Brown, L., Guo, J., Haines, S., Hearn, T., Klemperer, S., Ma, Y., Meissner, R. and Nelson, K., 2001. Crustal structure of central Tibet as derived from project INDEPTH wide-angle seismic data. Geophysical Journal International, 145(2): 486-498.

188. Zhao, Z., Mo, X., Dilek, Y., Niu, Y., DePaolo, D.J., Robinson, P., Zhu, D., Sun, C., Dong, G. and Zhou, S., 2009. Geochemical and Sr–Nd–Pb–O isotopic compositions of the post-collisional ultrapotassic magmatism in SW Tibet: Petrogenesis and implications for India intra-continental subduction beneath southern Tibet. Lithos, 113(1-2): 190-212.

189. Zheng, C., Zhang, R., Wu, Q., Li, Y., Zhang, F., Shi, K. and Ding, Z., 2019. Variations in Crustal and Uppermost Mantle Structures Across Eastern Tibet and Adjacent Regions: Implications of Crustal Flow and Asthenospheric Upwelling Combined for Expansions of the Tibetan Plateau. Tectonics.

190. Zhu, D.-C., Zhao, Z.-D., Niu, Y., Dilek, Y., Hou, Z.-Q. and Mo, X.-X., 2013. The origin and pre-Cenozoic evolution of the Tibetan Plateau. Gondwana Research, 23(4): 1429-1454.

Chapter 2

I do truly believe I am fortunate. I am fortunate because I have been able to spend my life in study of the world. As such, I have never felt insignificant. This life is a mystery, yes, and it is often a trial, but if one can find some facts within it, one should always do so – for knowledge is the most precious of all commodities

—— *《The Signature of All Things》*
Elizabeth Gilbert

Seismic anisotropy in the Tibetan lithosphere inferred from mantle xenoliths

Highlights

- We first report the crystal preferred orientation of mantle xenoliths in Lhasa terrane, Tibet.

- Seismic properties of the xenoliths are calculated based on the mineral fabric.

- The dominant fabric of olivine in peridotite xenoliths is considered to deform with melt-assisted.

- Anomalous delay times observed in Tibet is not only attributed from mineral orientation, but melt pocket orientation as well.

- Tibetan lithospheric architecture changes from east to west.

Chapter 2

Abstract

Shear wave splitting measurements in the Qiangtang terrane of central Tibet revealed extraordinarily large delay times of > 2.0s for SKS splitting and an abrupt change of the fast polarization direction from a NNE-SSW direction into an E-W direction in an about 100 km wide zone south of the Banggong-Nujiang Suture. Peridotite xenoliths brought to the surface from a depth of 55 km to 70 km by Cenozoic potassic volcanism in Sailipu in the north-western Lhasa terrane show lattice preferred orientation of their olivine with a concentration of [010] directions and a large circle girdle of the [100] and [001] directions defining an important fabric plane with a polarization anisotropy of 4.6 % on average in directions parallel to the plane. In contrast, the polarization anisotropy is very weak in the direction perpendicular to this fabric plane. According to the seismic anisotropy of the peridotite xenoliths, to match the delay times ranging from 1.5 s to more than 2.0 s in the Lhasa and Qiangtang terranes would require an anisotropic layer at least 150 km to 200 km thick even if the fabric plane with maximum seismic anisotropy were oriented vertically and the effect of the intrinsic elastic anisotropy of the peridotites on SKS splitting were maximized. This is unrealistic, and we propose to attribute the large delay times to an extraordinarily strong seismic anisotropy of the lithospheric mantle underneath central Tibet. We propose that this anisotropy is due to the presence of partially molten domains with high aspect ratio that are aligned sub-vertically enhancing the effect of the intrinsic elastic anisotropy of the peridotites on SKS splitting. The abrupt change of the fast polarization direction south of the Banggong-Nujiang Suture may reflect the change of the fabric of olivine which is fundamentally different in the northward subducting Indian lithospheric mantle and in the lithospheric mantle beneath northern Tibet.

2.1 Introduction

It is commonly agreed that seismic anisotropy is an important indicator of plastic deformation in the lithospheric mantle and of asthenospheric flow associated with plate motion (Nicolas et al., 1987). Shear-wave splitting is the most direct evidence of seismic anisotropy (Silver, 1996), and the most useful signal is provided by the birefringence of close to vertically propagating SKS phases, which are created by P-to-S wave conversion at the core-mantle boundary (CMB). The initial polarization of the SKS phases is radial, and they propagate steeply through the mantle and the crust (e.g. Silver 1996 and references therein). Any transversely anisotropic medium with a sub-horizontal axis of symmetry located between the CMB and the earth surface can potentially induce SKS splitting, in which an incident shear-wave is polarized into two orthogonal components propagating with different velocities. Generally speaking, the most important reason for the seismic anisotropy of the lithosphere is the crystal preferred orientation (CPO) of its constituent minerals (Mainprice, 2007). Olivine and pyroxene are the most abundant minerals in the upper mantle. The fabrics formed by these two minerals provide a record of mantle deformation (Mainprice, 2007). Based on crystal orientation analysis using Electron Backscatter Diffraction (EBSD) performed on the run products from dedicated deformation experiments, the different CPOs of olivine have been categorized into six types, referred to as A-, B-, C-, D-, E- and AG-type (Mainprice, 2007). Since both olivine and pyroxene are elastically anisotropic, each fabric type has different seismic properties. Mineral fabric related to the structural frame, greatly enhance our ability to address the questions of the seismic tomography data.
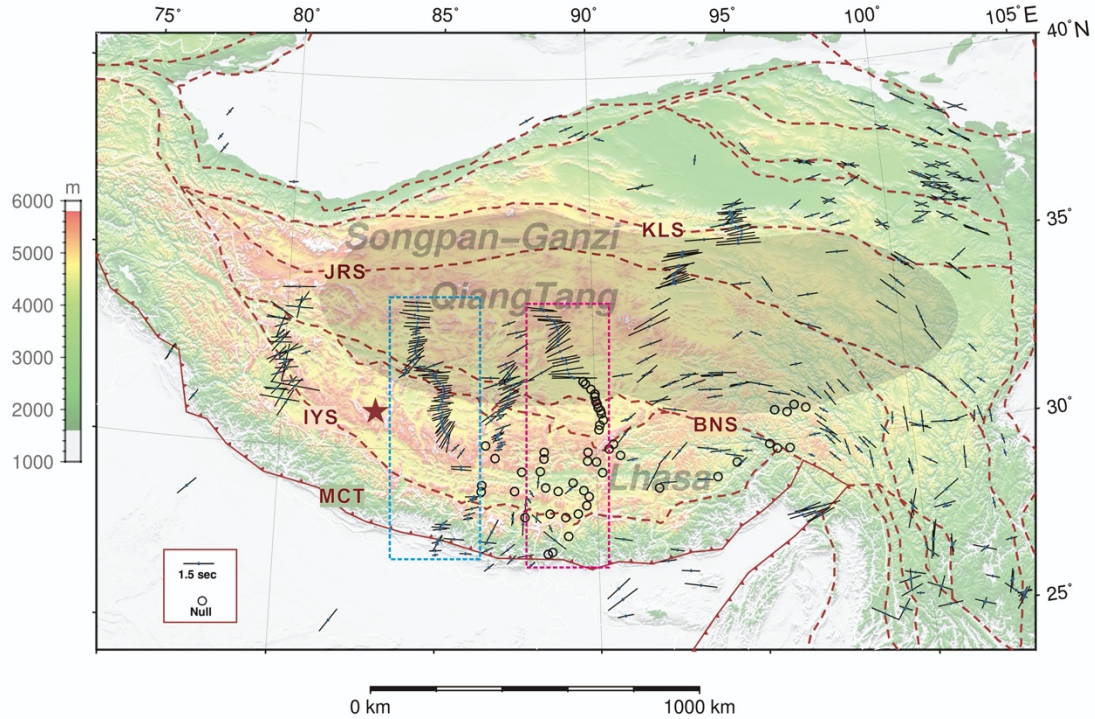
Fig. 2-1. Average splitting parameters including fast polarization direction (FPD) and delay time of SKS wave splitting in Tibet from 1994 to 2015. The orientations and lengths of the black bars indicate the FPDs and splitting delay times, respectively. The black circles without lines are stations with only null measurements. The red star (Sailipu) represents the sampling location of ultrapotassic magmatic rock containing mantle xenoliths. The blue square represents the Hi-Climb profile. The pink square represents the INDEPTH III and II profiles. The shadowed area is the zone of Sn-wave attenuation. (Acronyms are asame as Fig. 1-1)

The Tibetan Plateau is the youngest and most active orogen in the world, and it is characterized by complex deformation of its lithosphere (Xu et al., 2017; Yin and Harrison, 2000). Results from SKS and SKKS splitting measurements in the Tibetan Plateau indicate that the fast polarization direction (FPDs) is mainly NNE-SSW and NE-SW in the southern part of Tibet, south of the Indus-Yarlung Suture (IYS), NE-SW in the central part of the Lhasa terrane, between the IYS and the Bangong-Nujiang suture (BNS), and ENE-WSW to nearly E-W in the central part of Tibet, north of the BNS. The splitting time delays are in the range of 0.45-1.3s in the

southern part and increase to 0.9-2.54s in the northern part (Singh et al., 2016). The extraordinarily large delay times in excess of 2.0s that are observed in the Lhasa and the Qiangtang terranes testify to a strong and unusual anisotropy in this region (Fig. 2-1). The pronounced shear-wave splitting in Tibet, and the interpretation as a strong seismic anisotropy has been discussed controversially (Chen et al., 2010; Hirn et al., 1995; Yang et al., 2002). In particular, it has remained unclear how seismic anisotropy is linked to the deformation of the lithosphere. Several hypotheses have been proposed including decoupling of an anisotropic layer in the asthenosphere (Lavé et al., 1996), ductile flow in the lithospheric mantle (Hirn et al., 1995), north-south shortening of the lithospheric mantle (Zhang et al., 2004), and a two-layer model of anisotropy (Wu et al., 2015). Knowing the fabric of mantle peridotites and, in particular, the CPO of olivine and pyroxene, thus allows derivation of the seismic properties of the mantle, which is a key information needed for interpreting seismological measurements. The CPOs of olivine and pyroxene in the Tibetan lithospheric mantle have, however, not been studied in any systematic manner so far.

In this communication, we present new petrographic and fabric information from the Sailipu mantle xenoliths. These xenoliths were brought to the surface by Cenozoic potassic volcanism in the north-western Lhasa terrane and provide samples of the Tibetan upper mantle. Based on the xenolith fabric data, we calculate their seismic properties, analyze the cause of shear-wave splitting observed in this region and discuss its implications for the current deformation of the lithosphere.

2.2 Geological and Geophysical Background

In the early Mesozoic, the Lhasa terrane was separated from eastern Gondwana and collided with the Qiangtang terrane during the early Cretaceous (e.g., Yin and Harrison, 2000). Under the long-term influence of northward subduction of Neo-

Tethyan lithosphere, intra-plate magmatism is widespread in the Lhasa terrane, as, for example, the Gangdese batholiths (ca. 68 - 43 Ma) and the Linzizong rocks (ca. 65 – 45 Ma) (Zhao et al., 2009). Subsequently, the collision between the Greater Indian plate and Tibet generated an east-west trending magmatic belt (~24-8 Ma) in the Lhasa terrane (e.g., Xu et al., 2017). These magmatic rocks are mainly potassic and ultrapotassic basaltic trachyandesite. Based on their trace element compositions, a large fraction of partial melt was inferred to have existed in the metasomatized upper mantle source region during the Middle Miocene (Zhao et al., 2009). The Sailipu mantle xenoliths are peridotites hosted by ultrapotassic volcanic rocks (Fig. 2-1). According to radiometric dating (K-Ar, ^{40}Ar-^{39}Ar and U-Pb), the ultrapotassic lavas erupted 17 Ma ago (Zhao et al., 2009; Cheng and Guo, 2017).

In the Qiangtang terrane and in the northern Lhasa terrane, the fast polarization direction is near 77° , sub-parallel to the Bangong-Nujiang suture, which is considered as the boundary between the Lhasa- and the Qiangtang terranes. In the south of the Lhasa terrane, the FPDs rotate into a NNE-SSW direction (Fig. 2-1). The splitting time delays in Tibet is about 1.04 s on average (Yang, et al., 2002). This is similar to the global average delay times for continents (Silver, 1996) implying that the lithospheric anisotropy is distributed over a vertical distance of about 120 km and suggesting that the SKS splitting below Tibet mainly originates from the lithosphere. However, 9.4 % and 6.3 % of the observations in Tibet show delay times larger than 1.7 s and 2.0 s, respectively, which is much higher than the corresponding global percentages in continents (about 4.7 % and 1.2 %) (Yang, et al., 2002) and calls for specific reasoning.

2.3 Analytical Methods and Data-Processing

2.3.1 Crystal orientation and texture measurements

The mineral fabrics were measured by SEM-EBSD analysis using a *Zeiss EVOMA15* scanning electron microscope (SEM) coupled with a *HKL Nordlys Nano* EBSD detector at the Institute of Geology, China Earthquake Administration, China. We focused on the microstructures and textures of the three main minerals in the xenoliths, olivine, orthopyroxene and clinopyroxene, to infer their deformation history and determine their seismic properties as a proxy for the Tibetan lithospheric mantle. Crystal orientation images covering the entire xenoliths ($10 - 20$ mm long and $10 - 15$ mm wide) were obtained with a step size of 11 µm using the *Oxford Instruments HKL AZtec* software. A working distance of 25 mm was used for pattern acquisition and automatic indexing was performed using the *AZtec* software. The *CHANNEL 5* software was used for noise reduction and for filling the missing data with at least 8 identical neighbors with similar orientation. Then this procedure was repeated for filling the missing data with at least 7, 6, and 5 identical neighbors with similar orientation. The resulting EBSD data was optimized using *MTex* (Bachmann et al., 2010; Henry et al., 2017) to remove points with large angular deviation and to smooth intra-crystalline data.

The strength of a CPO may be quantified in terms of the J-index, which represents the volume-averaged integral of the squared orientation densities and is sensitive to peaks in the orientation distribution function (Ismaıl and Mainprice, 1998). For a random distribution the J-index is unity, and for a single crystal (perfect CPO) the J-index is infinity. The olivine in natural samples of mantle peridotite typically has a J-index in the range of $2 - 25$ with a peak at $8 - 10$. Only very few samples have a J-index > 20 (Ismail and Mainprice, 1998).

An axial symmetry of the orientation distribution is described by the BA index (Mainprice et al., 2015). The BA index is based on the eigenvalues of the orientation tensors for certain crystallographic directions. For example, for describing the texture of olivine, a BA index can be defined as:

$$BA \; index = 1/2 \left(2 - \left(\frac{P010}{G010 - P010} \right) - \left(\frac{G100}{G100 + P100} \right) \right)$$

where P010 and G010 are the point maximum and the girdle of the [010] directions, respectively. Any fabric with BA approximately zero or unity can be regarded as having a pronounced axial symmetry and thus an important fabric plane perpendicular to the asymmetry axis. Any fabric with a BA that is approximately 0.5 does not have axial symmetry and no important fabric plane defined by axial symmetry.

The seismic properties of the xenoliths were calculated following the method of (Mainprice and Humbert, 1994) using single-crystal elastic constants, mineral densities, the textures (CPO) obtained from SEM-EBSD analysis, and the modal proportions of the minerals. For the computations the *MTex* software (Mainprice et al., 2015) was used and Voigt - Reuss - Hill averaging of single-crystal elastic constants was applied (Mainprice 2007). The results are displayed in upper hemisphere, equal-area stereographic projection

2.3.2 Mineral chemical analysis

The major-element compositions of olivine, orthopyroxene, clinopyroxene, and spinel were measured using a Cameca SXFive FE Electron Probe Microanalyzer (EPMA) equipped with 5 wavelength- and one energy-dispersive spectrometer at the Department of Lithospheric Research, University of Vienna. An acceleration voltage of 15 kV and a beam current of 20 nA were employed. The counting time was 20 s at the peak position and 10 s on each background position. The PAP method (Pouchou and Pichoir, 1991) was applied for matrix corrections. Natural and synthetic standards were used for calibration. The relative error of the laboratory internal standard is below 1%.

2.3.3 Splitting time analysis

In this study, we include seismic data from more than 4500 earthquakes, which

are available for the period from 1992 to 2013 at 78°-104° E in the area of the Tibetan Plateau (Fig. 2-1). A total of 672 broadband stations from the open access data base "Splitting Database" (Wüstefeld et al., 2008) were used for splitting analysis. The data from stations that recorded less than three events were excluded. The splitting parameters, including the fast polarization direction (FPD) and the split time delay (δt), were determined following the approach of (Eken and Tilmann, 2014) In total we obtained 1532 SKS splitting events and calculated an average of the respective splitting parameters for each station.

2.4 Results

We analyzed 8 peridotite xenoliths from Sailipu. In Table 2-1 the modal compositions, microstructures, mineral compositions, olivine CPO, and results from thermometry are summarized.

2.4.1 Petrographic features of the Sailipu mantle xenoliths

The harzburgite xenoliths from Sailipu are coarse-grained, equigranular spinel-facies rocks (4 pieces), with porphyroblastic varieties (4 pieces) (Fig. 2-2a – d). The mantle xenoliths are represented by small (0.5–1.0 cm) fragments of harzburgite with rounded and elongated shape. They mostly consist of olivine (60–75 vol.%), orthopyroxene (10–25 vol.%), clinopyroxene (<3 vol.%), and minor phlogopite and spinel (<5 vol.%). The equigranular harzburgites (Fig. 2-2a) are coarse-grained rocks with a well-equilibrated microstructure characterized by abundant triple junctions.

Table 2-1 Sample description and calculated results for the Sailipu peridotite xenoliths.

Sample	Texture	Modal proportions% (EBSD Mapping)					Olivine CPO			T (K)	Mg# in Ol
		Ol	Opx	Cpx	Sp	CPO	J-index	BA-index		
T16-120	Porphyroblastic	77.6	12.9	9.1	0.4	B-type	2.65	0.55	1375	89.6
T16-137	Equigranular	79.7	17.4	2.5	0.4	B-type	4.25	0.43	1387	90.0
T16-146-1	Porphyroblastic	66.2	29.2	4.6	0.0	AG-type	1.87	0.34	1368	89.7
T16-150	Equigranular	68.6	25.8	5.3	0.3	AG-type	3.00	0.29	1385	88.6
T16-153	Equigranular	71.8	17.0	11.0	0.2	B-type	3.24	0.48	1382	89.4
T16-156-1	Porphyroblastic	61.4	36.1	2.2	0.3	A-type	2.22	0.57	1371	90.5
T16-156-3	Equigranular	65.7	18.3	16.0	0.0	AG-type	1.79	0.33	1377	87.5
T16-170	Porphyroblastic	75.4	19.2	5.3	0.1	AG-type	2.55	0.28	1357	88.5

In the coarse-grained samples the grain boundary morphology ranges between straight and curved. All phases tend to show straight boundaries at the 120° triple junctions and curved boundaries in mosaic texture (Fig. 2-2a). The grain size is ~1 mm and the grains display anhedral shapes and abundant late cracks. The porphyroblastic variety of the harzburgites (Fig. 2-2b) contains large, 2 to 4 mm sized, olivine and orthopyroxene grains, which are surrounded by sub-millimeter (~0.3 mm) sized grains of tabular recrystallized olivine and clinopyroxene.
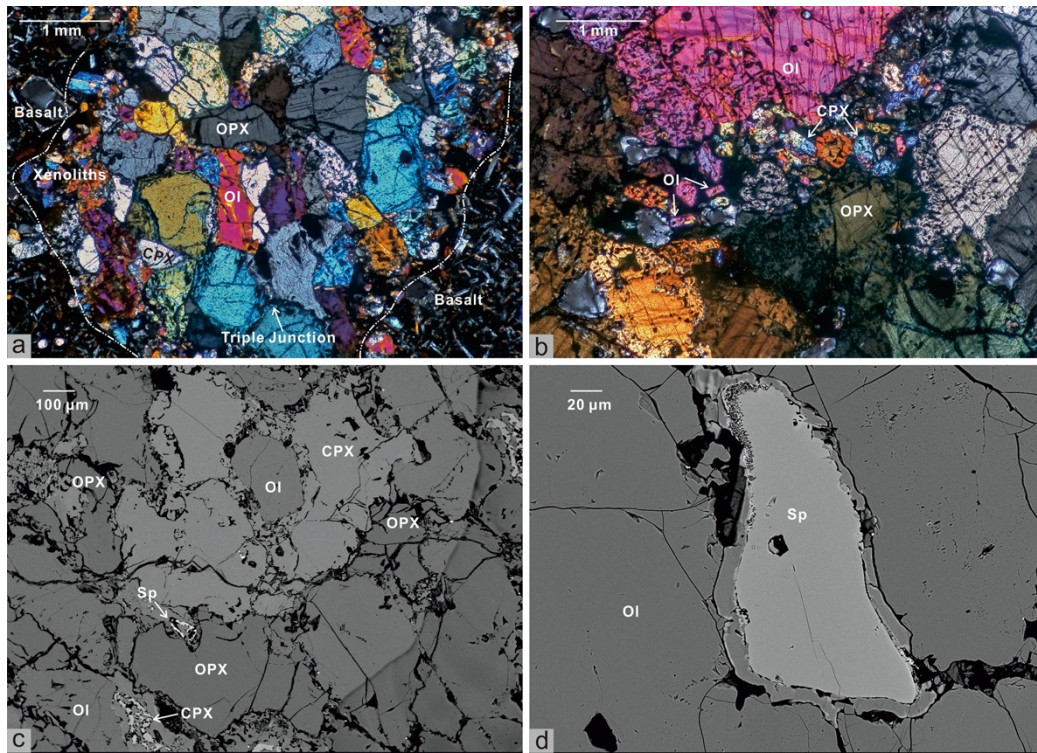
Fig. 2-2. Microphotographs of harzburgite xenoliths displaying typical microstructures of the lithospheric mantle from Sailipu in the north-western Lhasa terrane. (a) Coarse-grained xenolith entrained by the ultrapotassic magmas. Details of the microstructure such as the 120° triple junctions and subgrain boundaries in olivine can be observed. (b) Porphyroblastic peridotite xenoliths (c) lobate shaped clinopyroxene and spinel intergrowths with orthopyroxene (d) isolated spinel with amoeboid rim. Mineral abbreviations: Cpx, clinopyroxene; Ol, olivine; Opx, orthopyroxene; Sp, spinel

The grain shape does not show any obvious relationship with the nature of the phase. Clinopyroxene is only present in the matrix and often shows spongy rims and lobate shapes that embay large olivine grains (Fig. 2-2c). Clinopyroxene also occurs as inclusions in olivine. Spinel is present as small, sub-millimeter sized, anhedral grains forming intergrowths with orthopyroxene (Fig. 2-2c), or as isolated grains with amoeboid shapes located in interstitial positions between the silicate grains (Fig. 2-2d).

2.4.2 Mineral Compositions

The mineral compositions of eight peridotite xenoliths from Sailipu are given in Table 1. The olivine is Fe-rich with a Fo content ranging from 87.5% to 90.5% (1.75-1.80 apfu Mg, 0.19-0.25 apfu Fe). All olivine analyses except for one (T16-146-1) pertain to the low-Ca group, which is defined by 0.05 wt.% < CaO < 0.09 wt.%. The Cr_2O_3 contents range from 0.013 wt.% to 0.035 wt.% and the Al_2O_3 contents range from 0.015 wt.% to 0.023 wt.%. The $Cr^{\#}$ (molar ratio Cr/(Cr+Al)) of olivine ranges from 0.29 to 0.40, and the NiO contents range from 0.39 wt.% to 0.41 wt.%. There is no obvious distinction in element concentrations between the cores and the rims of the olivine crystals.

The orthopyroxene is Mg-rich (1.64-1.69 apfu Mg, 0.19-0.27 apfu Fe), with $Mg^{\#}$ between 0.86 - 0.90. It has slightly elevated Al contents (0.10-0.20 apfu Al) with 1.87-1.93 apfu Si and 0.03-0.05 apfu Ca. The calculated orthopyroxene end-member components are: (0.79-0.81) Enstatite + (0.10-0.12) $R_2R_3AlSi_2O_6$ (Tschermack's component) + (0.06-0.08) Ferrosilite + (0.01-0.02) $CaSi_2O_6$.

The clinopyroxenes contain 0.76-0.79 apfu Ca, 1.82-1.91 apfu Si and variable 0.12-0.30 apfu Al, with $Mg^{\#}$ of 0.85 - 0.89 (0.85-0.97 apfu Mg, 0.11-0.17 apfu Fe). The clinopyroxene end-member components are: (0.64-0.71) DiHd + (0.14-0.21) EnFs + (0.01-0.08) CaTs.

All spinel except for one (T16-156-1) has low (0.25-0.42 apfu) Cr, high (1.45-1.64 apfu) Al and 0.32-0.35 apfu Fe, with $Cr^{\#}$ of $0.13 - 0.22$.

The equilibrium temperatures of the Sailipu xenoliths were estimated using the two-pyroxene thermobarometer of (Putirka, 2008) from 8 opx-cpx pairs, which yields temperatures of 1375 ± 10 K. The equilibrium pressure of mantle-derived xenoliths from the spinel lherzolite field is estimated to be in the range of 1.6-2.0 GPa corresponding to a depth of 55 km - 70 km. Details of the mineral compositions are given in the supplementary material 2A-Table.

2.4.3 Fabric

Due to the small size of the xenoliths, the mesoscopic structure elements such as foliation and lineation are hard to identify macroscopically. The samples were thus cut in arbitrary orientations for thin-section preparation. Based on the notion that the [001] axes of clinopyroxene are commonly aligned sub-parallel to the lineation and the (010) plane is parallel to the foliation in naturally deformed rocks (Amiguet et al., 2009; Helmstaedt et al., 1972), we redefined the orthogonal XYZ structural framework by rotating datasets in order to have clustering of [001] and [010] of clinopyroxene in the X and Z direction respectively, where X is defined by the clustering of the [001] directions and the X-Y plane is defined by the orientation of the (010) planes of the clinopyroxenes.

The olivines show a fabric characterized by a CPO with a concentration of [010] perpendicular to the XY-plane and a large circle girdle in the XY-plane containing the [100] and [001] poles (AG-type). In addition, a few samples show a B-type fabric, which is characterized by the alignment of [010] perpendicular to the XY-plane and of [001] parallel to the X-direction. Finally, one sample exhibits an A-type fabric with (100) parallel to the XY-plane and [010] aligned parallel to the X-direction. (Fig.2-3).

In the studied xenoliths from Sailipu the J-index of the olivine CPO ranges between 1.79 and 4.68 (Table 2-1). The symmetry of the AG-type olivine fabric is characterized by a BA-index < 0.34, whereas A- and B-type olivine fabrics have higher BA-indexes in the range of 0.43 ~ 0.57 (Table 2-1). These values compare well

with the characteristics reported by (Higgie and Tommasi, 2014; Tommasi et al., 2016). Since the fabric type of olivine is mainly AG-type with subordinate B-type, which both have a concentration of the olivine [010]-directions perpendicular to the XY-plane, (010) is always parallel to the XY-plane, irrespective of whether the olivine exhibits an AG-type or a B-type fabric.
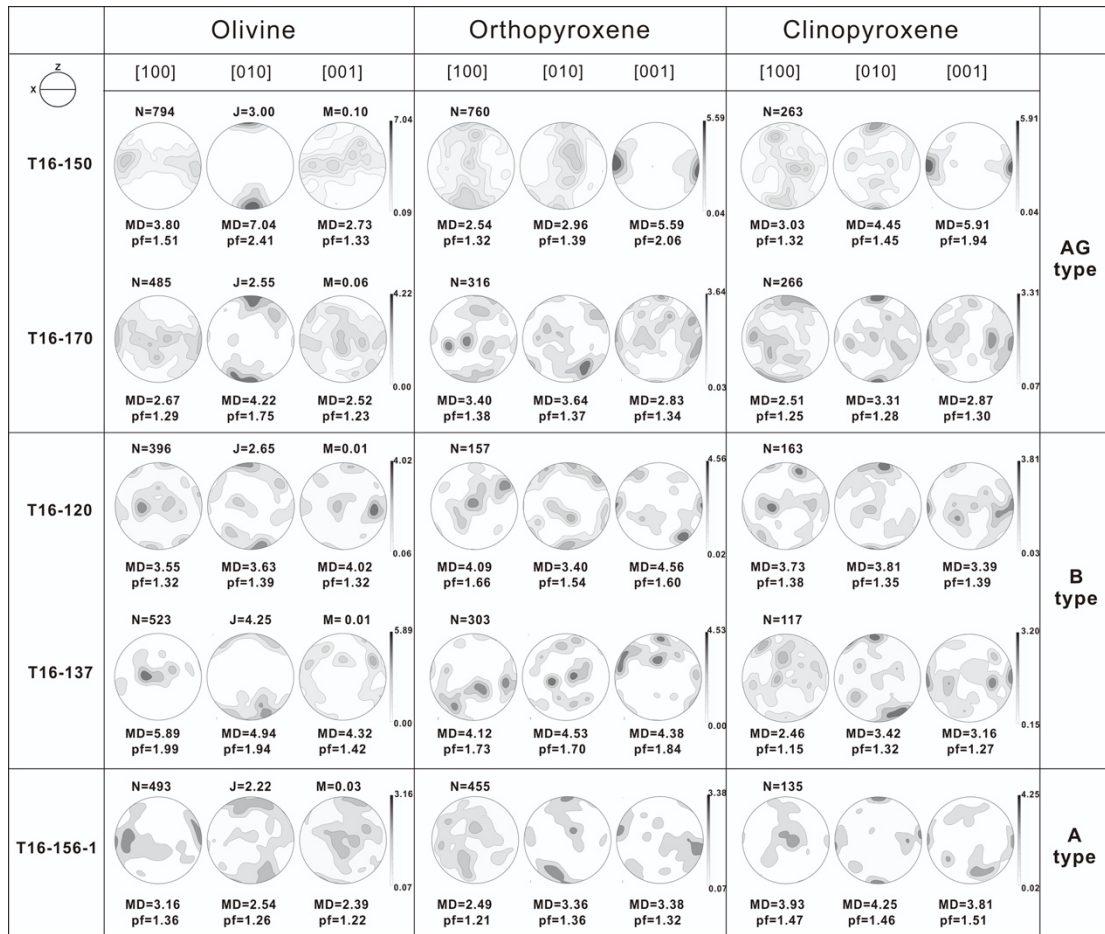
Fig. 2-3 Representative pole figures for the crystallographic axes of olivine, orthopyroxene and clinopyroxene in xenoliths from Sailipu. The CPOs are presented in equal-area, one point per grain, lower-hemisphere projections; the structural reference frame is shown as insert in the upper left. Contours (=6) show multiples of uniform distribution. N is the number of measurements, J-index and M-index is the fabric strength, pf is an index of fabric intensity, and MD is the maximum density.

The fabric of orthopyroxene develops weaker than the olivine fabric. Except for

the sample T16-153 and T16-156-3, which show a relatively weak fabric, the CPO of orthopyroxene in the porphyroblastic harzburgites is mostly characterized by the alignment of [010] perpendicular to the XY-plane and of [001] parallel to the X-direction (e.g. T16-120, Fig. 2-3), a fabric, which is referred to as (010)[001] type. More rarely a (100)[001] fabric type occurs in the equigranular grains, where [001] is aligned close to the X-direction, and [100] is perpendicular to the XY-plane (e.g. T16-137, Fig. 2-3).

The CPO of clinopyroxene was used for defining the structural reference frame. The alignment of [001] is rotated in parallel with the X-direction and concentration of the (010)-plane parallel to the XY-plane. The fabrics of clinopyroxene are well defined for all samples, although the fabric in T16-156-3 is relatively weak. Pole figure of the rest samples is given in the supplementary material 2B-Figure 1.

2.4.4 Seismic Anisotropy of the Peridotite Xenoliths

The seismic properties of the xenoliths were calculated following the method of Mainprice and Humbert (1994). The modal proportions of the major minerals (olivine, orthopyroxene and clinopyroxene) used in the calculations are listed in Table 2-1. Because olivine is the volumetrically dominant mineral in the peridotite xenoliths, the anisotropy patterns of the xenoliths are mainly controlled by the fabric of olivine. Here, we present the anisotropy of sample T16-137 and T16-170 as examples of the two main fabric types, AG- and B-type olivine, respectively (Fig. 2-4). Seismic anisotropy of other samples is given in the supplementary material 2B-Figure 2.

2.4.4.1 Olivine anisotropy

In olivine, the fastest and the slowest P-wave velocities are in the [100] and [010] directions, respectively. In the case of an AG-type fabric, the direction of the fastest velocity lies in the XY-plane, and the direction of the slowest velocity is parallel to the Z-axes of the structural frame (Fig. 2-4). Its minimum polarization anisotropy (AVs) displays a strong concentration close to the [010] axis, whereas the maximum AVs is

61

distributed subparallel to the XY-plane without any obvious concentration (Fig. 2-4).
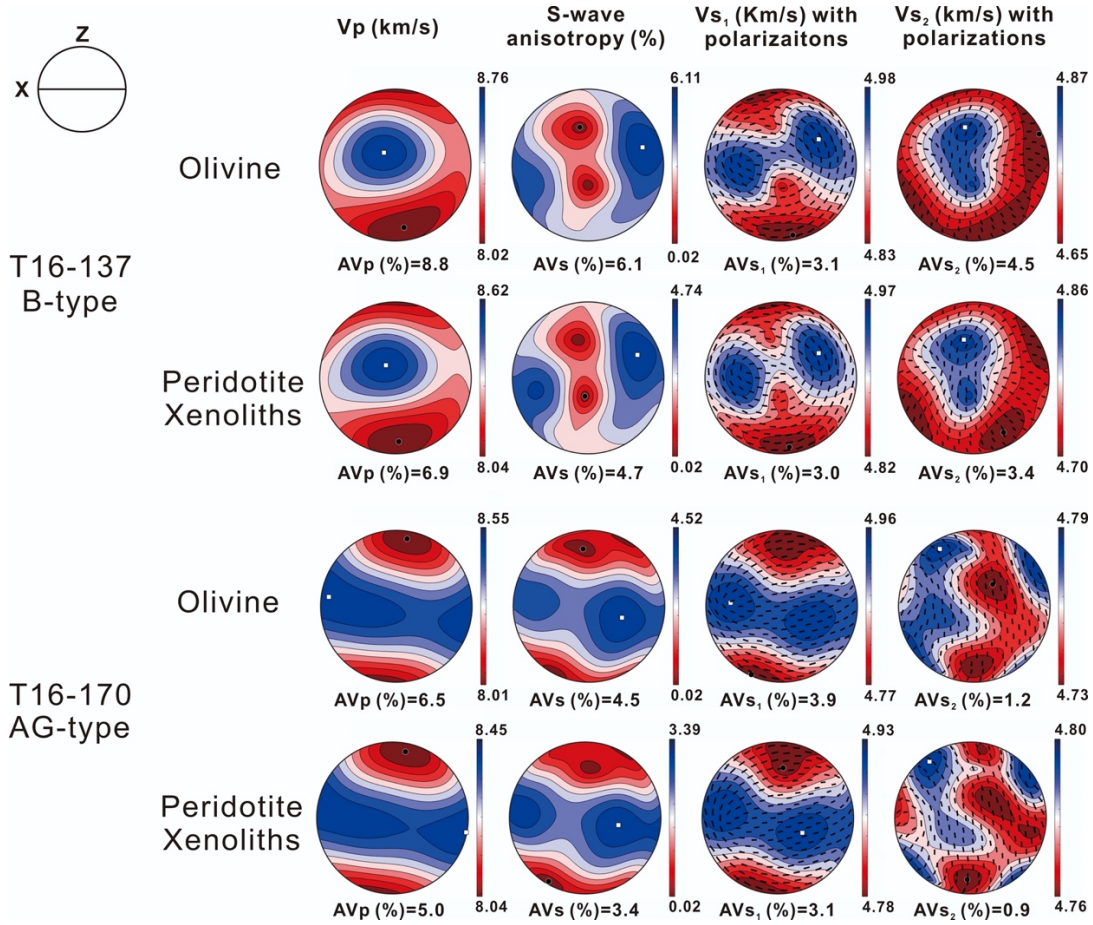
Fig. 2-4 Representative patterns of the seismic properties of the peridotite xenoliths in Sailipu calculated from the fabric of the xenoliths. The seismic properties are presented in equal-area, lower-hemisphere projections in the structural reference frame. Samples T16-170 and T16-137 represent seismic properties of AG-type and B-type olivine, respectively. The four columns are the P-wave velocity (Vp) with anisotropy of the P-waves (AVp); the polarization anisotropy (AVs) and the splitting S-wave velocity (Vs$_1$ and Vs$_2$) with their polarization directions. AVp = [(Vp^{max} − Vp^{min}) / (Vp^{max} + Vp^{min}) /2]×100% and AVs=[(Vs$_1$ −Vs$_2$)]/[(Vs$_1$ +Vs$_2$)/2], whereVs$_1$ andVs$_2$ are the velocities of the fast and slow split S-waves, respectively. AVs$_{1/s_2}$ = [(Vs$_{1/s_2}$^{max} − Vs$_{1/s_2}$^{min}) / (Vs$_{1/s_2}$^{max} + Vs$_{1/s_2}$^{min}) / 2]; insert on the middle left shows the structural reference frame.

The P-wave velocity patterns of all xenoliths in which olivine shows an AG-type CPO (T16-146-1, T16-150, T16-156-3 and T16-170, henceforth referred to as AG-

type samples) are similar, but there are some differences when examined in detail. All AG-type samples show low P-wave velocities sub-normal to the structural XY-plane, with the minimum velocity (V_p^{min}) usually close to the structural Z axis. For sample T16-170, the directions of fastest P-wave (Vp^{max}) propagation form an approximate girdle close to the XY-plane with a wide point maximum. Samples T16-150 and T-16-156-3 also exhibit a girdle of fast P-wave velocities, but there is greater variation of the P-wave velocities along different directions in the XY-plane. The velocity patterns of sample T16-146-1, which has higher BA-index (0.34), are almost identical to the velocity patterns of samples with B-type CPOs, as the fast Vp velocities are found concentrated subparallel to the structural Y-direction. The V_p^{max} of the AG-type samples range from 8.55 km/s to 8.82 km/s and their anisotropy of the Vp velocities are in the range of 6.5 % to 11.8%. The most extreme V_p^{max} and AV_p values are obtained from sample T16-150, which has a much stronger fabric (J =3.0) than the other AG-type samples.

For the samples with B-type olivine fabric (T16-120, T16-137 and T16-153) (henceforth referred to as B-type samples) and the AG-type sample T16-146-1, the fastest P-wave and S_2-wave velocities are sub-normal to the [001] (X-direction) in the XY-plane, while the slowest P-wave and the S_2-wave velocities are sub-parallel or slightly oblique to the Z-direction. The propagation of S_1-waves is faster in the XY-plane, with the highest velocities at approximately 45º to the X-direction. (Fig. 2-4). The Vp^{max} of B-type samples are approximately 8.6 km/s. The AVp reaches 8.8% for T16-137, while it is only 2% for T16-153. The Vs_1^{max} ranges from 4.89 km/s to 4.91 km/s, and the Vs_2^{max} ranges from 4.84 km/s to 4.87 km/s. The Vp/Vs_1 and Vp/Vs_2 ratio anisotropies range from 1.9 % to 7.0 % and from 2.2% to 5.6%, respectively. The AVs for B-type samples ranges from 2.3 % - 6.1 %, which is less than the AVs of the samples with AG-type fabric.

2.4.4.2 Peridotite xenolith anisotropy

For the AG-type fabric, the highest AVs lies in the XY-plane, and the minimum AVs in directions with variable angles to the XY-plane. The AG-type samples are characterized by moderate AVs with 4.5 % on average in large circle girdles comprised of olivine [100] and [001]. For B-type samples and sample T16-146-1, the AVs is 1.8%- 4.7% with the highest dVs sub-parallel to the X-direction and the lowest dVs nearly in the XY-plane and perpendicular to the X-direction. Only T16-156-1 is classified as A-like type peridotite xenoliths. The AVs reaches 3.8% with the highest dVs perpendicular to the X-direction in the XY-plane and the lowest dVs parallel to the X-direction.

2.5 Discussion

2.5.1 The genesis of the olivine fabric in the Upper Mantle of the Sailipu Region

The AG-type fabric, which is the most abundant CPO type of olivine in the Sailipu xenoliths, suggests that the dominant slip system activated involved the (010) slip plane and the [100] and [001] slip-directions, allowing girdles to form (AG type) (Holzmann et al., 2003). Based on former research, there are four hypotheses for the origin of the AG-type fabric: (1) axial shortening in the Z-direction (Z = c), under transpression or pure compression, which transforms the fabric of olivine from A-type into AG-type under shear deformation with increased pure shear component (Tommasi et al., 1999); (2) melt assisted shear deformation at high temperature and high pressure, as inferred from AG-type fabric produced during experimental simple shear deformation with 4% melt present at T = 1523K and P = 300 MPa (Holtzman and Hustoft., 2003; Le Roux et al., 2008; Higgie and Tommasi, 2014); (3) simultaneous activation of the (010)[100] and (010)[001] slip systems under high pressure (high temperature) conditions, which have been observed in shear

deformation experiments at conditions equivalent to a depth below 250 km (Vauchez et al., 2005); and (4) subgrain rotation and growth during static recrystallization of deformed rocks (annealing), which may modify a pre-existing microstructure and texture (Tommasi et al., 2008).

For axial shortening or transpression the CPO of orthopyroxene is usually in the same structural background as the CPO of olivine, which would imply a girdle distribution of the orthopyroxene [100] and [001] in the XY-plane or a concentration of [100] parallel to the X-direction of the structural reference frame (Le Roux et al., 2008; Higgie and Tommasi, 2014). The fabric of orthopyroxene in the Sailipu xenoliths, however, shows slip in the [001]-direction, rather than an obvious concentration of [100] or girdle distribution of [100] and [001], and hypothesis (1) must thus be rejected. The fabrics associated with hypotheses (3) and (4) usually occur in xenoliths that are related to high pressures (3.7 GPa - 4.7 GPa) and temperatures (~1337 K − 1637 K) (Tommasi et al., 2008), which is substantially higher than the P-T conditions estimated for the Sailipu xenoliths (1.6 GPa − 1.9 GPa, ~1375 K).

Hypothesis (2) invokes melt-assisted shear deformation, either during partial melting of the mantle (Soustelle et al., 2009) or during percolation of basaltic melts (Higgie and Tommasi, 2014; Le Roux et al., 2008). There are several lines of evidence from earlier studies that corroborate the generation of the AG-type olivine fabric by melt assisted shear deformation. The intensive ultrapotassic volcanism in the Sailipu region testifies to the presence of melt in the root of the lithospheric mantle (Zhao et al., 2009) The observed extremely high incompatible element (LREE, Sr, Rb, Cs, Th, U) concentrations of the ultrapotassic lavas also suggest melt-related enrichment of the mantle, which further supports hypothesis 2 (Zhao et al., 2009). The trace element compositions of clinopyroxene in mantle xenoliths from Sailipu suggest enrichment of the lithospheric mantle by melt metasomatism (Liu et al., 2011). Partial melting of the lithospheric mantle below the Tibetan Plateau is also indicated by geophysical data. Sailipu is next to an area of obvious Sn-wave attenuation and high conductivity,

which is interpreted as an indication for the presence of melt in the upper mantle (Wang, 2016). Furthermore, travel-time tomography reveals the existence of a low-velocity layer within the upper mantle in this region (Zheng et al., 2007). Moreover, high Vp/Vs ratios suggest partial melting within the upper mantle (Nakajima et al., 2001). In addition, from experimental studies it is known that B-type and AG-type fabrics of olivine preferentially develop in the course of simple shear deformation in partially molten mantle rocks at anhydrous conditions. The fabric transition from AG-type to B-type occurs, when the volume fraction of melt increases from 4% to 6% (Holtzman and Hustoft 2003). Thus, both fabric types found in this area are compatible with the presence of melt in the upper mantle beneath the northwestern Lhasa terrane.

Only one of the Sailipu samples shows the A-type olivine fabric, which is regarded as an indicator for low stress and water-poor deformation conditions. Jung et al., (2006) reported A-type olivine fabric from deformation experiments at P=0.5GPa, T=1570K under almost dry conditions and low stress (< 300 MPa, shear strains γ = 1.43).

2.5.2 Seismic Anisotropy of the Upper Mantle in the North-West of the Lhasa Terrane

Seismic anisotropy of the upper mantle is mainly a function of the intrinsic elastic anisotropy of the rock-forming minerals, mineral mode, P-T conditions, presence of melt, as well as fabric types and strength. The delay time depends on the thickness of the anisotropic layer and on the magnitude of its anisotropy.

Within 186 km east of Sailipu, it was shown in the frame of the Project Hi-CLIMB (Chen et al., 2010) that the fast polarization direction of split SKS waves (FPD) ranges from N75° to ESE100° with splitting delay times larger than 1.0 s on average. The main fabric pattern of the Sailipu peridotite xenoliths is AG-type. If the large delay time is attributed to the upper mantle, the XY-plane of the mantle in this

region should be approximately vertical, since the polarization anisotropy in the direction normal to the XY-plane is very weak or nearly zero for the AG-type fabric. In central Tibet the FPD is N83^o, which is approximately parallel to the BNS (Fig. 2-1) suggesting that in this area the FPD may be related to long-term left-lateral shear deformation in the lithospheric mantle.

South of the Main Central thrust (Fig. 2-1) the fast polarization direction of the split SKS waves (FPD) is quite uniform, with a direction of approximately N29°, which is consistent with the direction in the Indian shield. This direction also coincides with the present direction of absolute motion of the shield (Fig. 2-1). Dominantly A-type fabric, which is regarded as the most common fabric type of the lithospheric mantle underneath the Indian shield, was observed in the Luobusha (Fig. 2-5) peridotites (Sun et al., 2016). The stable FPD probably originated from the sub-horizontal northward motion of the lithospheric mantle of the Indian shield (Tiwari et al., 2018). In other words, this setting is consistent with [100] and (010) of olivine coinciding with the FPD and the XY plane respectively. The splitting time delays with 0.96 s on average suggest the existence of a relatively stable anisotropic layer with a thickness of approximately 100 km. The intermediate splitting time delay (0.8 s on average) and the variable FPDs observed in the Himalayas reveal a complex deformation pattern and can be best explained by the combined effects of deformation related to the northward movement of the Indian shield with possible contributions from the crust.

In central Tibet the shear-wave splitting time delay is approximately 1.5 s on average and ranging from 1.0 s to 2.4 s. In this region, the crustal anisotropy contributes a delay time of less than 0.5 s (Ozacar and Zandt, 2004), hence the large delay time must mainly originate from the upper mantle. Based on the data of the delay time (δt) measured in this area and the maximum polarization anisotropy (AVs^{max}) corresponding to the averaged shear wave velocity (Vs) calculated for the Sailipu peridotite xenoliths, the thickness of the anisotropic layer (H) beneath the

three-component stations located in central Tibet can be calculated using the equation H = δt × Vs / AVs, (Silver et al 1996). From this analysis the thickness of the anisotropic layer beneath central Tibet was estimated to be between 102 km and 245 km with an average of 153 km. Considering an anomalously thick crust in central Tibet with an average thickness of more than 60 km, the base of the anisotropic layer would be located at about 170 km to 305 km below the surface. This is too deep to be consistent with the observation of very small anisotropy at a depth of 200 km - 300km as reported by (Gung et al., 2003). Moreover, the estimated thickness is incompatible with a global Lehmann-discontinuity at about 200 km. At this depth, it usual regards as the base of anisotropic layer beneath continents (Gaherty and Jordan, 1995). A detailed lateral resolution of delay time data along Project Hi-CLIMB (Chen et al., 2010; Fig. 2-1) revealed a jump in delay time from 0.7 s (H1500) to 1.5 s (H1600) over a horizontal distance of 100 km east of Sailipu. If a AVs of about 4% were assumed, this would correspond to an incredible 80 km thickness change of the anisotropic layer within a distance of 55 km. In addition, the S receiver function technique indicates that the thickness of the Qiangtang lithospheric mantle is about 100-140 km on average (Zhao et al., 2011), implying that the anomalously large delay time observed in central Tibet cannot be attributed to an anomalously thick anisotropic layer and an alternative mechanism enhancing the anisotropy must be involved.

2.5.3 Enhanced Seismic Anisotropy by Melt Preferred Orientation

There are two potential mechanisms that may be responsible for the anomalously large delay time: One possibility would be a large contribution from asthenospheric anisotropy, which is equivalent to increasing the total thickness of the anisotropic layer. Alternatively, the large delay times may be explained by enhancement of the seismic anisotropy of the lithosphere by shape preferred orientation of oblate-shaped partially molten domains with high aspect ratios, which

will be referred to as melt preferred orientation (MPO).

At the high temperatures and pressures prevailing in the deep mantle as well as in fluid-bearing environments, the magnitude of anisotropy of olivine decreases, which is closely related to fabric transformation (Ohuchi et al., 2011). As a consequence, the anisotropy of the asthenosphere is much smaller than the anisotropy of the lithosphere (Conrad et al., 2007). Based on the assumption of a 100 km thick asthenosphere with AVs of 1.0 % on average (Chen et al., 2015), the asthenosphere would contribute a maximum of 0.3 s to the delay time. Contributions from the asthenosphere can thus not explain the anomalously large delay times observed in the northern Lhasa Terrane and in the Qiangtang terrane.

From experimental studies it is known that melt bands or penny-shaped melt pockets may be generated in peridotites during simple-shear and pure-shear deformation (Daines and Kohlstedt, 1997). Melt segregates from an initially homogeneous distribution into melt-rich bands or melt pockets which are aligned subparallel (20°) to the shear plane.

Based on the orientation relationship between oriented melt bands and/or penny-shaped melt pockets and the shear plane, the contribution of partially molten domains with specific shape orientation relations with the structural framework to the anisotropy of peridotites with AG-type fabric can be estimated. There are two end-member scenarios with respect to the structural frame (Mainprice., 2007), represented by horizontal and vertical shear planes with horizontal shear direction. For the former, alternation of solid rock with partially molten domains aligned with the shear plane has only a small effect on the anisotropy of the peridotite, since the SKS/SKKS phases propagate parallel to the symmetry axis, which is normal to the oriented melt domains. In contrast, if the shear plane is vertical, the symmetry axis of the alternation of solid rock and partially molten domains is horizontal, and an enhancement of SKS/SKKS splitting is expected. Although to date there are no

experimental data on which to base our estimation of the influence of MPO on the seismic anisotropy of peridotites, there are experiments performed on analogue materials, which qualitatively demonstrate that the presence of aligned partially molten domains results in an extra anisotropy (Yang et al., 2010). Model results indicate that an extra anisotropy of the S-wave velocities of about 3.0 % - 12.0 % can be induced by MPO, when the aspect ratio of the melt pockets and the melt fraction range from 0.2 to 0.5 and from 5 % to 7 %, respectively (Yang et al., 2010). Obviously, the contribution of aligned melt to the anisotropy is likely comparable to or larger than the contribution that is due to lattice preferred orientation of the olivine. We prefer to attribute the anomalously large delay time to melt-enhanced lithospheric anisotropy than to an anomalously thick anisotropic layer beneath the Qiangtang terrane.

2.5.4 Geodynamic Implications Inferred from Sailipu Mantle Xenolith Fabric

The most interesting SKS splitting result is the sudden change of FPD from the NNE direction with relatively small splitting time delays in the south to the E-W direction with large splitting time delays in the north along a N–S oriented profile such as Hi-CLIMB and INDEPTH III (Fig. 2-1). The boundary between the two realms is located at a distance of less than 150 km south of the BNS in the western Lhasa terrane and runs closer to the BNS in the eastern part. Two potential mechanisms can explain the sharp transition. (A) The horizontally northward advancing lithosphere of the Indian shield is subducting nearly vertically along the boundary with a change in olivine CPO from A-type to AG-type or/and B-type. (B) The sharp transition reflects a difference of the olivine fabric and of the structural configuration of the upper mantle between the Indian shield and the Qiangtang terrane.

As mentioned before, the olivine CPO in the Indian lithospheric mantle is

characterised by an A-type fabric where the [100]-direction aligns with the direction of absolute motion of the Indian lithosphere moving towards the north, with the FPD (NNE 20° - NNE 30°) perpendicular to the orogen. No matter what the angle of subduction is, an A-type fabric would not result in the switch of the FPD from the NNE direction to the E-W direction. About 100 km west of Sailipu, shear wave splitting measurements suggest the existence of a double-layer anisotropy (Wu et al., 2015, Fig. 2-1). The FPD of the lower layer is consistent with most of the FPD observed on the Indian shield. This not only suggests the presence of Indian lithosphere at least in the western Tibet Plateau (probably reaching to the northern boundary of the Qiangtang terrane), but it also implies that the olivine fabric is relatively stable during underthrusting. The fast orientation of the upper layer is in NE–SW direction, which can possibly be attributed to the Qiangtang mantle wedge and to lower crustal flow in western Tibet. Null birefringence along the southern portion of the INDEPTH-III and Hi-CLIMB profiles (INDEPTH-III; Chen et al., 2010) might provide evidence of northward downwelling Indian lithospheric mantle, which is supported by the observation of a sub-vertical high-velocity zone associated with cold Indian lithospheric mantle (Liang et al., 2016). Moreover, the null birefringence suggests that a fossil mantle CPO (A-type fabric) is likely preserved even though the downwelling Indian lithospheric mantle reached 400 km depth. Hence, we infer that the olivine fabric has been well preserved during the northward subduction of the Indian lithosphere. Also, an upwelling counter flow required for balancing the downwelling has not significantly contributed to the switch, because a vertical asthenospheric flow would lead to negligible shear wave splitting, if the [100] axis of olivine is assumed to be parallel to the direction of flow, as is implied by the fabric type A.
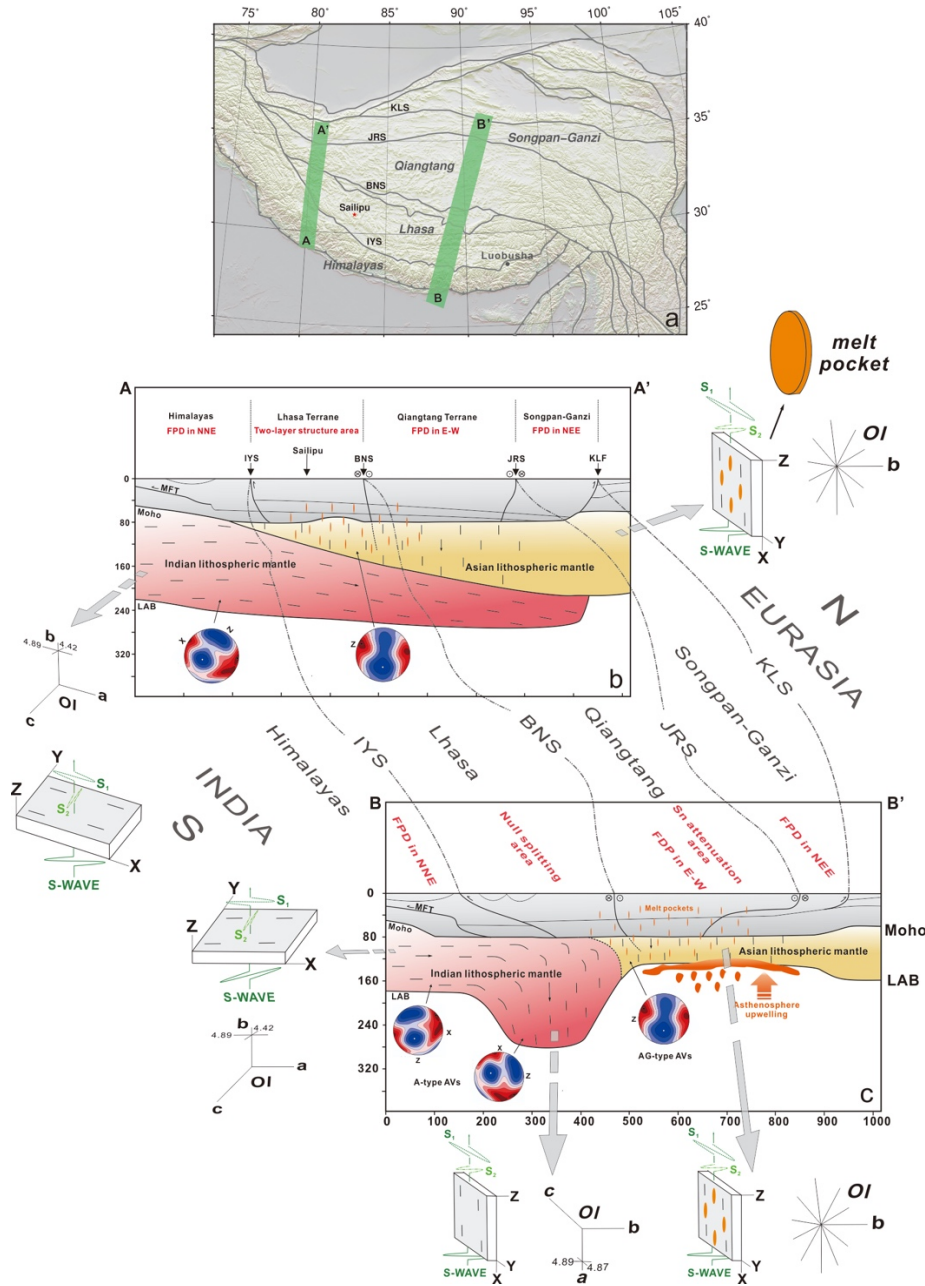
Fig. 2-5 Interpretative cross sections of the lithospheric mantle illustrating our model of the current processes in the Tibetan upper mantle. The northward advancing Indian lithospheric mantle subducts underneath eastern Tibet, where the [100] axis of olivine was sub-vertical and consequently null birefringence was observed south of BNS (Profile B-B'). Whereas, in western Tibet, the Indian lithosphere probably reaches to the northern boundary of the Qiangtang terrane and keeps the [100] axis of olivine sub- horizontally (Profile A-A'). The strike-slip shear deformation, which causes melt orientation in the northern Tibetan lithospheric mantle is probably superimposed on the asthenosphere convection and eastern extrusion. (Acronyms are asame as Fig. 1-1)

Considering the result that the olivine fabric in the Indian and Qiangtang lithospheric mantle is strongly different, the sharp transition of the fast polarization direction of split SKS waves and splitting time delays can be understood. Assuming that the dominant fabric of olivine in the northern Tibetan lithospheric mantle is AG-type as observed in the Sailipu mantle xenoliths, and under the condition that the northern Tibetan lithospheric mantle has continuously experienced strike-slip shear deformation, which matches with surface geologic structures, GPS results (Zhang et al., 2004) and lateral extrusion models , the switch of the FPD from the NNE direction to nearly E-W direction revealed by the INDEPTH-II, -III and the Hi-CLIMB profiles can be attributed to a change in olivine fabric from A-type in the Indian lithospheric mantle to AG-type in the northern Tibetan lithospheric mantle and to the transition of the structural configuration (Fig. 2-5).

2.6. Conclusion

The seismic properties of the lithospheric mantle underneath northern Tibet have been estimated from CPO data and modal compositions of a representative suite of mantle xenoliths from Sailipu in the north-western Lhasa terrane. Microstructure observations, crystallographic fabric measurements and calculations of seismic properties revealed that the CPOs of olivine in the Sailipu peridotite xenoliths are characterized by two fabrics: a concentration of [010] perpendicular to an important fabric plane referred to as the XY-plane with large circle girdles of [100] and [001] in the XY-plane (AG-type fabric), and a B-type fabric, where [010] is perpendicular to the XY-plane and [001] is parallel to the X-direction. The major fabric of orthopyroxene is characterized by the allignement of (100) parallel to the XY-plane and of [001] parallel to the X-direction. The olivine fabric strength is the highest in coarse-grained spinel harzburgites.

The seismic properties of the peridotite xenoliths are characterized by a high P-wave velocity with the highest velocity of 8.6 km/s found for a spinel harzburgite. The directions of fastest and slowest propagation of the P-waves are in the directions parallel and approximately perpendicular to the XY-plane, respectively. The polarization anisotropy (AVs) is highest for wave propagation in the direction nearly perpendicular to the Z-axes, with a value of 4.6 % on average, whereas the AVs is very weak or close to zero in the wave propagation direction approximately perpendicular to the XY-plane.

The AG-type olivine fabric observed in the Sailipu peridotite xenoliths is thought to be compatible with deformation during the presence of melt, which is supported by independent geophysical data from northern Tibet. We suggest that oblate shaped melt pockets with preferred shape orientations sub-parallel to the XY-plane enhance the anisotropy of the lithospheric mantle beneath northern Tibet and can induce strong SKS wave splitting, if the XY-plane in the lithospheric mantle is oriented close to vertical or at least has a high dip angle. We therefore propose to attribute the very large delay time to anomalously high anisotropy, which is, at least in part, due to melt preferred orientation (MPO). The switch of the fast polarization direction from a NNE to an E-W direction in the northern part of the Lhasa terrane is explained by the change of the olivine fabric from A-type in the Indian lithospheric mantle to AG-type in the mantle beneath northern Tibet, the architecture of which has been turned to strike-slip shear deformation, probably related to lateral extrusion of the upper mantle.

References:

1. Amiguet, E., Raterron, P., Cordier, P., Couvy, H., and Chen, J., 2009, Deformation of diopside single crystal at mantle pressure. 1: Mechanical data: Physics of the Earth and Planetary Interiors, v. 177, no. 3-4, p. 122-129.

2. Bachmann, F., Hielscher, R., and Schaeben, H., 2010, Texture Analysis with MTEX – Free and Open Source Software Toolbox: Solid State Phenomena, v. 160, p. 63-68.

3. Chen, W.-P., Martin, M., Tseng, T.-L., Nowack, R. L., Hung, S.-H., and Huang, B.-S., 2010, Shear-wave birefringence and current configuration of converging lithosphere under Tibet: Earth and Planetary Science Letters, v. 295, no. 1-2, p. 297-304.

4. Chen, Y., Li, W., Yuan, X., Badal, J., and Teng, J., 2015, Tearing of the Indian lithospheric slab beneath southern Tibet revealed by SKS-wave splitting measurements: Earth and Planetary Science Letters, v. 413, p. 13-24.

5. Cheng, Z., and Guo, Z., 2017, Post-collisional ultrapotassic rocks and mantle xenoliths in the Sailipu volcanic field of Lhasa terrane, south Tibet: Petrological and geochemical constraints on mantle source and geodynamic setting: Gondwana Research, v. 46, p. 17-42.

6. Conrad, C. P., Behn, M. D., and Silver, P. G., 2007, Global mantle flow and the development of seismic anisotropy: Differences between the oceanic and continental upper mantle: Journal of Geophysical Research, v. 112, no. B7.

7. Daines, M. J., and Kohlstedt, D. L., 1997, Influence of deformation on melt topology in peridotites: Journal of Geophysical Research: Solid Earth, v. 102, no. B5, p. 10257-10271.

8. Eken, T., and Tilmann, F., 2014, The Use of Direct Shear Waves in Quantifying Seismic Anisotropy: Exploiting Regional Arrays: Bulletin of the Seismological Society of America, v. 104, no. 6, p. 2644-2661.

9. Gaherty, J. B., and Jordan, T. H., 1995, Lehmann discontinuity as the base of an anisotropic layer beneath continents: Science, v. 268, no. 5216, p. 1468-1471.

10. Gung, Y. C., Panning, M., and Romanowicz, B., 2003, Global anisotropy and the thickness of continents: Nature, v. 422, no. 6933, p. 707-711.

11. Helmstaedt, H., Anderson, O. L., and Gavasci, A. T., 1972, Petrofabric studies of

eclogite, spinel-Websterite, and spinel-lherzolite Xenoliths from kimberlite-bearing breccia pipes in southeastern Utah and northeastern Arizona: Journal of Geophysical Research, v. 77, no. 23, p. 4350-4365.

12. Henry, H., Tilhac, R., Griffin, W. L., O'Reilly, S. Y., Satsukawa, T., Kaczmarek, M.-A., Grégoire, M., and Ceuleneer, G., 2017, Deformation of mantle pyroxenites provides clues to geodynamic processes in subduction zones: Case study of the Cabo Ortegal Complex, Spain: Earth and Planetary Science Letters, v. 472, p. 174-185.

13. Higgie, K., and Tommasi, A., 2014, Deformation in a partially molten mantle: Constraints from plagioclase lherzolites from Lanzo, western Alps: Tectonophysics, v. 615-616, p. 167-181.

14. Hirn, A., Jiang, M., Sapin, M., Diaz, J., Nercessian, A., Lu, Q, Lepine, J., Shi, D., Sachpazi, M., and Pandey, M., 1995, Seismic anisotropy as an indicator of mantle flow beneath the Himalayas and Tibet: Nature, v. 375, no. 6532, p. 571-574.

15. Holtzman, B. K., and Hustoft, J., 2003, Melt segregation and strain partitioning: implications for seismic anisotropy and mantle flow: Science, v. 301, no. 5637, p. 1227-1230.

16. Ismaıl, W. B., and Mainprice, D., 1998, An olivine fabric database: an overview of upper mantle fabrics and seismic anisotropy: Tectonophysics, v. 296, no. 1, p. 145-157.

17. Jung, H., Katayama, I., Jiang, Z., Hiraga, T., and Karato, S., 2006, Effect of water and stress on the lattice-preferred orientation of olivine: Tectonophysics, v. 421, no. 1-2, p. 1-22.

18. Lavé, J., Avouac, J., Lacassin, R., Tapponnier, P., and Montagner, J., 1996, Seismic anisotropy beneath Tibet: evidence for eastward extrusion of the Tibetan lithosphere?: Earth and Planetary Science Letters, v. 140, no. 1-4, p. 83-96.

19. Le Roux, V., Tommasi, A., and Vauchez, A., 2008, Feedback between melt percolation and deformation in an exhumed lithosphere–asthenosphere boundary: Earth and Planetary Science Letters, v. 274, no. 3, p. 401-413.

20. Liang, X., Chen, Y., Tian, X., Chen, Y. J., Ni, J., Gallegos, A., Klemperer, S. L., Wang, M., Xu, T., Sun, C., Si, S., Lan, H., and Teng, J., 2016, 3D imaging of subducting and fragmenting Indian continental lithosphere beneath southern and central Tibet using body-wave finite-frequency tomography: Earth and Planetary Science Letters, v. 443, p. 162-175.

21. Liu, C.-Z., Wu, F.-Y., Chung, S.-L., and Zhao, Z.-D., 2011, Fragments of hot and metasomatized mantle lithosphere in Middle Miocene ultrapotassic lavas, southern Tibet: Geology, v. 39, no. 10, p. 923-926.

22. Mainprice, D., 2007, Seismic anisotropy of the deep Earth from a mineral and rock physics perspective, Treatise Geophys., 2, 437–491, doi: 10.1016: B978-044452748-6.00045-6.

23. Mainprice, D., Bachmann, F., Hielscher, R., Schaeben, H., and Lloyd, G. E., 2015, Calculating anisotropic piezoelectric properties from texture data using the MTEX open source package: Geological Society, London, Special Publications, v. 409, no. 1, p. 223-249.

24. Mainprice, D., and Humbert, M., 1994, Methods of calculating petrophysical properties from lattice preferred orientation data: Surveys in Geophysics, v. 15, no. 5, p. 575-592.

25. Nakajima, J., Matsuzawa, T., Hasegawa, A., and Zhao, D., 2001, Three-dimensional structure of Vp, Vs, and Vp/Vs beneath northeastern Japan: Implications for arc magmatism and fluids: Journal of Geophysical Research: Solid Earth, v. 106, no. B10, p. 21843-21857.

26. Nicolas, A., Christensen, N. I., Nicolas, A., and Christensen, N. I., 1987, Formation of Anisotropy in Upper Mantle Peridotites - A Review: Composition, Structure and Dynamics of the Lithosphere-Asthenosphere System, p. 111-123.

27. Ohuchi, T., Kawazoe, T., Nishihara, Y., Nishiyama, N., and Irifune, T., 2011, High pressure and temperature fabric transitions in olivine and variations in upper mantle seismic anisotropy: Earth and Planetary Science Letters, v. 304, no. 1-2, p. 55-63.

28. Ozacar, A. A., and Zandt, G., 2004, Crustal seismic anisotropy in central Tibet: Implications for deformational style and flow in the crust: Geophysical Research Letters, v. 31, no. 23.

29. Pouchou, J.-L., and Pichoir, F., 1991, Quantitative analysis of homogeneous or stratified microvolumes applying the model "PAP", Electron probe quantitation, Springer, p. 31-75.

30. Putirka, K. D., 2008, Thermometers and Barometers for Volcanic Systems: Reviews in Mineralogy and Geochemistry, v. 69, no. 1, p. 61-120.

31. Silver, P. G., 1996, SEISMIC ANISOTROPY BENEATH THE CONTINENTS:

Probing the Depths of Geology: Annual Review of Earth & Planetary Sciences, v. 24, no. 1, p. 385-432.

32. Singh, A., Eken, T., Mohanty, D. D., Saikia, D., Singh, C., and Ravi Kumar, M., 2016, Significant seismic anisotropy beneath southern Tibet inferred from splitting of direct S-waves: Physics of the Earth and Planetary Interiors, v. 250, p. 1-11.

33. Soustelle, V., Tommasi, A., Bodinier, J. L., Garrido, C. J., and Vauchez, A., 2009, Deformation and Reactive Melt Transport in the Mantle Lithosphere above a Large-scale Partial Melting Domain: the Ronda Peridotite Massif, Southern Spain: Journal of Petrology, v. 50, no. 7, p. 1235-1266.

34. Sun, S., Ji, S., Michibayashi, K., and Salisbury, M., 2016, Effects of olivine fabric, melt-rock reaction, and hydration on the seismic properties of peridotites: Insight from the Luobusha ophiolite in the Tibetan Plateau: Journal of Geophysical Research: Solid Earth, v. 121, no. 5, p. 3300-3323.

35. Tiwari, A. K., Bhushan, K., Eken, T., and Singh, A., 2018, Upper mantle dynamics of Bangladesh by splitting analysis of core-mantle refracted SKS, PKS, and SKKS phases: Physics of the Earth and Planetary Interiors, v. 279, p. 21-32.

36. Tommasi, A., Baptiste, V., Vauchez, A., and Holtzman, B., 2016, Deformation, annealing, reactive melt percolation, and seismic anisotropy in the lithospheric mantle beneath the southeastern Ethiopian rift: Constraints from mantle xenoliths from Mega: Tectonophysics, v. 682, p. 186-205.

37. Tommasi, A., Tikoff, B., and Vauchez, A., 1999, Upper mantle tectonics: three-dimensional deformation, olivine crystallographic fabrics and seismic properties: Earth and Planetary Science Letters, v. 168, no. 1, p. 173-186.

38. Tommasi, A., Vauchez, A., and Ionov, D. A., 2008, Deformation, static recrystallization, and reactive melt transport in shallow subcontinental mantle xenoliths (Tok Cenozoic volcanic field, SE Siberia): Earth and Planetary Science Letters, v. 272, no. 1-2, p. 65-77.

39. Vauchez, A., Dineur, F., and Rudnick, R., 2005, Microstructure, texture and seismic anisotropy of the lithospheric mantle above a mantle plume: Insights from the Labait volcano xenoliths (Tanzania): Earth and Planetary Science Letters, v. 232, no. 3-4, p. 295-314.

40. Wang, Q., Hawkesworth, C. J., Wyman, D., Chung, S.-L., Wu, F. Y., Li, X. H., Li, Z. X., Gou, G. N., Zhang, X. Z., Tang, G. J., Dan, W., Ma, L., and Dong, Y. H., 2016, Pliocene-Quaternary crustal melting in central and northern Tibet and

insights into crustal flow: Nature Communications, v. 7.

41. Wu, J., Zhang, Z., Kong, F., Yang, B. B., Yu, Y., Liu, K. H., and Gao, S. S., 2015, Complex seismic anisotropy beneath western Tibet and its geodynamic implications: Earth and Planetary Science Letters, v. 413, p. 167-175.

42. Wüstefeld, A., Bokelmann, G., Zaroli, C., and Barruol, G., 2008, SplitLab: A shear-wave splitting environment in Matlab: Computers & Geosciences, v. 34, no. 5, p. 515-528.

43. Wood, B. J. and S. Banno., 1973, Garnet-orthopyroxene and orthopyroxene-clinopyroxene relationships in simple and complex systems: Contributions to Mineralogy and Petrology, v. 42, no. 2, p. 109-124.

44. Xu, B., Griffin, W. L., Xiong, Q., Hou, Z.-Q., O'Reilly, S. Y., Guo, Z., Pearson, N. J., Gréau, Y., Yang, Z.-M., and Zheng, Y.-C., 2017, Ultrapotassic rocks and xenoliths from South Tibet: Contrasting styles of interaction between lithospheric mantle and asthenosphere during continental collision: Geology, v. 45, no. 1, p. 51-54.

45. Yang, X., Jin, Z., MA, J., Huenges, E., and Schilling, F., 2002, Genesis of SKS splitting in the north-central Qinghai-Xizang plateau: melt alignment enhanced lithosphere anisotropy: Journal of Geophysical Research, v. 45, no. 6.

46. Yang, Y., Chen, J.-Y., Yang, X.-S., Yan, X.-B., and Zhang, G.-L., 2010, Does Alignment of Melt Enhance Seismic Anisotropy beneath Tibet?: Dizhen Dizhi(Seismology and Geology), v. 32, no. 1, p. 59-69.

47. Yin, A., and Harrison, T. M., 2000, Geologic Evolution of the Himalayan-Tibetan Orogen: Annual Review of Earth & Planetary Sciences, v. 28, no. 28, p. 211-280.

48. Zhang, P.-Z., Shen, Z., Wang, M., Gan, W., Bürgmann, R., Molnar, P., Wang, Q., Niu, Z., Sun, J., Wu, J., Hanrong, S., and Xinzhao, Y., 2004, Continuous deformation of the Tibetan Plateau from global positioning system data: Geology, v. 32, no. 9, p. 809.

49. Zhao, W., Kumar, P., Mechie, J., Kind, R., Meissner, R., Wu, Z., Shi, D., Su, H., Xue, G., Karplus, M., and Tilmann, F., 2011, Tibetan plate overriding the Asian plate in central and northern Tibet: Nature Geoscience, v. 4, no. 12, p. 870-873.

50. Zhao, Z., Mo, X., Dilek, Y., Niu, Y., DePaolo, D. J., Robinson, P., Zhu, D., Sun, C., Dong, G., and Zhou, S., 2009, Geochemical and Sr–Nd–Pb–O isotopic compositions of the post-collisional ultrapotassic magmatism in SW Tibet:

Chapter 2

Petrogenesis and implications for India intra-continental subduction beneath southern Tibet: Lithos, v. 113, no. 1-2, p. 190-212.

51. Zheng, H. W., Li, T. D., Gao, R., Zhao, D. P., and He, R. Z., 2007, Teleseismic P-Wave Tomography Evidence for the Indian Lithospheric Mantle Subducting Northward Beneath the Qiangtang Terrane: Chinese Journal of Geophysics, v. 50, no. 5, p. 1223-1232.

Supplementary

Supplementary 2A contain major element compositions of minerals in Sailipu mantle xenoliths, number of EBSD analysis points for each phase, and information on crystal elastic tensor and destiny.

Supplementary 2A-Table 1: Major elements of xenoliths from Sailipu, Tibet

Sample	Mineral	Major												Total	Mg#	Cr#
		SiO2	TiO2	Al2O3	Cr2O3	V2O3	FeO	MnO	NiO	ZnO	MgO	CaO	Na2O	Total	Mg#	Cr#
T16-120	OL	40.55	0.01	0.01	0.02	-	10.22	0.13	0.38	-	49.22	0.06	0.01	100.61	0.90	
	OPX	54.23	0.17	4.92	0.40	-	6.45	0.14	0.11	-	32.41	0.76	0.13	99.73	0.90	
	CPX	49.97	0.58	6.92	0.72	-	4.10	0.11	0.08	-	16.63	19.85	0.58	99.53	0.88	
	SP	0.08	0.34	49.67	14.80	0.08	15.16	0.17	0.43	0.12	18.90	0.00	-	99.74	0.69	0.17
T16-137	OL	40.29	0.02	0.02	0.02	-	9.89	0.13	0.37	-	49.30	0.08	0.01	100.14	0.90	
	OPX	54.37	0.16	4.81	0.44	-	6.13	0.13	0.08	-	32.95	0.75	0.11	99.96	0.91	
	CPX	52.14	0.39	3.21	0.93	-	3.24	0.11	0.05	-	18.03	20.80	0.26	99.15	0.91	
	SP	0.11	0.79	39.68	23.79	0.12	17.23	0.25	0.31	0.16	17.22	0.00	-	99.67	0.64	0.28
T16-146-1	OL	40.34	0.01	0.01	0.01	-	10.00	0.17	0.41	-	49.32	0.15	0.02	100.44	0.90	
	OPX	54.89	0.17	4.74	0.38	-	6.56	0.15	0.11	-	32.30	0.76	0.12	100.18	0.90	

Sample	Mineral	Major														
		SiO2	TiO2	Al2O3	Cr2O3	V2O3	FeO	MnO	NiO	ZnO	MgO	CaO	Na2O	Total	Mg#	Cr#
	CPX	51.73	0.47	4.73	0.87	-	3.76	0.11	0.06	-	17.63	19.74	0.53	99.64	0.89	
T16-150	OL	40.35	0.01	0.02	0.02	-	11.10	0.14	0.40	-	48.84	0.08	0.01	100.97	0.89	
	OPX	54.36	0.16	4.70	0.38	-	6.99	0.14	0.11	-	32.70	0.78	0.07	100.39	0.89	
	CPX	51.45	0.60	5.95	0.71	-	3.58	0.09	0.07	-	15.70	20.21	1.11	99.47	0.89	
T16-153	OL	40.47	0.00	0.03	0.02	-	10.38	0.13	0.41	-	49.16	0.08	0.01	100.69	0.90	
	OPX	54.32	0.17	4.91	0.34	-	6.71	0.16	0.10	-	32.91	0.73	0.11	100.46	0.90	
	CPX	50.05	0.60	6.58	0.70	-	3.77	0.10	0.07	-	17.31	20.14	0.42	99.74	0.89	
	OL	40.57	0.00	0.01	0.02	-	9.37	0.14	0.43	-	49.74	0.08	0.01	100.37	0.91	
	OPX	54.08	0.26	4.88	0.49	-	6.53	0.13	0.13	-	31.96	1.46	0.04	99.96	0.90	
T16-156-1	CPX	52.03	0.42	4.03	0.85	-	3.63	0.11	0.09	-	17.87	20.36	0.39	99.78	0.90	
	SP1	0.08	2.17	11.17	44.99	0.20	28.50	0.47	0.17	0.21	9.50	0.02	-	97.49	0.37	0.73
	SP2	0.11	0.50	45.15	19.31	0.10	15.47	0.20	0.35	0.12	18.58	0.00	-	99.91	0.68	0.22
	OL	39.83	0.00	0.01	0.03	-	12.06	0.16	0.39	-	47.42	0.09	0.01	100.00	0.88	
T16-156-3	OPX	55.14	0.20	2.29	0.38	-	9.10	0.18	0.08	-	31.41	1.25	0.05	100.08	0.86	
	CPX	52.35	0.42	2.89	0.74	-	5.46	0.15	0.06	-	17.74	19.54	0.46	99.81	0.85	
T16-170	OL	40.16	0.05	0.00	0.00	-	11.73	0.10	0.42	-	47.95	0.07	0.00	100.48	0.89	
	OPX	56.26	0.19	1.10	0.39	-	7.79	0.15	0.06	-	32.69	1.49	0.04	100.16	0.88	

Supplementary

Sample	Mineral	**Major**															
		SiO2	TiO2	Al2O3	Cr2O3	V2O3	FeO	MnO	NiO	ZnO	MgO	CaO	Na2O	Total	Mg#	Cr#
	CPX	53.76	0.41	1.13	0.36	-	4.93	0.17	0.05	-	18.72	19.70	0.23	99.46	0.87	
	SP	0.07	0.30	52.93	11.83	0.09	14.54	0.13	0.35	0.15	19.83	0.01	-	100.23	0.71	0.13

Seismic anisotropy in the Tibetan lithosphere inferred from mantle xenoliths

Sample	Mineral	Atoms per formula units										
		Si	Ti	Al	Cr	Fe	Mn	Ni	Mg	Ca	Na	Total
T16-120	OL	0.989	0.000	0.000	0.000	0.208	0.003	0.007	1.789	0.002	0.000	3.000
	OPX	1.879	0.004	0.201	0.011	0.187	0.004	0.003	1.674	0.028	0.009	4.000
	CPX	1.819	0.016	0.297	0.021	0.125	0.003	0.002	0.902	0.774	0.041	4.000
	SP	0.002	0.007	1.569	0.314	0.340	0.004	0.009	0.755	0.000	0.000	3.000
T16-137	OL	0.986	0.000	0.000	0.001	0.202	0.003	0.007	1.798	0.002	0.000	3.000
	OPX	1.875	0.004	0.012	0.195	0.177	0.004	0.003	1.694	0.028	0.007	4.000
	CPX	1.905	0.011	0.027	0.138	0.099	0.004	0.002	0.982	0.814	0.018	4.000
	SP	0.003	0.017	0.528	1.314	0.400	0.006	0.007	0.721	0.000	0.000	3.000
T16-146-1	OL	0.985	0.000	0.000	0.000	0.204	0.004	0.008	1.794	0.004	0.001	3.000
	OPX	1.896	0.004	0.193	0.011	0.189	0.004	0.003	1.663	0.028	0.008	4.000
	CPX	1.879	0.013	0.203	0.025	0.114	0.003	0.002	0.955	0.768	0.038	4.000
T16-150	OL	0.984	0.000	0.001	0.000	0.226	0.003	0.008	1.775	0.002	0.000	3.000
	OPX	1.873	0.004	0.191	0.010	0.201	0.004	0.003	1.679	0.029	0.005	4.000
	CPX	1.874	0.016	0.255	0.020	0.109	0.003	0.002	0.852	0.789	0.078	4.000
T16-153	OL	0.987	0.000	0.001	0.000	0.212	0.003	0.008	1.787	0.002	0.000	3.000
	OPX	1.867	0.004	0.199	0.009	0.193	0.005	0.003	1.686	0.027	0.007	4.000
	CPX	1.815	0.016	0.281	0.020	0.114	0.003	0.002	0.936	0.782	0.030	4.000

Supplementary

Sample	Mineral	Atoms per formula units										
		Si	**Ti**	**Al**	**Cr**	**Fe**	**Mn**	**Ni**	**Mg**	**Ca**	**Na**	**Total**
T16-156-1	OL	0.996	0.000	0.000	0.000	0.190	0.003	0.008	1.800	0.002	0.000	3.000
	OPX	1.875	0.007	0.200	0.013	0.189	0.004	0.004	1.652	0.054	0.002	4.000
	CPX	1.889	0.012	0.173	0.024	0.110	0.003	0.003	0.967	0.792	0.027	4.000
	SP1	0.003	0.055	0.444	1.199	0.803	0.013	0.005	0.477	0.001	0.000	3.000
	SP2	0.003	0.010	1.451	0.416	0.353	0.005	0.008	0.755	0.000	0.000	3.000
T16-156-3	OL	0.986	0.000	0.000	0.001	0.250	0.003	0.008	1.750	0.002	0.000	3.000
	OPX	1.928	0.005	0.095	0.010	0.266	0.005	0.002	1.637	0.047	0.003	4.000
	CPX	1.909	0.011	0.124	0.021	0.167	0.005	0.002	0.965	0.764	0.032	4.000
T16-170	OL	0.986	0.000	0.000	0.001	0.202	0.003	0.007	1.798	0.002	0.000	3.000
	OPX	1.955	0.005	0.011	0.045	0.226	0.004	0.002	1.693	0.055	0.003	4.000
	CPX	1.964	0.011	0.010	0.049	0.151	0.005	0.003	1.019	0.771	0.017	4.000
	SP	0.002	0.006	1.640	0.246	0.319	0.003	0.007	0.777	0.000	0.000	3.000

Supplementary 2A-Table 2: The end member components of clinopyroxene: Jadeite (Jd), CaTs, CaTi, CrCaTs, diopside + hedenbergite (DiHd),

and enstatite + ferrosilite (EnFs) (Putirka, 2008)

Sample	Cpx Components (Cations on the basis of 6 oxygens)								
	Jd	CaTs	CaTi	CrCaTs	DiHd	EnFs	En	Di	total
T16-120	0.041	0.085	0.044	0.010	0.639	0.197	0.172	0.560	1.000
T16-137	0.018	0.023	0.037	0.013	0.740	0.173	0.156	0.666	1.000
T16-146-1	0.038	0.049	0.033	0.012	0.675	0.198	0.177	0.601	1.000
T16-150	0.079	0.056	0.033	0.010	0.691	0.136	0.120	0.611	1.000
T16-153	0.030	0.079	0.048	0.010	0.650	0.203	0.180	0.578	1.000
T16-156-1	0.027	0.040	0.033	0.012	0.709	0.186	0.166	0.634	1.000
T16-156-3	0.032	0.009	0.037	0.011	0.710	0.213	0.181	0.603	1.000
T16-170	0.016	0.000	0.016	0.005	0.751	0.210	0.182	0.653	1.000

Supplementary 2A-Table 3: The end member components of orthopyroxene: $NaR_3Si_2O_6$, $NaTiAlSiO_6$, $R_2TiAl_2O_6$, $R_2R_{3+}AlSiO_6$, $Mg_2Si_2O_6$ (Enst), $Fe_2Si_2O_6$, $Mn_2Si_2O_6$, $Ca_2Si_2O_6$ (Wood & Banno, 1973)

Sample	Cpx Components (Cations on the basis of 6 oxygens)								
	Jd	CaTs	CaTi	CrCaTs	DiHd	EnFs	En	Di	total
T16-120	0.041	0.085	0.044	0.010	0.639	0.197	0.172	0.560	1.000
T16-137	0.018	0.023	0.037	0.013	0.740	0.173	0.156	0.666	1.000
T16-146-1	0.038	0.049	0.033	0.012	0.675	0.198	0.177	0.601	1.000
T16-150	0.079	0.056	0.033	0.010	0.691	0.136	0.120	0.611	1.000
T16-153	0.030	0.079	0.048	0.010	0.650	0.203	0.180	0.578	1.000
T16-156-1	0.027	0.040	0.033	0.012	0.709	0.186	0.166	0.634	1.000
T16-156-3	0.032	0.009	0.037	0.011	0.710	0.213	0.181	0.603	1.000
T16-170	0.016	0.000	0.016	0.005	0.751	0.210	0.182	0.653	1.000

Supplementary 2A-Table 4: Number of EBSD analysis points for each mineral

Sample	Mineral	Number of EBSD analysis points
T16-120	OL	396
	OPX	157
	CPX	163
T16-137	OL	523
	OPX	303
	CPX	117
T16-146-1	OL	1531
	OPX	1268
	CPX	368
T16-150	OL	794
	OPX	760
	CPX	263
T16-153	OL	358
	OPX	135
	CPX	103
T16-156-1	OL	493
	OPX	455
	CPX	135
T16-156-3	OL	523
	OPX	303
	CPX	217
T16-170	OL	485
	OPX	316
	CPX	266

Supplementary 2A-Information: The references of crystal elastic tensor and density we cited

Olivine: density of olivine d=3.355 g/cm3

Elastic tensor reference: Abramson, E. H., J. M. Brown, L. J. Slutsky, and J. Zaug (1997), The elastic constants of San Carlos olivine to 17 GPa, J. Geophys. Res., 102(B6), 12253–12263, doi:10.1029/97JB00682.

Orthopyroxene: density of orthopyroxene d=3.306 g/cm3

Elastic tensor reference: Chai, M., J. M. Brown, and L. J. Slutsky (1997), The elastic constants of an aluminous orthopyroxene to 12.5 GPa, J. Geophys. Res., 102(B7), 14779–14785, doi:10.1029/97JB00893.

Clinopyroxene: density of clinopyroxene d=3.327 g/cm3

Elastic tensor reference: Collins, M. & Brown, J (1998). Elasticity of an upper mantle clinopyroxene, Physics and chemistry of minerals, v. 26, no. 1, p. 7-13.

Supplementary 2B include figures to provide information on the additional samples in Sailipu, which shows the pole figures of olivine, orthopyroxene and clinopyroxene, and the seismic properties of the peridotite xenoliths.

Supplementary 2B-Figure 1
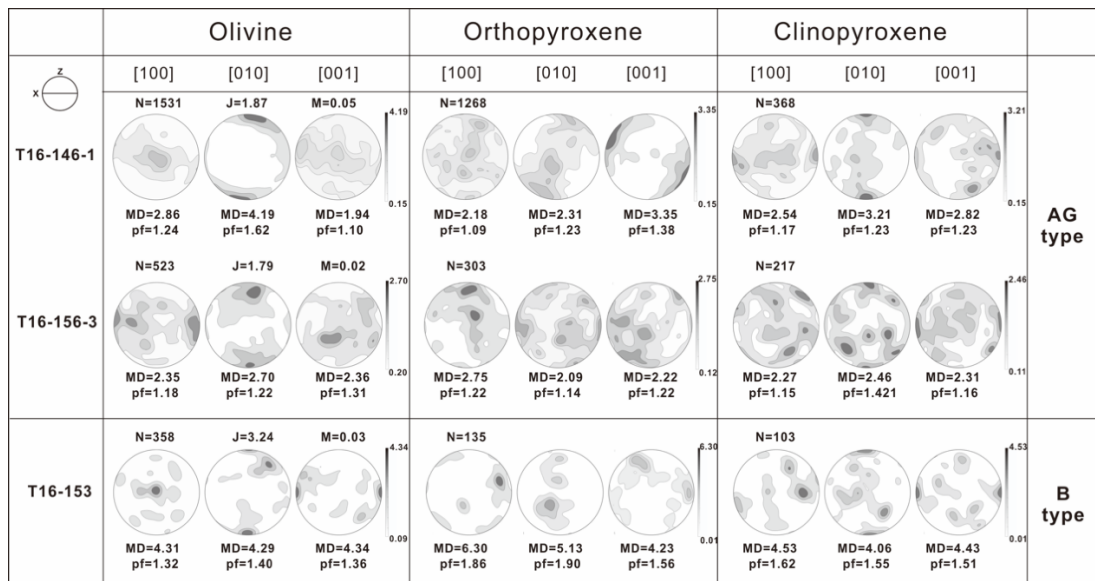
Supplementary 2B- Figure 1. The pole figures for the crystallographic axes of olivine, orthopyroxene and clinopyroxene in xenoliths from Sailipu. The CPOs are presented in equal-area, one point per grain, lower-hemisphere projections; the structural reference frame is shown as insert in the upper left. Contours (=6) show multiples of uniform distribution. N is the number of measurements, J-index and M-index is the fabric strength, pf is an index of fabric intensity, and MD is the maximum density.

Supplementary 2B-Figure 2
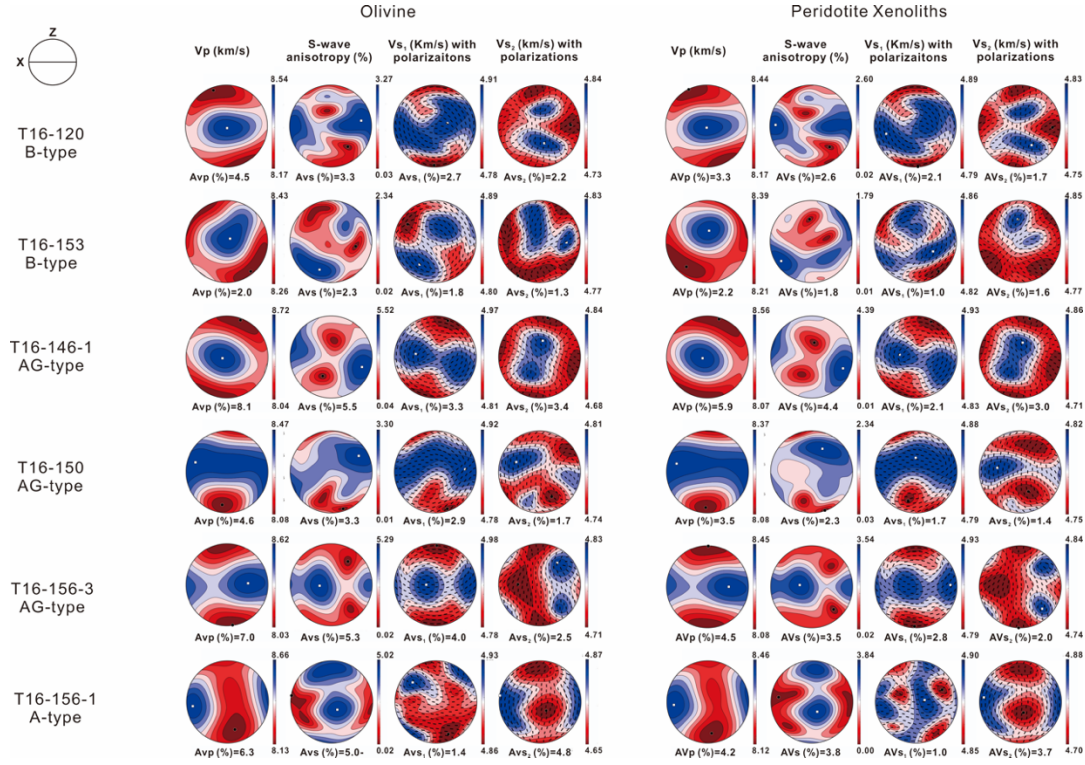
Supplementary 2B-Figure 2 The seismic properties of the peridotite xenoliths in Sailipu calculated from the fabric of the xenoliths. The seismic properties are presented in equal-area, lower-hemisphere projections in the structural reference frame. The four columns are the P-wave velocity (Vp) with anisotropy of the P-waves (AVp); the polarization anisotropy (AVs) and the splitting S-wave velocity (Vs_1 and Vs_2) with their polarization directions. $AVp = [(Vp^{max} - Vp^{min}) / (Vp^{max} + Vp^{min}) / 2] \times 100\%$ and $AVs = [(Vs_1 - Vs_2)] / [(Vs_1 + Vs_2)/2]$, where Vs_1 and Vs_2 are the velocities of the fast and slow split S-waves, respectively. $AVs_{1/s2} = [(Vs_{1/s2}^{max} - Vs_{1/s2}^{min}) / (Vs_{1/s2}^{max} + Vs_{1/s2}^{min}) / 2]$; insert on the middle left shows the structural reference frame.

Chapter 3

The crazed vision that sometimes sees further than our bleary, customary eyesight.

—— 《*The order of Time*》
Carlo Rovelli

New evidence for a heterogeneous lithospheric structure in central Tibet: implications for the Indian-Eurasian collision

Highlights

This manuscript aims to reconcile the long-standing discrepancy on competing hypotheses regarding the India-Asia collision center around: (1) a bidirectional subduction and (2) unidirectional northward underthrusting of the Indian plate below the Asian plate. We first present new geochemical and petrophysical data from mantle-derived peridotite xenoliths from central Tibet, which link to the observed lithospheric seismic anisotropy and seismic velocity pattern. Our result indicates the existence of a heterogeneous mantle, which differs from a fully metasomatized and thin lithosphere that is traditionally assumed for interpreting the geophysical and geochemical observations made in central Tibet. This finding simplifies the interpretation of the discontinuity observed by seismic tomography and renders the bidirectional subduction model obsolete.

Chapter 3

Abstract

The tectonic evolution of the Tibetan Plateau is discussed controversially. Two major hypotheses, one postulating a northward subduction of the Indian plate complemented by concomitant southward subduction of the Eurasian plate and another suggesting a unidirectional northward subduction of the Indian plate, have been proposed. We present new data from mantle xenoliths, which were exhumed by Eocene volcanism in the Qiangtang terrane. The systematic lateral and radial variation of the petrological, geochemical and microstructural signatures of the xenoliths reflect a heterogeneous structure of the lithospheric mantle below central Tibet. The uppermost lithospheric mantle is refractory and exhibits AG-type olivine fabric with a point maximum of the [010] axes normal to the foliation plane and a girdle distribution of the [100] and the [001] axes in the foliation plane. In contrast, the lower part was re-fertilized and displays a different fabric characterized by dominant activation of the [001](010) slip system. The vertical dichotomy of the mantle produces multiple seismic interferences, which correspond well with deep seismic observations and corroborate the model of a single northward subduction of the Indian plate.

3.1 Introduction

The Tibetan Plateau is the largest active continental collision zone worldwide. The structure of the Tibetan lithosphere and the mantle dynamics underlying the ongoing convergence have been subject to a controversial debate for a long time. From the latest Cretaceous onwards and until the 'hard' India-Eurasia collision at 25 Ma (van Hinsbergen et al., 2012), the Lhasa and Qiangtang terranes underwent substantial crustal shortening and thickening (van Hinsbergen et al., 2012). The Linzizong magmatism (65-40 Ma) is considered as a synchronous response to the

northward subduction of the Indian plate (Chung et al., 2005). In response to the continued collision between the Indian and the Eurasian plates, volcanic activity increasingly spread over the Tibetan Plateau during the Eocene and Miocene. The post-collisional potassic to ultrapotassic volcanism of the Qiangtang (50-28 Ma) (Ding et al., 2007), Lhasa (26-13 Ma) (Liu et al., 2011), and Songpan-Ganze (18-0.1 Ma) terranes (Lu et al., 2018) have a mantle origin and provide compelling evidence for the intensive underlying mantle evolution (Chung et al., 2005; Lu et al., 2018). Several successive stages of the Indian-Eurasian convergence have contributed to the current complex structure of the Tibetan lithospheric mantle including different terranes and heterogeneities within individual terranes (Zhao et al., 2011).

The Qiangtang terrane of central Tibet is separated from the Lhasa terrane in the south and from the Songpan-Ganze terrane in the north by the Bangong-Nujiang (BNS) and Jinsha (JS) sutures, respectively (Fig.3-1). The thickness of the lithosphere changes abruptly from ~210 km beneath the cold Lhasa terrane to 120-140 km beneath the hot Qiangtang and Songpan-Ganze terranes, while the Moho depth does not show any corresponding variation (Jiménez-Munt et al., 2008; Tunini et al., 2016). A large number of seismic analyses has been conducted on the Qiangtang terrane. There is agreement on several salient features: Firstly, shear wave splitting measurements in central Qiangtang revealed extraordinarily large delay times (δt) of ~ 2.0s for SKS splitting with only one predominant E-W to ENE-WSW fast polarization direction (FPD). Secondly, deep profiling by P- and S-receiver functions reveals multiple seismic discontinuities (Kumar et al., 2006; Zhao et al., 2010; Zhao et al., 2011) and shallow velocity anomalies (Liang et al., 2012) in the upper mantle. And thirdly, a layer with high-conductivity-low-velocity and with high Sn/Pn-wave attenuation is present in the lowermost crust and uppermost mantle in this terrane (Jiménez-Munt et al., 2008; Liang and Song, 2006)

Several geodynamic models have been proposed for explaining the present-day

lithospheric architecture of central Tibet. Two fundamentally different concepts are currently discussed. A bidirectional subduction model with southwards subduction of the Eurasian plate and simultaneous northwards subduction of the Indian plate has been proposed to account for the multiple discontinuities below central Tibet (Kumar et al., 2006; Zhao et al., 2011). In contrast, the tomographic model derived from P- and S-wave travel time measurements suggests a homogeneous velocity zone in the upper mantle of northern Tibet providing evidence against the existence of a southward subduction of the Eurasian plate (Chen et al., 2017; Liang et al., 2012). In detail, a diversity of ancillary models has been proposed. A model postulating slab breakoff at the frontal margin of the Indian plate is supported by geochemical evidence (Mahéo et al., 2002). Alternatively, slab breakoff at the front of the Eurasian plate was inferred from a gravity anomaly (He et al., 2014). Convective removal of the thickened lithospheric root was argued based on the observed magmatism (Chung et al., 2005; Lu et al., 2018); Finally, a combined model of slab tearing and/or slab breakoff/convective removal (Liang et al., 2016) was invoked. Although reasonable in the light of the specific observations and data they are based on, these models are rather diverse and new evidence or methodological approaches are needed to arrive at a more comprehensive picture.

In this paper, we present data from the typical mantle peridotite xenoliths from the Qiangtang terrane and use them to derive constraints on the evolution of the Tibetan lithosphere. Although, the number of samples is limited, it is the first time to get peridotite xenoliths in the central Tibet over past decades. To this end, we analyse the mineral fabrics of the xenoliths and infer the deformation history of the upper mantle. We present a new interpretation of the lithospheric architecture of central Tibet with implications for the reconstruction of the Tibetan lithosphere dynamics, which is compatible with the deep seismic observations.

New evidence for a heterogeneous lithospheric structure in central Tibet: implications for the Indian-Eurasian collision

Chapter 3
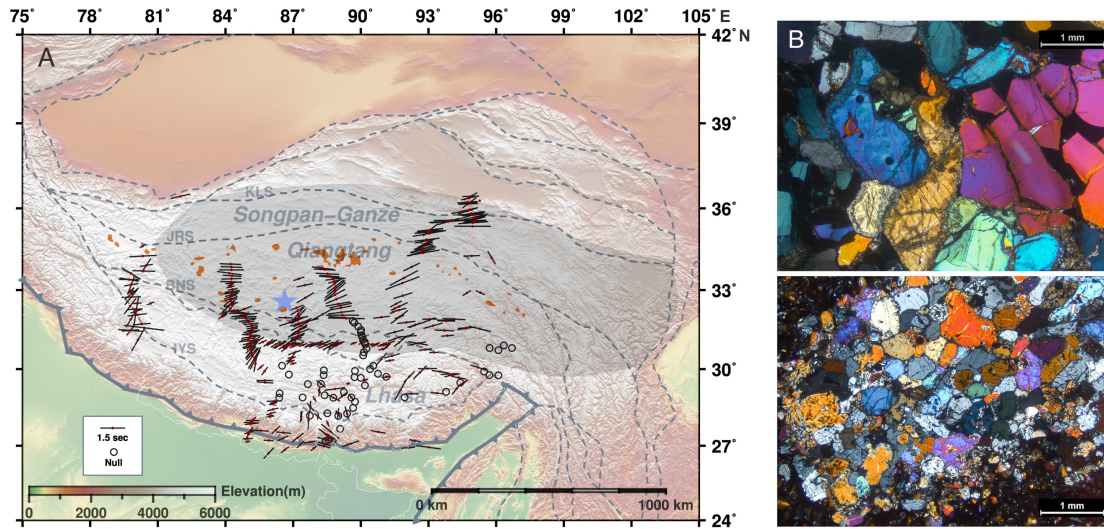
Fig. 3-1 (A) Average splitting parameters including fast polarization direction (FPD) and delay time of SKS wave splitting in Tibet. The orientations and lengths of the black bars indicate the FPDs and splitting delay times, respectively. The black circles without lines are stations with null splitting. The blue star represents the sampling location (Ejumaima). The purple spots represent Eocene to Early Oligocene igneous rocks. The shaded area is the zone of Sn-wave attenuation. (Acronyms are same as Fig. 1-1). (B) Photomicrographs of peridotite samples: Sample T16-57 (Upper): Coarse-grained depleted lherzolite showing tabular olivine crystals and clinopyroxene crystals with spongy borders; Sample T16-45 (Lower): Fine-grained fertile lherzolite showing isometric crystals.

3.2 Materials and Methods

3.2.1 Crystal orientation and texture measurements

The mineral fabrics were measured by SEM-EBSD analysis using a Zeiss EVOMA15 scanning electron microscope (SEM) coupled with a HKL Nordlys Nano EBSD detector at the Institute of Geology, China Earthquake Administration, China. We focused on the microstructures and textures of the three main minerals in the xenoliths, olivine, orthopyroxene and clinopyroxene, to infer their deformation history and determine their seismic properties as a proxy for the central Tibetan

96

lithospheric mantle. Crystal orientation images covering the entire xenoliths (20 − 30 mm long and 10 − 15 mm wide) were obtained with a step size of 10 µm using the Oxford Instruments *HKL AZtec* software. Modal composition, grain sizes and shape-preferred orientations were also obtained from the maps. A working distance of 25 mm was used for pattern acquisition and automatic indexing was performed using the AZtec software. The CHANNEL 5 software was used for noise reduction and for filling the missing data with at least 8 identical neighbors with similar orientation. Then this procedure was repeated for filling the missing data with at least 6 identical neighbors with similar orientation. The resulting EBSD data was optimized using MTex (Bachmann et al., 2010) to remove points with large angular deviation and to smooth intra-crystalline data.

The crustal orientation data are displayed in upper hemisphere, equal-area stereographic projection. To prevent over-representation of large grains, pole figures were plotted as one point per grain. Due to the small size of the xenoliths, the foliation and lineation are hard to identify macroscopically. The samples were thus cut in random orientations for thin section. To deal with the mantle xenoliths without obvious macroscopic structure, four methods are usually applied: (1) analysis of olivine's subgrain rotation axes, which indicates slip direction (Michibayashi et al., 2009; Passchier and Trouw, 2005); (2) determination of the spinel shape preferred orientation (SPO), which defined reference framework (Chatzaras et al., 2016; Liptai et al., 2019); (3) rotated the CPO of olivine to a similar A-type, which [100]-axis of olivine is parallel to the E-W direction and [010] axis of olivine is parallel to the N-S direction (Demouchy et al., 2018; Liu et al., 2019); (4) using the CPO of diopside, which main slip system of diopside at mantle P-T condition is [001](010) corroborated by natural and experimental deformation (Amiguet et al., 2009; Yang et al., 2019). As lacking enough spinel grains and obvious SPO to analysis, we rotated the CPO of samples to comply the CPO of diopside. We redefined the orthogonal XYZ structural framework by rotating datasets in order to have clustering of [001]

and [010] of clinopyroxene in the X and Z direction respectively, where X is defined by the clustering of the [001] directions and the X-Y plane is defined by the orientation of the (010) planes of the clinopyroxenes.

The strength of a CPO is quantified by the J-index, which represents the density distribution of crystallographic orientations (Ismail and Mainprice, 1998). For a random distribution the J-index is unity, and for a single crystal (perfect CPO) the J-index is infinity. The olivine in natural samples of mantle peridotite typically has a J-index in the range of $2 - 25$ with a peak at $5 - 10$. An axial symmetry of the orientation distribution is described by the BA index. The BA index is based on the eigenvalues of the orientation tensors for certain crystallographic directions (Mainprice et al., 2014). Any fabric with BA approximately zero or unity can be regarded as having a pronounced axial symmetry and thus an important fabric plane perpendicular to the asymmetry axis. Any fabric with a BA that is approximately 0.5 does not have axial symmetry and no important fabric plane defined by axial symmetry. Former studies are common classified the olivine CPO into three types by BA index (Tommasi et al., 2016): (i) BA-index < 0.35, defined by point concentrations of [010] and girdle distributions of [100] (fiber-[010]); (ii) 0.35 < BA-index < 0.65, defined by point concentrations in both three axis (orthorhombic pattern); and (iii) BA-index > 0.65, defined by a [100] point concentration and girdle distributions of [010] (fiber-[100]).

The seismic properties of the xenoliths were calculated following the method (Mainprice, 2007) of Mainprice and Humbert using single-crystal elastic constants, mineral densities, the textures (CPO) obtained from SEM-EBSD analysis, and the modal proportions of the minerals. For the computations the MTex software was used and Voigt - Reuss - Hill averaging of single-crystal elastic constants was applied (Mainprice, 2007). The results are displayed in upper hemisphere, equal-area stereographic projection

3.2.2 Mineral chemical analysis

The major-element compositions of olivine, orthopyroxene, clinopyroxene, and spinel were measured using a Cameca SXFive FE Electron Probe Microanalyzer (EPMA) equipped with 5 wavelength- and one energy-dispersive spectrometer at the Department of Lithospheric Research, University of Vienna. An acceleration voltage of 15 kV and a beam current of 20 nA were employed. The counting time was 20 s at the peak position and 10 s on each background position. The PAP method (Pouchou and Pichoir, 1991) was applied for matrix corrections. Natural and synthetic standards were used for calibration. The relative error of the laboratory internal standard is below 1%.

The trace element compositions of clinopyroxene and orthopyroxene were in-situ measured using laser ablation inductively coupled plasma mass spectrometry (LA-ICP-MS) (GeoLas 2005 + Agilent 7700x) with a spot size of 44 μm, at State Key Laboratory of Geological Processes and Mineral Resources, China University of Geosciences, Wuhan. Helium was used as a carrier gas, and nitrogen was added into the central gas flow (Ar + He) of the Ar plasma to increase the sensitivity (Hu et al., 2008). The detailed operating conditions for LA-ICP-MS were previously described (Liu et al., 2008). The off-line selection and integration of the background and analyte signals along with time-drift correction and quantitative calibration, were performed by ICPMSDataCal (Liu et al., 2008). The elemental concentrations were calibrated against multiple reference materials (BCR-2G, BHVO-2G and BIR-1G), and a summed metal oxide normalization was applied (Liu et al., 2008).

3.2.3 Splitting time analysis

In this study, we include seismic data from more than 4500 earthquakes, which are available for the period from 1992 to 2013 at 78˚-104˚ E in the area of the Tibetan Plateau (Fig. 1). A total of 672 broadband stations from the open access database were used for splitting analysis. The data from stations that recorded less than three events

were excluded. The splitting parameters includes the fast polarization direction (FPD) and the split time delay (δt). In total we obtained 1532 SKS splitting events and calculated an average of the respective splitting parameters for each station.

3.2.4 Calculation of seismic properties as a function of P and T

To test for any correlation between the petrophysical and geophysical data, we calculated the seismic properties over a large range of pressure (1.2–3.5 GPa) and temperature (750–1200 °C) according to the method described by Mainprice (Mainprice, 2007).

To calculate the elastic constants at various pressures and temperatures, the single-crystal elastic constants are given at the pressure and temperature of measurement using the following relationship:

$$C_{ij}(PT) = C_{ij}(P_0 T_0) + \left(\frac{dC_{ij}}{dP}\right)(P - P_0) + \frac{1}{2\left(\frac{d^2 C_{ij}}{dP^2}\right)(P - P_0)^2} + \left(\frac{d^2 C_{ij}}{dT}\right)(T - T_0)$$

$$+ \left(\frac{d^2 C_{ij}}{dPdT}\right)(P - P_0)(T - T_0)$$

where C_{ij} (PT) is the elastic constant at pressure P and temperature T, C_{ij} ($P_0 T_0$) is the elastic constant at a reference pressure P_0 (e.g., 0.1 MPa) and temperature T_0 (e.g., 25 °C), dC_{ij}/dP is the first-order pressure derivative, dC_{ij}/dT is the first-order temperature derivative, and $d^2 C_{ij}/dP^2$ is the second-order pressure derivative (Mainprice, 2007).

The seismic velocities also depend on the density of the minerals at a given pressure and temperature; this can be calculated using an appropriate equation of state. For the temperatures and pressures of the mantle, the density is described in this paper as follows Tasaka (2008):

$$\rho(P, T) = \rho_0 \left(\frac{\left[1 + \left(\frac{K'}{K}\right)(P - P_0)\right]}{K'[1 - \alpha_{av}(T - T_0)]}\right)$$

where K is the bulk modulus; K'=dK / dP, the pressure derivative of K; and ρ_0 is the density at reference pressure P_0 and temperature T_0; $\alpha_v(T) = 1 / V (\partial V / \partial T)$ is the volume thermal expansion coefficient as a function of temperature and α_{av} is an average value of thermal expansion.

The elastic constants of the minerals are presented in Supplementary 3A-Information, using the Voigt–Reuss–Hill average for the average sample shown in Fig. 3-5 and Supplementary 3B-Figure 4.

3.3 Results

3.3.1 The Ejumaima mantle xenoliths

Potassic and ultra-potassic volcanic rocks of Cenozoic age (45-27 Ma) are widespread in the northern Qiangtang terrane. In contrast, more Na-rich and calc-alkaline lavas were locally erupted in the southern part such as in Ejumaima and Nading Co (Ding et al., 2007) at the same time (65-28 Ma) (Fig.3-1). In this study, we focus on the Ejumaima mantle xenoliths (32°10'34" N, 86°45' 26" E). The xenoliths are hosted by grey trachytes and dark-red trachyandesites, which, according to [40]Ar-[39]Ar radiometric dating, have an age of 34.2±0.1 Ma (Ding et al., 2007).

The Ejumaima mantle xenoliths are represented by small, approximately ~1.0 cm sized fragments of lherzolite and pyroxenite with rounded and tabular shapes (Fig.2). Seven xenoliths were analysed, including 2 peridotite and 5 websterite xenoliths. Their deformation history was reconstructed from fabric analyses and taken as a proxy for the Qiangtang lithospheric mantle (Supplementary 3A-Table 1). Two types of lherzolite occur. A fertile variety with 62 vol. % olivine and 38 vol.% pyroxene is typically fine grained and is represented by sample T16-45. A comparatively refractory variant with 75 vol. % olivine and 25 vol. % pyroxene is typically coarse grained and is represented by sample T16-57. The websterites mainly

New evidence for a heterogeneous lithospheric structure in central Tibet: implications for the Indian-Eurasian collision

Chapter 3

consist of ~60-80 vol.% clinopyroxene and ~20-40 vol. % orthopyroxene, some varieties contain up to 5 vol. % olivine. The equilibrium temperatures of the xenoliths were estimated from 18 orthopyroxene-clinopyroxene pairs using different two-pyroxene geothermometers (Bertrand and Mercier, 1985). Each sample has been analysed more than 3 pyroxenes pairs. The inferred temperatures are in the range of 1119 ± 31°C for the peridotites and 1015± 28°C for the pyroxenites (Supplementary 3A-Table 1).

The olivine in the more refractory sample T16-57 has a high-$Mg^{\#}$ (=100 × Mg / (Mg + Fe)) of 91.05. In contrast, the olivine of the more fertile sample T16-45 has a relatively low $Mg^{\#}$ of 87.8. The NiO, Al_2O_3 and CaO contents are 0.37-0.38 wt%, 0.03-0.02 wt% and 0.06-0.07 wt%, respectively, in both samples. If present, the olivine in the websterites has an $Mg^{\#}$ of 77.9.

The orthopyroxene composition in the peridotites differs strongly from the orthopyroxene composition in the websterites. While in the peridotites the orthopyroxene $Mg^{\#}$ varies from 88.4 to 91.6, it is markedly lower in the websterites ranging from 75.6 to77.8. The orthopyroxene in the peridotites has slightly elevated Al (0.14-0.19 apfu Al) with 1.88-1.91 apfu Si and 0.03 apfu Ca. In the pyroxenites, the Al, Si and Ca contents of the orthopyroxene are in the range of 0.08-0.13 apfu Al, 1.90-1.93 apfu Si and 0.06 apfu Ca.

The clinopyroxene is quite similar in both, the peridotites and the pyroxenites, except for the $Mg^{\#}$, which is in the range of 88.6 to 91.5 in the peridotites and in the range of 75.6 to 77.8 in the pyroxenite. There is also a slight difference in the Si contents, which is about 1.92 in clinopyroxene of the peridotites and 1.87-1.89 apfu in clinopyroxene of the pyroxenite. Generally, the clinopyroxene contains 0.74-0.79 apfu Ca and variable 0.12-0.19 apfu Al. Accordingly, the main clinopyroxene end-member component is augite (0.42Wo+0.45En+0.13Fs).

The clinopyroxene of the fertile peridotite and the pyroxenites displays upward-

convex rare earth element (REE) patterns, with an enrichment in middle REE (Lan/Smn < 0.8) over both light (L) and heavy REE (HREE) (Lan/Ybn = 4.1-5.2). Whereas, the clinopyroxene in the depleted sample shows extremely LREE-enriched (Lan/Ybn = 66.3; Lan/Smn = 3.7) (Supplementary 3B-Fig. 1). Compared with the mantle xenolith from the ultrapotassic rocks in the Lhasa (Yang et al., 2019), the clinopyroxene of fertile peridotite have similar REE patterns with it from Lhasa xenolith (Supplementary 3B-Fig. 1). Trace element patterns of clinopyroxene are also comparable between all of xenoliths, with Ejumaima peridotite xenoliths having higher overall trace element abundances than the Lhasa xenolith and pyroxenites. Clear fractionated clinopyroxene patterns characterized by depleted in Nb, Zr, Hf (high-field strength elements, or HFSE) relative to large ion lithophile elements (LILE). The clinopyroxene of Lhasa xenolith and pyroxenite exhibit highly by very low Rb and Ba. In contrast, T16-57 and T16-45 shows high Rb and Ba abundances (Supplementary 3B-Fig. 1).

3.3.2 Mineral Fabric

The crystallographic orientations of the different phases were obtained from crystal orientation imaging based on electron backscatter diffraction (EBSD) and are shown in Fig 3-2. Following the classification of clinopyroxene CPOs observed in natural and experimental samples (Zhang et al., 2006), we use the CPO of clinopyroxene to define an orthogonal reference frame with axes X, Y, and Z, whereby the alignment of the [001] directions of clinopyroxene defines the X-direction, and the alignment of the [010] directions defines the Z-direction (detailed methods comparison are described in the Methods). Olivine shows a well-developed crystal preferred orientation. Two fabric types of olivine are observed. The first type is characterized by the alignment of the [010] axes close to the Z -direction and a large circle girdle in the XY-plane containing the [100] and [001] poles of olivine. This is a typical AG-type fabric according to the olivine fabric classification (Mainprice, 2007) (Fig.3-2 T16-57).

Chapter 3

	Olivine			Orthopyroxene			Clinopyroxene			
	[100]	[010]	[001]	[100]	[010]	[001]	[100]	[010]	[001]	
T16-57	N=811 J=4.52 M=0.09 BA=0.14 7.64			N=106 28.18			N=296 9.35			AG type
	MD=7.22 pf=2.08	MD=7.64 pf=2.52	MD=6.00 pf=1.66 0.05	MD=26.70 pf=11.64	MD=24.69 pf=11.08	MD=28.18 pf=15.07 0.00	MD=5.39 pf=2.20	MD=9.35 pf=2.56	MD=9.12 pf=2.75 0.00	
T16-45	N=786 J=1.73 M=0.02 BA=0.46 2.61			N=255 3.64			N=805 2.79			B type
	MD=2.61 pf=1.20	MD=2.54 pf=1.19	MD=1.92 pf=1.11 0.21	MD=3.64 pf=1.28	MD=3.09 pf=1.29	MD=2.74 pf=1.24 0.11	MD=1.54 pf=1.05	MD=2.15 pf=1.10	MD=2.79 pf=1.15 0.21	
T16-35	N=2			N=163 9.99			N=805 9.92			
				MD=7.30 pf=2.37	MD=7.20 pf=2.35	MD=9.99 pf=2.75 0.00	MD=6.79 pf=1.62	MD=9.92 pf=2.38	MD=8.16 pf=2.09 0.00	

Fig. 3-2 Representative pole figures for the crystallographic axes of olivine, orthopyroxene and clinopyroxene in xenoliths from Ejumaima. The CPOs are presented in equal-area, one point per grain, lower-hemisphere projections; the structural reference frame is shown as insert in the upper left. Contours (=6) show multiples of uniform distribution. N is the number of measurements. J-index and M-index is the fabric strength. BA-index is the axial symmetry of the orientation distribution. pf is an index of fabric intensity, and MD is the maximum density.

The other fabric type is comparatively weak. It is characterized by the preferential alignment of the [100] axes of olivine parallel to the Y-direction and of the [001] axes parallel to the X-direction (Fig.3-2 T16-45). This may be classified as a B-type fabric (Mainprice, 2007).

The CPO of orthopyroxenes is less pronounced. In the peridotites, the [010] directions of orthopyroxenes are aligned perpendicular to the XY-plane and the [001] directions are roughly aligned with the X-direction. The CPO of orthopyroxenes is thus similar to the one of olivine (Fig.3). By contrast, in the pyroxenites, the [001] poles of orthopyroxenes are ca. 60° off the X-direction, and the [010] poles are ca. 20° off the Z-direction within the XZ-plane (Fig. 3-2 T16-35).

3.3.3 Seismic Anisotropy of the Qiangtang Xenoliths

The seismic properties of the xenoliths were calculated following the method of Mainprice and Humbert (Mainprice, 2007). The modal proportions of the major minerals, olivine orthopyroxene and clinopyroxene, were obtained from EBSD measurements (Supplementary 3A-Table 1).

For the T16-57 (AG-type) olivine, low P-wave velocities (V_p^{min} =7.90 km/s) are calculated for the direction parallel to the structural Z axis, while the maximum P-wave velocities (V_p^{max} =8.66 km/s) lie in the plane normal to the Z-axis (Fig.4). The polarization anisotropy values (AV_s) are characterized by moderate AV_s in large circle girdles in the XY-plane comprising the olivine [100]- and [001]-directions, with the highest anisotropy of 7.9% for S-waves propagating close to the X-direction of the structural reference frame. The minimum AV_s is approximately parallel to the Z-direction of the structural reference frame (Fig.3-3).

For the T16-45 (B-type olivine), the fastest P-wave (V_p^{max} =8.43 km/s) direction is sub-parallel to the Y-direction, while the slowest one (=8.11 km/s) is sub-parallel to the Z-direction similar to the AG-type. The maximum of the AV_s of this sample is 2.4% with the highest dV_s (=V_{s1}-V_{s2}) slightly oblique to the X-direction in the XZ-plane and the lowest dV_s perpendicular to the X-direction and slightly (approx. 5°) off the Y-direction (Fig.3-3).

Chapter 3
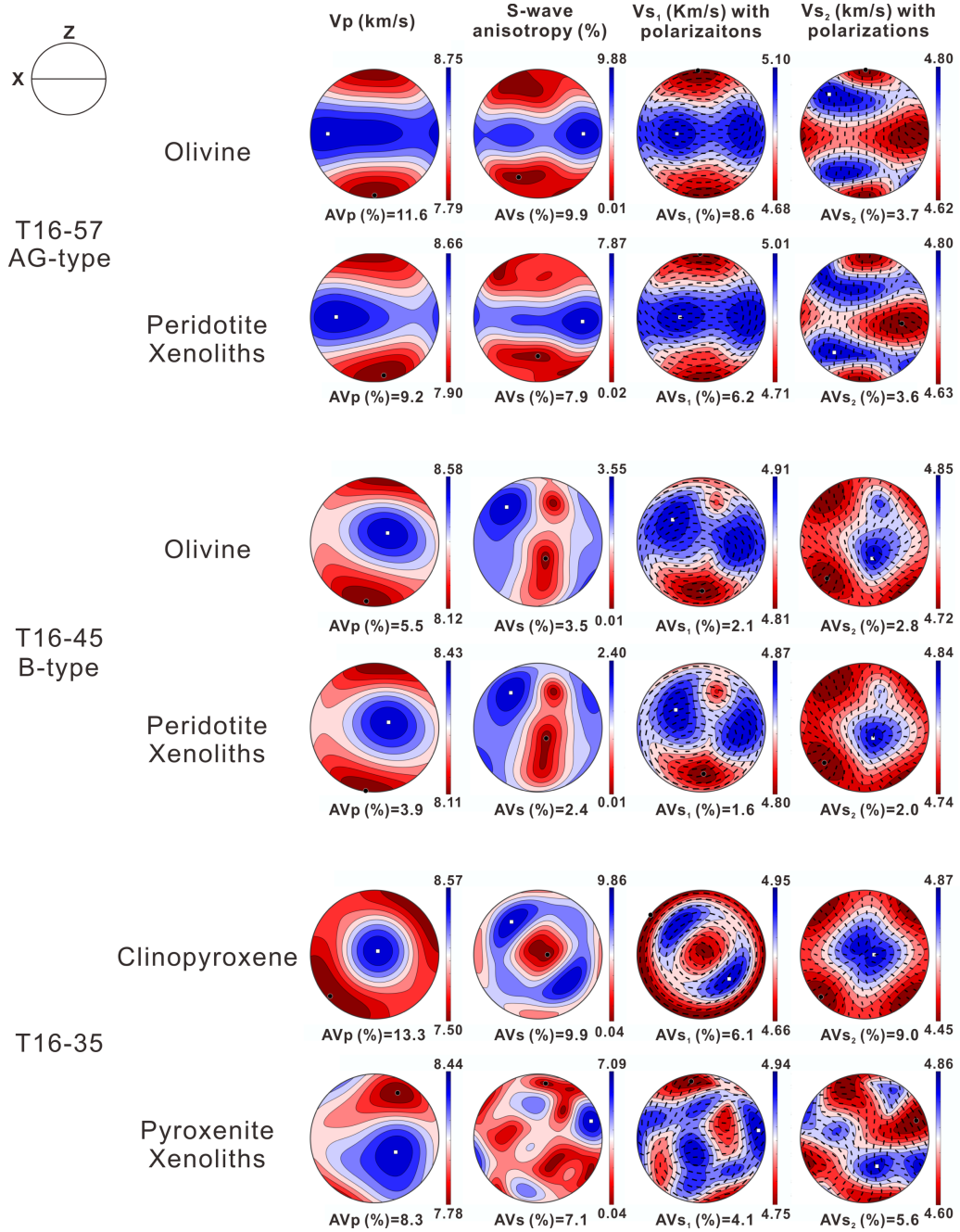
Fig. 3-3 Representative patterns of the seismic properties of the peridotite xenoliths in Ejumaima calculated from the fabric of the xenoliths. The seismic properties are presented in equal-area, lower-hemisphere projections relative to the structural XYZ reference frame. The four columns show P-wave velocity (V_p) with P-wave anisotropy (AV_p); polarization anisotropy (AV_s) and splitting S-wave velocity (V_{s1} and V_{s2}) with their polarization directions. $AV_p = [(V_p^{max} - V_p^{min}) / (V_p^{max} + V_p^{min}) / 2] \times 100\%$ and $AV_s = [(V_{s1} - V_{s2})] / [(V_{s1} + V_{s2}) / 2]$, where V_{s1} and V_{s2} are the velocities of the fast and slow split S-waves, respectively. $AV_{s1/s2} = [(V_{s1/s2}^{max} - V_{s1/s2}^{min}) / (V_{s1/s2}^{max} + V_{s1/s2}^{min}) / 2]$; insert on the middle left shows the structural reference frame.

3.3.4. Variation of seismic properties with depth

We consider a reasonable range of mineral modal proportions from the lower crust to the upper mantle. Our estimates are based on the modal compositions in the xenoliths, their calculated equilibrium temperatures (see the Supplementary 3A-Information & Table 6-8) and lithospheric structure (see the discussion). Considering the temperature distribution in the Tibetan lithosphere (Jiménez-Munt et al., 2008; Tunini et al., 2016), we infer that the olivine-bearing pyroxenites with the relatively high equilibration temperatures (~1060°C) were entrained from the crust-mantle boundary or from the uppermost mantle. The pyroxenites without olivine indicate relatively low temperatures (~1000°C) and were more likely sampled from the lower crust or crust-mantle transition. Based on mineral chemistry, the two peridotite xenoliths represent central Tibetan mantle. The more refractory one with the relatively low equilibration temperature (~1070°C) appears to have been entrained from relatively shallow domains within the lithospheric mantle as compared to the fertile one (~1144°C), which probably originated from deeper domains. To assess the influence of lateral change in lithospheric structure, corresponding calculations of the seismic properties were made for representative fertile peridotites from the Lhasa terrane (Yang et al., 2019) with different fabrics (Fig. 3-4 and Supplementary 3B-Fig. 4). For each rock type the seismic velocities are primarily controlled by the modal proportions of the constituent minerals obtained from xenoliths. To avoid the inaccurate proportions caused by the small size of xenoliths, we also consider the modal proportions based on the similar chemical compositions from experiments (Niu, 2004; Walter, 1998). Thus, the Qiangtang peridotites are in the range of 60ol+20cpx+20opx to 80ol+10cpx+10opx, deceasing step-by-step 10% olivine. The Lhasa peridotites are composed of 70ol+5cpx+25opx to 80ol+5cpx+15opx, deceasing step-by-step 5% olivine (Supplementary 3A-Table 6-8).
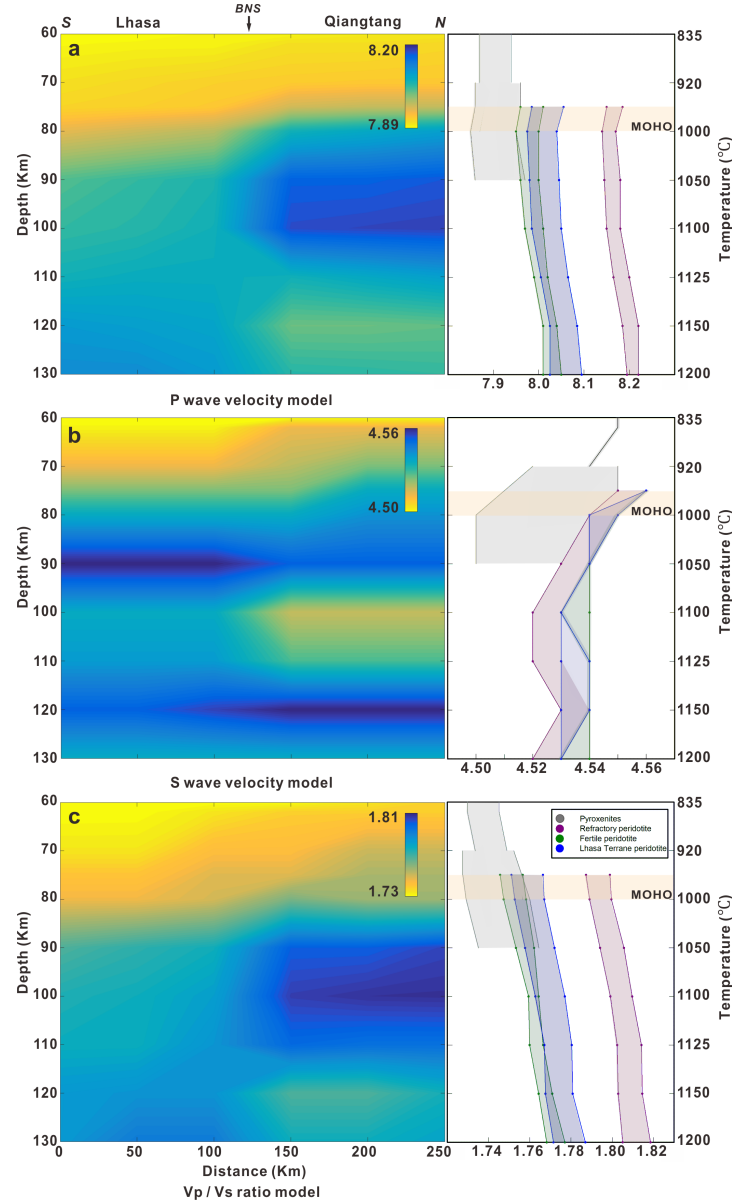
Fig. 3-4 Variation of seismic velocities as a function of P and T for different equilibration depth. The seismic properties were calculated using the elastic constants including theirs pressure-temperature derivatives for each mineral (Details in the Supplementary information and Table). Color bars indicate the maximum and minimum value based on the different mineral modal compositions for the peridotites. The shaded area represents the crust/mantle transition zone. The corresponding velocity model for the Lhasa-Qiangtang profile is shown on the left. (a) Mean (isotropic) P wave velocity in the radial direction (b) Mean S wave velocity (c) Mean V_p / V_s ratio. The seismic properties of the pyroxenites were computed for the lower crust and uppermost mantle and are presented as the grey area. The pink bars and the green bars represent the refractory and fertile Qiangtang mantle, respectively. The blue bars represent the fertile Lhasa mantle.

Generally, the seismic velocity is lower in the pyroxenites than in the peridotites. The calculated mean P wave velocities (V_p) of the pyroxenites along a depth profile are relatively constant above the crust-mantle transition zone (Fig. 3-4a). V_p in the radial direction of both, the refractory and fertile peridotite, show an apparent increase within the depth range of 100 to 120 km (Fig. 3-4a). The distinction in the V_p between the refractory and the fertile peridotite from the Qiangtang terrane is apparent. The refractory peridotite shows the highest V_p ranging from 8.14 km/s to 8.22 km/s (Fig. 3-4a). Compared to the refractory peridotites, the fertile peridotites display the lowest V_p with depth, ranging from 7.96 km/s to 8.05 km/s (Fig. 3-4a). The results from velocity modelling along the lateral profile exhibit obvious differences in the shallower lithosphere domains, where the V_p is higher in the refractory Qiangtang terrane than in the fertile Lhasa terrane (Fig. 3-4a). By contrast, in the deeper lithosphere domains, the V_p is faster in the Lhasa terrane than in the Qiangtang terrane, whereby the lowermost lithosphere is comprised of fertile peridotite in both cases (Fig. 3-4a). The V_p^{max} and V_p^{min} of the fertile peridotite in the Qiangtang terrane are somewhat higher than those of the corresponding properties in the peridotite from the Lhasa terrane (Supplementary 3B-Fig. 4c & d).

The average S wave velocities (V_s) show a weak decline with depth and are rather similar for all three peridotite types (Fig. 3-4b). The V_s are fastest in the fertile peridotite of the Qiangtang terrane (Fig. 3-4b), with fastest V_{s2}^{min} (4.40 km/s to 4.49 km/s) and the slowest V_{s1}^{max} (4.61 km/s to 4.64 km/s) splitting S-wave velocities (Supplementary 3B-Fig. 4a & b). The refractory peridotite shows the lowest V_s (Fig. 3-4b) with highest V_{s1}^{max} (4.73 km/s to 4.76 km/s) and lowest V_{s2}^{min} (4.61 km/s to 4.63 km/s) (Supplementary 3B-Fig. 4a & b), indicating a very strong anisotropy. The differences in the S-wave splitting velocities between the peridotite types from the Qiangtang terrane is obvious. In contrast, the fertile peridotite has a quite similar character as the peridotite from the Lhasa terrane (Supplementary 3B-Fig. 4a & b) with a moderate V_s that is between V_s of the two types of peridotite from the

New evidence for a heterogeneous lithospheric structure in central Tibet: implications for the Indian-Eurasian collision

Chapter 3

Qiangtang terrane (Fig. 3-4b). Fig. 3-4c shows the V_p / V_s ratio, which increases gradually with depth. The ratio calculated from the refractory peridotite is larger than the ratio from the fertile peridotites.

3.4 Discussion

The petro-chemical features of the Ejumaima peridotite xenoliths are in stark contrast to the corresponding properties of the olivine-bearing xenoliths reported earlier from the Southern Qiangtang terrane (Ding et al., 2007). The olivine-bearing xenoliths from the Southern Qiangtang terrane are considered to have been entrained from an unusual upper mantle lithosphere (Ding et al., 2007) since their olivine has a low Mg-number (~65-70), which is similar to the minor olivine (=77.8 Mg#) in our olivine-bearing pyroxenite samples.

3.4.1 Origin of olivine fabric in the Qiangtang lithospheric mantle

A well-preserved olivine B-type fabric has been found in the fine-grained peridotite and an AG-type has been found in the coarse-grained peridotite, in both xenoliths the olivine compositions is 88 Mg# and 91 Mg# testifying to a mantle origin. The olivine fabrics thus reflect the conditions and history of mantle deformation (Jung and Karato, 2001). Based on former experimental results, the B-type fabric is attributed to deformation dominantly by (010)[001] slip (Jung, 2017). Activation of this slip system was observed under at least four different experimental conditions: (1) high stresses (340 MPa) and pressure (1.9 GPa) with abundant water (≥800 H/Si) (Jung and Karato, 2001); (2) low stresses (<150 MPa) and pressure (300 MPa) with domains of rock encompassed by aligned melt pockets (Holtzman and Hustoft, 2003); (3) in harzburgite with 35-50% orthopyroxene at low stresses (<200 MPa) and moderate pressure (1.5 GPa) owing to diffusion creep (Sundberg and Cooper, 2008);

110

(4) low stress (<150 MPa) under high pressure (2.5-3.1 GPa with 3% orthopyroxene and 5-7 GPa without orthopyroxene) (Ohuchi et al., 2011). In natural mantle rocks, the B-type olivine fabric is mostly reported from metamorphic peridotites in a water-rich environment such as in subduction zones (Jung, 2017), from high-pressure diamond-bearing garnet peridotites under dry conditions (Jung, 2017), from garnet peridotites which experienced high-stresses at relatively low temperature (<750℃) and water content (Skemer et al., 2006), from fine-grained peridotite mylonites that deformedby grain-boundary sliding (GBS) at low temperature (<750℃) and dry conditions (Précigout and Hirth, 2014), and from peridotite xenoliths showing evidence of the presence of melt in a metasomatized mantle (Yang et al., 2019).

The AG-type fabric of olivine is considered as a transitional CPO between the A-type and the B-type fabric. It has been documented in various tectonic settings including peridotite massifs (Vauchez and Garrido, 2001), cratonic and sub-continental mantle xenoliths (Tommasi et al., 2008; Yang et al., 2019), subduction zone peridotite (Jung, 2017), and intra-oceanic settings (Vonlanthen et al., 2006). Four hypotheses have been proposed for the generation of the AG-type fabric: (1) An A-type fabric of olivine may be transformed into an AG-type fabric by axial compression in Z-direction ($Z = [001]_{ol}$) under dominantly pure shear deformation (Mainprice, 2007); (2) An AG-type fabric may be formed by simultaneous activation of the (010)[100] and (010)[001] slip systems under high-pressure or high-stress conditions (Mainprice, 2007); (3) Furthermore it may be generated by melt assisted shear deformation at high temperature (Holtzman and Hustoft, 2003); and (4) by static recrystallization of deformed rocks, which may modify a pre-existing microstructure by sub-grain rotation and growth (Vonlanthen et al., 2006).

Based on the P-T conditions obtained from the Ejumaima xenoliths deformation settings that require high pressures or high temperatures can be excluded. Thus hypothesis 4 for the B-type fabric, and hypothesis 2 for the AG-type fabric, which would be applicable for deep-rooted cratonic xenoliths (3.7 - 4.7 GPa and ~1140-

1400 °C) must be eliminated. Other specific requirements, such as the presence of more than 35 vol.% orthopyroxene (hypothesis 3 for B-type) and annealing features in olivine to support static recrystallization (hypothesis 4 for AG-type), can also be ruled out. Finally, axial compression as invoked by hypothesis 1 for the AG-type fabric is inconsistent with the alignment of the [001]-axes of orthopyroxene forming a point maximum close to the lineation (Fig. 3). This leaves the hypothesis of melt-assisted formation of the AG-type olivine fabric as the most likely scenario for the observed CPO in the Ejumaima xenoliths. Whether the formation of the B-type olivine fabric was related to the presence of melt or water is uncertain. According to literature[8,50,51], formation of a B-type fabric under elevated water contents typically occurs in supra-subduction mantle wedges (Michibayashi et al., 2016) and in trench zones (Michibayashi et al., 2016) usually in association with serpentinization. At ~1100°C. the solubility of hydrogen in olivine with $Mg^{\#} = 88$ is ~100 $H/10^6$ Si (Zhao et al., 2004). This is outside the B-type fabric regime (Jung, 2017) supporting the hypothesis that the B-type fabric in the peridotites from the Qiangtang terrane formed in the presence of a melt.

The collective petrographic, compositional and fabric evidence suggests that the deformed xenoliths from the Qiangtang terrane are derived from a lithospheric mantle that experienced partial melting. This interpretation is further corroborated by independent geophysical and geologic observations. Abundant post-collisional potassic magmatism and rifts related to extensional faults have been observed in the Qiangtang terrane indicating partial melting of the lithospheric mantle (Chung et al., 2005). The abrupt thickness change between the Lhasa- and the Qiangtang terranes and a wholesale uplift of the Qiangtang- and the Songpan-Ganze terranes during the Oligocene-early Miocene are interpreted as a response to the removal of the lithospheric root due to asthenosphere upwelling (Chung et al., 2005; Lu et al., 2018). Moreover, low seismic velocity (Liang et al., 2016), high Sn/Pn-wave attenuation (Jiménez-Munt et al., 2008), and Pn tomography (Liang and Song, 2006) all indicate

partial melting of a metasomatized lithospheric mantle beneath the Qiangtiang terrane. Thus, the occurrence of the AG-type and B-type olivine fabrics is compatible with a large-scale hot and deformable melt-bearing lithospheric mantle.

3.4.2 Seismic anisotropy of the upper mantle in the Qiangtang terrane

The seismic stations surrounding the Ejumaima region show that the FPD of split SKS waves ranges from N72° to N82° with splitting time delays of 1.5s on average (Fig. 3-1). If the large time delay is attributed to the upper mantle, both the refractory and the fertile peridotite must contribute to the anisotropy. For the shallower refractory domains of the mantle with strong anisotropy, the XY-plane is inferred to be approximately vertical, since the polarization anisotropy in the direction normal to the XY-plane is very weak or nearly zero for the AG-type fabric. The orientation of the FPD is rather constant throughout the study area indicating that, despite of different fabric types, both lithosphere domains contribute to the approximate E-W polarization of the fast wave of split SKS waves. This implies that in the lower lithosphere the [001] direction of olivine is in upright orientation with the [100] direction being horizontal (E-W) in the foliation. In fact, the deeper fertile mantle domains have experienced long-term asthenospheric upwelling, which promoted the evolution of a close to vertical foliation defining the XY-plane during the convective movement in the lower lithosphere. Considering the thickness of the anisotropic layer in the upper mantle beneath the Qiangtang terrane and the magnitude of anisotropy calculated from the peridotite fabric, the entire lithospheric mantle can only cause about 1s delay time, which is substantially less than the average delay time of 1.5-2.0s in the Qiangtang terrane. Thus, an additional or alternative mechanism needs to be invoked to explain the anomalously large delay time. Melt that is present in domains with preferred shape orientation has been proposed (Yang et al., 2019) (Fig. 3-5).

New evidence for a heterogeneous lithospheric structure in central Tibet: implications for the Indian-Eurasian collision

Chapter 3
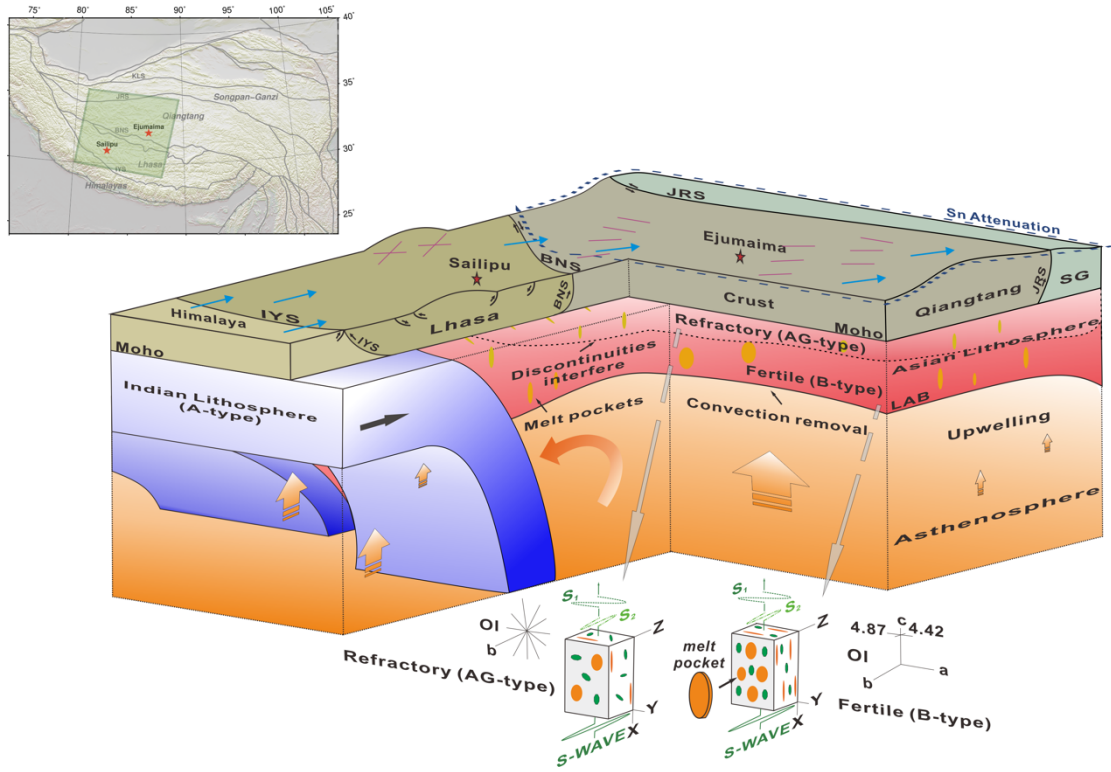
Fig. 3-5 Interpretative 3D model showing the relationships between slab structure, asthenosphere upwelling and lithospheric mantle architecture in the Tibetan upper mantle. The shallower refractory mantle domains caused a heterogenous mantle beneath the Tibetan mantle. (Acronyms are same as in Fig .1-1. The purple lines show the FPD of SKS. The blue arrows indicate the GPS direction and the dashed line outlines the area of Sn attenuation. The green tabular and hexagonal grains represent olivine appearing at the refractory domains and fertile domains, respectively.)

3.4.3 Heterogeneity of the velocity structure in the lithospheric mantle

Hitherto, inferences on the deformation mechanisms and patterns of the lithospheric mantle beneath central Tibet have primarily been based on seismic data. For example, large scale structures and the plate boundaries in the Tibetan lithosphere were reconstructed from receiver function inversion (Kumar et al., 2006; Zhao et al., 2011), surface and teleseismic wave tomography (Zhang et al., 2016), and

adjoint tomography (Chen et al., 2017).

It is generally thought that the velocity of wave propagation through mantle rocks is primarily determined by the rock fabric and its orientation with respect to structural frame. On the basis of the inferred vertical orientation of the XY-plane of the structural reference frame and the geothermal gradient (Tunini et al., 2016) in central Tibet, sample T16-57 indicates a relatively refractory mantle domain above a more fertile mantle domain represented by sample T16-45. The velocity structure that we derived from our fabric measurements corresponds well to the transition from refractory to fertile with increasing depth and to the lateral transition between the Lhasa and the Qiangtang terranes.

The shallower lithospheric mantle in the Qiangtang terrane is characterized by high V_p, low V_s, and high V_p / V_s ratios and by a strong seismic anisotropy (Fig.4 & 5). Based on these features it is distinguished from the deeper lithospheric mantle in the Qiangtang terrane and from the laterally adjoining lithospheric mantle of the Lhasa terrane, which are both characterized by low V_p, high to moderate V_s, and generally low V_p / V_s ratios and by a weaker anisotropy (Fig. 3-3 & 3-4).

This situation is in good agreement with the seismic observations in the upper mantle made along a traverse from the Lhasa terrane to the Qiangtang terrane. There, a decrease of the average V_s (Hung et al., 2011; Zhang et al., 2016; Zhao et al., 2011), an increase of the V_p / V_s ratios (Hung et al., 2011; Zhang et al., 2016) and an increase of V_p (Hung et al., 2011; Tunini et al., 2016; Zhang et al., 2016; Zhao et al., 2010; ZHENG et al., 2007) is observed in the shallower domains. In contrast, a weak reverse trend is observed in the deeper domains. Also, the variation with depth is compatible with the S-wave velocity structure with a low-velocity anomaly in the shallower domains (Hung et al., 2011; Zhao et al., 2011) and P-wave velocity structure with a low-velocity anomaly in the deeper domains (Hung et al., 2011; Zhang et al., 2016; ZHENG et al., 2007) beneath the Qiangtang terrane. A discontinuity at 100-

New evidence for a heterogeneous lithospheric structure in central Tibet: implications for the Indian-Eurasian collision

Chapter 3

110km depth as observed by the S and P receiver function technique (Kumar et al., 2006; Zhao et al., 2010; Zhao et al., 2011) is also consistent with our model. Finally, additional evidence from petrology and geochemistry of the volcanic rocks also supports the vertical and lateral heterogeneity of the lithospheric mantle in central Tibet (Zhang et al., 2019). Thus, we suggest that a heterogeneous lithospheric mantle exists beneath central Tibet.

The velocity discontinuity at 100 km depth was interpreted as an indication of a thin but separated Tibetan lithosphere, overlapping with the Asian lithosphere (Kumar et al., 2006; Zhao et al., 2011). This interpretation motivated the bidirectional subduction model to explain the complex reflection tomography. Based on the notion that the depth of this seismic discontinuity closely coincides with the depth of the velocity change inferred from the Ejumaima xenoliths (Fig. 3-4b), we rather consider it as the boundary between a shallower refractory and a deeper fertile mantle domain. This view is corroborated by the observation of a single FPD in central Tibet. While, the bidirectional subduction model, which probably entails a double layer anisotropy, seems contradictory. Hence, we ascribe the complex reflection tomography to a heterogeneous mantle.

3.4.4 Origin of the heterogeneous lithospheric mantle beneath central Tibet

The differences in the modal compositions, Mg# of olivine, trace elements of clinopyroxene and in the microstructures between the two types of Ejumaima peridotite xenoliths testify to the existence of a heterogeneous mantle beneath central Tibet. Melt re-fertilization is very common in the Tibetan mantle (Liu et al., 2011). A correlation between mineral fabric and melt metasomatism has been observed in peridotite xenoliths from southern Tibet (Yang et al., 2019). In the Qiangtang terrane, relatively fertile peridotite xenoliths with similar geochemical signatures and seismic properties as the xenoliths from the Lhasa terrane occur together with peridotite

xenoliths of a more refractory nature, raising the question, whether two pieces of lithospheric mantle with different melting and deformation histories were juxtaposed?

The Ejumaima xenoliths exhibit compositional and microstructural evidence of re-fertilization. If the re-fertilization occurred under static conditions (Vauchez and Garrido, 2001), the newly forming pyroxenes would be expected to form overgrowth on pre-existing pyroxene crystals and to fill interstitial space (Tommasi et al., 2016). However, we generally observe equigranular microstructures lacking evidence of overgrowth, which suggests re-fertilization associated with deformation. During melt-related deformation the re-fertilized low Mg# peridotites attained a B-type fabric, which is widespread throughout the Lhasa and Qiangtang terranes. The AG-type fabric in xenoliths from the central Tibetan refractory mantle is also pertinent to the presence of melt during deformation. The diversity of clinopyroxene REE patterns observed between xenolith of the two different fabric types could reflect different melt metasomatic stages or episodes. The clinopyroxene with B-type fabric displays convex upward REE patterns with a strong enrichment of the MREE indicating equilibrium with LREE-enriched silicate melts (Navon and Stolper, 1987). The clinopyroxene in the AG-type fabric shows strong enrichment of the LREE, which could result from interaction with carbonatite melt (Ntaflos et al., 2017). Based on its depleted geochemical signature, the deformation process producing the AG-type fabric is ascribed to an earlier melting event. It has been demonstrated experimentally that the transition from an olivine AG-type to a B-type fabric occurs with an increase of the melt fraction from 4% to 6% (Holtzman and Hustoft, 2003) or by increasing strain under the presence of melt (Qi et al., 2018). Thus, we infer that the fabric of part of the lithospheric mantle was transformed from AG-type into B-type fabric during melt-related deformation associated with re-fertilization. Convective removal of the lowermost lithosphere is the most likely scenario driving this re-fertilization in the lower sections of the lithospheric mantle. At the same time, the refractory 'ghost lithosphere' residing in shallower regions beneath the Qiangtang terrane preserved

the earlier AG-type fabric. It may thus represent a residual subcontinental lithospheric mantle, which was incorporated into the current lithospheric mantle. The Mg# of 91 in the depleted sample is higher than that of all reported xenoliths from the southern Qiangtang terrane (Ding et al., 2007) and most of the peridotite xenoliths from the northern Lhasa terrene (Liu et al., 2011; Yang et al., 2019) corroborating the view that the AG-type fabric was inherited.

3.4.5 New insight into the mantle dynamics

Attribution of the heterogeneous Tibetan lithosphere in the Qiangtang terrane to the presence of domains of more refractory material in the upper mantle above a re-fertilized lower mantle (Fig. 3-5), has several interesting implications. Firstly, a fully fertile mantle does not represent the entire mantle beneath central Tibet, but it only represents the hot and highly metasomatized lithospheric fraction of the mantle. It does thus not necessarily constrain the compositions and properties of the overall lithospheric mantle. Allowing for existence of a heterogeneous mantle simplifies the interpretation of geophysical data. In particular, it renders the hypothesis postulating the presence of three different lithospheric domains pertaining to India-, Tibet- and Eurasia obsolete (Zhao et al., 2010; Zhao et al., 2011). Secondly, the occurrences of multiple reflectors and the observations in xenoliths from lithospheric mantle peridotites, shed light on the extent of partial melting within the lithospheric mantle. Both olivine fabric types found beneath the Qiangtang terrane indicate the presence of melt. We infer that at an early stage a pre-existing refractory lithospheric mantle experienced small degree of partial melting. Subsequently, it was heated from the bottom and formed a fertile mantle in the lower part with B-type olivine fabric. The heterogenous mantle arrangement is consistent with the observed distribution of seismic reflectors. Thirdly, taking the peridotite xenoliths from Ejumaima as proxies for the lithospheric mantle of central Tibet, we infer the presence of refractory mantle despite of the comparatively thin lithospheric mantle in this area. In any case, the

findings from the peridotite xenoliths are incompatible with a fully metasomatized mantle below central Tibet.

References:

1. Abramson, E., Brown, J., Slutsky, L. and Zaug, J., 1997. The elastic constants of San Carlos olivine to 17 GPa. Journal of Geophysical Research: Solid Earth, 102(B6): 12253-12263.

2. Amiguet, E., Raterron, P., Cordier, P., Couvy, H. and Chen, J., 2009. Deformation of diopside single crystal at mantle pressure. 1: Mechanical data. Physics of the Earth and Planetary Interiors, 177(3-4): 122-129.

3. Anders, E. and Grevesse, N., 1989. Abundances of the elements: Meteoritic and solar. Geochimica et Cosmochimica acta, 53(1): 197-214.

4. Bachmann, F., Hielscher, R. and Schaeben, H., 2010. Texture Analysis with MTEX – Free and Open Source Software Toolbox. Solid State Phenomena, 160: 63-68.

5. Bertrand, P. and Mercier, J.-C.C., 1985. The mutual solubility of coexisting ortho-and clinopyroxene: toward an absolute geothermometer for the natural system? Earth and Planetary Science Letters, 76(1-2): 109-122.

6. Chai, M., Brown, J.M. and Slutsky, L.J., 1997. The elastic constants of an aluminous orthopyroxene to 12.5 GPa. Journal of Geophysical Research: Solid Earth, 102(B7): 14779-14785.

7. Chatzaras, V., Kruckenberg, S.C., Cohen, S.M., Medaris, L.G., Withers, A.C. and Bagley, B., 2016. Axial-type olivine crystallographic preferred orientations: The effect of strain geometry on mantle texture. Journal of Geophysical Research: Solid Earth, 121(7): 4895-4922.

8. Chen, M., Niu, F., Tromp, J., Lenardic, A., Lee, C.A., Cao, W. and Ribeiro, J., 2017. Lithospheric foundering and underthrusting imaged beneath Tibet. Nat Commun, 8: 15659.

9. Chung, S.-L., Chu, M.-F., Zhang, Y., Xie, Y., Lo, C.-H., Lee, T.-Y., Lan, C.-Y., Li, X., Zhang, Q. and Wang, Y., 2005. Tibetan tectonic evolution inferred from spatial and temporal variations in post-collisional magmatism. Earth-Science Reviews, 68(3-4): 173-196.

10. Demouchy, S., Tommasi, A., Ionov, D., Higgie, K. and Carlson, R., 2018. Microstructures, Water Contents, and Seismic Properties of the Mantle Lithosphere beneath the Northern limit of the Hangay Dome, Mongolia. Geochemistry, Geophysics, Geosystems.

11. Ding, L., Kapp, P., Yue, Y. and Lai, Q., 2007. Postcollisional calc-alkaline lavas and xenoliths from the southern Qiangtang terrane, central Tibet. Earth and Planetary Science Letters, 254(1): 28-38.

12. Frisillo, A.L. and Barsch, G.R., 1972. Measurement of single-crystal elastic constants of bronzite as a function of pressure and temperature. Journal of Geophysical Research, 77(32): 6360-6384.

13. He, R., Liu, G., Golos, E., Gao, R. and Zheng, H., 2014. Isostatic gravity

anomaly, lithospheric scale density structure of the northern Tibetan plateau and geodynamic causes for potassic lava eruption in Neogene. Tectonophysics, 628: 218-227.

14. Holtzman, B.K. and Hustoft, J., 2003. Melt segregation and strain partitioning: implications for seismic anisotropy and mantle flow. Science, 301(5637): 1227-30.

15. Hu, Z., Gao, S., Liu, Y., Hu, S., Chen, H. and Yuan, H., 2008. Signal enhancement in laser ablation ICP-MS by addition of nitrogen in the central channel gas. Journal of Analytical Atomic Spectrometry, 23(8).

16. Hung, S.-H., Chen, W.-P. and Chiao, L.-Y., 2011. A data-adaptive, multiscale approach of finite-frequency, traveltime tomography with special reference toPandSwave data from central Tibet. Journal of Geophysical Research, 116(B6).

17. Isaak, D.G., 1992. High-temperature elasticity of iron-bearing olivines. Journal of Geophysical Research: Solid Earth, 97(B2): 1871-1885.

18. Isaak, D.G., Ohno, I. and Lee, P.C., 2005. The elastic constants of monoclinic single-crystal chrome-diopside to 1,300 K. Physics and Chemistry of Minerals, 32(10): 691-699.

19. Ismail, W.B. and Mainprice, D., 1998. An olivine fabric database: an overview of upper mantle fabrics and seismic anisotropy. Tectonophysics, 296(1): 145-157.

20. Jiménez-Munt, I., Fernàndez, M., Vergés, J. and Platt, J.P., 2008. Lithosphere structure underneath the Tibetan Plateau inferred from elevation, gravity and geoid anomalies. Earth and Planetary Science Letters, 267(1-2): 276-289.

21. Jung, H., 2017. Crystal preferred orientations of olivine, orthopyroxene, serpentine, chlorite, and amphibole, and implications for seismic anisotropy in subduction zones: a review. Geosciences Journal, 21(6): 985-1011.

22. Jung, H. and Karato, S., 2001. Water-induced fabric transitions in olivine. Science, 293(5534): 1460.

23. Kumar, P., Yuan, X., Kind, R. and Ni, J., 2006. Imaging the colliding Indian and Asian lithospheric plates beneath Tibet. Journal of Geophysical Research: Solid Earth, 111(B6): n/a-n/a.

24. Liang, C. and Song, X., 2006. A low velocity belt beneath northern and eastern Tibetan Plateau from Pn tomography. Geophysical Research Letters, 33(22).

25. Liang, X., Chen, Y., Tian, X., Chen, Y.J., Ni, J., Gallegos, A., Klemperer, S.L., Wang, M., Xu, T., Sun, C., Si, S., Lan, H. and Teng, J., 2016. 3D imaging of subducting and fragmenting Indian continental lithosphere beneath southern and central Tibet using body-wave finite-frequency tomography. Earth and Planetary Science Letters, 443: 162-175.

26. Liang, X., Sandvol, E., Chen, Y.J., Hearn, T., Ni, J., Klemperer, S., Shen, Y. and Tilmann, F., 2012. A complex Tibetan upper mantle: A fragmented Indian slab and no south-verging subduction of Eurasian lithosphere. Earth and Planetary Science Letters, 333-334: 101-111.

27. Liptai, N., Hidas, K., Tommasi, A., Patkó, L., Kovács, I.J., Griffin, W.L., O'Reilly, S.Y., Pearson, N.J. and Szabó, C., 2019. Lateral and vertical heterogeneity in the lithospheric mantle at the northern margin of the Pannonian Basin reconstructed from peridotite xenolith microstructures. Journal of Geophysical Research: Solid Earth.

28. Liu, C.-Z., Wu, F.-Y., Chung, S.-L. and Zhao, Z.-D., 2011. Fragments of hot and metasomatized mantle lithosphere in Middle Miocene ultrapotassic lavas, southern Tibet. Geology, 39(10): 923-926.

29. Liu, S., Tommasi, A., Vauchez, A. and Mazzucchelli, M., 2019. Deformation, Annealing, Melt‐Rock Interaction, and Seismic Properties of an Old Domain of the Equatorial Atlantic Lithospheric Mantle. Tectonics.

30. Liu, Y., Hu, Z., Gao, S., Günther, D., Xu, J., Gao, C. and Chen, H., 2008. In situ analysis of major and trace elements of anhydrous minerals by LA-ICP-MS without applying an internal standard. Chemical Geology, 257(1-2): 34-43.

31. Lu, H., Tian, X., Yun, K. and Li, H., 2018. Convective removal of the Tibetan Plateau mantle lithosphere by ~26 Ma. Tectonophysics, 731-732: 17-34.

32. Mahéo, G., Guillot, S., Blichert-Toft, J., Rolland, Y. and Pêcher, A., 2002. A slab breakoff model for the Neogene thermal evolution of South Karakorum and South Tibet. Earth & Planetary Science Letters, 195(1): 45-58.

33. Mainprice, D., 2007. Seismic anisotropy of the deep Earth from a mineral and rock physics perspective, Treatise Geophys., 2, 437–491, doi: 10.1016, B978-044452748-6.00045-6.

34. Mainprice, D., Bachmann, F., Hielscher, R. and Schaeben, H., 2014. Descriptive tools for the analysis of texture projects with large datasets using MTEX: strength, symmetry and components. Geological Society, London, Special Publications, 409(1): 251-271.

35. Matsui, M. and Busing, W.R., 1984. Calculation of the elastic constants and high-pressure properties of diopside, $CaMgSi_2O_6$. American Mineralogist, 69.

36. Michibayashi, K., Mainprice, D., Fujii, A., Uehara, S., Shinkai, Y., Kondo, Y., Ohara, Y., Ishii, T., Fryer, P., Bloomer, S.H., Ishiwatari, A., Hawkins, J.W. and Ji, S., 2016. Natural olivine crystal-fabrics in the western Pacific convergence region: A new method to identify fabric type. Earth and Planetary Science Letters, 443: 70-80.

37. Michibayashi, K., Oohara, T., Satsukawa, T., Ishimaru, S., Arai, S. and Okrugin, V.M., 2009. Rock seismic anisotropy of the low-velocity zone beneath the volcanic front in the mantle wedge. Geophysical Research Letters, 36(12).

38. Navon, O. and Stolper, E., 1987. Geochemical consequences of melt percolation: the upper mantle as a chromatographic column. The Journal of Geology, 95(3): 285-307.

39. Niu, Y., 2004. Bulk-rock Major and Trace Element Compositions of Abyssal Peridotites: Implications for Mantle Melting, Melt Extraction and Post-melting

Processes Beneath Mid-Ocean Ridges. Journal of Petrology, 45(12): 2423-2458.

40. Ntaflos, T., Bizimis, M. and Abart, R., 2017. Mantle xenoliths from Szentbékálla, Balaton: Geochemical and petrological constraints on the evolution of the lithospheric mantle underneath Pannonian Basin, Hungary. Lithos, 276: 30-44.

41. Ohuchi, T., Kawazoe, T., Nishihara, Y., Nishiyama, N. and Irifune, T., 2011. High pressure and temperature fabric transitions in olivine and variations in upper mantle seismic anisotropy. Earth and Planetary Science Letters, 304(1-2): 55-63.

42. Passchier, C.W. and Trouw, R.A., 2005. Microtectonics. Springer Science & Business Media.

43. Pouchou, J.-L. and Pichoir, F., 1991. Quantitative analysis of homogeneous or stratified microvolumes applying the model "PAP", Electron probe quantitation. Springer, pp. 31-75.

44. Précigout, J. and Hirth, G., 2014. B-type olivine fabric induced by grain boundary sliding. Earth and Planetary Science Letters, 395: 231-240.

45. Qi, C., Hansen, L.N., Wallis, D., Holtzman, B.K. and Kohlstedt, D.L., 2018. Crystallographic Preferred Orientation of Olivine in Sheared Partially Molten Rocks: The Source of the "a-c Switch". Geochemistry, Geophysics, Geosystems, 19(2): 316-336.

46. Skemer, P., Katayama, I. and Karato, S.-i., 2006. Deformation fabrics of the Cima di Gagnone peridotite massif, Central Alps, Switzerland: evidence of deformation at low temperatures in the presence of water. Contributions to Mineralogy and Petrology, 152(1): 43-51.

47. Sun, S.s. and McDonough, W.F., 1989. Chemical and isotopic systematics of oceanic basalts: implications for mantle composition and processes. Geological Society, London, Special Publications, 42(1): 313-345.

48. Sundberg, M. and Cooper, R.F., 2008. Crystallographic preferred orientation produced by diffusional creep of harzburgite: Effects of chemical interactions among phases during plastic flow. Journal of Geophysical Research: Solid Earth, 113(B12).

49. Tasaka, M., Michibayashi, K. and Mainprice, D., 2008. B-type olivine fabrics developed in the fore-arc side of the mantle wedge along a subducting slab. Earth and Planetary Science Letters, 272(3-4): 747-757.

50. Tommasi, A., Baptiste, V., Vauchez, A. and Holtzman, B., 2016. Deformation, annealing, reactive melt percolation, and seismic anisotropy in the lithospheric mantle beneath the southeastern Ethiopian rift: Constraints from mantle xenoliths from Mega. Tectonophysics, 682: 186-205.

51. Tommasi, A., Vauchez, A. and Ionov, D.A., 2008. Deformation, static recrystallization, and reactive melt transport in shallow subcontinental mantle xenoliths (Tok Cenozoic volcanic field, SE Siberia). Earth and Planetary Science Letters, 272(1-2): 65-77.

52. Tunini, L., Jiménez-Munt, I., Fernandez, M., Vergés, J., Villaseñor, A., Melchiorre, M. and Afonso, J.C., 2016. Geophysical-petrological model of the crust and upper mantle in the India-Eurasia collision zone. Tectonics, 35(7): 1642-1669.

53. van Hinsbergen, D.J., Lippert, P.C., Dupont-Nivet, G., McQuarrie, N., Doubrovine, P.V., Spakman, W. and Torsvik, T.H., 2012. Greater India Basin hypothesis and a two-stage Cenozoic collision between India and Asia. Proceedings of the National Academy of Sciences, 109(20): 7659-64.

54. Vauchez, A. and Garrido, C.J., 2001. Seismic properties of an asthenospherized lithospheric mantle: constraints from lattice preferred orientations in peridotite from the Ronda massif. Earth & Planetary Science Letters, 192(2): 235-249.

55. Vonlanthen, P., Kunze, K., Burlini, L. and Grobety, B., 2006. Seismic properties of the upper mantle beneath Lanzarote (Canary Islands): Model predictions based on texture measurements by EBSD. Tectonophysics, 428(1-4): 65-85.

56. Walter, M.J., 1998. Melting of garnet peridotite and the origin of komatiite and depleted lithosphere. Journal of Petrology, 39(1): 29-60.

57. Wood, B.J. and Banno, S., 1973. Garnet-orthopyroxene and orthopyroxene-clinopyroxene relationships in simple and complex systems. Contributions to mineralogy and petrology, 42(2): 109-124.

58. Yang, Y., Abart, R., Yang, X., Shang, Y., Ntaflos, T. and Xu, B., 2019. Seismic anisotropy in the Tibetan lithosphere inferred from mantle xenoliths. Earth and Planetary Science Letters, 515: 260-270.

59. Zhang, H., Zhao, J., Zhao, D., Yu, C., Liu, H. and Hu, Z., 2016. Complex deformation in western Tibet revealed by anisotropic tomography. Earth and Planetary Science Letters, 451: 97-107.

60. Zhang, J., Greenii, H. and Bozhilov, K., 2006. Rheology of omphacite at high temperature and pressure and significance of its lattice preferred orientations. Earth and Planetary Science Letters, 246(3-4): 432-443.

61. Zhang, P.-F., Zhou, M.-F., Robinson, P.T., Pearce, J.A., Malpas, J., Liu, Q.-Y. and Xia, X.-P., 2019. Evolution of nascent mantle wedges during subduction initiation: Li-O isotopic evidence from the Luobusa ophiolite, Tibet. Geochimica et Cosmochimica Acta, 245: 35-58.

62. Zhao, J., Yuan, X., Liu, H., Kumar, P., Pei, S., Kind, R., Zhang, Z., Teng, J., Ding, L., Gao, X., Xu, Q. and Wang, W., 2010. The boundary between the Indian and Asian tectonic plates below Tibet. Proceedings of the National Academy of Sciences, 107(25): 11229-11233.

63. Zhao, W., Kumar, P., Mechie, J., Kind, R., Meissner, R., Wu, Z., Shi, D., Su, H., Xue, G., Karplus, M. and Tilmann, F., 2011. Tibetan plate overriding the Asian plate in central and northern Tibet. Nature Geoscience, 4(12): 870-873.

64. Zhao, Y.-H., Ginsberg, S.B. and Kohlstedt, D.L., 2004. Solubility of hydrogen in olivine: dependence on temperature and iron content. Contributions to Mineralogy and Petrology, 147(2): 155-161.

65. ZHENG, H.W., LI, T.D., GAO, R., ZHAO, D.P. and HE, R.Z., 2007. Teleseismic P‑Wave Tomography Evidence for the Indian Lithospheric Mantle Subducting Northward Beneath the Qiangtang Terrane. Chinese Journal of Geophysics, 50(5): 1223-1232.

Supplementary

Supplementary 3A contain major element compositions of minerals in Ejumaima mantle xenoliths, mineral model composition, and trace elements of pyroxene.

Supplementary 3A-Table 1: Major elements of xenoliths from Ejumaima, Tibet

Sample	Mineral	Major												Total	Mg#
		SiO2	TiO2	Al2O3	FeOt	MnO	MgO	CaO	Na2O	K2O	Cr2O3	NiO		
T16-57	OL	41.28	0.02	0.03	8.88	0.13	50.20	0.06	0.02	0.02	0.00	0.37	101.00	91.05
	OPX	55.67	0.06	3.39	5.68	0.13	33.81	0.79	0.11	0.00	0.69	0.06	100.39	91.47
	CPX	52.97	0.29	4.45	2.78	0.04	16.88	19.32	1.48	0.01	1.43	0.00	99.65	91.61
T16-45	OL	40.53	0.02	0.02	11.93	0.13	47.70	0.07	0.01	0.00	0.01	0.38	100.79	87.80
	OPX	54.51	0.27	4.78	7.42	0.14	32.18	0.74	0.11	0.00	0.33	0.11	100.60	88.64
	CPX	52.99	0.38	2.89	4.35	0.10	18.44	19.62	0.31	0.01	0.69	0.06	99.84	88.42
T16-31	OL	38.58	0.02	0.04	20.55	0.36	40.18	0.20	0.02	0.02	0.03	0.14	100.14	77.87
	OPX	53.10	0.36	2.88	14.28	0.27	27.40	1.57	0.06	0.01	0.12	0.03	100.10	77.55
	CPX	50.85	0.80	3.91	8.65	0.21	15.23	18.56	0.70	0.00	0.16	0.02	99.10	76.03

Supplementary

Sample	Mineral	Major												
		SiO2	TiO2	Al2O3	FeOt	MnO	MgO	CaO	Na2O	K2O	Cr2O3	NiO	Total	Mg#
T16-35	OPX	53.05	0.35	3.12	14.02	0.27	27.27	1.61	0.11	0.00	0.16	0.07	100.02	77.78
	CPX	50.54	0.95	4.51	8.29	0.20	15.25	18.63	0.62	0.00	0.19	0.01	99.19	76.81
T16-48-1	OPX	53.35	0.36	2.62	14.58	0.28	26.71	1.54	0.06	0.01	0.13	0.03	99.65	76.73
	CPX	51.28	0.74	3.66	7.97	0.18	15.29	19.74	0.61	0.00	0.31	0.02	99.80	77.54
T16-48-2	OPX	53.20	0.29	1.95	15.40	0.29	26.48	1.51	0.06	0.01	0.09	0.02	99.30	75.58
	CPX	50.37	0.74	3.66	8.37	0.20	15.12	19.72	0.62	0.00	0.31	0.04	99.16	76.48
T16-49	OPX	53.62	0.34	2.67	14.72	0.27	26.58	1.53	0.06	0.01	0.13	0.03	99.96	76.47
	CPX	51.01	0.70	3.58	8.48	0.22	14.96	19.50	0.64	0.00	0.20	0.02	99.30	76.06

New evidence for a heterogeneous lithospheric structure in central Tibet: implications for the Indian-Eurasian collision

Sample	Mineral	Atoms per formula units											
		Si	Ti	Cr	Al	Fe	Mn	Ni	Mg	Ca	Na	K	Total
T16-57	OL	0.998	0.000	0.000	0.001	0.180	0.003	0.007	1.809	0.002	0.001	0.001	3.000
	OPX	1.910	0.002	0.019	0.137	0.162	0.004	0.002	1.728	0.029	0.007	0.000	4.000
	CPX	1.915	0.008	0.041	0.190	0.084	0.001	0.000	0.909	0.748	0.104	0.000	4.000
T16-45	OL	0.995	0.000	0.000	0.001	0.245	0.003	0.008	1.746	0.002	0.000	0.000	3.000
	OPX	1.880	0.007	0.009	0.194	0.214	0.004	0.003	1.654	0.027	0.008	0.000	4.000
	CPX	1.925	0.010	0.020	0.124	0.132	0.003	0.002	0.998	0.764	0.022	0.001	4.000
T16-31	OL	0.994	0.000	0.001	0.001	0.443	0.008	0.003	1.543	0.006	0.001	0.000	3.000
	OPX	1.902	0.010	0.004	0.122	0.428	0.008	0.001	1.462	0.060	0.004	0.000	4.000
	CPX	1.891	0.022	0.005	0.171	0.269	0.007	0.001	0.844	0.740	0.051	0.000	4.000
T16-35	OPX	1.900	0.009	0.005	0.132	0.419	0.008	0.002	1.455	0.062	0.008	0.000	4.000
	CPX	1.877	0.026	0.006	0.197	0.257	0.006	0.000	0.844	0.741	0.045	0.000	4.000
T16-48-1	OPX	1.925	0.010	0.004	0.111	0.440	0.008	0.001	1.437	0.059	0.004	0.000	4.000
	CPX	1.893	0.021	0.009	0.159	0.246	0.006	0.001	0.841	0.781	0.044	0.000	4.000
T16-48-2	OPX	1.932	0.008	0.003	0.084	0.468	0.009	0.001	1.433	0.059	0.004	0.000	4.000

Supplementary

Sample	Mineral	Atoms per formula units												
		Si	**Ti**	**Cr**	**Al**	**Fe**	**Mn**	**Ni**	**Mg**	**Ca**	**Na**	**K**	**Total**
	CPX	1.873	0.021	0.009	0.160	0.260	0.006	0.001	0.838	0.786	0.045	0.000	4.000
T16-49	OPX	1.932	0.008	0.003	0.084	0.468	0.009	0.001	1.433	0.059	0.004	0.000	4.000
	CPX	1.873	0.021	0.009	0.160	0.260	0.006	0.001	0.838	0.786	0.045	0.000	4.000

Supplementary 3A-Table 2: Temperature of Ejumaima xenoliths from two-pyroxene geo-thermobarometer:

Sample	T (°C)				
	TP(08)	TT(98)	TBM(85)	TBK(90)	Average
T16-57	1097	1066	1088	1042	1073
T16-45	1138	1139	1150	1149	1144
T16-31	1041	1073	1061	1061	1059
T16-35	1034	1039	1024	1057	1039
T16-48-1	1005	1009	979	993	997
T16-48-2	1019	1011	1017	998	1011
T16-49	1010	1010	993	1004	1004

TP(08): Putirka (2008). Thermometers and Barometers for Volcanic Systems: Reviews in Mineralogy and Geochemistry, v. 69, no. 1, p. 61-120.

TT(98): Taylor, W.R. (1998). An experimental test of some geothermometer and geobarometer formulations for upper mantle peridotites with application to the thermobarometry of fertile lherzolite and garnet websterite. Neues Jahrbuch fur Mineralogie, Abhandlungen 172, 381-408.

TBM(85): Bertrand, P. & Merrier, J.C.C. (1985). The mutual solubility of coexisting ortho- and clinopyroxene: toward an absolute geothermometer for the natural system? Earth and Planetary Science Letters 76, 109-122.

TBK(90): Brey, G.P. & Koehler, T. (1990). Geothermobarometry in four-phase lherzolites II. New thermobarometers, and practical assessment of existing thermobarometers. Journal of Petrology 31, 1353–1378.

Supplementary 3A-Table 3: The end member components of clinopyroxene: Jadeite (Jd), CaTs, CaTi, CrCaTs, diopside + hedenbergite (DiHd), and enstatite + ferrosilite (EnFs) (Putirka, 2008)

Sample	Cpx Components (Cations on the basis of 6 oxygens)								
	Jd	CaTs	CaTi	CrCaTs	DiHd	EnFs	En	Di	total
T16-57	0.104	0.000	0.043	0.020	0.685	0.154	0.141	0.626	1.000
T16-45	0.017	0.046	0.028	0.010	0.724	0.174	0.152	0.633	1.000
T16-31	0.038	0.014	0.044	0.003	0.694	0.213	0.165	0.536	1.000
T16-35	0.044	0.024	0.041	0.002	0.673	0.219	0.168	0.517	1.000
T16-48-1	0.039	0.007	0.061	0.005	0.719	0.181	0.138	0.549	1.000
T16-48-2	0.034	0.000	0.063	0.005	0.718	0.190	0.144	0.545	1.000
T16-49	0.041	0.009	0.045	0.004	0.722	0.186	0.142	0.552	1.000

Supplementary 3A-Table 4: The end member components of orthopyroxene: $NaAlSi_2O_6$, $FmTiAlSiO_6$ (Fm is the sum FeO + MgO), $CrAl_2SiO_6$, $FmAl_2SiO_6$, $CaFmSi_2O_6$, $Fm_2Si_2O_6$ (Putirka, 2008)

Sample	Opx Components (Cations on the basis of 6 oxygens)								
	NaAlSi2O6	FmTiAlSiO6	CrAl2SiO6	FmAl2SiO6	CaFmSi2O6	Fm2Si2O6	En	Di	total
T16-57	0.007	0.002	0.018	0.023	0.029	0.920	0.839	0.027	1.000
T16-45	0.008	0.007	0.009	0.059	0.028	0.890	0.786	0.024	1.000
T16-31	0.006	0.009	0.004	0.018	0.059	0.903	0.702	0.046	1.000
T16-35	0.004	0.009	0.004	0.013	0.060	0.911	0.704	0.046	1.000
T16-48-1	0.004	0.010	0.003	0.034	0.060	0.888	0.677	0.046	1.000
T16-48-2	0.004	0.010	0.004	0.029	0.059	0.894	0.680	0.045	1.000
T16-49	0.004	0.010	0.004	0.019	0.061	0.903	0.679	0.046	1.000

The end member components of orthopyroxene: $NaR_3Si_2O_6$, $NaTiAlSiO_6$, $R_2TiAl_2O_6$, $R_2R_3AlSiO_6$, $Mg_2Si_2O_6$ (Enst), $Fe_2Si_2O_6$, $Mn_2Si_2O_6$, $Ca_2Si_2O_6$ (Wood and Banno, 1973)

Sample	Opx Components (Cations on the basis of 6 oxygens)						X(Fe) OPX	En	Di
	NaR3Si2O6	R2TiAl2O6	R2R3AlSiO6	Enst	Fe2Si2O6	Mn2Si2O6			
T16-57	0.007	0.002	0.087	0.824	0.064	0.002	0.014	0.077	0.839
T16-45	0.008	0.007	0.106	0.778	0.086	0.002	0.013	0.106	0.786
T16-31	0.005	0.010	0.079	0.697	0.177	0.004	0.029	0.211	0.702
T16-35	0.008	0.009	0.082	0.694	0.174	0.004	0.029	0.209	0.704
T16-48-1	0.005	0.010	0.055	0.694	0.203	0.004	0.029	0.229	0.677
T16-48-2	0.004	0.008	0.052	0.695	0.208	0.004	0.029	0.236	0.680
T16-49	0.005	0.009	0.050	0.692	0.211	0.004	0.029	0.235	0.679

133

Supplementary 3A-Table 5: Trace element of xenoliths from Ejumaima

Sample	T16-57		T16-45		T16-31		T16-35		T16-48-1		T16-48-2		T16-49		xenoliths from Lhasa	
Mineral	CPX		CPX		CPX		CPX		CPX		CPX		CPX		CPX	
Position	r	c	r	c	r	c	r	c	r	c	r	c	r	c	r	c
Be	2.08	1.25	0.95	1.27	0.55	0.43	0.38	0.2	0.36	0.48	9.45	5.65	0.48	0.54	1.29	1.04
Sc	46.6	49.1	42.7	38.8	46.1	46.6	45.8	43.1	58.3	60.8	50.2	49	60.36	50.52	37.5	37.5
V	271	275	185	167	293	299	271	253	281	269	311	293	263.29	268.33	212	217
Cr	9834	9739	4832	3142	1359	1191	1399	1558	1681	1722	1322	1201	1085.05	1299.53	4509	4522
Co	22	22.2	31.5	32.4	44.7	48.3	45.7	48	43.4	42.2	43.3	42.2	42.88	41.95	25.5	24.3
Ni	393	405	488	470	107	147	134	168	144	112	99.7	118	100	124.48	413	413
Cu	0.22	3.03	6.6	6.36	3.51	2.42	2.22	6.47	3.76	3.25	8.71	4.13	3.83	1.62	4.13	1.84
Zn	11.7	12.7	29.2	39.3	103	97.1	101	63.9	85.1	89	111	107	104.44	98.7	14.2	14.6
Ga	4.04	4.15	6.21	7.76	11.7	12.7	11.4	10.2	11.5	10.2	12.5	12	11.4	12.05	5.35	5.34
Ge	1.38	0.81	1.56	1.74	1.83	2.06	1.73	2.08	1.75	2.27	1.99	1.95	1.69	1.81	1.91	1.41
Rb	16.4	4.97	0.11	0.63	0	0.078	0	0.078	0	0.017	60.5	2.88	0	0.03	0	0.035
Sr	146	125	102	126	82.1	94.3	84.3	108	106	98.7	111	126	84.48	93.07	167	176

Supplementary

Sample	T16-57		T16-45		T16-31		T16-35		T16-48-1		T16-48-2		T16-49		xenoliths from Lhasa	
Mineral	CPX		CPX		CPX		CPX		CPX		CPX		CPX		CPX	
Position	r	c	r	c	r	c	r	c	r	c	r	c	r	c	r	c
Y	4.33	4.17	23	20.8	12.5	13.4	12.2	12.4	16	16.5	17.7	16.6	16.29	14.3	11.7	12.2
Zr	47.3	44.8	78	77.7	48.8	53	49.8	40.5	63.6	60.8	188	172	63.09	59.24	81.3	80.9
Nb	4.52	3.88	0.16	0.17	0.12	0.14	0.16	0.16	0.16	0.13	0.68	0.57	0.14	0.15	1.41	1.34
Cs	0.098	0	0.078	0.036	0	0.04	0.0077	0.0065	0.008	0	1.2	0.25	0.01	0.01	0.0013	0
Ba	43.4	6.14	0.8	2.82	0.015	0.057	0.11	0.4	0.1	0.052	3.67	3.18	0.3	0.03	0.24	0.026
La	19.4	19.4	7.72	7.59	5.84	6.75	6.25	5.06	7.12	7.5	84.7	79	7.23	7.15	6.07	6.58
Ce	52.8	54.8	39	39.2	30.9	31	30.1	24.1	27	27.4	248	230	28.88	29.08	36.1	37.8
Pr	7.47	7.21	8.65	8.73	4.82	5.32	4.78	3.92	4.95	5.03	29.6	27.5	5.35	5.07	7.55	7.68
Nd	24.5	22.5	54.4	54.1	22.3	24.5	21.6	19.5	25.2	26	84.9	84.8	26.19	24.99	40	40.1
Sm	3.29	3.41	16.4	16.1	5.24	5.48	5.34	4.82	6.49	6.38	11.6	11.6	6.8	6.02	9.64	9.94
Eu	0.8	0.73	2.74	2.73	1.4	1.65	1.44	1.33	1.77	1.65	2.26	2.35	1.86	1.67	2.19	2.11
Gd	1.91	1.95	11.5	9.29	4.01	4.52	4.12	3.81	5.3	5.18	6.5	6.61	5.41	4.89	6.1	6.07
Tb	0.22	0.2	1.19	1.1	0.56	0.65	0.56	0.55	0.68	0.73	0.86	0.81	0.7	0.65	0.66	0.71
Dy	1.28	1.13	5.86	4.99	3.26	3.48	2.84	2.77	3.8	3.91	4.41	3.95	3.82	3.56	3.06	3.29
Ho	0.17	0.18	0.88	0.79	0.52	0.53	0.47	0.49	0.63	0.66	0.68	0.7	0.65	0.6	0.48	0.51

Sample	T16-57		T16-45		T16-31		T16-35		T16-48-1		T16-48-2		T16-49		xenoliths from Lhasa	
Mineral	CPX		CPX		CPX		CPX		CPX		CPX		CPX		CPX	
Position	r	c	r	c	r	c	r	c	r	c	r	c	r	c	r	c
Er	0.39	0.34	2.25	1.91	1.12	1.24	1.09	1.32	1.49	1.57	1.68	1.61	1.69	1.41	0.98	1
Tm	0.033	0.051	0.26	0.24	0.14	0.18	0.14	0.14	0.18	0.18	0.22	0.21	0.2	0.15	0.12	0.1
Yb	0.2	0.21	1.39	1.32	1.04	0.96	0.95	0.85	1.05	1.03	1.38	1.28	1.1	0.97	0.67	0.66
Lu	0.032	0.024	0.19	0.18	0.13	0.11	0.11	0.12	0.16	0.14	0.19	0.13	0.16	0.13	0.084	0.074
Hf	1.51	1.64	3.26	3.51	1.65	1.91	1.71	1.47	2.1	2.45	5.68	4.86	2.42	2.05	1.8	1.81
Ta	0.91	0.82	0.02	0.025	0.011	0.017	0.019	0.032	0.025	0.019	0.13	0.067	0.01	0.01	0.41	0.38
Pb	0.313	0.2288	0.5839	0.901	0.2555	0.254	0.271	0.2422	0.254	0.2939	0.622	0.37	0.3	0.29	1.604	1.603
Th	15.7	13	0.91	1.08	0.057	0.053	0.047	0.039	0.063	0.054	31.8	6.83	0.07	0.06	0.98	1.01
U	0.9	0.48	0.13	0.13	0.012	0.0087	0.0079	0.013	0.0098	0.0066	1.24	0.31	0.01	0.01	0.12	0.12

Supplementary 3A-Table 6: Variation of mineral modal composition and the corresponding fabric of samples with equilibration depth

T(°C)	P(GPa)	D(KM)	Model			Fabric
			Ol	CPX	OPX	
850	**1.74**	**62**	0	95	5	T16-48-1 & T16-49 (Pyroxenite)
			0	90	10	
900	**1.91**	**68**	0	95	5	
			0	90	10	
950	**2.13**	**75**	0	95	5	T16-48-1 & T16-49 (Pyroxenite)
			0	90	10	
			0	80	20	T16-48-1 & T16-49 & T16-48-2 & T16-35 (Pyroxenite)
			0	70	30	
			0	60	40	T16-48-2 & T16-35 (Pyroxenite)
—	**—**	**—**	5	80	15	T16-31 (Olivine-bearing pyroxenite)
1000	**2.28**	**80(MOHO)**	60	20	20	T16-45 & T16-57 (Peridotite from the Qiangtang terrane)
			70	15	15	
			80	10	10	
			70	5	25	T16-150 & T16-170 (Peridotite from the Lhasa terrane)

			Sample
75	5	20	T16-48-2 & T16-35 (Pyroxenite)
80	5	15	
0	70	30	T16-31 (Olivine-bearing pyroxenite)
0	60	40	
5	80	15	
60	20	20	T16-45 & T16-57 (Peridotite from the Qiangtang terrane)
70	15	15	
80	10	10	
70	5	25	T16-150 & T16-170 (Peridotite from the Lhasa terrane)
75	5	20	
80	5	15	
60	20	20	T16-45 & T16-57 (Peridotite from the Qiangtang terrane)
70	15	15	
80	10	10	
70	5	25	T16-150 & T16-170 (Peridotite from the Lhasa terrane)
75	5	20	
80	5	15	

1050	2.60	90
1100	2.92	100
—	—	—
1150	3.56	120

Supplementary 3A-Table 7: Mineral model composition for xenoliths

Sample	Mineral Model Composition		
	Ol	CPX	OPX
T16-57	80	10	10
T16-45	60	20	20
T16-31	5	80	15
T16-35	0	60	40
T16-48-1	0	95	5
T16-48-2	2	88	10
T16-49	0	90	10

New evidence for a heterogeneous lithospheric structure in central Tibet: implications for the Indian-Eurasian collision

Chapter 3

Supplementary 3A-Table 8: Variation of samples with depth in two terranes for velocity structure modelling

	Lhasa	Qiangtang
D(KM)		
60 **|** **70**	T16-48-1 & T16-49 (Pyroxenite)	
70 **|** **80(MOHO)**	T16-48-2 & T16-35 (Pyroxenite) T16-31 (Olivine-bearing pyroxenite)	
90 **|** **110**	T16-150 & T16-170 (Peridotite from the Lhasa terrane)	T16-57 (Peridotite from the Qiangtang terrane)
110 **|** **130**		T16-45 (Peridotite from the Qiangtang terrane)

Supplementary 3A-Information: The references of crystal elastic tensor and density we cited

We employed the elastic constants of Abramson (1997) for olivine and the first- and second-order pressure derivatives by the same authors, and first-order temperature derivatives of Isaak (1992). For orthopyroxene, we used the elastic constants and first- and second-order pressure derivatives of Chai (1997) and first-order temperature derivatives of Frisillo and Barsch (1972). For clinopyroxene, we used the elastic constants and first- and second-order pressure derivatives of Matsui and Busing (1984) and first-order temperature derivatives of Isaak (2005).

According to the mineral modal composition (Supplementary 3A-Table 7), we set a resendable range for lithosphere from lower crust to upper mantle (Supplementary 3A-Table 6). The velocity structure modelling is based on this premise (Supplementary 3A-Table 8).

Supplementary 3B include trace element figure of clinopyroxene from Ejumaima. The pole figures and seismic properties in additional samples of the peridotite xenoliths.

Supplementary 3B-Figure 1.
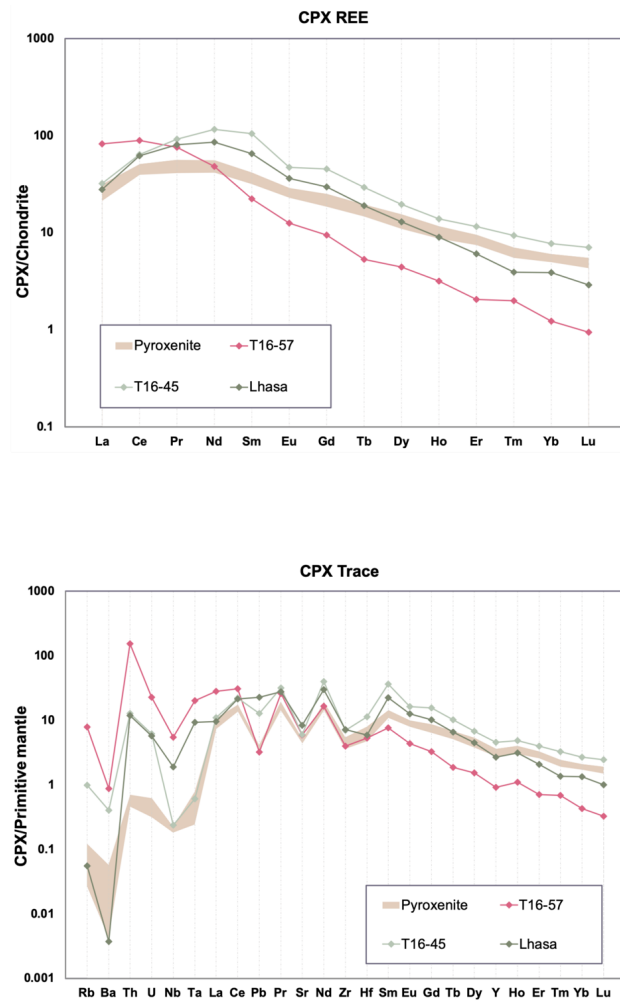
Supplementary Figure 3B-1. Rare earth elements (REE) and Trace element compositions of clinopyroxene from Ejumaima and Lhasa mantle xenoliths normalized to Cl chondrite（Anders and Grevesse, 1989）and primitive mantle (Sun and McDonough, 1989) respectively.

Supplementary 3B-Figure 2.
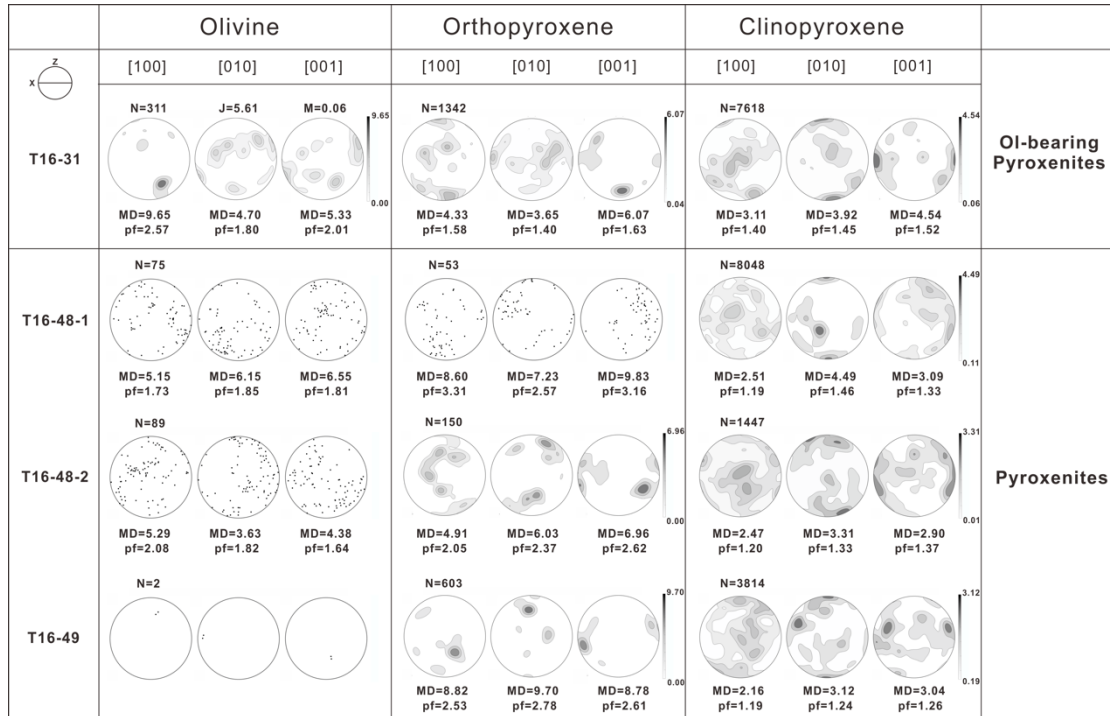
Supplementary 3B-Figure 2. The pole figures for the crystallographic axes of olivine, orthopyroxene and clinopyroxene in xenoliths from Sailipu. The CPOs are presented in equal-area, one point per grain, lower-hemisphere projections; the structural reference frame is shown as insert in the upper left. Contours (=6) show multiples of uniform distribution. N is the number of measurements, J-index and M-index is the fabric strength, pf is an index of fabric intensity, and MD is the maximum density.

New evidence for a heterogeneous lithospheric structure in central Tibet: implications for the Indian-Eurasian collision

Chapter 3

Supplementary 3B-Figure 3.
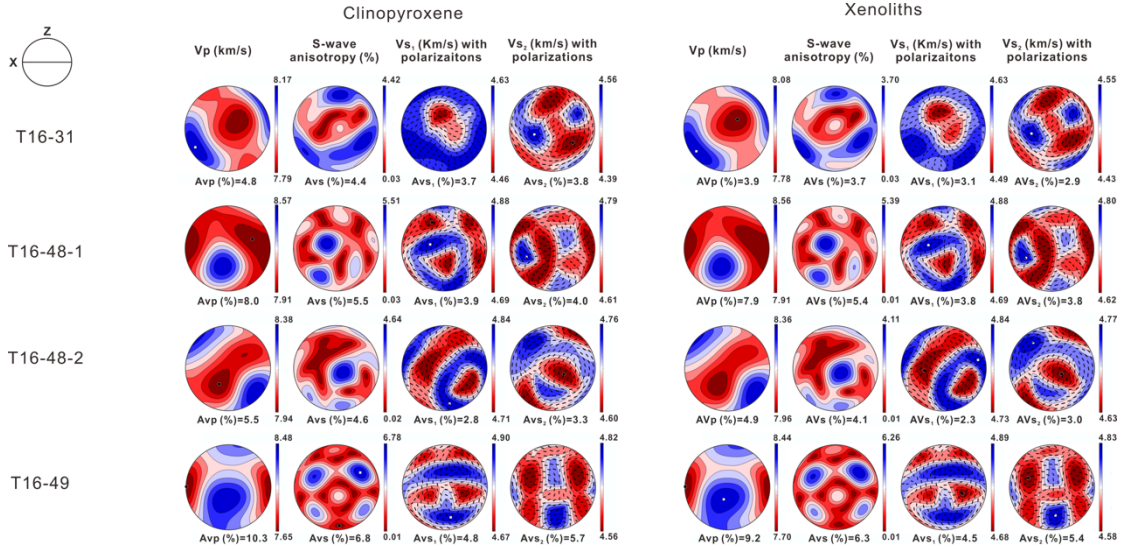
Supplementary 3B-Figure 3 The seismic properties of the peridotite xenoliths in Ejumaima calculated from the fabric of the xenoliths. The seismic properties are presented in equal-area, lower-hemisphere projections in the structural reference frame. The four columns are the P-wave velocity (Vp) with anisotropy of the P-waves (AVp); the polarization anisotropy (AVs) and the splitting S-wave velocity (Vs_1 and Vs_2) with their polarization directions. $AVp = [(Vp^{max} - Vp^{min}) / (Vp^{max} + Vp^{min}) /2] \times 100\%$ and $AVs = [(Vs_1 - Vs_2)]/[(Vs_1 + Vs_2)/2]$, where Vs_1 and Vs_2 are the velocities of the fast and slow split S-waves, respectively. $AVs_{1/s2} = [(Vs_{1/s2}^{max} - Vs_{1/s2}^{min}) / (Vs_{1/s2}^{max} + Vs_{1/s2}^{min}) / 2]$; insert on the middle left shows the structural reference frame.

Supplementary 3B-Figure 4.
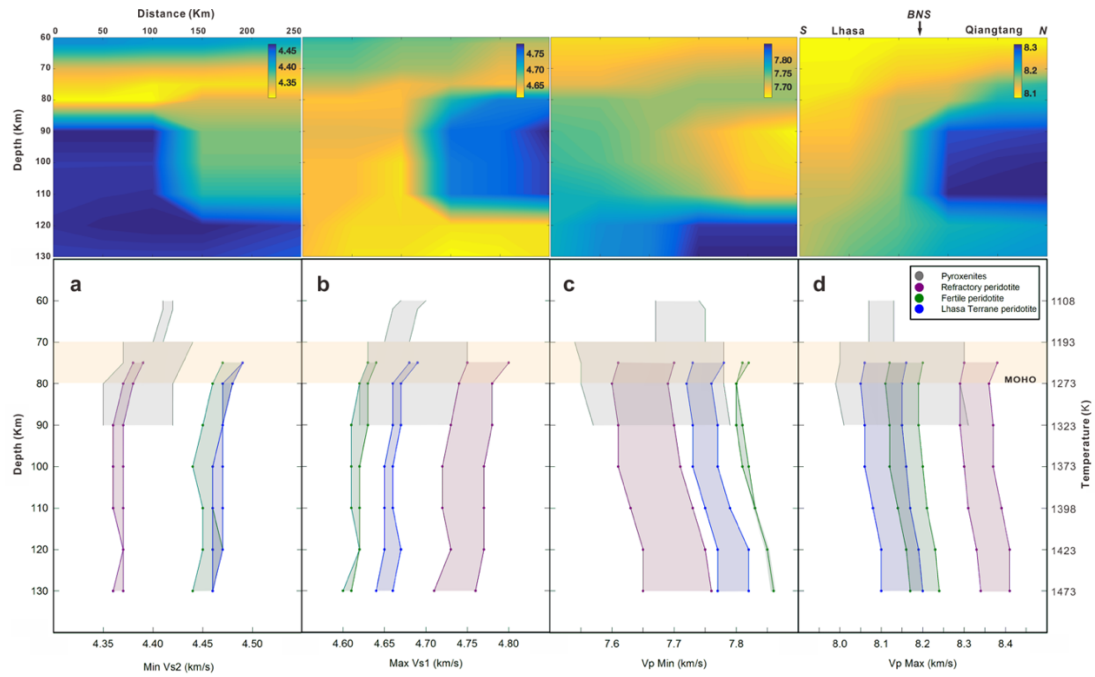
Supplementary 3B-Figure 4 Variation in seismic velocity components and corresponding velocities models with equilibration depth (cf. Fig.3-4). (a) Minimum Vs2 wave velocity (b) Maximin Vs1 wave velocity (c) Minimum P wave (Vpmin) velocity (d) Maximin P wave (Vpmax) velocity.

Chapter 4

我要看看在这片寸草不生的沙漠里，人们
为什么同样能有生命的喜悦和爱憎。

—— 《撒哈拉的故事》
三毛

Insight into the seismic anisotropy beneath northeastern Tibetan from mantle xenoliths

Highlights

- We revealed the crystal preferred orientation of mantle xenoliths in the NETP and its anisotropy.

- High instinct seismic anisotropy of mantle beneath the NETP is well explain large delay time observed in this region.

- No other mechanism is required for anisotropy explanation.

Abstract

The Northeastern Tibetan Plateau is characterized by pronounced shear-wave splitting, which produces delay times of ~1.5s between the arrival times of teleseismic shear waves (SKS) with fast and slow polarization direction. Traditionally, this has been interpreted based on the assumption of A-type olivine fabric in the lithospheric mantle which typically leads to about 4% seismic anisotropy. This anisotropy is too small for explaining the observed delay times given a 70 km maximum thickness of the lithospheric mantle as indicated by geophysical data. Thus, alternative mechanisms invoking complicated deformation patterns were suggested. Here we present fabric evidence from peridotite xenoliths from the NE margin of the Tibetan plateau, which provide new insights into the seismic anisotropy of the subcontinental mantle in this region. The olivine fabric of these peridotites is mainly of AG-type, which is characterized by a concentration of the [010]-directions perpendicular to the foliation plane and large circle girdles of the [100]- and [001]-directions in the foliation plane. Only rarely A-type fabric occurs, which is also characterized by [010]-directions clustering perpendicular to the foliation plane and in addition shows maxima of [100] and [001] directions in the foliation plane. For the peridotites with AG-type olivine fabric an average anisotropy of 8 % for the shear wave splitting was calculated, which can account for delay times of 1.16s over a 70 km thick anisotropic layer. In combination with a crustal anisotropy contribution of ~0.5s this anisotropy can explain the observed delay times and no other mechanism needs to be involved. An important and interesting reference from the AG-type olivine fabric detected here is that the lithosphere beneath the NE Tibetan Plateau is undergoing shear deformation with vertical shear plane predominantly, which is associated with asthenosphereic upwelling and eastward escape.

4.1 Introduction

The northeastern Tibetan Plateau (NETP) is a tectonically active region at the junction of the South China- and the North China cratons. This area is subject to active eastward expansion (Yu and Chen, 2016), whereby the displacement of the NETP is slow compared to but intimately linked with the India-Eurasian convergence, which is active some 1000 km further south (Huang et al., 2017). The adjacent South China- and North China cratons including the Alxa- and Ordos Block act as strong obstacles to a northeastward movement of the plateau and deflect the lithosphere-scale translation from the original S-N collision direction (Fig. 4-1). As a result, the junction region has undergone complex deformation (Li et al., 2018b), whereby the coupling between different levels of the lithospheric column is still poorly understood.

Most of the insight into the structure of the sub-cratonic lithosphere beneath the NETP was obtained from geophysical investigations. SKS shear wave splitting yields large delay times, which are consistently high at δt = 1.5s over large areas with the fast polarization direction (FPD) persistently trending 120° SE-NW (Huang et al., 2017) (Fig. 4-1). The results from analyzing receiver functions and surface wave tomography indicate a low-velocity zone (LVZ) and high Poisson's ratios in the mid-lower crust which has been interpreted as an indication of partial melting (Wang et al., 2017a; Wei et al., 2017). GPS and levelling measurements revealed strain partitioning and showed that in the NETP the fastest uplift regions do not coincide with those of the strongest convergence (Li et al., 2018b). Three main geodynamic models have been proposed to explain the complex situation. (1) Lower crustal flow was inferred from the low seismic velocities and was invoked to explain the spatial dichotomy between the domains of strongest convergence and highest uplift rates (Li et al., 2018b; Wei et al., 2017). (2) The P- and S-wave velocity structures and an azimuthal anisotropy that is consistent over the entire lithospheric column corroborate vertically coherent lithospheric deformation (Chang et al., 2017; Deng et

al., 2018; Pandey et al., 2015). (3) A model of asthenospheric flow leading to an exceedingly thick anisotropic layer is supported by the large delay times and low-gravity anomalies (Bi et al., 2016; Yu and Chen, 2016). The currently discussed models for the NETP include mutually incompatible hypotheses, where in some models the motion of the lithospheric mantle and the crust are coupled (Chen and Gerya, 2016) and in other models they are decoupled (Li et al., 2018b). Asthenospheric flow seems to be compatible with either one of these presumptions, and it is invoked as a supplementary contribution to large delay times (Huang et al., 2017). In summary, the available models do not provide a coherent framework for integrating the perplexing observations made in the NETP, and basic questions regarding the deformation and evolution of the sub-cratonic lithosphere remain unanswered.

Textural features such as grain-internal strain and crystal preferred orientation (CPO) of the constituent minerals of the lithospheric mantle provide direct information about the conditions and the mechanisms of deformation (Miyazaki et al., 2013). The CPO of minerals in the upper mantle is of key importance for deciphering lithospheric deformation and in the interpretation of seismic anisotropy. Generally speaking, the anisotropy of the lithosphere is mainly due to the CPO of its major constituent minerals. Olivine and pyroxene are the volumetrically by far dominant phases in the upper mantle, and their fabrics largely control the seismic properties including lithospheric anisotropy (Mainprice, 2007). On the other hand, dedicated deformation experiments showed that the olivine and pyroxene fabrics depend on the conditions, rates and mechanisms of mantle deformation (Mainprice, 2007). The olivine fabrics have been categorized into six types, referred to as A-, B-, C-, D-, E- and AG-type (Mainprice, 2007). All of these fabric types may occur in mantle peridotites leading to different seismic properties of the lithospheric mantle.

In this paper, we present new petrographic and fabric information from mantle

xenoliths collected in the NETP. Based on fabric data, we calculate the seismic properties of the xenoliths, constrain on the generation of the mantle anisotropy and make inferences with respect to the lithospheric deformation in the NETP. Finally, a new model of the lithospheric architecture is proposed that accounts for the deep seismic observations.
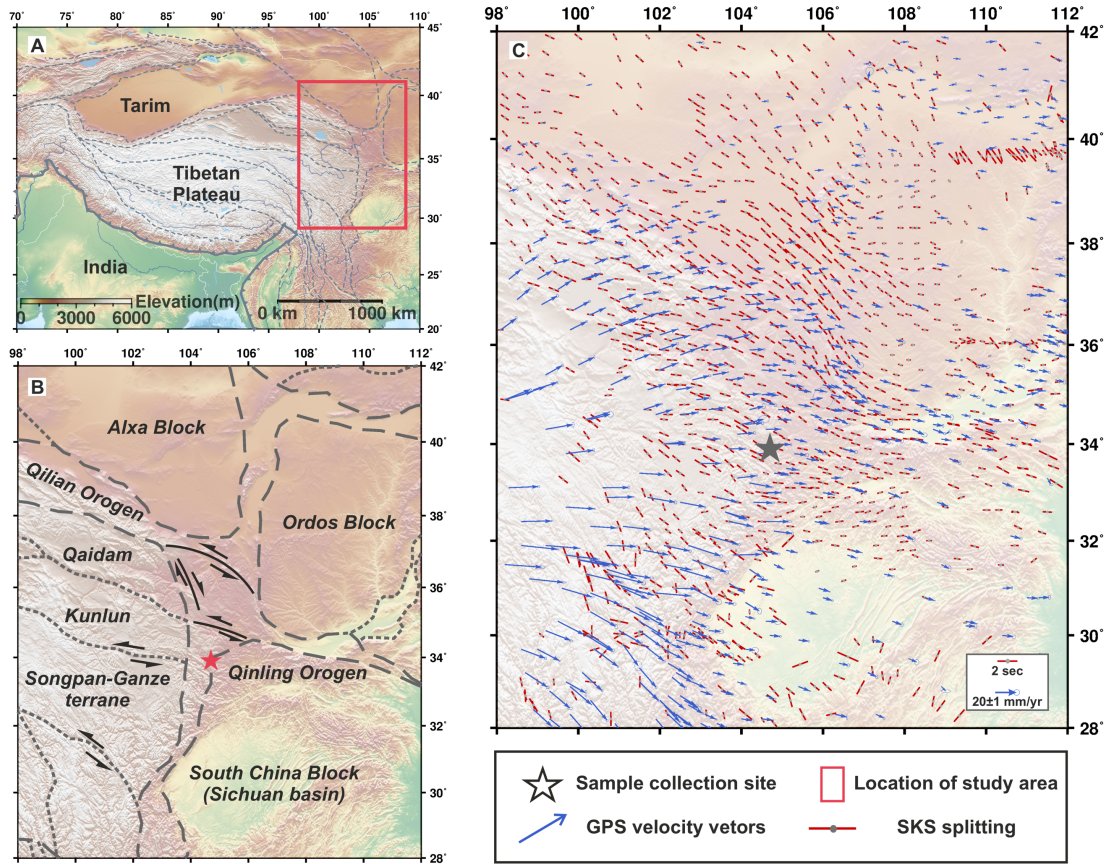
Fig 4-1. (A) Sketch of the tectonic setting in and around the Tibetan plateau. (B) Close up of the study area as indicated by the red frame in (A). (C) Average splitting parameters including fast polarization direction (FPD) and delay time of SKS wave splitting in northeastern Tibet. The orientations and lengths of the red bars indicate the FPDs and splitting delay times, respectively. The blue arrows display GPS velocity vectors calculated with respect to the Eurasian-fixed reference frame (Liang et al., 2013). The star represents the sampling location.

4.2 Geological and Geophysical Background

The NETP is connected to the westernmost part of the E-W trending Qinling orogen, one of the most important orogenic belts in China (Fig. 4-1). In the junction area, a series of alkaline and ultra-mafic volcanic pipes with ages ranging from 7.1 to 23 Ma (Su et al., 2010) are distributed within tens of kilometers. In this study, we focus on the Haoti pipes (33°59'4" N, 104°54'4" E), where mantle xenoliths are hosted by dark grey kamafugite, with an ^{40}Ar-^{39}Ar radiometric age of 18 Ma (Yu et al., 2006).

The study area is characterized by pronounced shear-wave splitting (Fig. 4-1C). Seismic waves that penetrate the Earth's core and propagate from the core-mantle boundary (CMB) upwards in radial direction, including SKS (S converted to P when entering the core and P converted to S when leaving the core), SKKS (P reflected once from the inner side of CMB and converted to S at the CMB) or PKS (P converted to S at the CMB) waves, are very well suited for measuring the anisotropy of the mantle and the crust (Silver, 1996). When such P-to-S converted SKS waves propagate through an anisotropic region between the CMB and the receiver, they split into two orthogonal waves with different propagation velocities referred to as the waves of the fast and the slow polarization directions. Here, a total of 1440 broadband stations from the open access "Splitting Database" (Wüstefeld et al., 2008) were used for SK(K)S splitting analysis. In the study area, the splitting time delays are in the range of 1.16-1.8s, with an average delay time of 1.5s. It decreases to ~0.8s on average in the Ordos Block and to ~0.9s in the South China Block (Fig. 4-1C). In the NETP and in the western Qinling, the FPD is mainly near 120°, which is subparallel to the strike of faults and mountain ranges. In the Southeastern Tibetan Plateau, the South China Block and the Ordos Block, the FPDs rotate into an NNE-SSW direction (Fig. 4-1C). The anisotropy contributed by the crust could be estimated from the analysis of P_ms waves, which are the waves that are P-to-S converted at the Moho.

The inferred bulk crustal anisotropy contributes about 0.4s to the delay time of split SKS waves in the NETP (Kong et al., 2016).

Along a NE-SW transect, the thickness of lithosphere changes from ~140 km under the Alxa- and Ordos cratonic blocks to 110 km beneath the NETP including the Songpan-Ganze terranes in the west and the western Qinling in the east. The lithospheric mantle beneath the western Qinling has similar thickness, but due to a ~15km reduced Moho depth it accounts for a higher proportion in lithosphere than in the Songpan-Ganze terranes (Zheng et al., 2019). Crustal low-velocity zones (LVZs) appear in all blocks at a depth of ~20-40km. An upper mantle LVZ only exists beneath the NETP, whereas the upper mantle of the surrounding cratonic blocks represents a high velocity zone. It is noteworthy that in the junction area between the cratonic blocks and the NETP, a high S-wave velocity zone is located directly above the LVZs (Deng et al., 2018).

Combining GPS observations with SKS splitting data in block scale allows to discriminate between coupled and decoupled deformation of the lithosphere (León Soto et al., 2012). Here, GPS data collected at 569 stations in the time from 1999 to 2014 are used this study (Zhao et al., 2015). The horizontal velocities decline from the Songpan-Ganze (in the southwest), where they are about 21.0 mm/a, to the Ordos Block (in the northeast) about 3.0 mm/a. The velocities also show a subtle decrease from about 10 mm/a in the NETP to about 7 mm/a in the western Qinling (Fig. 4-1).

4.3 Analytical Methods and Data-Processing

4.3.1 Crystal orientation and texture measurements

Crystal orientation analysis was done by means of SEM-EBSD using a *Zeiss*

EVOMA15 scanning electron microscope (SEM) coupled with a *HKL Nordlys Nano* EBSD detector at the Institute of Geology, China Earthquake Administration, China. Thereby the focus was on the microstructures and textures of the three main minerals in the xenoliths: olivine, orthopyroxene and clinopyroxene. Crystal orientation maps covering the entire xenoliths ($20 - 40$ mm long and $10 - 20$ mm wide) were obtained with 11 µm step size and 25 mm working distance, by using the *Oxford Instruments HKL AZtec* software. Modal composition, grain sizes and shape-preferred orientations were obtained from the maps. The *CHANNEL 5* software was used for noise reduction and for filling missing pixels with at least 8 identical neighbors with similar orientation. The resulting crystal orientation mapping was improved to remove large angular deviation points and to smooth intra-crystalline data using *MTex* (Bachmann et al., 2010; Henry et al., 2017).

The crystal orientation data are displayed in upper hemisphere, equal-area stereographic projections. To prevent over-representation of large grains, pole figures were plotted as one point per grain. Due to the small size of the xenoliths, a foliation or lineation cannot be identified macroscopically. The samples were thus cut in random orientations for the preparation of thin sections. Four different methods are in use for connecting an orthogonal reference system with directions X, Y, Z to mantle xenoliths without obvious macroscopic foliation: (1) If the rotation axes of olivine subgrains and thus the slip direction and the slip plane can be inferred from texture measurement, then the slip direction defines the X-direction and the slip plane defines the X-Y plane of the reference system (Michibayashi et al., 2009; Passchier and Trouw, 2005; Wieser et al., 2020). (2) The spatial distribution of spinel grains as obtained from X-ray tomography, may define a foliation, which is then taken as the X-Y plane and the shape preferred orientation (SPO) of elongated grains defines the X-direction (Chatzaras et al., 2016; Liptai et al., 2019); (3) If present, an orthorhombic texture of olivine may be used to define the reference frame by assigning X to the olivine [100]-axes cluster and Z to the olivine [010] axes cluster, which corresponds to arbitrarily

assigning A-type fabric (Demouchy et al., 2018; Liu et al., 2019b); (4) If present, the texture of diopside, which is known to deform by the [001](010) slip system at mantle P-T condition can be used to define X parallel to [001] and the Z normal to (010) (Amiguet et al., 2009; Yang et al., 2019). In this study, we used elongated olivine grains to mark the lineation and subsequently rotated the datasets in order to have clustering of [001] and [010] of clinopyroxene in the X and Z direction respectively.

The strength of a CPO may be quantified by the J-index, which represents the density distribution of crystallographic orientations (Ismail and Mainprice, 1998). For a random distribution the J-index is unity, and for a single crystal (perfect CPO) the J-index is infinity. The olivine in natural samples of mantle peridotite typically has a J-index in the range of $2 - 25$ with a peak at $5 - 10$. In a similar manner, the intensity of the preferred orientation of crystallographic axes, is described by the pf-index which assumes a value of unity for a random distribution and infinity for a perfect alignment (Michibayashi and David, 2004). The degree of axial symmetry of an orientation distribution may be described by the BA index, which is based on the eigenvalues of the orientation tensors for certain crystallographic directions and 0 < BA < 1 (Mainprice et al., 2014). Any fabric with BA approximately zero has pronounced axial symmetry and thus an important fabric plane perpendicular to the symmetry axis. Any fabric with a BA that is approximately 0.5 does not have axial symmetry and no important fabric plane defined by axial symmetry. The olivine CPO has commonly been classified into three types based on the BA index (Tommasi et al., 2016): (i) A fabric with a BA-index < 0.35, defined by point concentrations of [010] and girdle distributions of [100] is referred to as the AG-type; (ii) A fabric with 0.35 < BA-index < 0.65, defined by point concentrations of all three axis (orthorhombic) is referred to as the A-type; and (iii) A fabric with a BA-index > 0.65, defined by a [100] point concentration and girdle distributions of [010] is referred to as the D-type.

4.3.2 Seismic property analysis

The seismic properties of the xenoliths were calculated following the method of Mainprice and Humbert (1994) using single-crystal elastic constants, mineral densities, modal proportions and CPOs. The modal proportions of olivine, orthopyroxene and clinopyroxene used in the calculations are listed in Table 4-1; the Voigt - Reuss - Hill averaging method was employed (Mainprice et al., 2015). The results are displayed in upper hemisphere, equal-area stereographic projections.

Table 4-1 Sample description and calculated results for the Haoti peridotite xenoliths.

Sample		G16-40	G16-20-2	G16-25	G16-48	G16-55
Grains		Coarse	Coarse and Elongated	Coarse and Elongated	Coarse and Elongated	Coarse and Elongated
Modal proportions %	**Ol**	60.1	78.4	92.2	82.1	74.2
	Opx	18.5	9.5	5.8	14.8	16.2
	Cpx	19.8	12	1.7	3.1	9.6
	Sp	1.6	0.1	0.4	0.1	0
Olivine CPO	**CPO**	A	AG	AG	AG	AG
	J	4.32	9.89	6.46	7.66	4.94
	BA	0.7	0.24	0.13	0.1	0.24
	Mean grain size (µm)	227.15	168.17	174.5	196.94	132.32
	Mean M2M(º)	2.87	3.39	3.81	2.65	2.35
Seismic properties	**AV$_p$ (%)**	6.5	12.7	13.93	11.8	9.7
	AV$_s$ (%)	4.7	8.8	10.23	9.4	6.9
	Vp (km/s)	8.33	8.31	8.28	8.24	8.29
	Vs (km/s)	4.83	4.82	4.80	4.81	4.82
T (ºC)		965	1148	1137	1151	1088
Mg# in Ol		90.4	90.6	91.6	88.4	91

Due to the P-T dependence of the single-crystal elastic constants, the resulting bulk rock elastic constants and seismic properties vary with pressures and temperature (Mainprice, 2007; Mainprice et al., 2000). For better correlation between the petrophysical and geophysical properties, the seismic velocities were calculated for a reasonable range of pressures (1.6-2.5 GPa) and temperature (950 - 1200℃) according to the P-T condition derived from the xenoliths (Mainprice et al., 2015).

4.3.3 Mineral chemical analysis

The major-element compositions of olivine, orthopyroxene, clinopyroxene, and spinel were measured using a Cameca SXFive FE Electron Probe Microanalyzer (EPMA) equipped with 5 wavelength- and one energy-dispersive spectrometer at the Department of Lithospheric Research, University of Vienna. An acceleration voltage of 15 kV and a beam current of 20 nA were employed. The counting time was 20 s at the peak position and 10 s on each background position. Natural and synthetic standards were used for calibration. The relative error of the laboratory internal standard is below 1%.

The trace element compositions of clinopyroxene and orthopyroxene were measured using laser ablation inductively coupled plasma mass spectrometry (LA-ICP-MS) (GeoLas 2005 + Agilent 7700x) with a spot size of 44 µm, at State Key Laboratory of Geological Processes and Mineral Resources, China University of Geosciences, Wuhan. Helium was used as a carrier gas, and nitrogen was added into the central gas flow (Ar + He) of the Ar plasma to increase the sensitivity (Hu et al., 2008). The detailed operating conditions for LA-ICP-MS were described previously (Liu et al., 2008). The off-line selection and integration of the background and analytical signals along with time-drift correction and quantitative calibration, were performed by ICPMSDataCal (Liu et al., 2008). The elemental concentrations were calibrated against multiple reference materials (BCR-2G, BHVO-2G and BIR-1G),

and a summed metal oxide normalization was applied (Liu et al., 2008).

4.4 Results

The petrographic and geochemical features of five peridotite xenoliths from the Haoti peridotites are shown in Figure 4-2 and Table 4-1, including the modal proportions of the main constituent minerals, microstructures, the CPO of olivine, and results from geo-thermometry. The chemical compositions of the minerals are presented in Supplementary Tables 4A-1 and 4A-3.
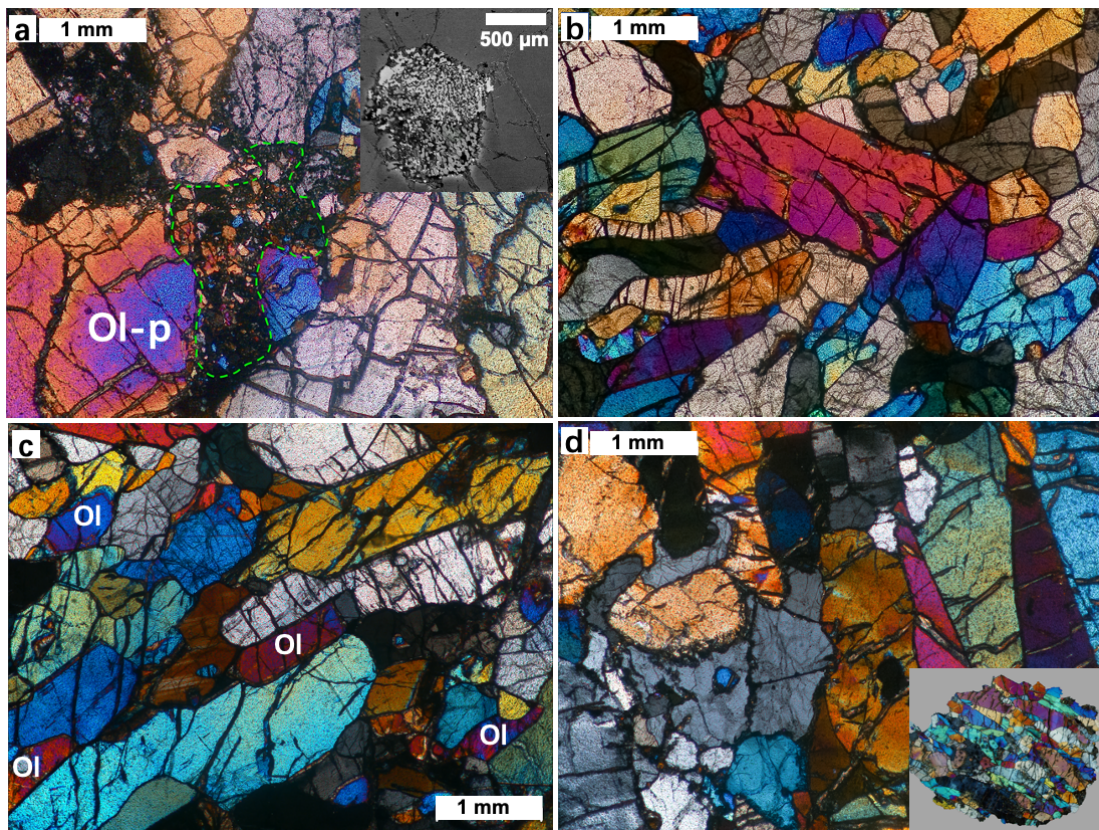
Fig. 4-2 Microphotographs of harzburgite xenoliths from Haoti displaying typical microstructures of the lithospheric mantle in the NETP. (a) Partially recrystallized type: A fine-grained, recrystallized domain is indicated by the green dashed line. The insert shows a back scattered electron image of a melt pocket. (b-c) Sinuous grain boundaries. Irregularly shaped crystals with cusp-like terminations. (d) Elongated crystals with polygonal grain boundaries. Interstitial shapes of pyroxenes. The inserted figure shows

shape preferred orientations on the scale of the whole xenoliths. Mineral abbreviations: Cpx, clinopyroxene; Ol, olivine; Opx, orthopyroxene; Sp, spinel

4.4.1 Petrographic features of the Haoti mantle xenoliths

The Haoti mantle xenoliths are represented by small (1.0-4.0 cm) fragments of dunite (1 piece), harzburgite (2 pieces) and lherzolite (2 pieces) with rounded and elongated shape. They mostly consist of olivine (60–92 vol.%), orthopyroxene (6-18 vol.%), clinopyroxene (2-20 vol.%), and minor phlogopite and spinel (<3 vol.%) (Figure 4-2 and Table 4-1). Previous studies (Su et al., 2009; Su et al., 2010) have correlated optical observations of the microstructures with chemical compositions and equilibrium temperatures to divide the Haoti peridotite xenoliths into two types: intensely deformed types with mineral elongation and weakly deformed types with large, anhedral grains. In our samples, we identified fine-porphyroclastic microstructures comprised of fine-grained olivine at interstitial positions between coarse grains (Fig. 4-2a). Very fine-grained recrystallized olivine and pyroxnene neoblasts occur in a melt pocket, which likely is located at a triple junction (Fig. 4-2a). In the coarse-porphroyroclastic types, olivine commonly shows irregular shape with intracrystalline deformation features (Fig. 4-2b). Sinuous olivine-pyroxene boundaries and cusp-like shapes of pyroxenes occur generally with obvious undulose extinction and subgrain boundaries (Fig. 4-2c). Both olivine and pyroxenes have curvilinear to straight grain boundaries, evolving locally into polygonal shapes with 120° triple junctions (Fig. 4-2d).

4.4.2 Mineral Compositions of the mantle xenoliths

All minerals of the xenoliths are chemically homogeneous. Representative EPMA analyses of the major constituent minerals are given in the Supplementary

158

Table 4A-1. The olivines have a high Fo (=100 × Mg / (Mg + Fe) atomic units) from 90.6-91.5 in all xenoliths except for G16-48, where the Fo of olivine is 88.4. With respect to all other elements, the olivines show quite uniform compositions in all samples with CaO contents of 0.05 - 0.12 wt.%, Al_2O_3 contents of 0.003 - 0.029 wt.%, and NiO contents of 0.32 - 0.40 wt.% (Supplementary Table 4A-1).

The clinopyroxenes contain 0.73-0.78 apfu Ca, 1.90-1.93 apfu Si, variable 0.09-0.26 apfu Al and 0.04-0.13 apfu Na, with $Mg^{\#}$ of 89 - 92 (0.90-1.01 apfu Mg, 0.07-0.12 apfu Fe). The clinopyroxenes display a wide variation in trace element compositions and can be roughly divided into two main trends (Supplementary Fig. 4B-1). One compositionally distinct group is represented by the clinopyroxenes from samples with the fine-porphyroclastic microstructures and melt pockets. These clinopyroxenes show substantial enrichment in the light REE (LREE) over the heavy REE (HREE) (La_N/Yb_N = 7.36 − 13.35). They are characterized by low Yb_N/Y_N (0.43 - 0.55), high Sr/Y (26.02 −53.51). The other compositionally distinct group of clinopyroxenes comes from the samples with the coarse-porphyroclastic microstructures. These clinopyroxenes have a relatively flat REE pattern with (La_N/Yb_N) from 0.47 to 2.53, high Yb_N/Y_N (0.74 - 0.99), and low Sr/Y (6.02 − 8.27) (Supplementary Fig. 4B-1 and Table 4A-3). All clinopyroxenes have positive Eu anomalies (Eu_N/Eu^* = 1.01-1.24), negative anomalies of Pb and of the high field strength elements (HFSE; e.g. Nb, Ta, Zr and Hf).

The $Mg^{\#}$-number of orthopyroxenes varies from 89 to 91. The Al, Si and Ca contents are 0.08-0.16 apfu Al, 1.89-1.94 apfu Si and 0.02-0.05 apfu Ca, respectively. The orthopyroxenes in all samples are slightly depleted in LREE over HREE and have positive anomalies in Pb, Zr, and Hf. The spinel has Al contents of 1.17-1.20 apfu and Fe contents of 0.32-0.46 apfu Fe, with high $Cr^{\#}$ (= Cr/(Cr+Al), molar ratio) of 0.32 − 0.38 and an $Mg^{\#}$-number of 61-70 (Supplementary Table 4A-3).

The equilibrium temperatures of the Haoti xenoliths were estimated using

different calibrations of the two-pyroxene geothermobaromer (e.g. Putirka (2008). See the Supplementary Table 4A-2 for details.). Nine opx-cpx pairs were analyzed, which yield temperatures of 1092 ± 70 °C. Based on the Western Qinling geothermal gradient (Su et al., 2009), the equilibrium pressure of the mantle-derived xenoliths is estimated to be in the range of 1.6-2.5 GPa corresponding to a depth of 60 km - 90 km.

4.4.2 Fabric

In most samples, the olivine shows a well-developed CPO characterized by a concentration of the [010]-directions perpendicular to the XY-plane and a large circle girdle in the XY-plane containing the [100] and [001] poles (AG-type). In addition, only one sample (G16-40) exhibits an A-type fabric with (010) parallel to the XY-plane and [100] aligned parallel to the X-direction (Fig. 4-3 and Fig. 4B-2). The J-index of the olivine CPO ranges between 4.32 and 9.89 (Table 4-1). The AG-type olivines with elongated shapes have higher fabric strength than the A-type olivines, which are typically coarse grained and have isometric shapes. The symmetry of the AG-type olivine fabric is characterized by a BA-index < 0.24, whereas the A-type olivine fabrics have higher BA-indexes of 0.7 (Table 4-1). Since the fabric type of olivine is mainly AG-type with subordinate A-type, which both have a concentration of the olivine [010]-directions perpendicular to the XY-plane so that the (010) plane is always parallel to the XY-plane, irrespective of whether the olivine exhibits an AG-type or an A-type fabric.

The CPO of orthopyroxene in the xenoliths is mostly characterized by the alignment of [010] perpendicular to the XY-plane and of [001] parallel to the X-direction (Fig. 4-3 and Fig. 4B-2). The fabric of orthopyroxene is generally weaker than the olivine fabric.
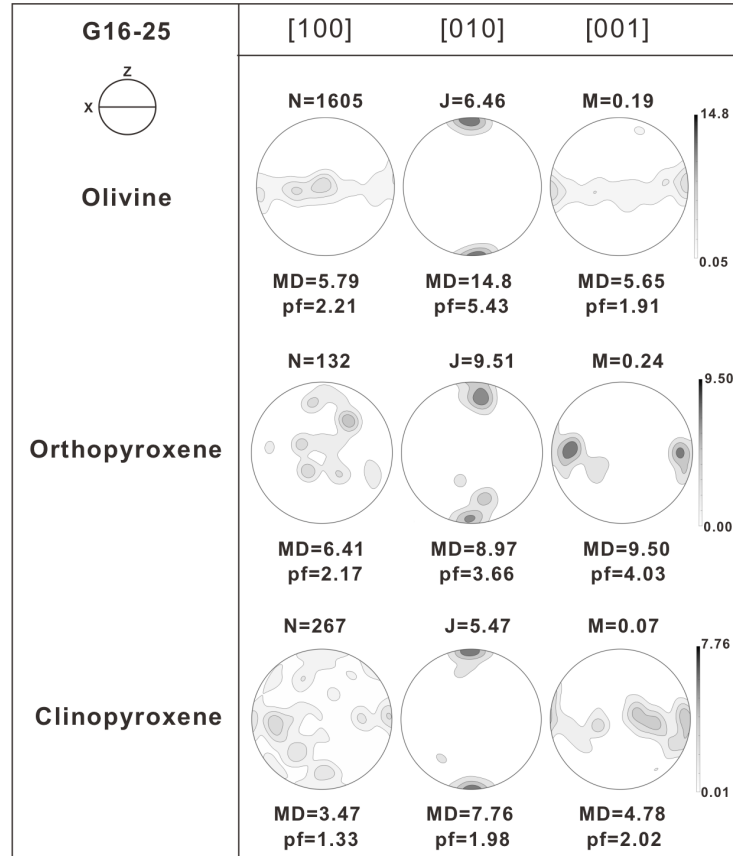
Fig. 4-3 Representative pole figures for the crystallographic axes of olivine, orthopyroxene and clinopyroxene in xenolith sample G16-25 from Haoti. The CPOs are presented in equal-area, one point per grain, lower-hemisphere projections; the structural reference frame is shown as insert in the upper left. Contours (=6) show multiples of uniform distribution. N is the number of measurements, J-index and M-index refer to the fabric strength, pf is an index of fabric intensity, and MD is the maximum density given in multiples of the uniform distribution.

4.3.3 Seismic Anisotropy of the Peridotite Xenoliths

Since olivine is the volumetrically dominant mineral in the peridotite xenoliths, the anisotropy patterns of the xenoliths are mainly controlled by the texture of olivine. Here, we present the olivine and xenoliths anisotropy of sample G16-25 as an example of the AG-fabric type (Fig. 4-4).

The fastest (V_p^{max}) and the slowest (V_p^{min}) P-wave velocities lie in the [100] and [010] directions of olivine, which in the AG-type fabric samples are subparallel to the

XY-plane and the Z-axes of the structural frame, respectively (Fig. 4-4 and Fig. 4B-3). The V_p^{max} of the AG-type samples, including orthopyroxene and clinopyroxene, range from 8.69 km/s to 8.86 km/s and the anisotropy of the V_p velocities is in the range of 9.7 % to 12.7%.
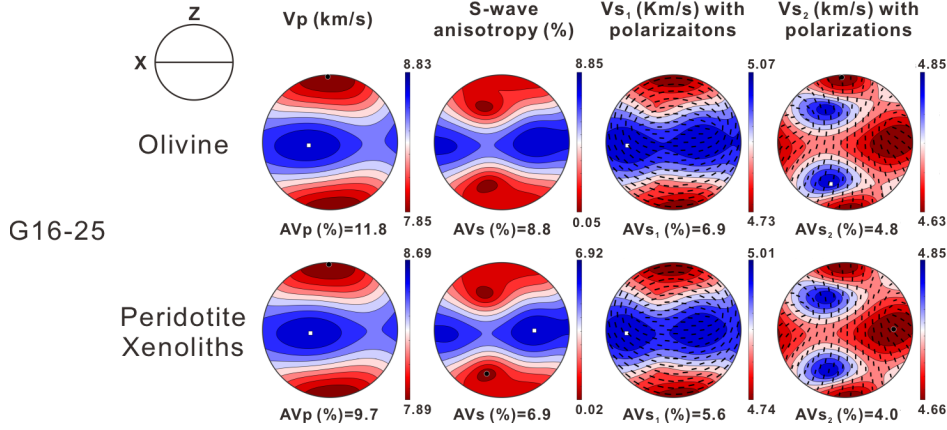
Fig. 4-4 Representative patterns of the seismic properties of the peridotite xenoliths in Haoti calculated from the fabric of the xenoliths. The seismic properties are presented with respect to the structural reference frame in equal-area, lower-hemisphere projections. Sample G16-25 represents the AG-type fabric. The four columns are the P-wave velocity (Vp) with anisotropy of the P-waves (AVp); the polarization anisotropy (AVs) and the splitting S-wave velocity (V_{s1} and V_{s2}) with their polarization directions. $AVp = [(Vp^{max} - Vp^{min}) / (Vp^{max} + Vp^{min}) /2] \times 100\%$ and $AVs = [(V_{s1} - V_{s2})]/[(V_{s1} + V_{s2})/2]$, where V_{s1} and V_{s2} are the propagation velocities of the fast and the slow polarization direction of split S-waves. $AV_{s1/s2} = [(V_{s1/s2}^{max} - V_{s1/s2}^{min}) / (V_{s1/s2}^{max} + V_{s1/s2}^{min}) / 2]$; insert on the upper left shows the structural reference frame.

In the samples with AG-type fabric, the polarization anisotropy of shear waves as expressed by the AV_s values show a minimum for waves propagating approximately parallel to the Z-axis of the structural reference frame, and moderately high AV_s for waves propagating in directions lying in the XY-plane. The highest anisotropies are in the range of 6.9% - 9.4% for waves propagating in the XY-plane of the structural reference frame (Fig. 4-4 and Fig. 4-S3). The S_1-wave (fast split wave V_{s1max}) velocity

ranges from 5.01 km/s to 5.11 km/s and V_{s2min} (slow split wave) ranges from 4.60 km/s to 4.66 km/s.

For the A-type sample G16-40, the fastest propagation direction of P-waves is sub-parallel to the X-direction, where V_p^{max} =8.60 km/s, while the slowest one is sub-parallel to the Z-direction with V_p^{min} =8.06 km/s. The maximum of the AV_s of this sample is 4.7% for waves propagating close to the Y-direction in the XY-plane, which corresponds to the olivine [001] direction, and the lowest dV_s lies in the X-direction, which corresponds to the olivine [100] direction (Supplementary Fig. 4B-3).

4.2.4. Variation of Seismic Properties with Depth

We calculated the seismic properties of the xenoliths as a function of pressure and temperature (the variation of the elastic constants with changing *P-T* conditions are presented in Supplementary Table 4A-2). For the sample with A-type fabric the lowest equilibrium temperature, ~950°C, was calculated. According to the geothermal gradient (Su et al., 2009), the A-type sample was exhumed from a depth of 55-65 km, which corresponds to the uppermost mantle in the area under study. The samples show the highest mean P wave velocity (V_p = 8.01-8.07 km/s), the highest mean S wave velocity (V_s = 4.57-4.61 km/s) and the lowest AV_s (= 4.47-5.86 %). For one of the AG-type samples, equilibrium temperatures in the range of 1050 to1150°C were calculated corresponding to a depth range of 65-75km. As compared to the other samples, it displays moderate V_p (= 7.93-8.00 km/s), low V_s (= 4.50-4.59 km/s) and moderate to high AV_s (= 6.59-11.85%). The AG-type sample from the 85-95km depth range shows moderate V_p (=7.91-8.05 km/s), moderate V_s (= 4.51-4.57 km/s) and the highest AV_s (= 9.20-10.53%).

To assess the dispersions of the seismic properties due to compositional heterogeneity, we considered a reasonable range of mineral modal proportions in the

upper mantle from shallow to deep. Our estimates are based on the modal compositions of the xenoliths and on their calculated equilibrium temperatures. The seismic velocities are primarily controlled by the modal proportions of the constituent minerals and intensity of the fabric. For each depth we varied the mantle composition from 90% olivine + 5% orthopyroxene +5% clinopyroxene to 60% olivine + 20% orthopyroxene +20% clinopyroxene (see Supplementary Table 4A-4 and information). The resulting spread in seismic velocities is indicated by the horizontal bars in Figure 4-5. Three different end-member structural settings, a vertical, lateral and horizontal shear framework, were considered for calculating the seismic properties along a depth profile (Fig. 4-5). The vertical shear framework regards as a vertical orientation of the shear plane and shear direction corresponding to a vertical orientation of the foliation plane and mineral elongation. The lateral shear framework represents a vertical shear and thus foliation plane and horizontal shear direction and mineral elongation. The horizontal shear framework implies horizontal orientation of the shear plane and shear direction corresponding to horizontal orientation of the foliation plane and mineral elongation.

We consider the SKS phases to propagate in a radial direction implying vertical propagation through the mantle and the crust (Silver, 1996). Thus, we only focus on the radial wave path from the depth to the surface. Fig. 4-5 shows the calculated velocity structure along the depth profile given as the average V_p, V_s, V_p/V_s and AV_s of the peridotites for the different structural settings and a vertical ray path.
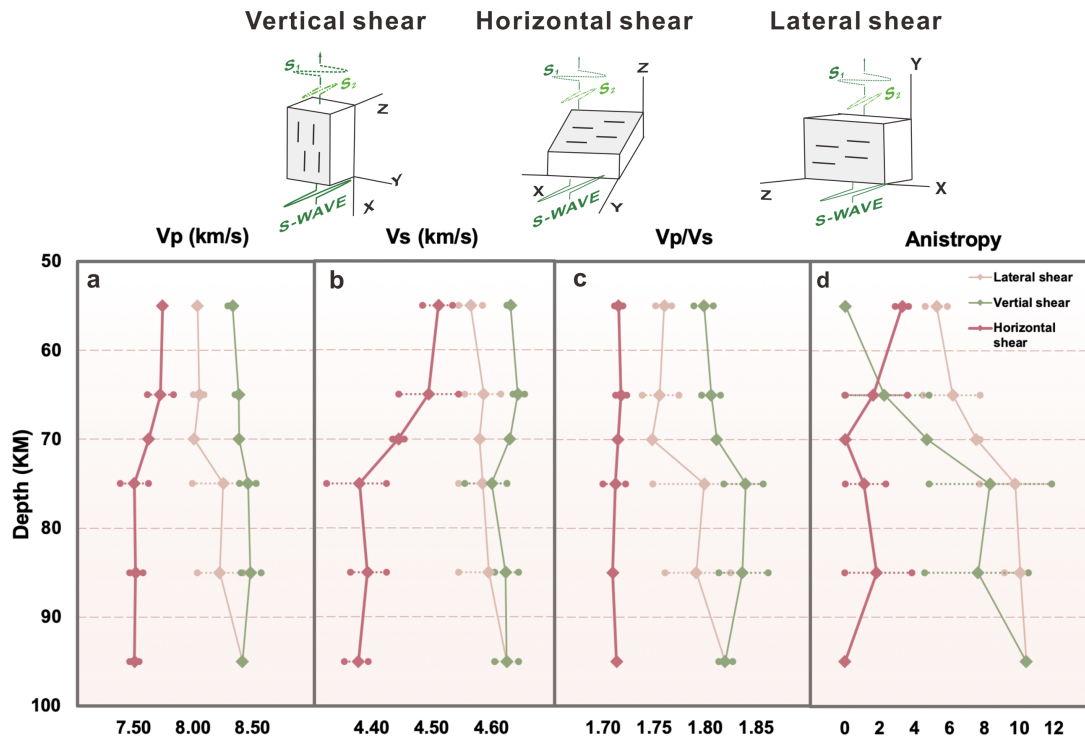
Fig. 4-5 Variation of seismic velocity (a) Vp, (b) Vs, (c) Vp/Vs and (d) AVs as a function of P and T for different equilibration depth. Contours are shown for three geodynamic models: red for horizontal extension, yellow for lateral shear, and green for vertical shear (upwelling). In the three structural models, the shaded area represents the plane of the foliation, the black lines on the plane indicate the lineation and the green line indicates the S-wave propagation direction.

The results show significant differences between the three structural frameworks with corresponding fabric setting. For the model invoking a horizontal foliation plane, the V_p and the V_s decrease from 7.72 to 7.48 km/s and from 4.51 to 4.37 km/s, respectively, with increasing depth. Compared to the other two structural models, the horizontal framework represents the lowest velocities (Fig. 4-5a&5b). For the models invoking a vertical foliation plane with lateral or vertical lineation, the V_p ranges between 8.01 and 8.39 km/s along the depth profile (Fig. 4-5a). The trend of V_s shows a disparity between the two structural models. A slight rise from 4.56 km/s to 4.62 km/s is obtained for the model with lateral lineation, whereas a decline from 4.64 km/s to 4.62 km/s is calculated for the model with vertical shear (Fig. 4-5b). The

V_p/V_s ratio is the highest (=1.837) for the vertical shear model (Fig. 4-5c). The variation of AV_s with depth is complicated: owing to the obvious higher intrinsic anisotropy of the AG-type than the A-type fabric, and the direction with strongest anisotropy between the two fabric types is different (Fig. 4-5d). For ideal AG-type fabric olivine, the [100] and [001]-axes form homogeneous girdle distributions in the XY-plane, leading to a constant velocity and anisotropy characteristics between X-direction and Y-direction. In the realistic case, the AG-type fabric probably shows somewhat heterogeneous girdle distributions. Thus, for the samples with the AG-type fabric, the small differences in the seismic properties between the X-direction and the Y-direction explains the different velocity structures for the vertical shear and lateral shear model.

4.5 Discussion

4.5.1 The Genesis of Olivine Microstructures and CPO

The mineral fabrics and the well-preserved deformation features like undulose extinction and subgrain boundaries indicate that the peridotites from Haoti essentially deformed by dislocation creep (Liu et al., 2019a; Tommasi et al., 2016) (Fig. 4-2). The coarse grain sizes point to low-stress conditions. The AG-type fabric with a BA-index below 0.24, the most abundant CPO type of olivine in the xenoliths, suggests that the dominant slip system activated involved the (010) slip plane which is oriented parallel to the foliation. One sample displays orthorhombic CPO patterns (A-type) with a BA-index of 0.7 indicating dominant [100](010) slip. Olivine with orthorhombic CPO patterns is usually produced in simple shear under dry conditions at moderate to high temperatures and low pressure and stress conditions (Mainprice, 2007; Tommasi et al., 2000).

According to the literature, the AG-type fabric may originate from: (1) simultaneous activation of the [100](010) and [001](010) slip systems under high-pressure and high-stress conditions, which have been observed in shear deformation experiments at conditions equivalent to a depth below 250 km (Mainprice et al., 2005); (2) melt assisted shear deformation, as inferred from AG-type fabric produced during experimental simple shear deformation (Holtzman and Hustoft, 2003); (3) axial shortening in the Z-direction (Z = c), under transpressional deformation or pure compression (Tommasi et al., 1999); and (4) subgrain rotation and growth during recrystallization of deformed rocks, which may modify a pre-existing microstructure by the evolution of grain boundaries (Tommasi et al., 2008).

In our study, the estimated equilibration pressures of the xenoliths are too low to support hypotheses (1) which is applicable to deep-rooted cratonic xenoliths which record pressures of 3.7 GPa - 4.7 GPa (Mainprice et al., 2005; Tommasi et al., 2008). Neither does axial shortening (hypotheses 3) apply to our samples, because it should cause a girdle distribution of the orthopyroxene and clinopyroxene [001] axes, similar to the girdle displayed in the olivine (Tommasi and Ishikawa, 2014). The fabric of pyroxenes in the xenoliths, however, shows obvious point concentrations of the [001]-directions. The present fabric and microstructural data do not allow for distinguishing between the other two hypotheses. The AG-type olivine CPO may therefore result from melt-assisted deformation, or from oriented growth during recrystallization, or recrystallization with concomitant melt-assisted deformation.

Hypothesis (2) invokes melt-assisted shear deformation, either during partial melting of the mantle (Soustelle et al., 2009) or during percolation of basaltic melts (Higgie and Tommasi, 2014; Le Roux et al., 2008). There are several lines of evidence from earlier studies that corroborate the presence of melt, suggesting that melt might have contributed to the generation of the AG-type olivine fabric. The trace element compositions of clinopyroxenes in this study and former geochemical analyses on the

xenoliths (Su et al., 2010) reveal depletion in HFSE (Supplementary Fig. 4B-1) and positive Eu, which indicate that melt was involved in mantle metasomatism. The 7.1 to 23 Ma old ultrapotassic magmatism in the study region testifies to the presence of melt in the lithospheric mantle (Yu et al., 2006). Partial melting of the lithospheric mantle below the Tibetan Plateau is also indicated by geophysical data. Low gravity anomalies suggest that the upper mantle is affected by elevated heat-flow related to an upwelling mantle (Bi et al., 2016). Low-velocity anomalies inferred from receiver functions and surface wave methods have been ascribed to partial melting in the upper mantle (Deng et al., 2018; Li et al., 2017). Thus, melt-assisted deformation is likely a reasonable explanation for the AG-type fabric of the olivine observed beneath the NETP.

Hypothesis (4), which invokes recovery and grain growth to modify the fabric, would imply a low density of intracrystalline dislocations due to recovery, and due to a high volume fraction of recrystallized grains (Tommasi et al., 2008). The Haoti xenoliths mainly exhibit variable degrees of elongated coarse grains, with small proportions of irregularly shaped crystals. Partially recrystallized grains of olivine could be discerned from the granular grains based on their lower average intergranular misorientation (usually < 2.2°). Generally, the average intergranular misorientation decreases with both an increase of the recrystallized area fraction and with the recovery of the dislocation microstructure (Tommasi et al., 2016). The presence of SPO and an elevated average intergranular misorientation (2.35° - 3.81°) reflects a low degree of recrystallization. We suggest that static recrystallization contributed only subordinately to the formation of the AG-type fabric in the Haoti xenoliths.

4.5.2 Seismic Anisotropy of the Upper Mantle in the NETP

The anisotropy of the upper mantle is primarily a function of the intrinsic elastic

anisotropy of the rock-forming minerals, mineral mode, as well as rock fabric. Once the CPO is known, seismic anisotropy is a useful method to infer the structure of the lithosphere, mantle deformation, and to complement geophysical data. The shear-wave splitting in teleseismic shear waves (e.g. SKS) records anisotropy that is present anywhere between the core-mantle boundary and the surface. The large observed delay times associated with shear wave splitting require a very thick anisotropic layer and/or a particularly high seismic anisotropy (Silver, 1996).

The seismic stations surrounding the NETP show that the FPD of split SKS waves trends persistently in the SE120° direction with average splitting time delays of 1.5s (Fig. 4-1). Combined with previously revealed average delay times of 0.4s caused by crustal anisotropy (Kong et al., 2016), we expect that the upper mantle contributes about 1s to the delay time. The thickness of the lithospheric mantle in the NETP is about 70km, according to the estimated Moho depth (50 km) and the estimated 120 km depth of the Lithosphere-Asthenosphere Boundary (LAB) (Xu et al., 2019; Zheng et al., 2019). It should be noted that for the AG-type fabric, the polarization anisotropy for waves with a propagation direction normal to the XY-plane is very weak or nearly zero (Fig. 4-4). Thus, if the structural frame in the lithospheric mantle was generated predominantly by horizontal shearing (Fig. 4-5d), only weak anisotropy could be expected for the A-type olivine, which is the dominant fabric in the shallowest xenolith, which corresponds to the uppermost mantle. Also, the deeper upper mantle, where the AG-type fabric dominates, would contribute very little to shear wave splitting, if shearing and, hence, the XY-plane of the reference frame were horizontal (Fig. 4-5d). A horizontal structural frame is thus in conflict with the large delay times observed in the NETP. Based on the analyses of surface waves, it was shown that in the upper mantle beneath the NETP the propagation velocity of horizontally polarized horizontally propagating shear waves, V_{SH}, is lower than the velocity of vertically polarized horizontally propagating shear waves, V_{SV}, (Li, 2013; Li et al., 2016). This rather indicates a vertical structure beneath the NETP. Given a

vertical structure, a 70 km thick upper mantle with AV_s in the range of 6.9% - 9.4% would contribute about 1.16s delay time, which matches the anticipated upper mantle contribution of 1s delay time.

4.5.3 Does asthenosphere flow contribute to SKS splitting in NETP?

Compared with other mantle xenoliths found elsewhere in the Tibetan Plateau (Yang et al., 2019), the mantle xenoliths from the NETP present indeed higher seismic anisotropy. Based on our results, there is no other mechanisms needed to explain the large delay times in the NETP. Lacking the information about mineral fabrics, former studies proposed that asthenospheric flow (AF) was responsible for the observed seismic anisotropy. This hypothesis is equivalent to extending the anisotropic layer beyond the asthenosphere-lithosphere boundary and corresponds to an increase of its total thickness (e.g. Chang et al., 2017; Huang et al., 2017). At this point the question arises to what extent asthenosphere flow contributes to SKS splitting in the NETP.

The fact that the FPD of the SKS is persistent across different tectonic blocks extending from the NETP to the southwestern Ordos block indicates an underlying mechanism operating on a large scale. Eastward directed AF beneath the entire region is a viable hypothesis (Yu and Chen, 2016). The continuous LVZ observed at a depth of 100-200 km also corroborates the view that AF towards the Ordos block is currently active (Li et al., 2018a). The slight obliquity of ~8° between the direction of absolute plate motion (APM) and the FPD implies that AF may drive the lithosphere to generate left lateral shearing (Chang et al., 2017). In summary, several lines of evidence support the existence of AF. In fact, AF needs to be invoked for explaining the observed delay times, if a hot and thin lithosphere of < 100km thickness with moderate seismic anisotropy is considered (Huang et al., 2017). As discussed above, the intrinsic anisotropy of the lithospheric mantle beneath the NETP

is sufficiently high to induce large delay times, even for a thin lithospheric mantle of 70km. In the light of the intrinsic anisotropy of the mantle beneath the NETP a potential contribution of eastward horizontal asthenospheric flow to the observed delay times can neither be confirmed nor can it be ruled out. Circumstantial evidence points towards a rather limited contribution of asthenospheric flow.

Experimental results showed that CPO of olivine may also be produced in the course of deformation by diffusion creep, which is considered as the dominant deformation mechanism beyond the field of dislocation creep (Miyazaki et al., 2013). Olivine that is involved in ductile flow of the asthenosphere could thus develop anisotropy for shear waves propagation in vertical direction by forming an A-type fabric, if the P-T conditions are suitable (Miyazaki et al., 2013). If the A-type olivine fabric were indeed dominant in the asthenosphere below the NETP, the surface wave analysis should show $V_{SH} > V_{SV}$ below the LAB for a horizontal flow. This does, however, not match with the observations, which indicate that the V_{SV} gradually increases relative to V_{SH} and $V_{SV} > V_{SH}$ below about 130km (Agius and Lebedev, 2013; Chen et al., 2009). A decoupled movement between lithosphere and asthenosphere is also in conflict with large scale AF. Multiple evidence from surface wave dispersion, receiver function, SKS splitting and GPS analysis indicates that the lithosphere beneath the NETP experiences uniform shortening in NE-SW direction, and bottom to the east shearing associated with AF (Chang et al., 2017; Deng et al., 2018; Huang et al., 2017). Given a decoupled movement, a double-layer anisotropy would be expected, if the asthenosphere also contributed to the anisotropy. But no obvious evidence of a double-layer anisotropy exists. On the other hand, normally the foliation plane and the lineation direction are both horizontal for AF and the lineation should coincide with the flow line, which is, in turn, parallel to the APM. Around the globe, significant variations in the regional scale FPD and in the delay times have been observed within plates, accompanied by a relatively uniform APM direction and asthenosphere thickness. This suggests that AF cannot be the dominant

source of anisotropy for SKS splitting (Silver, 1996). Steep oceanic subduction areas, where melt-rich layers in the asthenosphere (Kawakatsu et al., 2009) are sub-vertical may be an exception. In this case, an enhancement of shear wave splitting is expected since SKS phase propagate sub-normal to the symmetry axis of the layered structure. But for the NETP, we exclude AF as a substantial contribution for large delay times.

4.5.4 Geodynamic Implications Inferred from Mantle Xenolith Fabric

Seismic tomographic studies (Deng et al., 2018; Wang et al., 2017b; Xu et al., 2019) revealed a LVZ in the upper mantle beneath the NETP. According to the results of our velocity modelling, the samples from the upper mantle where the A-type fabric dominates show relatively low V_s as compared to the deeper mantle, where the AG-type fabric dominates. The inferred vertical structure is in line with the velocity structure obtained from geophysical analysis (Wang et al., 2017b; Xu et al., 2019). Considering the long history of complex deformation in the NETP including sustained compression, localized faults, lateral extrusion, as well as interaction of the lithospheric mantle with obstacles such as the Ordos and the Alxa block, the observed patchy distribution of fast and slow anomalies in the mantle is expected (Deng et al., 2018). The presence of relatively low shear-wave velocities in the uppermost mantle is taken as an indication of mantle flow (Chang et al., 2017; Yu and Chen, 2016), which is associated with asthenosphere upwelling caused by delamination of a thick lithospheric root (Li et al., 2017; Wang et al., 2017b). The occurrence of different fabric types in the peridotites observed in this study may explain the velocity structures inferred from seismic explorations. Therefore, the velocity variation with depth could be a consequence of lithospheric mantle heterogeneity in this area.

Our new observations from xenolith fabrics suggest a vertical foliation in the lithosphere underlying the NETP. Hitherto, there is no additional information that would help deciphering the specific movement direction (lineation) in this region,

because the corresponding velocity properties and anisotropy associated with the dominant AG-fabric type are similar for both, vertical shear and lateral shear motion. Previous studies suggested that the influx of hot asthenosphere not only delaminated lithospheric mantle but also induced isostatic uplift of the NETP (Xu et al., 2019). The ongoing compression caused by the collision of the Indian- and the Eurasian plates probably lead to the lateral escape of material combined with isostatic uplift (Molnar et al., 1993). Several thousand kilometers sinistral faults distributed in this region are strong evidence for accommodation by left-lateral extrusion (Li et al., 2016). Therefore, both, strike-slip shearing and asthenospheric upwelling play a fundamental role in the deformation of the NETP. The current lithospheric structure was probably produced by the combined effects of these two factors. This implies both vertical shear due to asthenosphereic upwelling and lateral shear due to strike slip accommodated eastward escape combining the two feasible model scenarios.

References:

1. Agius, M.R. and Lebedev, S., 2013. Tibetan and Indian lithospheres in the upper mantle beneath Tibet: Evidence from broadband surface-wave dispersion. Geochemistry, Geophysics, Geosystems, 14(10): 4260-4281.

2. Amiguet, E., Raterron, P., Cordier, P., Couvy, H. and Chen, J., 2009. Deformation of diopside single crystal at mantle pressure. 1: Mechanical data. Physics of the Earth and Planetary Interiors, 177(3-4): 122-129.

3. Bachmann, F., Hielscher, R. and Schaeben, H., 2010. Texture Analysis with MTEX – Free and Open Source Software Toolbox. Solid State Phenomena, 160: 63-68.

4. Bi, B.-T., Hu, X.-Y., Li, L.-Q., Zhang, H.-L., Liu, S. and Cai, J.-C., 2016. Multi-scale analysis to the gravity field of the northeastern Tibetan plateau and its geodynamic implications. CHINESE JOURNAL OF GEOPHYSICS-CHINESE EDITION, 59(2): 543-555.

5. Chang, L., Ding, Z., Wang, C. and Flesch, L.M., 2017. Vertical coherence of deformation in lithosphere in the NE margin of the Tibetan plateau using GPS and shear-wave splitting data. Tectonophysics, 699: 93-101.

6. Chatzaras, V., Kruckenberg, S.C., Cohen, S.M., Medaris, L.G., Withers, A.C. and Bagley, B., 2016. Axial-type olivine crystallographic preferred orientations: The effect of strain geometry on mantle texture. Journal of Geophysical Research: Solid Earth, 121(7): 4895-4922.

7. Chen, L. and Gerya, T.V., 2016. The role of lateral lithospheric strength heterogeneities in orogenic plateau growth: Insights from 3‐D thermo‐mechanical modeling. Journal of Geophysical Research: Solid Earth, 121(4): 3118-3138.

8. Chen, Y., Badal, J. and Zhang, Z., 2009. Radial anisotropy in the crust and upper mantle beneath the Qinghai-Tibet Plateau and surrounding regions. Journal of Asian Earth Sciences, 36(4-5): 289-302.

9. Demouchy, S., Tommasi, A., Ionov, D., Higgie, K. and Carlson, R., 2018. Microstructures, Water Contents, and Seismic Properties of the Mantle Lithosphere beneath the Northern limit of the Hangay Dome, Mongolia. Geochemistry, Geophysics, Geosystems.

10. Deng, Y., Li, J., Song, X. and Zhu, L., 2018. Joint inversion for lithospheric structures: Implications for the growth and deformation in Northeastern Tibetan Plateau. Geophysical Research Letters, 45(9): 3951-3958.

11. Henry, H., Tilhac, R., Griffin, W.L., O'Reilly, S.Y., Satsukawa, T., Kaczmarek, M.-A., Grégoire, M. and Ceuleneer, G., 2017. Deformation of mantle pyroxenites

provides clues to geodynamic processes in subduction zones: Case study of the Cabo Ortegal Complex, Spain. Earth and Planetary Science Letters, 472: 174-185.

12. Higgie, K. and Tommasi, A., 2014. Deformation in a partially molten mantle: Constraints from plagioclase lherzolites from Lanzo, western Alps. Tectonophysics, 615-616: 167-181.

13. Holtzman, B.K. and Hustoft, J., 2003. Melt segregation and strain partitioning: implications for seismic anisotropy and mantle flow. Science, 301(5637): 1227-30.

14. Hu, Z., Gao, S., Liu, Y., Hu, S., Chen, H. and Yuan, H., 2008. Signal enhancement in laser ablation ICP-MS by addition of nitrogen in the central channel gas. Journal of Analytical Atomic Spectrometry, 23(8).

15. Huang, Z., Tilmann, F., Xu, M., Wang, L., Ding, Z., Mi, N., Yu, D. and Li, H., 2017. Insight into NE Tibetan Plateau expansion from crustal and upper mantle anisotropy revealed by shear-wave splitting. Earth and Planetary Science Letters, 478: 66-75.

16. Ismail, W.B. and Mainprice, D., 1998. An olivine fabric database: an overview of upper mantle fabrics and seismic anisotropy. Tectonophysics, 296(1): 145-157.

17. Kawakatsu, H., Kumar, P., Takei, Y., Shinohara, M., Kanazawa, T., Araki, E. and Suyehiro, K., 2009. Seismic evidence for sharp lithosphere-asthenosphere boundaries of oceanic plates. Science, 324(5926): 499-502.

18. Kong, F., Wu, J., Liu, K.H. and Gao, S.S., 2016. Crustal anisotropy and ductile flow beneath the eastern Tibetan Plateau and adjacent areas. Earth and Planetary Science Letters, 442: 72-79.

19. Le Roux, V., Tommasi, A. and Vauchez, A., 2008. Feedback between melt percolation and deformation in an exhumed lithosphere–asthenosphere boundary. Earth and Planetary Science Letters, 274(3): 401-413.

20. León Soto, G., Sandvol, E., Ni, J.F., Flesch, L., Hearn, T.M., Tilmann, F., Chen, J. and Brown, L.D., 2012. Significant and vertically coherent seismic anisotropy beneath eastern Tibet. Journal of Geophysical Research: Solid Earth, 117(B5): n/a-n/a.

21. Li, L., 2013. Seismic Velocity, Radial Anisotropy in the Crust and Upper Mantle of Northeastern Tibetan Plateau from Surface Wave Tomography thesis Thesis, University of Houston, Houston.

22. Li, L., Li, A., Murphy, M.A. and Fu, Y.V., 2016. Radial anisotropy beneath northeast T ibet, implications for lithosphere deformation at a restraining bend in the K unlun fault and its vicinity. Geochemistry, Geophysics, Geosystems, 17(9): 3674-3690.

23. Li, S., Guo, Z., Chen, Y.J., Yang, Y. and Huang, Q., 2018a. Lithospheric Structure

of the Northern Ordos From Ambient Noise and Teleseismic Surface Wave Tomography. Journal of Geophysical Research: Solid Earth.

24. Li, Y., Liu, M., Wang, Q. and Cui, D., 2018b. Present-day crustal deformation and strain transfer in northeastern Tibetan Plateau. Earth and Planetary Science Letters, 487: 179-189.

25. Li, Y., Pan, J., Wu, Q. and Ding, Z., 2017. Lithospheric structure beneath the northeastern Tibetan Plateau and the western Sino-Korea Craton revealed by Rayleigh wave tomography. Geophysical Journal International, 210(2): 570-584.

26. Liptai, N., Hidas, K., Tommasi, A., Patkó, L., Kovács, I.J., Griffin, W.L., O'Reilly, S.Y., Pearson, N.J. and Szabó, C., 2019. Lateral and vertical heterogeneity in the lithospheric mantle at the northern margin of the Pannonian Basin reconstructed from peridotite xenolith microstructures. Journal of Geophysical Research: Solid Earth.

27. Liu, S., Tommasi, A., Vauchez, A. and Mazzucchelli, M., 2019a. Crust-mantle coupling during continental convergence and break-up: Constraints from peridotite xenoliths from the Borborema Province, northeast Brazil. Tectonophysics, 766: 249-269.

28. Liu, S., Tommasi, A., Vauchez, A. and Mazzucchelli, M., 2019b. Deformation, Annealing, Melt‐Rock Interaction, and Seismic Properties of an Old Domain of the Equatorial Atlantic Lithospheric Mantle. Tectonics.

29. Liu, Y., Hu, Z., Gao, S., Günther, D., Xu, J., Gao, C. and Chen, H., 2008. In situ analysis of major and trace elements of anhydrous minerals by LA-ICP-MS without applying an internal standard. Chemical Geology, 257(1-2): 34-43.

30. Mainprice, D., 2007. Seismic anisotropy of the deep Earth from a mineral and rock physics perspective, Treatise Geophys., 2, 437–491, doi: 10.1016, B978-044452748-6.00045-6.

31. Mainprice, D., Bachmann, F., Hielscher, R. and Schaeben, H., 2014. Descriptive tools for the analysis of texture projects with large datasets using MTEX: strength, symmetry and components. Geological Society, London, Special Publications, 409(1): 251-271.

32. Mainprice, D., Bachmann, F., Hielscher, R., Schaeben, H. and Lloyd, G.E., 2015. Calculating anisotropic piezoelectric properties from texture data using the MTEX open source package. Geological Society, London, Special Publications, 409(1): 223-249.

33. Mainprice, D., Barruol, G. and Ismaïl, W.B., 2000. The Seismic Anisotropy of the Earth's Mantle: from Single Crystal to Polycrystal. American Geophysical Union, 237-264 pp.

34. Mainprice, D. and Humbert, M., 1994. Methods of calculating petrophysical

properties from lattice preferred orientation data. Surveys in Geophysics, 15(5): 575-592.

35. Mainprice, D., Tommasi, A., Couvy, H., Cordier, P. and Frost, D.J., 2005. Pressure sensitivity of olivine slip systems and seismic anisotropy of Earth's upper mantle. Nature, 433(7027): 731.

36. Michibayashi, K. and David, M., 2004. The Role of Pre-existing Mechanical Anisotropy on Shear Zone Development within Oceanic Mantle Lithosphere: an Example from the Oman Ophiolite. Journal of Petrology, 45(2): 405-414.

37. Michibayashi, K., Oohara, T., Satsukawa, T., Ishimaru, S., Arai, S. and Okrugin, V.M., 2009. Rock seismic anisotropy of the low-velocity zone beneath the volcanic front in the mantle wedge. Geophysical Research Letters, 36(12).

38. Miyazaki, T., Sueyoshi, K. and Hiraga, T., 2013. Olivine crystals align during diffusion creep of Earth's upper mantle. Nature, 502(7471): 321-6.

39. Molnar, P., England, P. and Martinod, J., 1993. Mantle dynamics, uplift of the Tibetan Plateau, and the Indian monsoon. Reviews of Geophysics, 31(4): 357-396.

40. Pandey, S., Yuan, X., Debayle, E., Tilmann, F., Priestley, K. and Li, X., 2015. Depth‐variant azimuthal anisotropy in Tibet revealed by surface wave tomography. Geophysical Research Letters, 42(11): 4326-4334.

41. Passchier, C.W. and Trouw, R.A., 2005. Microtectonics. Springer Science & Business Media.

42. Putirka, K.D., 2008. Thermometers and Barometers for Volcanic Systems. Reviews in Mineralogy and Geochemistry, 69(1): 61-120.

43. Silver, P.G., 1996. Seismic anistropy beneath the continents: probing the depths of geology. Annual Review of Earth & Planetary Sciences, 24(1): 385-432.

44. Soustelle, V., Tommasi, A., Bodinier, J.L., Garrido, C.J. and Vauchez, A., 2009. Deformation and Reactive Melt Transport in the Mantle Lithosphere above a Large-scale Partial Melting Domain: the Ronda Peridotite Massif, Southern Spain. Journal of Petrology, 50(7): 1235-1266.

45. Su, B., Zhang, H., Ying, J., Xiao, Y. and Zhao, X., 2009. Nature and processes of the lithospheric mantle beneath the western Qinling: Evidence from deformed peridotitic xenoliths in Cenozoic kamafugite from Haoti, Gansu Province, China. Journal of Asian Earth Sciences, 34(3): 258-274.

46. Su, B.-X., Zhang, H.-F., Sakyi, P.A., Ying, J.-F., Tang, Y.-J., Yang, Y.-H., Qin, K.-Z., Xiao, Y. and Zhao, X.-M., 2010. Compositionally stratified lithosphere and carbonatite metasomatism recorded in mantle xenoliths from the Western Qinling (Central China). Lithos, 116(1-2): 111-128.

47. Tommasi, A., Baptiste, V., Vauchez, A. and Holtzman, B., 2016. Deformation,

annealing, reactive melt percolation, and seismic anisotropy in the lithospheric mantle beneath the southeastern Ethiopian rift: Constraints from mantle xenoliths from Mega. Tectonophysics, 682: 186-205.

48. Tommasi, A. and Ishikawa, A., 2014. Microstructures, composition, and seismic properties of the Ontong Java Plateau mantle root. Geochemistry, Geophysics, Geosystems, 15(11): 4547-4569.

49. Tommasi, A., Mainprice, D., Canova, G. and Chastel, Y., 2000. Viscoplastic self-consistent and equilibrium-based modeling of olivine lattice preferred orientations: Implications for the upper mantle seismic anisotropy. Journal of Geophysical Research: Solid Earth, 105(B4): 7893-7908.

50. Tommasi, A., Tikoff, B. and Vauchez, A., 1999. Upper mantle tectonics: three-dimensional deformation, olivine crystallographic fabrics and seismic properties. Earth and Planetary Science Letters, 168(1): 173-186.

51. Tommasi, A., Vauchez, A. and Ionov, D.A., 2008. Deformation, static recrystallization, and reactive melt transport in shallow subcontinental mantle xenoliths (Tok Cenozoic volcanic field, SE Siberia). Earth and Planetary Science Letters, 272(1-2): 65-77.

52. Wang, W., Wu, J., Fang, L., Lai, G. and Cai, Y., 2017a. Sedimentary and crustal thicknesses and Poisson's ratios for the NE Tibetan Plateau and its adjacent regions based on dense seismic arrays. Earth and Planetary Science Letters, 462: 76-85.

53. Wang, X., Li, Y., Ding, Z., Zhu, L., Wang, C., Bao, X. and Wu, Y., 2017b. Three-dimensional lithospheric S wave velocity model of the NE Tibetan Plateau and western North China Craton. Journal of Geophysical Research: Solid Earth, 122(8): 6703-6720.

54. Wei, X., Jiang, M., Liang, X., Chen, L. and Ai, Y., 2017. Limited southward underthrusting of the Asian lithosphere and material extrusion beneath the northeastern margin of Tibet, inferred from teleseismic Rayleigh wave tomography. Journal of Geophysical Research: Solid Earth, 122(9): 7172-7189.

55. Wieser, P.E., Edmonds, M., Maclennan, J. and Wheeler, J., 2020. Microstructural constraints on magmatic mushes under Kīlauea Volcano, Hawai'i. Nature Communications, 11(1).

56. Wüstefeld, A., Bokelmann, G., Zaroli, C. and Barruol, G., 2008. SplitLab: A shear-wave splitting environment in Matlab. Computers & Geosciences, 34(5): 515-528.

57. Xu, Q., Pei, S., Yuan, X., Zhao, J., Liu, H., Tu, H. and Chen, S., 2019. Seismic evidence for lateral asthenospheric flow beneath the northeastern Tibetan Plateau derived from S receiver functions. Geochemistry, Geophysics, Geosystems.

58. Yang, Y., Abart, R., Yang, X., Shang, Y., Ntaflos, T. and Xu, B., 2019. Seismic anisotropy in the Tibetan lithosphere inferred from mantle xenoliths. Earth and

Planetary Science Letters, 515: 260-270.

59. Yu, X., Zhao, Z., Deqing, Z. and Wang, Y., 2006. 40Ar/39Ar dating for Cenozoic kamafugite from western Qinling in Gansu Province. Chinese Science Bulletin, 51(13): 1621-1627.

60. Yu, Y. and Chen, Y.J., 2016. Seismic anisotropy beneath the southern Ordos block and the Qinling-Dabie orogen, China: Eastward Tibetan asthenospheric flow around the southern Ordos. Earth and Planetary Science Letters, 455: 1-6.

61. Zhao, B., Huang, Y., Zhang, C., Wang, W., Tan, K. and Du, R., 2015. Crustal deformation on the Chinese mainland during 1998–2014 based on GPS data. Geodesy and Geodynamics, 6(1): 7-15.

62. Zheng, C., Zhang, R., Wu, Q., Li, Y., Zhang, F., Shi, K. and Ding, Z., 2019. Variations in Crustal and Uppermost Mantle Structures Across Eastern Tibet and Adjacent Regions: Implications of Crustal Flow and Asthenosph

Supplementary

Supplementary 4A contain major element compositions of minerals in Haoti mantle xenoliths, mineral model composition, and trace elements of pyroxene.

Supplementary 4A-Table 1: Major elements of xenoliths from NETP

Sample	Mineral	Major														
		SiO_2	TiO_2	Al_2O_3	Cr_2O_3	V_2O_3	FeO	MnO	NiO	ZnO	MgO	CaO	Na_2O	Total	Mg#	Cr#
G16-20-2	OL	40.79	0.01	0.03	0.05	-	9.42	0.12	0.40	-	50.03	0.10	0.01	100.96	0.91	
	OPX	55.24	0.04	3.93	0.92	-	5.77	0.12	0.12	-	33.59	1.15	0.08	100.95	0.91	
	CPX	53.15	0.11	4.17	1.39	-	2.95	0.09	0.07	-	17.84	19.28	0.80	99.84	0.91	
	SP	0.11	0.22	34.41	32.00	0.10	13.37	0.12	0.23	0.12	17.49	0.00	-	98.17	0.70	0.38
G16-25	OL	41.08	0.02	0.02	0.04	-	8.46	0.14	0.38	-	50.77	0.12	0.01	101.04	0.91	
	OPX	56.59	0.02	2.02	0.84	-	5.19	0.13	0.13	-	34.34	1.22	0.06	100.55	0.92	
	CPX	54.25	0.02	2.18	1.29	-	2.55	0.10	0.07	-	18.83	20.00	0.52	99.81	0.92	
	SP	0.09	0.06	19.16	48.94	0.11	14.50	0.16	0.31	0.11	15.01	0.01	-	98.47	0.65	0.21
G16-40	OL	40.87	0.02	0.00	0.02	-	9.53	0.12	0.32	-	49.92	0.05	0.00	100.84	0.90	
	OPX	55.58	0.12	4.02	0.34	-	6.04	0.14	0.08	-	33.87	0.66	0.08	100.93	0.91	

Supplementary

Sample	Mineral	**Major**														
		SiO2	TiO2	Al2O3	Cr2O3	V2O3	FeO	MnO	NiO	ZnO	MgO	CaO	Na2O	Total	Mg#	Cr#
	CPX	53.05	0.54	6.18	0.76	-	2.37	0.06	0.07	-	15.23	19.85	1.82	99.93	0.91	
G16-48	OL	40.46	0.02	0.03	0.03	-	11.55	0.16	0.40	-	48.29	0.11	0.00	101.04	0.88	
	OPX	54.82	0.28	3.96	0.69	-	7.21	0.12	0.12	-	32.14	1.25	0.10	100.70	0.89	
	CPX	52.70	0.41	4.26	1.25	-	3.81	0.09	0.06	-	17.48	18.86	0.87	99.80	0.89	
	SP	0.13	2.04	35.46	24.54	0.10	19.23	0.09	0.36	0.13	16.81	0.00	-	98.90	0.61	0.32
G16-55	OL	40.97	0.01	0.02	0.03	-	8.96	0.11	0.39	-	50.40	0.07	0.01	100.97	0.91	
	OPX	55.89	0.07	3.30	0.66	-	5.61	0.15	0.10	-	33.74	0.83	0.11	100.46	0.91	
	CPX	53.40	0.27	4.55	1.41	-	2.81	0.08	0.04	-	16.63	19.20	1.50	99.89	0.91	

Insight into the seismic anisotropy beneath northeastern Tibetan from mantle xenoliths

Sample	Mineral	Atoms per formula units										
		Si	Ti	Al	Cr	Fe	Mn	Ni	Mg	Ca	Na	Total
G16-20-2	OL	0.988	0.000	0.001	0.001	0.191	0.002	0.008	1.806	0.003	0.000	3.000
	OPX	1.887	0.001	0.158	0.025	0.165	0.003	0.003	1.710	0.042	0.005	4.000
	CPX	1.922	0.003	0.178	0.040	0.089	0.003	0.002	0.961	0.747	0.056	4.000
	SP	0.003	0.005	1.174	0.732	0.323	0.003	0.005	0.754	0.000	0.000	3.000
G16-25	OL	0.993	0.000	0.001	0.001	0.171	0.003	0.000	1.828	0.003	0.000	3.000
	OPX	1.938	0.001	0.082	0.023	0.149	0.004	0.004	1.752	0.045	0.004	4.000
	CPX	1.961	0.000	0.093	0.037	0.077	0.003	0.002	1.015	0.775	0.037	4.000
	SP	0.003	0.001	0.704	1.205	0.378	0.004	0.008	0.697	0.000	0.000	3.000
G16-40	OL	0.991	0.000	0.000	0.000	0.193	0.002	0.006	1.805	0.001	0.000	3.000
	OPX	1.896	0.003	0.162	0.009	0.172	0.004	0.002	1.722	0.024	0.005	4.000
	CPX	1.913	0.015	0.263	0.022	0.071	0.002	0.002	0.819	0.767	0.127	4.000
G16-48	OL	0.989	0.000	0.001	0.001	0.236	0.003	0.008	1.759	0.003	0.000	3.000
	OPX	1.892	0.007	0.161	0.019	0.208	0.004	0.003	1.653	0.046	0.007	4.000
	CPX	1.912	0.011	0.182	0.036	0.116	0.003	0.002	0.945	0.733	0.061	4.000
	SP	0.004	0.044	1.201	0.558	0.462	0.002	0.008	0.720	0.000	0.000	3.000
G16-55	OL	0.990	0.000	0.001	0.001	0.181	0.002	0.008	1.815	0.002	0.000	3.000
	OPX	1.917	0.002	0.133	0.018	0.161	0.004	0.003	1.725	0.031	0.007	4.000

Supplementary

Sample	Mineral	Atoms per formula units										
		Si	Ti	Al	Cr	Fe	Mn	Ni	Mg	Ca	Na	Total
	CPX	1.928	0.007	0.194	0.040	0.085	0.003	0.001	0.895	0.743	0.105	4.000

Supplementary 4A-Table 2: Temperature of Haoti xenoliths from two-pyroxene geo-thermobarometer:

Sample	T (°C)				
	TP(08)	TT(98)	TBM(85)	TBK(90)	Average
G16-20-2	1137	1135	1149	1172	1148
G16-25	1127	1112	1147	1160	1137
G16-40	985	944	940	990	965
G16-48	1131	1138	1164	1171	1151
G16-55	1089	1069	1081	1112	1088

TP(08): Putirka (2008). Thermometers and Barometers for Volcanic Systems: Reviews in Mineralogy and Geochemistry, v. 69, no. 1, p. 61-120.

TT(98): Taylor, W.R. (1998). An experimental test of some geothermometer and geobarometer formulations for upper mantle peridotites with application to the thermobarometry of fertile lherzolite and garnet websterite. Neues Jahrbuch fur Mineralogie, Abhandlungen 172, 381-408.

TBM(85): Bertrand, P. & Merrier, J.C.C. (1985). The mutual solubility of coexisting ortho- and clinopyroxene: toward an absolute geothermometer for the natural system? Earth and Planetary Science Letters 76, 109-122.

TBK(90): Brey, G.P. & Koehler, T. (1990). Geothermobarometry in four-phase lherzolites II. New thermobarometers, and practical assessment of existing thermobarometers. Journal of Petrology 31, 1353–1378.

Supplementary 4A-Table 3: Trace element compositions of xenoliths from Haoti, NETP

Sample	G16-20-2				G16-25				G16-40				G16-48				G16-55			
Mineral	CPX		OPX		CPX		OPX		CPX		OPX		CPX		OPX		CPX		OPX	
Position	r	c	r	c	r	c	r	c	r	c	r	c	r	c	r	c	r	c	r	c
Li	3.53	0.99	0.81	0.80	36.32	2.54	0.74	1.15	11.90	1.47	6.43	3.07	25.80	48.90	5.55	11.80	42.70	35.20	25.10	1.31
Sc	25.40	25.40	9.98	10.20	40.42	38.75	17.00	15.81	57.28	56.60	10.52	10.15	30.00	27.10	10.60	9.52	37.60	37.60	11.80	11.90
V	230.0	226.0	113.0	113.0	157.9	153.6	77.8	79.4	274.4	272.3	89.3	86.1	396.0	379.0	100.00	99.70	259.0	262.0	95.4	95.1
Cr	9855	9694	5979	5961	8990	9083	5804	5762	4576	5315	2163	2037	8259	8276	2298	2127	9689	9684	4393	4439
Co	28.30	28.70	60.40	60.90	27.73	27.94	61.54	62.29	19.07	19.24	58.69	57.02	28.40	30.60	60.10	60.50	23.20	23.20	58.80	59.20
Ni	481	480	904	886	474	502	954	950	316	331	707	736	430	508	867	788	411	414	834	844
Cu	1.99	1.57	1.29	1.58	2.30	0.09	12.07	0.00	1.56	1.14	1.21	0.10	2.18	4.22	2.57	1.65	1.52	2.00	2.35	2.68
Rb	0.00	0.05	0.02	0.01	0.04	0.00	0.04	0.00	0.06	0.06	0.00	0.07	2.45	1.89	0.00	0.00	0.02	0.00	0.00	0.00
Sr	10.90	12.40	0.05	0.56	69.17	66.31	1.82	0.33	80.94	84.69	0.16	0.17	190.00	206.00	0.19	0.16	85.90	87.30	0.21	0.23
Y	1.49	1.50	0.13	0.13	2.86	2.55	0.35	0.27	14.03	14.06	0.56	0.48	8.47	3.85	0.57	0.50	2.47	2.52	0.17	0.20
Zr	1.09	1.35	0.07	0.18	15.59	15.27	2.88	1.89	21.14	21.42	0.42	0.59	30.90	23.40	1.50	1.49	10.40	11.20	0.87	0.84
Nb	0.22	0.30	0.03	0.05	0.41	0.37	0.26	0.07	0.10	0.09	0.00	0.00	1.21	1.52	0.01	0.01	0.71	0.73	0.06	0.04
Cs	0.00	0.00	0.00	0.02	0.05	0.02	0.03	0.00	0.03	0.00	0.00	0.02	0.21	0.07	0.01	0.00	0.00	0.00	0.00	0.00

Insight into the seismic anisotropy beneath northeastern Tibetan from mantle xenoliths

Sample	G16-20-2				G16-25				G16-40				G16-48				G16-55			
Mineral	CPX		OPX		CPX		OPX		CPX		OPX		CPX		OPX		CPX		OPX	
Position	r	c	r	c	r	c	r	c	r	c	r	c	r	c	r	c	r	c	r	c
Ba	0.36	1.16	0.00	0.04	0.20	0.20	0.69	0.00	0.03	0.08	0.25	0.02	6.97	3.99	0.00	0.05	0.09	0.16	0.01	0.00
La	0.36	0.44	0.00	0.01	1.78	1.74	0.12	0.01	1.06	0.98	0.00	0.00	6.61	3.35	0.00	0.00	1.42	1.54	0.01	0.00
Ce	0.76	0.99	0.01	0.03	6.58	6.24	0.25	0.05	4.27	4.48	0.02	0.00	25.00	17.90	0.01	0.01	6.90	6.85	0.02	0.02
Pr	0.13	0.14	0.00	0.01	1.10	1.00	0.03	0.02	0.66	0.72	0.00	0.00	4.21	3.23	0.00	0.00	1.17	1.22	0.01	0.01
Nd	0.54	0.82	0.05	0.05	4.65	5.05	0.20	0.04	3.24	3.21	0.03	0.01	20.40	15.30	0.01	0.02	6.07	6.30	0.07	0.05
Sm	0.26	0.19	0.02	0.00	1.30	1.38	0.04	0.05	1.25	1.62	0.00	0.01	4.36	3.18	0.03	0.01	1.27	1.42	0.02	0.04
Eu	0.09	0.11	0.01	0.00	0.33	0.39	0.00	0.01	0.51	0.63	0.01	0.00	1.40	0.99	0.01	0.01	0.46	0.47	0.01	0.01
Gd	0.36	0.39	0.02	0.03	1.06	1.03	0.10	0.05	1.69	2.00	0.04	0.02	3.25	1.98	0.06	0.02	1.08	0.95	0.06	0.06
Tb	0.05	0.08	0.00	0.00	0.15	0.13	0.01	0.00	0.34	0.37	0.01	0.00	0.43	0.26	0.01	0.01	0.13	0.13	0.01	0.01
Dy	0.30	0.41	0.03	0.02	0.69	0.71	0.04	0.07	2.48	2.56	0.08	0.03	2.02	1.10	0.11	0.07	0.69	0.62	0.05	0.04
Ho	0.08	0.07	0.01	0.01	0.10	0.08	0.01	0.00	0.51	0.57	0.02	0.03	0.36	0.18	0.02	0.02	0.08	0.10	0.01	0.01
Er	0.14	0.15	0.01	0.03	0.24	0.22	0.05	0.00	1.50	1.72	0.06	0.11	0.81	0.32	0.03	0.06	0.20	0.26	0.03	0.01
Tm	0.02	0.01	0.01	0.01	0.03	0.04	0.01	0.00	0.21	0.26	0.01	0.00	0.09	0.03	0.02	0.01	0.02	0.04	0.00	0.00
Yb	0.11	0.12	0.05	0.01	0.23	0.14	0.03	0.01	1.52	1.51	0.11	0.11	0.64	0.18	0.11	0.08	0.13	0.15	0.01	0.02
Lu	0.02	0.01	0.00	0.00	0.02	0.02	0.01	0.01	0.21	0.18	0.03	0.03	0.08	0.03	0.01	0.02	0.02	0.01	0.00	0.00
Hf	0.08	0.07	0.01	0.00	0.24	0.26	0.03	0.04	0.71	0.66	0.03	0.02	1.09	1.03	0.01	0.02	0.44	0.41	0.04	0.02

Supplementary

Sample	G16-20-2				G16-25				G16-40				G16-48				G16-55			
Mineral	CPX		OPX		CPX		OPX		CPX		OPX		CPX		OPX		CPX		OPX	
Position	r	c	r	c	r	c	r	c	r	c	r	c	r	c	r	c	r	c	r	c
Ta	0.01	0.01	0.00	0.00	0.05	0.04	0.01	0.01	0.02	0.01	0.00	0.00	0.09	0.13	0.00	0.00	0.14	0.14	0.00	0.00
Pb	0.02	0.00	0.00	0.01	0.13	0.10	0.03	0.01	0.19	0.20	0.08	0.00	0.66	0.51	0.01	0.03	0.19	0.16	0.01	0.01
Th	0.03	0.03	0.00	0.00	0.05	0.07	0.01	0.00	0.01	0.01	0.00	0.00	0.14	0.24	0.00	0.00	0.09	0.07	0.01	0.00
U	0.00	0.01	0.00	0.00	0.02	0.02	0.01	0.00	0.01	0.00	0.00	0.00	0.03	0.06	0.00	0.00	0.02	0.01	0.00	0.00

Supplementary 4A-Table 4: Variation of mineral modal composition and the corresponding fabric of samples with equilibration depth

T(°C)	P(GPa)	D(KM)	Model			Fabric
			OI	CPX	OPX	
950	**1.05**	**55**				
—	**—**	**—**	60	20	20	G16-40
1000	**1.81**	**65**				
1000	**1.81**	**65**	60	20	20	
—	**—**	**—**	70	10	20	G16-55 & G16-40
1100	**2.33**	**75**	75	10	15	
1100	**2.33**	**75**	75	10	15	
—	**—**	**—**	85	5	10	G16-55 & G16-25
1150	**2.70**	**85**	95	0	5	
1150	**2.70**	**85**	75	15	10	
—	**—**	**—**	80	10	10	G16-48 & G16-20-2
1200	**3.00**	**100**	85	5	15	

Supplementary 4A-Information: The references of crystal elastic tensor and density we cited

We employed the elastic constants of Abramson (1997) for olivine and the first- and second-order pressure derivatives by the same authors, and first-order temperature derivatives of Isaak (1992). For orthopyroxene, we used the elastic constants and first- and second-order pressure derivatives of Chai (1997) and first-order temperature derivatives of Frisillo and Barsch (1972). For clinopyroxene, we used the elastic constants and first- and second-order pressure derivatives of Matsui and Busing (1984) and first-order temperature derivatives of Isaak (2005).

According to the mineral modal composition (Table 4-1), we set a resendable range for lithospheric mantle (Supplementary 4A-Table 4).
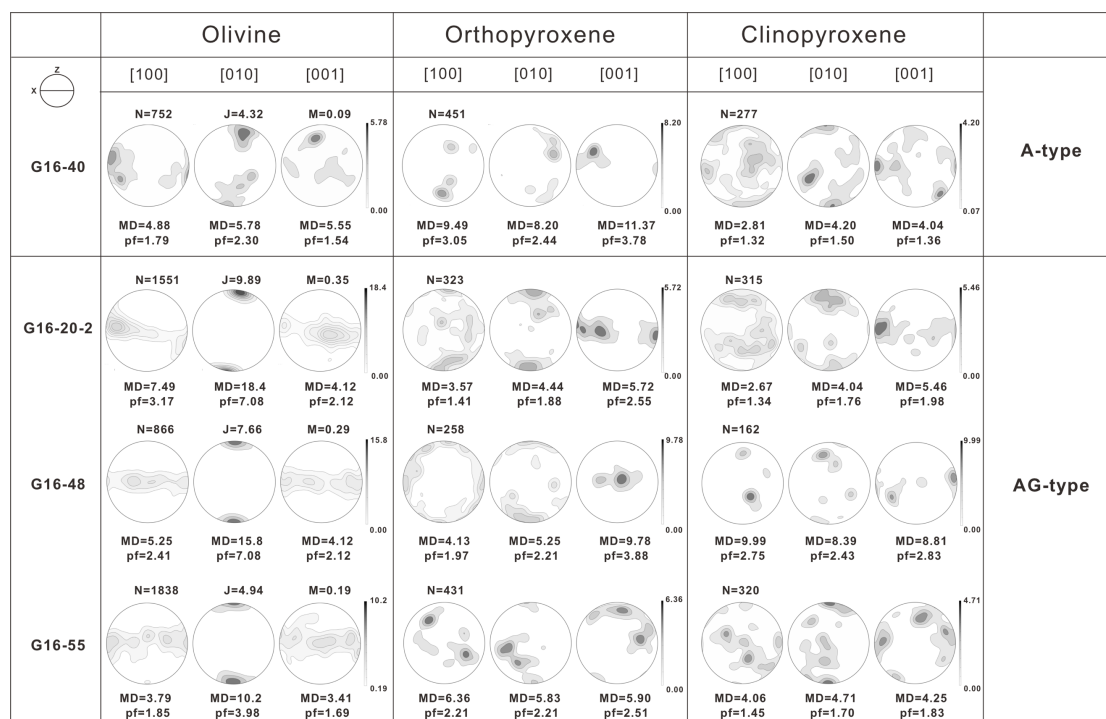
1   Abramson, E., Brown, J., Slutsky, L. & Zaug, J. The elastic constants of San Carlos olivine to 17 GPa. Journal of Geophysical Research: Solid Earth 102, 12253-12263 (1997).

2   Isaak, D. G. High-temperature elasticity of iron-bearing olivines. Journal of Geophysical Research: Solid Earth 97, 1871-1885, doi:10.1029/91jb02675 (1992).

3   Chai, M., Brown, J. M. & Slutsky, L. J. The elastic constants of an aluminous orthopyroxene to 12.5 GPa. Journal of Geophysical Research: Solid Earth 102, 14779-14785 (1997).

4   Frisillo, A. L. & Barsch, G. R. Measurement of single-crystal elastic constants of bronzite as a function of pressure and temperature. Journal of Geophysical Research 77, 6360-6384, doi:10.1029/JB077i032p06360 (1972).

5   Matsui, M. & Busing, W. R. Calculation of the elastic constants and high-pressure properties of diopside, $CaMgSi_2O_6$. American Mineralogist 69 (1984).

6   Isaak, D. G., Ohno, I. & Lee, P. C. The elastic constants of monoclinic single-crystal chrome-diopside to 1,300 K. Physics and Chemistry of Minerals 32, 691-699, doi:10.1007/s00269-005-0047-9 (2005).

Chapter 4

Supplementary 4B include trace element figure of clinopyroxene from Haoti. The pole figures and seismic properties in additional samples of the peridotite xenoliths.
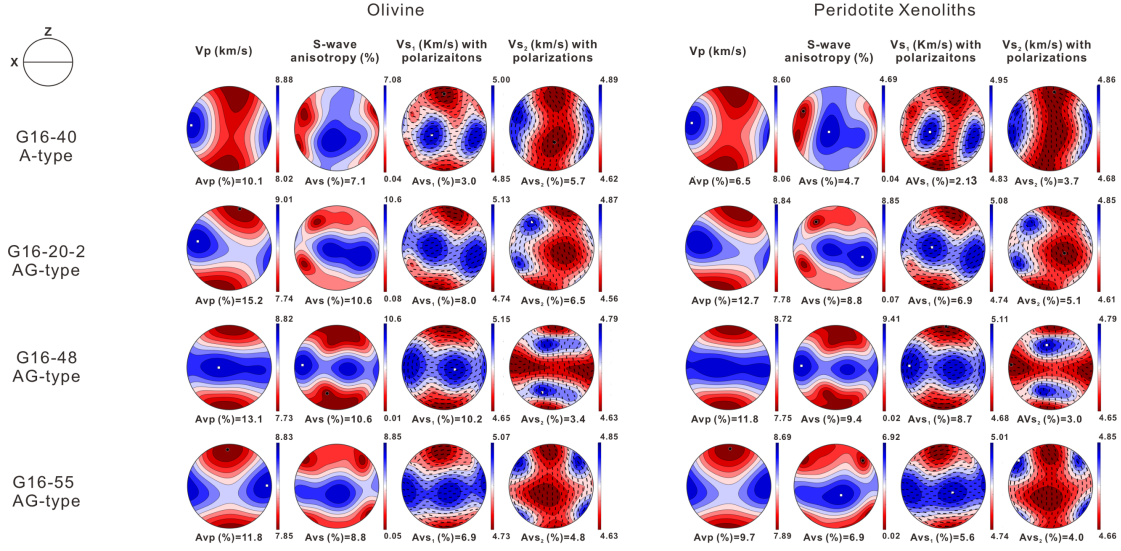
Supplementary 4B-Figure 1.
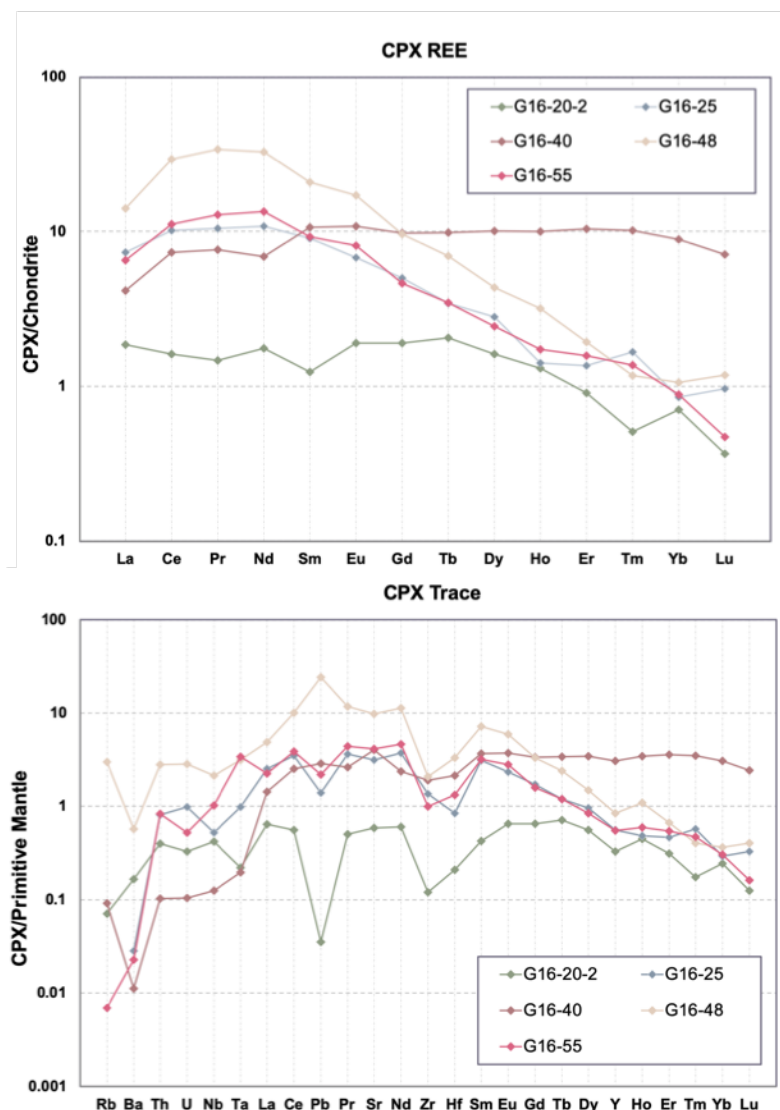
Supplementary Figure 4B-1. Rare earth elements (REE) and Trace element compositions of clinopyroxene from Haoti xenoliths normalized to Cl chondrite (Anders and Grevesse, 1989) and primitive mantle (Sun and McDonough, 1989) respectively.

Supplementary 4B-Figure 2.

	Olivine			Orthopyroxene			Clinopyroxene			
	[100]	[010]	[001]	[100]	[010]	[001]	[100]	[010]	[001]	
G16-40	N=752 MD=4.88 pf=1.79	J=4.32 MD=5.78 pf=2.30	M=0.09 MD=5.55 pf=1.54	N=451 MD=9.49 pf=3.05	MD=8.20 pf=2.44	MD=11.37 pf=3.78	N=277 MD=2.81 pf=1.32	MD=4.20 pf=1.50	MD=4.04 pf=1.36	**A-type**
G16-20-2	N=1551 MD=7.49 pf=3.17	J=9.89 MD=18.4 pf=7.08	M=0.35 MD=4.12 pf=2.12	N=323 MD=3.57 pf=1.41	MD=4.44 pf=1.88	MD=5.72 pf=2.55	N=315 MD=2.67 pf=1.34	MD=4.04 pf=1.76	MD=5.46 pf=1.98	**AG-type**
G16-48	N=866 MD=5.25 pf=2.41	J=7.66 MD=15.8 pf=7.08	M=0.29 MD=4.12 pf=2.12	N=258 MD=4.13 pf=1.97	MD=5.25 pf=2.21	MD=9.78 pf=3.88	N=162 MD=9.99 pf=2.75	MD=8.39 pf=2.43	MD=8.81 pf=2.83	
G16-55	N=1838 MD=3.79 pf=1.85	J=4.94 MD=10.2 pf=3.98	M=0.19 MD=3.41 pf=1.69	N=431 MD=6.36 pf=2.21	MD=5.83 pf=2.21	MD=5.90 pf=2.51	N=320 MD=4.06 pf=1.45	MD=4.71 pf=1.70	MD=4.25 pf=1.83	

Supplementary Figure 4B-2. The pole figures for the crystallographic axes of olivine, orthopyroxene and clinopyroxene in xenoliths from Haoti. The CPOs are presented in equal-area, one point per grain, lower-hemisphere projections; the structural reference frame is shown as insert in the upper left. Contours (=6) show multiples of uniform distribution. N is the number of measurements, J-index and M-index is the fabric strength, pf is an index of fabric intensity, and MD is the maximum density.

Supplementary 4B-Figure 3.

Supplementary Figure 4B-3 The seismic properties of the peridotite xenoliths in Haoti calculated from the fabric of the xenoliths. The seismic properties are presented in equal-area, lower-hemisphere projections in the structural reference frame. The four columns are the P-wave velocity (Vp) with anisotropy of the P-waves (AVp); the polarization anisotropy (AVs) and the splitting S-wave velocity (Vs$_1$ and Vs$_2$) with their polarization directions. AVp = [(Vp^{max} – Vp^{min}) / (Vp^{max} + Vp^{min}) /2]×100% and AVs=[(Vs$_1$ –Vs$_2$)]/[(Vs$_1$ +Vs$_2$)/2], whereVs$_1$ andVs$_2$ are the velocities of the fast and slow split S-waves, respectively. AVs$_{1/s_2}$ = [(Vs$_{1/s_2}$^{max} – Vs$_{1/s_2}$^{min}) / (Vs$_{1/s_2}$^{max} + Vs$_{1/s_2}$^{min}) / 2]; insert on the middle left shows the structural reference frame.

Chapter 5

If you imagine the 4,500 million years of Earth's history compressed into a normal earthly day, then humans emerge one minute and seventeen seconds before midnight. The whole of our recorded history, on this scale, would be no more than a few seconds, a single human lifetime barely an instant. Throughout this greatly speeded-up day, continents slide about and bang together at a clip that seems positively reckless. Mountains rise and melt away, ocean basins come and go, ice sheets advance and withdraw. Nothing does for long.

—— 《*A short history of nearly everything*》
Bill Bryson

Summary and conclusions

This dissertation studied the microstructural, petrochemical and seismic properties of mantle peridotite xenoliths from the Tibetan Plateau, which were brought to the surface during different evolutionary stages of the India-Eurasia collision. The presented chapters cover three different groups of xenoliths from southwestern to northeastern Tibet and aim to resolve the deformation mechanisms and processes of the upper mantle and construct a reasonable model for the lithospheric architecture beneath Tibet. Each observation represents a snapshot of the deformation history and can be seen as puzzle piece of the larger picture of the largest active continental collision zone.

5.1 Southwestern Tibet (Lhasa terrane)

Peridotite xenoliths in the southwestern Tibet brought to the surface from upper mantle by Miocene potassic volcanism show crystal preferred orientation of their olivine with a concentration of the [010] directions and a large circle girdle of the [100] and [001] directions (AG-type) with a polarization anisotropy of 4.6 % on

average in directions parallel to the girdle plane. To match the large delay times (1.5 - 2.0 s) observed in southwestern Tibet, the thickness of the lithosphere composed of peridotite with 4.6% anisotropy on average, would require a lithosphere that is at least 150 km to 200 km thick even if the effect of the intrinsic elastic anisotropy of the peridotites on SKS splitting were maximized. Combining the ~70km thick crust, this is in conflict with the known depth of the lithosphere-asthenosphere boundary (~150km). Thus, other mechanisms must be involved to provide a strong seismic anisotropy of the lithospheric mantle underneath southern-central Tibet to attribute to the large delay times. We propose that this mechanism is due to the presence of partially molten domains with high aspect ratio that are aligned sub-vertically enhancing the effect of the intrinsic elastic anisotropy of the peridotites on SKS splitting. The abrupt change of the fast polarization direction from the Lhasa terrane to the Qiangtang terrane may reflect the change of the fabric of olivine which is fundamentally different in the northward subducting Indian lithospheric mantle and in the lithospheric mantle beneath northern Tibet.

5.2 Central Tibet (Qiangtang terrane)

Peridotite and pyroxenite xenoliths from central Tibet were exhumed by Eocene volcanism in the Qiangtang terrane. The peridotite xenoliths can be divided into two fabric types. The xenoliths representing the uppermost lithospheric mantle are refractory and exhibit an AG-type olivine fabric. In contrast, the xenoliths from the lower part were re-fertilized and displays a different fabric characterized by B-type with dominant activation of the [001](010) slip system. By using the seismic properties of xenoliths, we reconstructed the velocity structure from lower crust to upper mantle, which is well comparable to the receiver function imaging from central Tibet. The vertical dichotomy of the mantle simplifies the interpretation of geophysical data. In particular, it renders the hypothesis postulating the presence of three different

lithospheric domains pertaining to India-, Tibet- and Eurasia obsolete. A possible deformation history in central Tibet is that at an early stage a pre-existing refractory lithospheric mantle experienced a small degree of partial melting. Subsequently, it was heated from the bottom and formed a fertile mantle in the lower part with B-type olivine fabric.

5.3 Northeastern Tibet (Songpan-Ganze terrane)

Peridotite xenoliths from northeastern Tibet record complex deformation processes at the margin of the Tibetan Plateau. A series of alkaline and ultra-mafic volcanoes is situated on the Songpan-Ganze terrane and actively erupted between 7.1 and 23 Ma. The olivine fabric mainly shows AG-type, with a few (010)[100] patterns (A-type). Unlike the xenoliths from southwestern and central Tibet, these peridotite xenoliths are characterized as extraordinary with strong anisotropy of 8 % on average, which would cause about 1.16s delay times within a 70 km thick lithospheric mantle. If it is combined with the crustal contribution to anisotropy (~0.5s), no other mechanism is required to explain the delay times of about ~1.5s delay observed in this area. This finding may well explain the apparent long-term discrepancy between delay times that are comparable to those in central Tibet, while the lithosphere in northeastern Tibet is thinner than in southern-central Tibet.

Acknowledgement

First and foremost, special thanks go to my supervisors, Prof. Rainer Abart and Prof. Theo Ntaflos, who all supported and mentored me throughout this work. By looking back at what happened on me in the past three years, I knew I was very lucky to have such outstanding supervisors. Rainer kept me well, as a whole, on the right track of the project, despite he is very busy as a director of lithospheric research faculty. He taught me how to think and organize the evidence into words. Theo help me a lot on the analytical measurements and understanding the use of analytical data. Their mentoring inspired me with a better understanding of how to raise and approach scientific questions. More important, their attitude to science and knowledge in addressing problems led to a positive direction towards my future research. They taught me how the work should be appropriately presented to audience. They also provided me enormous help in speaking and particularly writing English.

Thanks to everyone who helped with sample collection and experiments: to Shang Yongmei, Cheng Lining, Duan qingbao for sample collection preparation; to thank Ma Xi, Luo Tao and Franz Kiraly for helping the EBSD, LA-ICP-MS, LA-MC-ICP-MS, and EMPA analysis; to Eric Löberich and Xie Chengliang for their knowledge and expert of code work; to Prof. Wang Qin and Hadrien Henry for their expert instruction in the use of the MTEX; and to Thomas Griffiths for suggestions on the manuscript. I also thank my fellow PhD students, visitors and post-docs (Roman Schuster, Annika Stockinger, Bian Ge, Gerlinde Habler, Olga Ageeva, Franz mikysek, Elena Petrischcheva, Zhang Shaohui, Hou Lei, Hou Zhaoliang, ...) who helped me to live and work well in Wien.

I could not use any words (both English and Chinese) to fully express how I appreciate what they gave me. Everything I learned from them will benefit me continuously through my life.

Thanks

Curriculum Vitae

Yu Yang   **Email:** yangy29@unet.univie.ac.at

yangyugeo@gmail.com

_____

Education

2006.9 –2010.6	**China University of Geosciences in Beijing** *Bachelor of Geophysics*

2012.9 –2014.06	**China University of Geosciences in Beijing** *Master of in Petrology, Mineralogy, Ore Geology,* *Supervisor: Jun Deng*

2014.9 – present	**Utrecht University** *PhD Candidate in Geosciences (until 06.2017)* *Supervisors: Christopher Spider* **University of Vienna** *PhD Candidate in Geosciences* *Supervisors: Rainer Abart；Theo Ntaflos*

Research experience

<u>Doctoral studies</u>

'*Deformation Behavior and Seismic Anisotropy of Tibetan Lithosphere: constraints from mantle xenoliths*'

Focus on the fabrics of mantle xenoliths and seismic anisotropy of Tibetan Plateau.

Integrated microstructural analysis combining optical microscopy, SEM, EBSD,

Integrated mineral chemical analysis combining Microprobe, in-situ LA-ICP-MS, in-situ LA-MC-ICP-MS.

Acquisition and evaluation of EBSD data using AZtect software, CHANNEL 5 and

the Matlab toolbox MTEX.

Acquisition and evaluation of SKS data using GMT.

Calculation of seismic anisotropy of mantle xenoliths using the MTEX

Evaluation of seismic velocity of lithospheric mantle beneath Tibet using the Matlab

Master studies

'*Petrophysical Experiments of Polymetallic Deposit and numerical simulations of hydrothermal gold mineralization*'

'*Numerical studies on temporal - spatial distribution of pore pressure in response to reservoir impoundment—exemplified by Zipinpu reservoir*'

Study on the transport property in low permeability materials.

Experience of permeability experiments with host rock and fault zone.

Experience of conductivity experiments to describe the fluid diffusion.

Simulation the fluid transport in the weak zone. i.e.: the process of hydrothermal gold mineralization; the reservoir trigger earthquake.

Publication

Scientific papers:

1. **Yang, Y.**, Abart, R., Yang, X., Shang, Y., Ntaflos, T. and Xu, B., **2019,** Seismic anisotropy in the Tibetan lithosphere inferred from mantle xenoliths. ***Earth and Planetary Science Letters,*** 515: 260-270.

2. **Yang, Y.,** Duan, Q.B., **2015**, Numerical studies on temporal - spatial distribution of pore pressure in response to reservoir impoundment—exemplified by Zipinpu reservoir, ***Seismology and Geology,*** 37(2): 510-523

3. **Yang, Y.**, Chen, J., Yang, X., **2014,** Experimental studies on the relationship between compressional wave velocity and porosity, ***Chinese Journal of Geophysics,*** 57(6): 1883-1890***.***

4. **Yang, Y.,** Chen, J., Yang, X., et al., **2010,** Does Alignment of Melt Enhance Seismic Anisotropy beneath Tibet? ***Seismology and Geology,*** 32:59-69.

5. Shang, Y., **Yang, Y.** (***Corresponding Author***), Yang, X., **2020,** Origin of the middle-lower crust seismic anisotropy in SE Tibetan Plateau-constrained from the EBSD data on deep-derived xenoliths in Liuhe, Yunnan Province, ***Chinese Journal of Geophysics,*** 63(2): 460-477***.***

6. Shang, Y., Yang, X., **Yang, Y**., **2019,** Crystallographic preferred orientation (CPO) of anisotropic minerals in the lithosphere and its significance to the study of lithosphere dynamic, ***Seismology and Geology,*** 41(3): 704-725.

7. Yang, X. S., Chen J.Y., Duan Q.B., **Yang, Y.,** Chen, J.Y., **2014,** Geochemical and Petrophysical Responses to Fluid Processes within Seismogenic Fault Zones: Implications from Mineralogical, Petro-chemical and Petrophysical Data, ***Seismology and Geology,*** 36(3): 862-881.

8. Yang, X., **Yang, Y.,** Chen, J., **2013,** Pressure dependence of density, porosity, compressional wave velocity of fault rocks from the rupture of the 2008 Wenchuan earthquake, China, ***Tectonophysics,*** 619–620:1-194.

9. Yang, X., Chen, J., **Yang, Y., 2011,** Experimental Studies on Seismic Anisotropy Enhanced by Alignment of Melt: Implication for the Origin of Abnormal Anisotropy in Tibetan Crust, ***Journal of Earth Science***, 22: 32-39.

Thesis：

- **Yang, Y.,** 2010, Filter Design and Application: Abnormal Natural-Potential Detection and Extraction, ***B.Sc. Thesis of China University of Geosciences,*** Beijing.

- **Yang, Y.,** 2014, Petrophysical Experiments of Polymetallic Deposit and Numerical Modeling for Hydrothermal Mineralization, Songxian, Henan, ***M.Sc. Thesis of China University of Geosciences,*** Beijing.

International Conferences

Poster: **American Geophysical Union Fall Meeting**, 2008, San Francisco, USA., Experimental studies on seismic anisotropy enhanced by melt

Talk: **European Geosciences Union,** 2018, Vienna. Geodynamic Implication and Constraint of seismic anisotropy in Tibetan Lithosphere: Inferred from Mantle Xenoliths

Poster: **European Geosciences Union**, 2019, Vienna, Fabric and seismic anisotropy of mantle xenoliths from the NE margin of the Tibetan plateau and their dynamic implications

Talk: **Goldschmidt Conference** 2020, Heterogeneous lithosphere in Central Tibet: insights from the Mantle Xenoliths